Managing Tritium Inventory and Release with Carbon Materials in a Fluoride Salt-Cooled High-Temperature Reactor

by

Stephen Tsz Tang Lam

B.A.Sc., Chemical Engineering, 2013

University of British Columbia

Submitted to the department of Nuclear Science and Engineering
in partial fulfillment of the requirements for the degree of
Master of Science in Nuclear Science and Engineering

at the
MASSACHUSETTS INSTITUTE OF TECHNOLOGY
September 2017

Signature of Author:____
Stephen T. Lam
July 26, 2017

Certified by:____
Ronald G. Ballinger
Professor of Nuclear Science and Engineering, and Materials Science and Engineering
Thesis Supervisor

Certified by:____
Charles W. Forsberg
Principal Research Scientist, Nuclear Science and Engineering
Thesis Reader

Accepted by:____
Professor Ju Li
Battelle Energy Alliance Professor of Nuclear Science and Engineering
Professor of Materials Science and Engineering
Chair, Department Committee on Graduate Students

THIS PAGE IS LEFT INTENTIONALLY BLANK

Managing Tritium Inventory and Release with Carbon Materials in a Fluoride Salt-Cooled High-Temperature Reactor

by

Stephen Tsz Tang Lam

Submitted to the Department of Nuclear Science and Engineering
On July 26, 2017, in partial fulfillment of the
requirements for the degree of
Master of Science in Nuclear Science and Engineering

Abstract

The Fluoride Salt-Cooled High-Temperature Reactor (FHR) is an advanced reactor concept, that uses molten-salt coolant and solid-uranium fuel composed of graphite and silicon carbide-encapsulated tri-structural isotropic (TRISO) particles. The primary coolant salt is known as flibe ($^7Li_2BeF_4$), which was chosen for its desirable thermal-hydraulic and neutronic properties. Under irradiation, coolant salts containing lithium capture neutrons generating tritium in quantities that are several orders of magnitude larger than the amounts generated by existing light water reactors. Adsorption technology is proposed, using chemically compatible carbon materials for the capture and control of tritium in the FHR.

Various nanoporous activated carbon, graphene and nuclear graphite materials have been characterized. This includes the determination of BET surface area, total pore volume, average pore size, and pore size distribution by performing low-temperature gas adsorption experiments and applying microscopic thermodynamic theory. In addition, morphological analysis was conducted with scanning electron microscopy. Hydrogen was used as a surrogate. Its chemisorption on these materials have been measured and modeled at the reactor conditions of 700°C and pressures under 4 kPa. Models suggest that the total measured solubility of hydrogen includes a combination of dissociative and molecular adsorption. Carbon materials containing larger volumetric fractions of micropores (width < 2 nm) generally exhibited a higher hydrogen capacity. Further, the presence of micropores was associated with a relatively weak and reversible form of hydrogen chemisorption. At 500 Pa, microporous carbon materials captured 50 times more hydrogen than graphite, which was previously known to be the largest hydrogen sink at reactor conditions.

The coupled effects of generation, chemical speciation, adsorption and diffusion of tritium in the FHR system were simulated over 200 full-power days. It was found that an adsorption column using high-performance carbon-based catalyst adsorbed substantial amounts of tritium and reduced the peak release rate from 2400 Ci/day to 40 Ci/day for the 236 MWt FHR. Further, the total tritium inventory in the system decreased by more than 70%, from 68,400 Ci to 19,400 Ci. This demonstrates that adsorption technology can greatly reduce the risk of radiological release during normal operation and reactor transient events.

Thesis Supervisor: Ronald G. Ballinger
Title: Professor, Nuclear Science and Engineering and Materials Science and Engineering

Thesis Reader: Charles W. Forsberg
Title: Principal Research Scientist, Director and Principal Investigator of the Fluoride Salt-Cooled High-Temperature Reactor Project, Nuclear Science and Engineering

Thesis Acknowledgements

Above all, I would like to thank my advisors Professor Ron Ballinger and Dr. Charles Forsberg for their constant insights and support, without which this work would not have been possible. Next, I would like to thank my collaborators: Cristian Contescu, Tim Burchell and their colleagues from Oak Ridge National Laboratory who have provided valuable consultation and Professor Raluca Scarlat and her group members from UW Madison with whom I have had many fruitful discussions. I would like to show my gratitude to John Stempien as he did a tremendous amount of work on tritium prior to my arrival and made himself available for discussion as well as provide valuable resources. Additionally, I would like to thank our UROP student Jacob Miske, who has provided a helping hand around the lab. Finally, I would like to acknowledge the Chinese Academy of Sciences for supporting this work.

On a personal level and in no particular order, I would like give thanks to those who have positively contributed to my life during the completion of this work: My mother, father and siblings; my roommates, Shikhar and Guillaume; colleagues & comrades at the Fusion Center who I hold in high regard, Artyom, Christopher, Malik and Samuel; those with whom I've had significant relations, Emily; my cat, Pawl Ryan; friends who were kind enough to visit during my time in Cambridge, Abhinav, Mehul, Ashish, Bobby, Bhavik, Wilson, David, Elina, Gerard, Siobhan, Jae, Louis and Andrew; and my interest group, Andrew, Benjamin, Kevin, Kiki, and Matthew.

Table of Contents

List of Tables

List of Figures

List of Acronyms

AC	Activated Carbon
AHTR	Advanced High-Temperature Reactor
ASTM	American Society for Testing and Materials
BET	Brunauer–Emmett–Teller
CAS	Chinese Academy of Sciences
CFR	Code of Federal Regulations
CTAH	Coiled Tube Air Heaters
DHX	DRACS Heat Exchanger
dpa	displacements per atom
DWHX	Double-walled Heat Exchanger
DOE	United States Department of Energy
DRACS	Direct Reactor Auxiliary Cooling System
EAC	Extruded Activated Carbon
EDS	Energy Dispersive Spectroscopy
EPA	Environmental Protection Agency
FHR	Fluoride Salt-Cooled High-Temperature Reactor
flibe	LiF - BeF_2 molten salt
GAC	Granular Activated Carbon
GNP	Graphene Nanoplatelets
HTGR	High-Temperature Gas-Cooled Reactor
HX	Heat Exchanger
IPyC	Inner Pyrolytic Carbon
INL	Idaho National Laboratory
ISO	International Standards Organization
IUPAC	International Union of Pure and Applied Chemistry
MIT	Massachusetts Institute of Technology
Mk-1	Mark-1 Pebble-Bed FHR Design Concept
MSBR	Molten Salt Breeder Reactor
MSR	Molten Salt Reactor
MSRE	Molten Salt Reactor Experiment
MW/e/t	Megawatt/electric/thermal

NEUP	Nuclear Energy University Program
NGCC	Natural Gas Combined Cycle
NLDFT	Non-local Density Functional Theory
NRC	Nuclear Regulatory Commission
OPyC	Outer Pyrolytic Carbon
ORNL	Oak Ridge National Laboratory
OSU	Ohio State University
PAC	Powdered Activated Carbon
PB-FHR	Pebble-Bed FHR
PRF	Permeation Reduction Factor
QSDFT	Quenched-Solid Density Functional Theory
REBCO	Rare-earth Barium Copper Oxide
SA	Surface Area
SEM	Scanning Electron Microscopy
TCHX	Thermosyphon-Cooled Heat Exchangers
TRISO	Tristructural Isotropic Coated Particle Fuel
UCB	University of California, Berkeley
UNM	University of New Mexico
UW	University of Wisconsin
XPS	X-ray Photoelectron Spectroscopy
XRD	X-Ray Diffraction

Chapter 1.

Introduction

A new reactor concept was proposed in the last decade by Forsberg, Peterson and Pickard [1] that combines emergent technologies including a low vapor-pressure fluoride molten salt, structurally robust coated-particle fuel, and an open-air Brayton cycle. This concept is called the Fluoride Salt-Cooled High-Temperature Reactor (FHR). Due to interest and support from the U.S. Department of Energy (DOE) through the Nuclear Energy University Program (NEUP), an integrated research project between universities, national laboratories and Westinghouse Electric Company was conducted, enabling continued research and development of the FHR concept [2][3].

The FHR offers various economic and safety improvements in comparison to conventional light water reactors. The molten-salt coolant's high boiling point allows operation at high temperature and atmospheric pressure, resulting in a thermal-to-electric efficiency of nearly 42.7% and a greatly reduced demand on pressure vessel and containment design. The high volumetric heat capacity of the coolant (4.67 J/cm^3-K) and high design temperature of the particle fuel (1650^{o}C) allows passive decay heat rejection and significantly reduces the probability of fuel failure in the event of active system failures [4]. Further, the fuel's tristructural encapsulation with SiC improves the proliferation resistance of spent fuel and provides additional barriers to degradation and thus higher spent fuel retention in waste repositories.

The first chapter of this thesis provides context for the work done by briefly describing the design basis of the FHR and outlining the major challenges that are currently faced. The research objectives that deal with these challenges are outlined along with the potential impact of the work that has been completed. The remaining chapters of the thesis will provide further required background information and describe the methods of simulation, modeling and experimentation that were employed and outline the results. These sections are summarized in more detail at the end of this chapter.

1.1. The Fluoride High-Temperature Salt-Cooled Reactor

While tritium control is generally applicable to a variety of molten-salt systems, the current focus of this work is on the FHR. As such, the FHR design is used to define the requirements of the mitigation systems investigated, and is described in this section.

The combination of the fuel and coolant properties coupled to an air-Brayton cycle results in the possibility of a power reactor that operates with much higher thermal safety margins, improved economics and resistance to catastrophic events in comparison to conventional light water reactors. While most systems have not yet been fully designed and the FHR can take many different configurations, a design basis was provided by University of California, Berkeley (UCB) in 2014 [5] for the Mark-1 (Mk-1) reactor, which will serve here as a functional guideline for technology development associated with FHRs. This section provides a general overview of the reactor system, and outlines in detail the components of the FHR most relevant to the thesis topic.

A system overview of the FHR is provided in Figure 1.1, which shows the primary system coupled to the Brayton cycle. In this system, heat is transferred from primary salt operating at 600 – 700 °C and atmospheric pressure to compressed atmospheric air at 418.7°C and 18.58 bar via the coiled tube air heaters (CTAHs). One feature unique to FHRs that is shown in the diagram is the gas co-firing capability whereby natural gas is injected and combusted in a gas turbine. This allows for better load following on the grid and plant optimization by allowing the purchase of gas when costs are low to produce electricity at a lower per megawatt (MW) cost. This provides a more flexible power output with peaking capabilities able to bring the reactor/system from the normal operating power of 100 MWe to 242 MWe. The outlet stream from the gas turbine enters the heat-recovery steam generator, which can power a Rankine cycle to provide process heat or generate more electricity. In combination, these have the effect of increasing the thermal efficiency to 66.4 % and increasing plant revenues by more than 40% [5][2][6].s

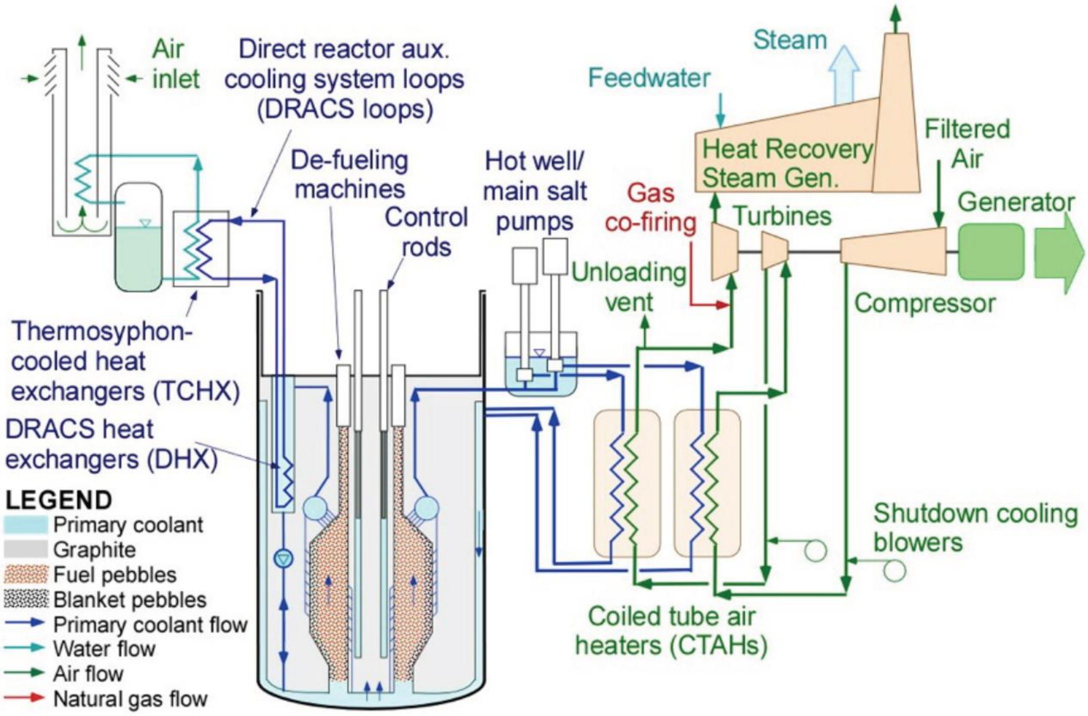

Figure 1.1: FHR system level overview

Another feature of the FHR that is made possible by the high-heat-capacity coolant is the use of a passive decay-heat removal system named the Direct Reactor Auxiliary Cooling System (DRACS). During a loss of flow incident where the primary pumps stop, the DRACS system allows passive removal of the decay heat by natural circulation. In the event where inlet flow to the reactor stops, a fluidic diode activates to allow natural circulation of fluid from the reactor core to the DRACS heat exchanger (DHX) where heat is transferred to a secondary molten salt. That secondary salt rises in the DRACS to exchange heat with water in the thermosyphon-cooled heat exchangers (TCHX), where the heat is then transferred to the air via a chimney-condenser system [5].

1.1.1. Reactor Core and Fuel

The reactor vessel proposed by UCB consists of an annular reactor core where the pebble fuel is fed through injection channels placed around the circumference of the core. The pebble fuel can be fed while operating, eliminating the down time that would be required for refueling outages. The fuel pebbles, which have a lower density than the salt, slowly rises to the top and are removed from the core. To improve operability and neutron economy, an outer blanket of graphite pebbles surrounds the fuel pebbles and stationary graphite reflectors make up the inner and outer core annulus, allowing greater neutron thermalization. The outer graphite blanket can be assessed for maintenance and can be readily removed and replaced online to control radiation damage. Control rods, shutdown blades, and instrument guide tubes are located in the center of the upper core region. The outer reflectors would be held against the barrel using a system of alignment and retaining rings similar to the design of the Molten Salt Breeder Reactor (MSBR) [7]. In a test reactor, the core barrel would be constructed of the same metallic material as the outer vessel for simplicity.

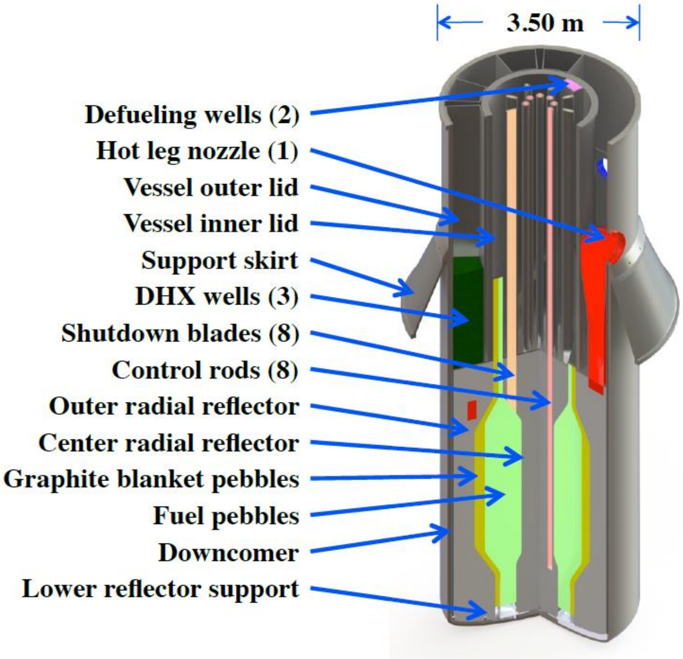

Figure 1.2: Mk-1 PB-FHR reactor core layout

The handling and processing of the fuel and blanket pebbles are not shown in the diagram but consist of various separation stages described in the UCB technical description [5]. The fuel pebbles themselves are 3.0 cm diameter spheres with an annular fuel region consisting of 20% low-enriched uranium, shown in Figure 1.3. The fuel region in the pebble is isolated from the salt with an outer layer of high density graphite and the inner region of the pebble is a low density supporting graphite. The annular design of the fuel reduces peak temperature, and aids in limiting the release of fission products, which increases strongly with increasing temperature [8].

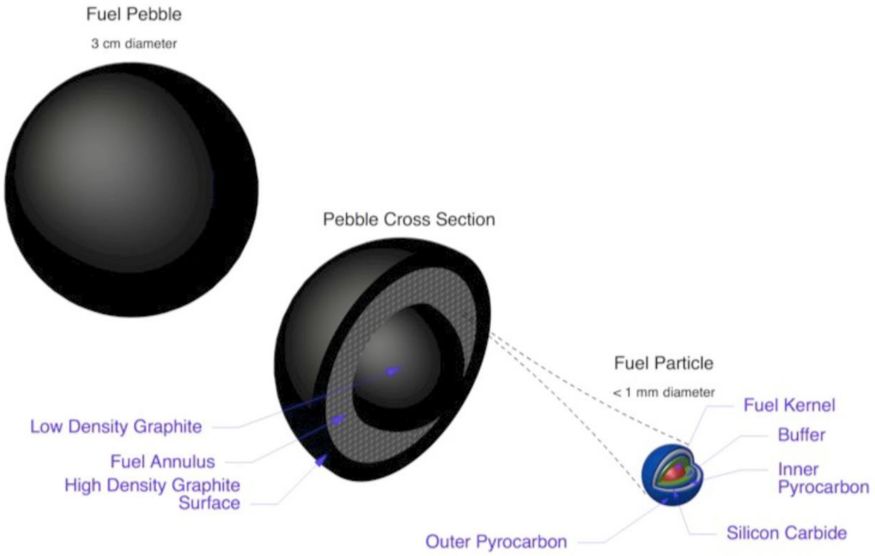

Figure 1.3: PB-FHR fuel element schematic [5]

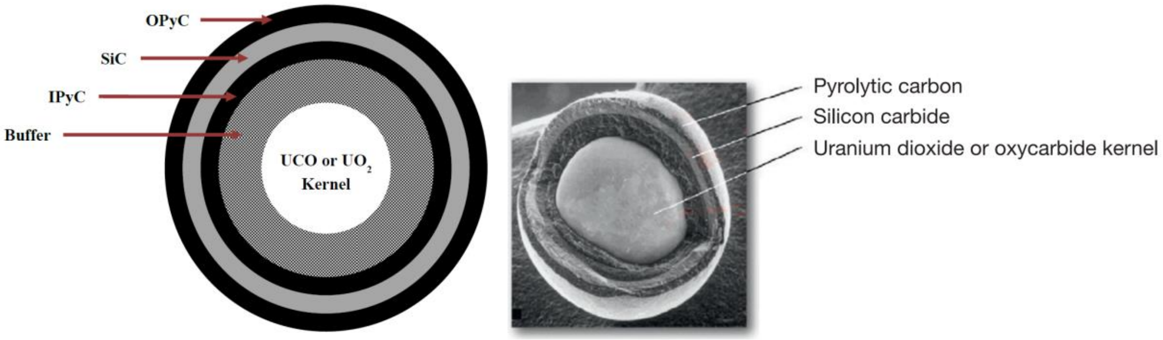

Figure 1.4: a) Schematic representation of TRISO particle on left. b) 3D photomicrograph of TRISO particle showing layers [9]

The fuel region in the pebble is composed of smaller tristructural isotropic (TRISO) coated particle fuel held in a graphite matrix, which have been under development since the 1960s, originally for High-Temperature Gas-Cooled Reactors (HTGRs) [10]. There are various forms in which TRISO particles can be made into fuel elements, including cylindrical compacts as in the case of the Peach Bottom Reactor, plates as originally proposed by Oak Ridge National Laboratory (ORNL) or spherical pebbles as shown in Figure 1.1, which is proposed for the Mk-1 PB-FHR [10]. The TRISO particles are typically less than 1 mm in diameter and contain several barriers for encapsulation of fission products. The fuel itself is at the center of the particle and is surrounded first by the 'buffer', a layer of porous carbon which accommodates fission recoils, fuel swelling and fission gases produced during operation. A dense layer of pyrolytic carbon, referred to as the inner pyrolytic (IPyC) carbon layer is used to protect the fuel kernel from reactive chlorine compounds that are used for the chemical vapor deposition of the surrounding SiC layer. The SiC layer provides the particle with structural integrity and strength to prevent fracture as a result of thermal and mechanical stresses. On the external surface, a pyrolytic carbon, referred to as outer pyrolytic carbon (OPyC) layer, protects the particle during bonding and formation of the fuel element. For reference, typical dimensions of TRISO particles are shown below for a couple types of TRISO fuels.

Table 1.1: Particle dimensions of two types of TRISO fuel [10]

	EUO 2308	**AGR-1**
Fuel Diameter (μm)	497	350
Buffer Thickness (μm)	94	104
IPyC Thickness (μm)	41	39
SiC Thickness(μm)	36	36
OPyC Thickness (μm)	40	41
Overall Particle Diameter (μm)	895	800

The batch of TRISO named EUO 2308 described in Table 1.1, was first manufactured and tested in Julich, Germany around 1990 and was part of several irradiation experiments including in experiments FRJ2-K13 and SL-P1 [10]. The second TRISO particle type shown in Table 1.1 is the baseline TRISO for advanced gas reactors AGR-1 and underwent irradiations up until 2009 as a part of a fuel development program at Idaho National Laboratory (INL) [11].

1.1.2. Reactor Materials

The selection of materials for the key reactor components involve balancing various trade-offs and engineering constraints, which were reviewed in detail in the 3rd FHR workshop in August 2012 [12]. These constraints include the design stresses specified by the ASME Boiler Pressure Vessel Code Section III, Div. 5, resistance to corrosion, material aging, and thermal creep. To limit the corrosion, it was determined that one metallic material should be used for all metallic components facing the salt. Stainless steel types 316 or 304 are good choices due to the large base of experience that exists for these materials, and low cost relative to Alloy N. Further, during the MSBR experiments, salt loops operated with both of these materials. Stainless steel type 316 was operated in a LiF-BeF2-ZrF4-UF4-ThF4 salt for 4491 hours [13]. Thus, for the baseline test-reactor design, type 316SS was chosen for the reactor pressure vessel, reactor internals including core barrel, structural supports, CTAH tubes, cold legs and hot legs and is estimated to have a required mass of

408, 420 kg in the Mk-1 PB-FHR. In the power conversion part of the cycle, the most commonly used material is high-alloy steel, where it is estimated that 710, 000 kg would be required based on typical amounts used in conventional natural-gas combined-cycle (NGCC) power plants. The next most prevalent material in the system is graphite, with an estimated density of 1, 740 kg/m^3, which as shown in the previous section is used for the outer and center reflector core of the vessel and is estimated to have a total required mass of 49, 250 kg in the Mk-1. Other important materials that are used in the system in much smaller quantities include carbon fiber reinforced composites (CRFC) for lining the instrument guide tubes and sample holes, and SiC composites used as structural materials in shutdown blades and control rods [5].

1.1.3. Reactor Coolant

There are many different options for the choice of molten salt mixture in a PB-FHR. Grimes originally published a study on the selection of mixtures, which analyzed the various demands required by different types of molten salt reactors [14]. The most important and FHR-relevant of these system demands are as follows:

- The fuel constituents must have a reasonably low capture cross section for neutrons in the chosen flux spectrum
- The fuel must have some capacity to dissolve and accommodate fission products generated during operation
- The coolant must be thermally stable and have a low vapor pressure under the full range of operating temperatures of the reactor
- The coolant must have heat transfer properties that allow sufficient cooling to minimize peak temperatures of the system
- Reactor materials in contact with the coolant must be relatively inert
- The coolant must be stable under irradiation

Concerning the economics of the reactor, it is preferable that the coolant is inexpensive and have a low life cycle cost, which includes the cost of the processing and decontamination steps. Based on Grimes' original analysis, Williams performed a coolant assessment for an Advanced High-Temperature Reactor (AHTR) operating in the thermal spectrum in 2006 [15]. Williams gave a summary of important properties for various candidate salts. His results are shown in Table 1.2. First considering the base elements of the salt constituents, he narrowed the list of possible elements based on neutron capture cross sections in the thermal range. He identified the main suitable elements to be fluorine, beryllium, boron-11, lithium-7, zirconium, rubidium, and sodium [15]. For boron-11 to be used as a salt component, a high isotopic enrichment would be required. To date, this has not been technically considered or economically evaluated. Thus, the main non-metal of interest among the species listed is Fluorine. From the candidate salts, LiF-BeF_2 (also known as flibe) has by far the best neutronic properties, as indicated by the low neutron capture and the high moderating ratio.

Table 1.2: Summary of properties of possible coolants from Williams [15]

			Heat Transfer Properties at 700°C				
Salt[a]	Melting Point	900°C Vapor Pressure	ρC_p	Viscosity	Thermal Conductivity	Neutron Capture[b,c]	Moderating Ratio[b]
Units	°C	mmHg	cal/cm^3-°C	cP	W/m-K	-	-
LiF-BeF_2	460	1.2	1.12	5.6	1.0	8	60
NaF-BeF_2	340	1.4	1.05	7	0.87	28	15
LiF-NaF-BeF_2	315	1.7	0.98	5	0.97	20	22
LiF-ZrF_4	509	77	0.90	> 5.1	0.48	9	29
NaF-ZrF_4	500	5	0.88	5.1	0.49	24	10
KF-ZrF_4	390	-	0.70	< 5.1	0.45	67	3
Rb-ZrF_4	410	1.3	0.64	5.1	0.39	14	13
LiF-NaF-ZrF_4	436	~5	0.84	6.9	0.53	20	13
LiF-NaF-KF	454	~0.7	0.91	2.9	0.92	90	2
LiF-NaF-RbF	435	~0.8	0.63	2.6	0.62	20	8

[a] Salt compositions are given by Williams; nuclear calculations use 9.995% Li-7
[b] Compositions based on energy range from 0.1 to 10 eV
[c] Neutron capture relative to graphite

For the thermochemical properties, the principle consideration is the melting point, which dictates the allowable minimum operating temperature of the system. At any point in the reactor, a sufficient margin, typically 100°C, above the melting point must be maintained to ensure that the salt remains in the liquid phase. Thus, mixtures with prohibitively high freezing points can be eliminated as candidate salts. Other desirable considerations include fluid density, heat capacity, conductivity and viscosity. Fluids that experience a large density change with temperature can improve natural circulation, high heat capacity and density promotes better heat transfer by increasing the product of Reynolds and Prandtl number, and high conductivity increases the overall heat transfer coefficient. As shown in the table, all the salts have relatively good heat transfer characteristics, with the flibe having the highest density*heat capacity (ρ_{C_p}) and highest thermal conductivity. A lower viscosity is clearly desirable as it increases the turbulent heat transfer and decreases the load on the pumps. The majority of the candidate salts all exhibit a relatively low viscosity at 700°C. Finally, low vapor pressure is a desirable property, as low vapor pressure salts exert significantly less pressure on the system and escape via the gas phase at a much slower rate. Inevitably, molten salt reactors require a purge gas or blanket gas system and thus both the vapor pressure and vapor species are important considerations. The candidate salt with the lowest vapor pressure is LiF-NaF-KF although the lithium and beryllium based salts also exhibit relatively low vapor pressures.

Finally, salt choice must account for corrosion. One must consider both the oxidative species in the salt and any unstable species that are present in the material, with respect to the salt chemical potential. Unlike in conventional aqueous systems, it has previously been found that oxidation products are often soluble in fluoride molten salt mixtures [16], which means that a passivation layer may not form to inhibit corrosion. In this context, the thermodynamic condition of the salt becomes a key driver of corrosion. This thermodynamic condition is considered in terms of species Gibbs free energies and coolant redox potential. Based on free energy calculations of all the metal fluorides that can be formed by attack on the different elements in structural materials, Cr in the metal is the most active. For example, in comparison between Cr and Ni, the corrosion of Cr would proceed as shown in (1.1):

$$\mathrm{Cr} + \mathrm{NiF_2} \rightarrow \mathrm{CrF_2} + \mathrm{Ni} \tag{1.1}$$

Where the Gibbs free energy is minimized by the formation of CrF_2, which shows that Cr would be selectively attacked before Ni. By applying redox controls to make a salt mixture more reducing, oxidation of metals can be significantly limited. However, depending on the salt and material combinations, a salt that is too reducing could create compatibility issues such as the reduction of the salt itself or the formation of carbides where graphite materials are used. The effects of redox, specifically with respect to FHR systems, are discussed further in Chapter 2.2.2.

On the basis of its thermal hydraulic and neutronic properties, flibe is clearly among one of the best candidates and therefore has been chosen as a baseline coolant in the FHR design basis.

Specifically, the expected flibe eutectic composition of 66.7 LiF-33.3 BeF_2 has been chosen where the melting point is 460°C as given in the phase diagrams from Williams [15] and Sohal [17]. However, there are significant drawbacks that must be highlighted. Primarily, one of the key concerns with flibe is the generation of radioactive tritium in the form of TF. Tritium is both a radiological and corrosion concern and is one of the key challenges in the FHR roadmap [4]. Additionally, beryllium toxicity must be strictly managed and controlled [5].

1.2. The Tritium Challenge

Tritium production in molten salt reactors was first observed during the Oak Ridge National Laboratory Molten Salt Reactor Experiment (MSRE), which operated from 1965 to 1969 [18]. Near the end of the MSRE operation, tritium production increasingly gained attention and was considered one the key problems that needed to be solved in molten salt systems. The best estimate for tritium generation rates was approximately 54 Ci/full-power day for the 7.3 MWt test reactor [19]. After shutdown of the reactor, tritium was measured in various reactor components by radiographic analysis. The tritium distribution in the system is shown in Figure 1.5, where the majority of the tritium simply escaped to the environment via the off-gas system. The next largest known sink for tritium was the graphite inside the core, which adsorbed approximately 8 Ci/full-power day or 15% of the total tritium that was generated.

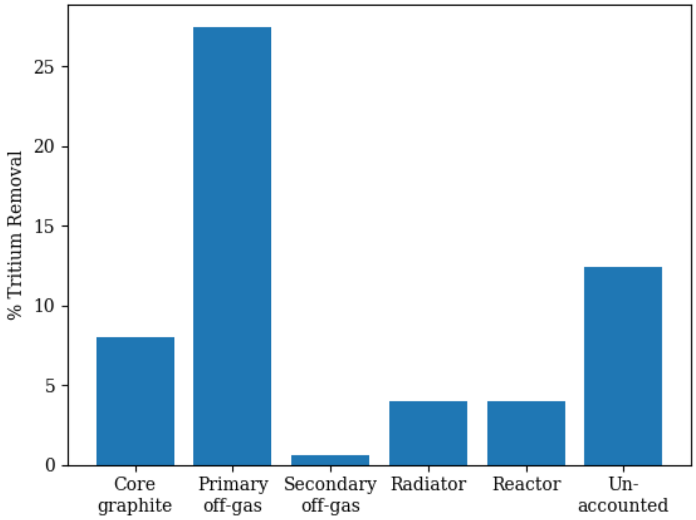

Figure 1.5: Graphical representation of measured tritium distribution in the MSRE [19]

In 2013, ORNL published an FHR technology development and demonstration roadmap, which provided recommendations for the most immediately relevant focus areas, based on current technology gaps [20]. Tritium generation was considered among the most important problems to resolve due to the unique challenges it posed in FHRs. In the FHR, the amounts of tritium produced are significantly larger than in conventional water reactors. However, a tritium capture technology that can be directly used in molten salt systems has yet to be demonstrated in any existing applications. Further, tritium presents a greater challenge in molten-salt reactors than in water reactors due to the corrosiveness of the tritium species that is formed in salt as well as the high temperature of operation, which results in increased tritium release to atmosphere. Tritium in an FHR system is generated through the following reaction pathways:

$$ {}^{6}_{3}\mathrm{LiF} + \mathrm{n} \rightarrow {}^{4}_{2}\mathrm{He} + {}^{3}_{1}\mathrm{HF} \tag{1.2}$$

$$ {}^{7}_{3}\mathrm{LiF} + \mathrm{n} \rightarrow {}^{4}_{2}\mathrm{He} + {}^{3}_{1}\mathrm{HF} + \mathrm{n}' \tag{1.3}$$

$$ {}^{19}_{9}\mathrm{F} + \mathrm{n} \rightarrow {}^{17}_{8}\mathrm{O} + {}^{3}_{1}\mathrm{H} \tag{1.4}$$

$$ {}^{9}_{4}\mathrm{BeF}_2 + \mathrm{n} \rightarrow {}^{4}_{2}\mathrm{He} + {}^{6}_{2}\mathrm{He} + 2\mathrm{F} \tag{1.5}$$

$$ {}^{6}_{2}\mathrm{He} \rightarrow {}^{6}_{3}\mathrm{Li} + \mathrm{e}^- + \bar{\nu}_e \left(t_{\frac{1}{2}} = 0.8\ \mathrm{sec}\right) \tag{1.6}$$

In a flibe-cooled FHR, tritium is produced as TF (also written as ^{3}HF) predominately due to the thermal neutron reaction of Li-6 shown in Equation (1.2). In order to limit the tritium production, the Mk-1 proposes to use 99.995% enriched Li-7. However, Li-7, F-19 and Be-9 also have threshold neutron reactions, which contribute to the long-term generation of tritium as shown in Equations (1.3) to (1.6). Thus, a large quantity is generated at the beginning of the reactor life where most of the Li-6 is consumed. Over time, Be-9 generates He-6, which decays to Li-6, which then continuously and gradually generates tritium during operation. While tritium in the form of TF does not permeate through metal piping [21], accumulation of TF facilitates corrosion, which can generate T_2. This occurs by selective attack on the most active element in the system, which is chromium. The reaction proceeds as shown in Equation (1.7).

$$ 2\mathrm{TF}_{(d)} + \mathrm{Cr}_{(s)} \rightarrow \mathrm{CrF}_{2(d)} + \mathrm{T}_{2(g)} \tag{1.7}$$

The corrosion reaction generates T_2, which can readily permeate through steel piping as atomic tritium, creating a radiological concern. Stempien calculated that at the beginning of life, the tritium production for an FHR is over 10, 000 Ci/GWt/d. He found that equilibrium was reached within 20 days of full power operation and the production rate stabilizes at approximately 2900 Ci/GWt/d. For comparison, Table 1.3 shows the average daily generation rates of different types in reactors per GWt, assuming a cycle efficiency of 33%.

Table 1.3: Estimated tritium production rates for various types of reactors converted from data given in Ref [22]

	Tritium Generation Rate (Ci/GWt/day)
PWR	13.6
BWR	12.7
HWR	1324
GCR	14.92
FBR	19.89

Thus, the tritium generation rate for an FHR is a couple of orders of magnitude larger than conventional light water reactors and more than two times larger than a typical heavy water reactor.

In the United States, the Nuclear Regulatory Commission (NRC) and Environmental Protection Agency (EPA) set various limits and recommendations for tritium emissions as shown in Table 1.4. The lowest limit of annual radiation dose is 25 mrem/year from 10 CFR 20.1301 as shown in Table 1.4, while the limits of production are not given. However, guidelines for limiting tritium concentrations in the effluents are provided. For FHRs, the effluent concentration would depend on the flow rates and processing steps of the effluent streams, which have not yet been determined through detailed design. As a point of reference, the total release rates of tritium are shown for different types of reactors in Table 1.5.

Without mitigation, it was calculated that the release rate peaks at 2400 Ci / EFPD for the 236 MWt PB-FHR [9], greatly exceeding the quantities of water reactors shown in Table 1.5. It is clear that from both a corrosion and radiological release perspective, tritium must be controlled and contained for the successful development of the FHR.

Table 1.4: Regulatory constraints on tritium emission in the United States

		Annual Radiation Dose		Effluent Concentration			
				Air		Water	
	Regulation	(mrem)	(mSv)	(μCi/ml)	(Bq/ml)	(μCi/ml)	(Bq/ml)
Limit	10 CFR 20.1301(a)1	100	1	-	-	-	-
	Table 2 of Appendix B to 10 CFR 20	50	0.5	1E-7	3.7E-3	1E-3	37
Standard	10 CFR 20.1301(e)	25	0.25	(5E-8)[a]	(1.85E-3)[a]	(5E-4)[a]	(18.5)[a]
ALARA	Appendix I to 10 CFR 50	20 (β,air)	0.20	(4E-8)[a]	(1.48E-3)[a]	-	-
		3 (water)	0.03	-	-	1.5E-5	0.56
Drinking Water	EPA standard	4	0.04	-	-	2E-5	0.74

a. Calculated by assuming the linear relationship between the annual dose of 50 mrem and the values in Table 2 of Appendix B of 10 CFR 20.
ALARA = as low as reasonably achievable
CFR = Code of Federal Regulations

Table 1.5: Typical total discharge rates per GWt including liquid and gaseous effluents

	Average Release Rate (Ci/GWt/day)
PWR (Zircaloy Cladding)	0.72
BWR	0.14
HWR	22.6

1.2.1. Tritium Control Solutions

A review of tritium capture technologies applicable to molten-salt systems was presented in *Nuclear Technology* by Forsberg et. Al [23], which is briefly summarized here. The main technologies currently under development include gas-sparging, permeators, double-walled heat exchangers (DWHXs) and direct-contact solid adsorption columns. Gas-sparging technologies involve introducing an inert gas such as helium to the molten-salt system in order to absorb and remove fission gases including krypton, xenon and tritium. This technique was used during the MSRE to remove xenon and krypton and is currently being developed by the Chinese Academy of Sciences (CAS) [24]. A variation of this technology coupled to ultrasound is also being proposed by the University of New Mexico (UNM). Ultrasound causes small gas bubbles to nucleate, which increases the mass transfer area and improves the performance of a gas sparger [25]. The schematic of the prototype test loop is that is currently under development at UNM is shown in Figure 1.6.

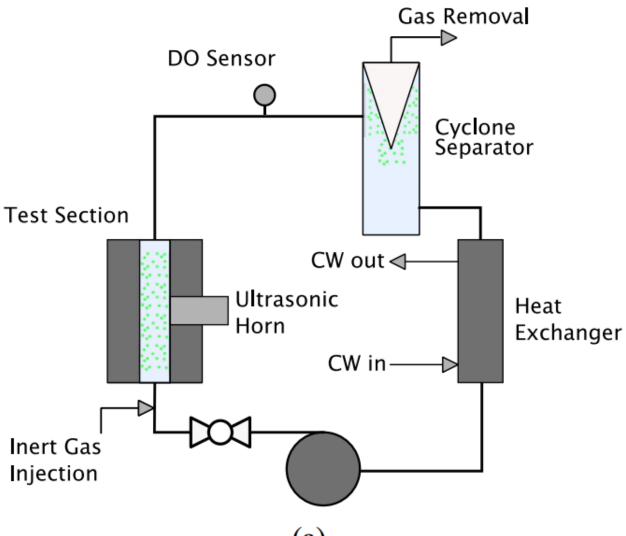

(a)

Figure 1.6. Schematic of prototype test section for ultrasonic-enhanced gas sparging [25]

The second technological category is gas permeation, which is currently under development by Ohio State University (OSU) and ORNL, where initial computational simulations have been completed [26]. A gas permeator involves contacting the molten salt with tubes made of a permeable metal, where the tritium will selectively pass through the tubes and become captured on the opposite side. The tritium is collected by a solid tritium getter such as yttrium or removed by a vacuum or a flowing carrier gas. Currently, this design is still in the concept stage and a small-scale validation experiment is under development. The technological basis of a permeator is similar to that of the proposed DWHX. DWHXs are used in chemical industries where heat is transferred between two incompatible fluids. In theory, this technology is applicable to the primary HX tubing of the FHR. However, a major disadvantage of this would be the large temperature drop across the heat exchanger, resulting in a loss of thermal efficiency. Currently, codes are being developed at OSU to analyze DWHXs and experiments are being planned at UNM [23].

Lastly, a direct-contact solid tritium adsorbent column is under investigation by MIT, which will be the focus of this thesis. This technology involves placing a solid getter inside an adsorption column where flowing salt will contact a high-tritium-solubility getter. While many adsorbents can perform well for hydrogen capture at low temperatures, most do not adsorb appreciable amounts of hydrogen at the FHR conditions of 700°C. A more detailed review of current knowledge is presented in Chapter 2. Perhaps the most obvious choice of adsorbent would be graphite, which is known from MSRE to have a high hydrogen uptake. A concept of an adsorption process is shown in Figure 1.7.

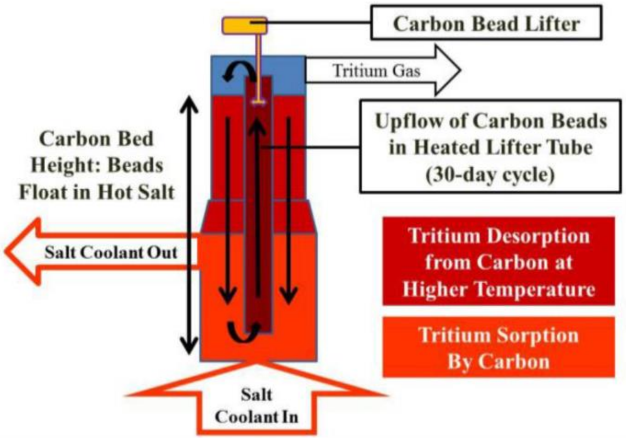

Figure 1.7: Concept drawing of direct-contact carbon adsorption column [27]

For each of the three main technologies: 1) Gas sparging columns, 2) permeator windows and 3) graphite-based solid adsorption columns, Stempien performed preliminary analyses using typical engineering specifications [27]. For the permeation tower with a nickel tubes, a surface area of 20, 164 m^2 and a size roughly twice that of the primary heat exchanger, the maximum release rate was reduced from 2410 Ci/day without mitigation to 800 Ci/day. For a gas-stripping column with 50% of the primary loop coolant flow continuously passing over a sparger with 10 equilibrium stages and a stripping-gas flow rate of 20, 000 L/hr, the maximum release rate reduced to 439 Ci/day. With a 1.2 m R (radius) x 3.6 m H (height) graphite adsorption tower filled with 1.5 cm radius ISO-88 graphite pebbles, he calculated that the maximum release rate reduced the most, to 7.5 Ci/day. This calculation has since been updated as discussed in Chapter 2.

Each of these technologies show a potential for removing significant amounts of tritium from the FHR and could be potentially sufficient with further technological advancements and optimizations. However, the simplest and most well-developed technology will likely be used for building a test reactor in order to ensure near-term deployment. In theory, the graphite adsorber column would contain the fewest process steps and has been demonstrated by MSRE experience to work. Furthermore, significant improvements can be gained based on current knowledge of adsorbent materials. Strehlow showed that for oxidized graphite, the hydrogen adsorption increased roughly with linearly with BET surface area [28]. Atsumi and Tanabe obtained similar findings but also found a positive correlation with both the crystalline edge surface area and the degree of graphitization [29][30]. In addition, the FHR system will already contain large amounts of carbon and graphite materials in the core region as TRISO particles, fuel pebbles, reflectors and core structures. The outer and central reflectors of the core are stationary and are composed of 49, 250 kg of IG-110U nuclear grade graphite. The core consists of 644, 000 mixed fuel and graphite pebbles of 3 cm radius, which contain another 14, 348 kg of graphite. Additionally, the core pebbles can be recirculated online at a maximum rate of 3600 pebbles/hr, which corresponds to possible graphite replacement rate of up to 2125 kg/day [5]. Thus, a comprehensive study on the kinetics and thermodynamics of tritium interaction in graphitic material is called for and can dually apply to both development of a tritium control technology and improving understanding of tritium uptake in the core.

1.3. Research Objectives and Thesis Goals

The main goal of this thesis is to provide initial study on the feasibility of carbon-based materials for use in an adsorption column to capture and control tritium in the FHR. Through this investigation, the thesis results will provide a starting point and enable development of guidelines that help focus future studies in search for applicable tritium adsorbents. Specifically, this thesis aims to 1) improve modeling and simulation to demonstrate that carbon materials can substantially reduce tritium release and system inventory, and 2) demonstrate experimental methods capable of studying hydrogen-adsorption interactions at high temperature and low hydrogen pressures, and 3) screen materials to determine the properties that yield a high hydrogen solubility.

1.3.1. Tritium Adsorber Performance Requirements

While the main experimental goals of the thesis are to prove experimental methods, develop understanding of the thermodynamics of hydrogen adsorption, and provide an initial screening for materials with high hydrogen solubility, there are many other criteria that must be met for an adsorbent material to be considered suitable for the FHR application. Although not treated explicitly in the scope of this thesis, considerations should be made for the following:

- Transport Kinetics - While a higher tritium solubility results in a higher uptake, it is not the only factor influencing the release rate of tritium. If for example, the rate of surface adsorption and bulk diffusion in the graphite is low, significant amounts may leave the adsorption column shown in Figure 1.7 without being adsorbed. Thus, a full study must also measure uptake rates.

- Reversibility of Adsorption – Reversibility refers typically to the energy of adsorption and the ability to desorb tritium that is captured by a material. A highly negative heat of adsorption means a stable adsorption. This results in increasing the heat input required to desorb the gas and reverse the reaction. This reversibility determines the temperature at which the adsorbent must be regenerated. This temperature must be below the thermal design limits of the fuel and coolant. Note that if the process is spontaneous, the Gibbs free energy, defined as $\Delta G = \Delta H - T\Delta S$, is negative. The change in entropy during adsorption is negative due to loss in translational and rotational degrees of freedom of the adsorbate, and thus ΔH of adsorption is necessarily negative [31].

- Thermo-mechanical Resistance – The material must be resistant to the thermal gradients that are imposed both during normal operation and during the regenerative heating steps. This includes a resistance to swelling, creep and sintering of the material. Over the long term, the tritium transport properties must be adequately conserved. Secondly, adsorbent pebbles must move within the column and thus shear stresses are imposed. Under these stresses, the material must maintain structural integrity. Production of carbon dust from the graphite moderator has been a known issue in HTGRs and would need to be minimized and managed in an adsorption system using carbon materials in an FHR.

- Manufacturing Consistency – The production of carbon materials such as graphite consists of mixing of petroleum coke and coal-tar pitch, the chemical purity of which are not always well controlled. Further, the raw materials undergo a series of process steps, including calcination at 1300°C, baking at 800 – 1000°C and graphitization at 2500 – 2800°C in large furnaces where it can difficult to maintain uniform heating of the product [32]. While high chemical purity isotropic behavior can be achieved for high-grade nuclear graphite, this is not guaranteed for other carbon materials. In the demonstration of a material for this application, it is therefore necessary to understand the achievable consistency of materials that are proposed, and determine the minimum limits required.

1.3.2. Impact of a Successful Tritium Adsorbent

Demonstrating that an adsorbent can sufficiently control tritium levels in a molten salt operating at 700°C will enable the continued development of different advanced nuclear energy systems. Over the past decade, technological advancement has spurred interest in three such systems including 1) high-field fusion devices with a lithium breading blanks, 2) molten salt reactor (MSR) systems with dissolved fuel, and 3) molten salt reactor systems with solid fuel (FHR) [23], all of which have a role to play in a low-carbon energy future.

In fusion, development of the rare-earth barium copper oxide (REBCO) superconducting tape over the last few years has allowed a large increase in power density of fusion devices [33]. As a result, a traditionally solid lithium blanket used to breed tritium through the reaction: $^{6}\mathrm{Li} + \mathrm{n} \rightarrow {}^{3}\mathrm{H} + {}^{4}\mathrm{He}$, will need to be changed to a molten-salt lithium blanket to increase heat transfer. Unlike fission reactors, fusion reactors require high Li-6 enrichment with the intent of breeding tritium, and thus the concentrations are orders of magnitude larger than in fission reactors. In these devices, a low-conductivity coolant medium like molten salt is preferred over pure liquid metal, as this limits hydro-dynamically induced interference of magnetic fields.

The second category is the dissolved-fuel molten salt reactor in which the fissile material is dissolved in the liquid phase. This concept originated in the 1950s from an aircraft nuclear propulsion program. The first experimental reactors built were the Aircraft Reactor Experiment (ARE) and the Molten Salt Reactor Experiment (MSRE). In the early 1970s these programs were shut down due a change in focus to the development of sodium-cooled breeder reactors [23]. However, in the last decade, interest has been renewed due to 1) versatility of a fuel cycle enabling the use of thorium fuel, 2) advances in technology since the 1960s which have eliminated many of the MSRE challenges, and 3) improved safety by removing of the possibility of fuel melt-down since the fuel is already in a molten state. This concept has gained considerable private and governmental interest and is currently under research and development [34].

Lastly, as discussed in earlier sections, the solid-fuel molten salt reactor (FHR) has gained traction due to its combination of advanced solid fuel enabling reliable fuel and fission-product encapsulation, operation at high temperature yielding high efficiency, and adaptability with a gas cycle enabling grid optimization. Due to the employment of mostly known technologies, the FHR is seen as the near-term deployment option and is currently being investigated by various university institutions (MIT, UW-Madison, UCB, UNM, CAS) in collaboration with national laboratories (INL, ORNL) and nuclear start-up companies (Kairos Power). While the focal point of this thesis is on the FHR system, the other two technologies both require the use of lithium salts that generate tritium at high temperatures (700°C or greater) and are both limited by lack of experimental data and validation. Thus, any mechanisms that is demonstrated to successfully control tritium is naturally extendable to all three classes of technology.

1.4. Thesis Outline

Chapter 2 provides background to 1) give further context on the current state of knowledge in the research topic of this thesis and 2) provide information necessary to understand the main results, analyses and discussions in the thesis. Tritium generation in molten salt is explained as well as the speciation of tritium into different forms based on redox potential. Physical and chemical adsorption on carbon materials and graphite surfaces are discussed. Effects of irradiation on tritium transport is examined.

Chapter 3 outlines system-level phenomena and explains the codes that were used to simulate tritium transport in an operating reactor. The various coupled effects that were modeled are discussed. The results of modeling an adsorption column coupled with a 236 MWt Mk-1 PB-FHR are examined and the results of the sensitivity analyses that were conducted for the optimization of an adsorption tower with graphite adsorbent are presented. Finally, based on the results of the tritium simulations, potential alternative materials are suggested.

Chapter 4 discusses experimental methods that were used to firstly characterize the materials, and then secondly analyze hydrogen sorption behavior. The characteristics analyzed include BET surface area, pore volume and pore size distribution. The macroscopic methods for deterimnation of surface area, pore volume and average pore size are explained. Then microscopic theories (liquid density functional theory) allowing the calculation of pore size distribution are discussed. Measurement of volumetric hydrogen adsorption on different material surfaces using manometric methods is explained. The data acquired and interpretation of this data is given. Additionally, the specifications for the scanning electron microscopy used for qualitative analysis is given. In the final part of this chapter, experimental uncertainties and errors of the adsorption methods are examined.

Chapter 5 discusses the experimental results for different carbon materials using the methods described in Chapter 4. Known characteristic data of each material is given as well as the new data that was measured using adsorption techniques. Various adsorption isotherms for each material were collected at 700°C. This allowed the determination of different types of interactions of hydrogen on the material surface, including a strong chemical interaction versus a weak interaction. SEM micrographs were also taken and are briefly discussed.

Chapter 6 provides an in-depth analysis of the data collected in chapter 5. Different thermodynamic models were used to analyze the chemisorption data and the mechanisms of adsorption are discussed. The difference between molecular and dissociative adsorption is determined. The physical characterization data was correlated against hydrogen solubility to determine causal relationships. The effect of material properties on hydrogen uptake behavior was analyzed. Materials with high uptake were used to perform simulations and determine the ability of these materials to influence system-level tritium behavior.

Key results and conclusions are then summarized and the original contributions of this work are emphasized. Materials and material properties of interest are discussed based on their ability to provide desired tritium performance. Finally, the future work is outlined including mention of screening plans an additional tests that must be conducted to ensure the success of an adsorbent material.

Chapter 2.

Background

2.1. Tritium Production in Molten Salt Reactors

As introduced in Chapter 1, in equation (1.2) – (1.6), large amounts of tritium are generated at the beginning of life due to neutron reaction with Li-6, which has a large thermal cross section. After Li-6 is depleted, small amounts of tritium are continuously generated due to the transmutation of Be-9. Solving the Bateman equations for the rate of change of tritium in the system, Cisneros provides the estimate for tritium generation as follows [35]:

$$\frac{dN_T}{dt} = \phi\sigma^T_{Li-7}N_{Li-7} + \phi\sigma^T_{Li-6}\left[N^o_{Li-6}e^{-\frac{V_{core}}{V_{loop}}\phi\sigma^a_{Li-6}t} + \frac{\phi\sigma^\alpha_{Be-9}N_{Be-9}}{\phi\sigma^a_{Li-6}}\left(1 - e^{-\frac{V_{core}}{V_{loop}}\phi\sigma^a_{Li-6}t}\right)\right] \qquad (2.1)$$

Where $N_T[\text{atom cm}^{-3}]$ is the number density of atoms of tritium, $\phi[\text{ncm}^{-2}\text{s}^{-1}] = 3.41 \cdot 10^{14}$ is average neutron flux, $\sigma^T_{Li-7}[b] = 1.00 \cdot 10^{-3}$ is the microscopic tritium production cross section from Li-7, $N_{Li-7}[\text{atom cm}^{-3}]$ is the atomic density of Li-7, $\sigma^T_{Li-6}[b] = 148.026$ is the microscopic Li-6 tritium production cross section, $N^o_{Li-6}[\text{atom cm}^{-3}]$ is initial number density of Li-6 in flibe, $V_{core}[m^3] = 7.2$ is the total volume of flibe in the reactor core, $V_{loop}[m^3] = 46.82$ is the total volume of coolant in the reactor primary system, $\sigma^a_{Li-6}[b] = 148.032$ is the microscopic absorption cross section of Li-6, $\sigma^\alpha_{Be-9}[b] = 3.63 \cdot 10^{-3}$ is the microscopic cross section of the (n, α) reaction of Be-9, $N_{Be-9}[\text{atom cm}^{-3}]$ is the number density of Be-9 in flibe and $t[s]$ is time. For the baseline Mk-1 FHR, the Li-7 enrichment is 99.995 wt. %. Here, the rate of tritium generation rapidly increases initially but approaches equilibrium over time. Stempien [9] calculated that the rate of tritium generation at the beginning of reactor life is 10, 000 Ci / day and equilibrium is reached in approximately 20 days where the generation rate levels to approximately 2900 Ci /day. For system calculations, only the generation in the flibe is considered. Normally in HTGRs, small amounts of lithium impurities in the graphite will also produce tritium [22]. However this is relatively small compared to the generation in the salt, and it is reasonable to assume that the tritium generated by the pebbles in the fuel is completely encapsulated by the TRISO particles [36][37].

2.2. Corrosion in Molten Salts

The sections below discuss the thermodynamics of corrosion in molten salt reactors and methods of corrosion control as they relate to tritium generation and material selection. In the simulations in this thesis, the corrosion was assumed to be limited by redox control methods, which are discussed. The calculation of corrosion kinetics is not discussed here but is explained in detail by Stempien [9].

2.2.1. Thermodynamic Stability of Materials

While the corrosion products of aqueous systems produce oxide layers that passivate the surface and can limit further corrosion, the same is not true for molten-salt systems. The oxidizing species in flibe is fluorine, which means that any corrosion of metals occurring will produce metal fluorides that are soluble in flibe. The stability of a metal can thus be determined based on the energetic favourability of its corresponding metal fluoride, which can be represented by the Gibbs free energy. A negative Gibbs free energy indicates that a spontaneous reaction is possible. The standard Gibbs formation energy of a molecule is the change in Gibbs free energy due to the formation from its base elements at standard conditions. Thus, a more negative formation energy means a more energetically favourable molecule since formation causes a minimization of system energy. The main elements of structural steels are Cr, Ni, and Fe. The Gibbs formation energies of the fluorides of these metals in pure flibe is compared to those of LiF and BeF_2. This is done using data that was collected during the MSRE experiments by Baes [38] are shown in Figure 2.1.

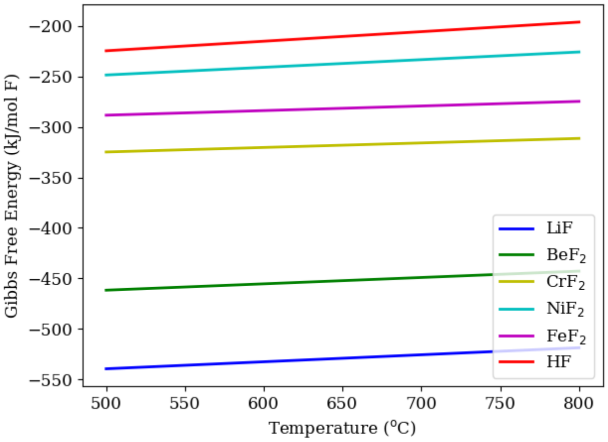

Figure 2.1: Ellingham diagram showing the Gibbs formation energy of main structural metal fluorides compared to Li and Be fluoride from data given by Baes [38]

This figure shows that the energy of fluorides of these structural metals are all above that of LiF and BeF_2, which indicates that the structural metals will be stable in flibe since the corrosion product is less stable than the salt constituents. As well, the plot of Gibbs energy versus temperature (Ellingham representation) shows that CrF_2 has the lowest energy, which means that chromium is the first species that would react under an oxidizing potential. While clean salt is corrosive, trace impurities can be found in the salt such as Ni and Fe [39], which raises the redox potential of the bulk coolant causing corrosion of chromium through the following reactions:

$$\mathrm{NiF_{2(d)} + Cr_{(s)} \rightarrow CrF_2 + Ni_{(s)}} \tag{2.2}$$

$$\mathrm{FeF_{2(d)} + Cr_{(s)} \rightarrow CrF_2 + Fe_{(s)}} \tag{2.3}$$

Where the subscript (d) represents the species dissolved in the molten salt, and (s) represents the solid state. The nickel and iron impurities can displace chromium to produce a lower energy system. Additionally, one must recall from Chapter 2.1 that TF is continuously generated in the molten salt, which also contributes to a shift in the oxidizing potential of the solution. From Figure 2.1, HF has the highest potential in comparison to the rest of the metal fluorides and thus will contribute to an overall increase in the redox potential of the solution. Thus, corrosion in TF proceeds as shown:

$$\mathrm{2TF_{(g)} + Cr_{(s)} \rightarrow CrF_{2(d)} + T_{2(g)}} \tag{2.4}$$

Hence, the TF can corrode structural metals (Cr, Fe, and Ni) to form tritium as T_2. While a comparison of the Gibbs formation energy provides an indication of relative stability of metal fluorides, it alone does not provide the equilibrium concentration of the corrosion products in the molten salt that is in contact with a metal surface. To understand the extent of corrosion, the equilibrium constants must be used. These were measured by Baes during the MSRE and takes the form of the Van't Hoff Equation [38] for the reaction (2.4):

$$\ln \mathrm{K_{eq}} = \ln\left(\frac{[\mathrm{CrF_2}]\mathrm{p_{T_2}}}{[\mathrm{Cr_{(s)}}]\mathrm{p_{TF}}^2}\right) = -5.12 + 9.06 \cdot \left(\frac{1000}{\mathrm{T}}\right) \tag{2.5}$$

Where $\mathrm{K_{eq}}$ is the equilibrium constant, T[K] is the temperature valid from 700 – 1000 K, $[\mathrm{CrF_2}]$ is the mole fraction of $\mathrm{CrF_2}$ in flibe, $[\mathrm{Cr_{(s)}}]$ is the Cr mole fraction in steel, $\mathrm{p_{TF}}$ is the partial pressure of TF and $\mathrm{p_{T_2}}$ is the partial pressure of $\mathrm{T_2}$. Thus, using equation (2.5), the extent of corrosion can be determined based on the ratio of p_{T_2} to ${p_{TF}}^2$ that is maintained in the system. If the redox is not controlled, the TF generated in the salt will corrode Cr, which causes generation of CrF_2 and T_2. As T_2 increases relative to TF, the equilibrium concentration of CrF_2 decreases, slowing down the reaction. The corrosion reaction will progress until the equilibrium condition is met.

2.2.2. Redox and Corrosion Control

As introduced in 2.2.1, the corrosion can be controlled by the ratio of TF and T_2. This control can be generalized by defining the redox potential in terms of the species that controls the salt reactivity. In the case of flibe, the controlling anionic oxidizing species is fluorine. First, we state a general reaction with F_2 gas upon which the cationic species M changes its oxidation state. For example, the reaction of M and F with stoichiometric ratio of 1:1 is shown below.

$$\mathrm{M} + \frac{1}{2}\mathrm{F}_2 \leftrightarrow \mathrm{MF} \tag{2.6}$$

By the law of mass action, the activities can be expressed in terms of the standard Gibbs energy of the reaction ΔG^o_{Rxn}, where $\Delta G_{Rxn} = 0$ at equilibrium:

$$K_{eq} = \frac{a_{MF}}{\left(p_{F_2}\right)^{1/2} a_M} = \exp\left(-\frac{\Delta G^o_{Rxn}}{RT}\right) \tag{2.7}$$

Where a_{MF} and a_M represents the activities of the cation-fluoride and cationic species respectively, p_{F_2} is the partial pressure of fluorine gas, T is absolute the temperature and R is the ideal gas constant. Olander defined the bulk potential of the solution in terms of the diatomic fluorine in which we can substitute for p_{F_2} using (2.7) [40]:

$$\Delta\overline{G}_{F_2} = RT \ln p_{F_2} = 2RT \ln\left(\frac{a_{MF}}{a_M}\right) + \Delta G^o_{MF} \tag{2.8}$$

This is the Gibbs free energy of 1 mole of fluorine gas at a partial pressure of p_{F_2} and temperature T, relative to free energy at standard condition. This potential dictates the corrosiveness of the solution and is set by the theoretical F_2 partial pressure. Note that the F does not actually need to exist as F_2 gas in the solution, as the potential shown in Equation (2.8) can be established by just the activities of the cation-fluoride and the cation species. Olander described at least three ways in which redox can be directly controlled: 1) by introducing a gas mixture of HF/H_2, 2) by using Be metal to change oxidation state in a reaction with F, or 3) by using a salt that changes valence states. In each of the these cases, an expression for the fluorine potential was derived in terms of the activity of the reaction product and Gibbs energy of reaction shown in Table 2.1 [40].

Table 2.1: Redox control using 1) gas phase HF/H_2 mix, 2) Be metal and 3) CeF_3/CeF_4 salt pair to control the fluorine potential

Diatomic Fluorine Reaction	Fluorine Potential ΔG_{F_2}
$\frac{1}{2}H_{2(g)} + \frac{1}{2}F_{2(g)} \leftrightarrow HF_{(g)}$	$\Delta\overline{G}_{F_2} = 2RT\ln\left(\frac{P_{HF}}{\sqrt{P_{H_2}}}\right) + 2\Delta G^{o}_{HF}$
$Be_{(s)} + F_{2(g)} \leftrightarrow BeF_{2(d)}$	$\Delta\overline{G}_{F_2} = RT\ln\left(a_{BeF_2}\right) + 2\Delta G^{o}_{BeF_2}$
$CeF_{3(d)} + \frac{1}{2}F_{2(g)} \leftrightarrow CeF_{4(d)}$	$\Delta\overline{G}_{F_2} = 2RT\ln\left(\frac{a_{CeF_4}}{a_{Ce_{F_3}}}\right) + 2(\Delta G^{o}_{CeF_4} - \Delta G^{o}_{CeF_3})$

The fluorine potentials derived in the Table 2.1 show that the redox potential (i.e. fluorine potential) of the solution can be controlled by one of three methods. With the redox potential of the solution defined, the extent of corrosion can be determined. For the corrosion reaction in (2.4), the equilibrium equation is expressed as follows:

$$K_{eq} = \frac{a_{CrF_2}p_{T_2}}{a_{Cr_{(s)}}(p_{TF})^2} = \exp\left(-\frac{\Delta G^{o}_{CrF_2} - 2\Delta G_{TF}}{RT}\right) \tag{2.9}$$

Since the HF/H_2 couple controls the corrosion in the system, the fluorine potential of the first reaction in Table 2.1 can be used to eliminate the ratio of partial pressures $p_{H_2}:(p_{HF})^2$ in Equation (2.9). Since the chemistry is determined by the valence electrons of the reacting species, the partial pressure and Gibbs free energies of TF and T_2 are interchangeable with those of HF and H_2. Using Equation (2.9) and assuming the activity coefficients $\gamma_{CrF_2,Cr_{(s)}} = 1$, the concentration of the CrF_2 can be determined as a function redox potential and temperature:

$$[CrF_2] = \left[Cr_{(s)}\right]\exp\left(\frac{\Delta\overline{G}_{F_2} - \Delta G^{o}_{CrF_2}}{RT}\right) \tag{2.10}$$

This means that the extent of corrosion can be known directly at a given fluorine potential ΔG_{F_2}. The standard energy of formation of TF was calculated by Stempien as shown in Equation (2.11).

$$\Delta G^{o}_{TF} = -4.6976 \cdot 10^{-10}T^3 + 3.1425 \cdot 10^{-6}T^2 - 8.8612 \cdot 10^{-3}T - 2.7305 \cdot 10^2 \tag{2.11}$$

Where $\Delta G_{HF}^{o}\left[\frac{kJ}{mol}\right]$ is the gibbs free energy of formation of HF. Plotting the equilibrium $[CrF_2]$ concentration against the partial pressure ratio and fluorine potential, Figure 2.2 shows the calculated CrF_2 concentration in the salt at a given redox potential, and the corresponding molar ratio of $p_{T_2}: p_{TF}^2$.

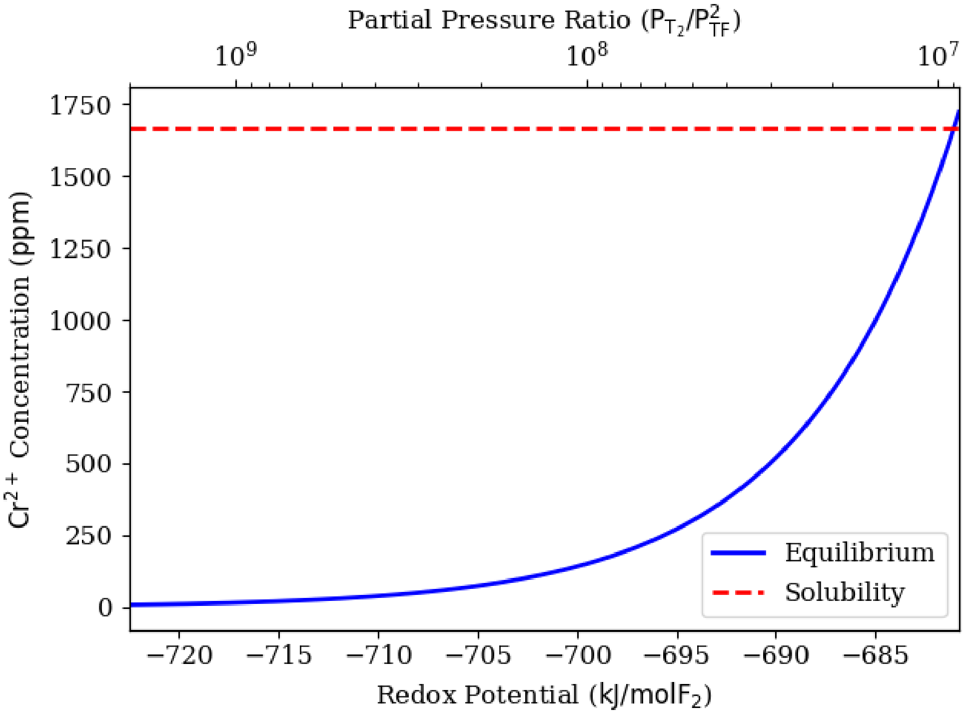

Figure 2.2: Partial pressure ratio $p_{T_2}:(p_{TF})^2$ and the corresponding fluorine potential versus the Cr^{2+} ion concentration from the formation of CrF_2

In Figure 2.2, the solubility of CrF_2 is shown as a reference point, which indicates a definite upper limit for the redox control. Since the tritium is generated in the form of TF, the redox potential in the salt can be controlled by injection of H_2 to achieve the required ratio. The second method of redox control discussed above was the introduction of a major metal into the system that would corrode and dissolve in the flibe. For flibe, the preferred choice is beryllium over lithium since LiF has a lower Gibbs free energy than BeF_2 as shown in Figure 2.1. Therefore, lithium metal can displace BeF_2 in the salt. With beryllium metal in the salt, the redox potential and speciation of TF and T_2 would be controlled with the reaction in Equation (2.12).

$$Be_{(s)} + 2TF_{(g)} \leftrightarrow BeF_{2(d)} + T_{2(g)} \qquad (2.12)$$

Where the mole ratio concentration [BeF_2] can be used to set the redox potential, indirectly setting the tritium speciation. The redox potential in the salt as a function of [BeF_2] concentration can be calculated with the second equation in Table 2.1, which can then be used to calculate the corrosion of Cr in Equation (2.10). The third method proposed by Olander [40] was the use of a dissolved salt, which upon the exchange of cation valence state will lower the system's Gibbs free energy more than an attack on Cr. The controlling reaction as an example with Ce-fluoride is shown:

$$2CeF_{3(d)} + 2TF \leftrightarrow 2CeF_{4(d)} + T_2 \qquad (2.13)$$

Where the Ce ion changes from an oxidation state of 3+ to 2+ to control the fluorine potential, which can be calculated by the last equation in Table 2.1.

With the first method of introducing H_2, it is clear that the amount required would be several of orders of magnitude more than the amount of TF that is generated in order to maintain a sufficient ratio for redox control. Further, hydrogen can displace tritium in removal systems, which may influence the type of tritium control system that is chosen. On the other hand, the other two methods discussed involve the addition of a species that would not otherwise be in the salt, which would incur a neutronic penalty. Further, it has been noted in literature that highly reducing environments have the potential to form carbides such as Be_2C if metallic Be were used for redox control [39][41][15]. This is unacceptable since the fuel pebbles and large amounts of structural materials are composed of graphite that would decompose in the process of carbide formation. Due to the low Gibbs energy of BeF_2, the task of finely controlling redox could be more difficult with Be [141][121][148]. Ultimately, the choice of redox control must balance the drawbacks while considering the method of tritium control, which is currently under investigation by various universities including UNM, UCB, MIT and GeorgiaTech [23].

2.3. Tritium Diffusion and Release

The primary loop of the FHR system is shown in Figure 2.3 with the paths taken by tritium in the system. The transport from the point of generation to release occurs in several dependent steps. First, TF is generated in the reactor core and is transported by diffusion/convection, which is driven by concentration gradient within the coolant and by the velocity of the bulk fluid. These effects transport the tritium species from the core towards the heat exchanger. Some of the tritium is captured by core graphite. Based on the redox conditions of the salt, the TF reacts to from T_2 throughout, by a form of redox control discussed in Chapter 2.2.2 or by corrosion of the structural metal in the system. T atoms diffuse through the metal tubing in the heat exchangers due to a concentration gradient between the primary coolant and the power cycle. At the opposite side of the tubing, which faces the power cycle, T atoms undergo re-combination and are then liberated as T_2. Finally, convective and diffusive transport of the power cycle fluid carries the tritium away from the heat exchanger and releases it to atmosphere.

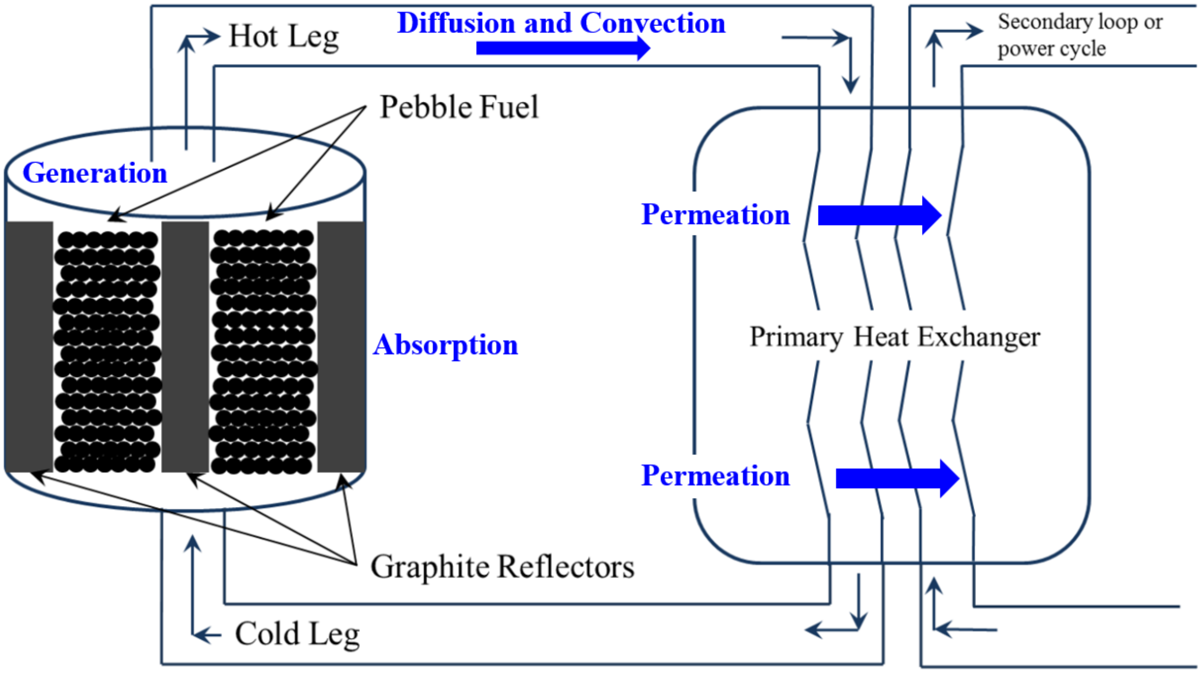

Figure 2.3: System schematic for tritium transport and release

In order to determine the rate of release, the transport and reaction of tritium species (TF, T_2, or atomic T) must be accounted for in different mediums described above. The general mass conservation equation that must be solved is shown in (2.14):

$$\frac{\partial c_{T_i}}{\partial t} + \nabla \cdot j_{T_i} = R_{T_i} \tag{2.14}$$

Where T_i represents a general form of tritium, $c_{T_i}[\mathrm{mol\ m^{-3}}]$ represents the concentration of tritium species in a control volume, $j_{T_i}[\mathrm{mol\ m^{-2} s^{-1}}]$ represents the net flux of tritium into and out of the control volume, and R_{T_i} represents tritium reactions that contribute as a source or sink of the tritium form. In the following sections, the transport (flux and reaction) of tritium in the molten salt, metal piping and graphite in the system are discussed in more detail, which allow the solution of the equation (2.14).

2.3.1. Tritium Transport in Flibe

The transport properties of tritium (i.e. solubility and diffusivity) are dependent on the species (TF or T_2). While various experiments have been conducted to determine specific properties, it is important to note that the speciation can vary significantly depending on the redox condition of the salt, corrosion in the system and impurities present, which are difficult to precisely control. Further, hydrogen has a significant permeability at reactor operating conditions (700°C), adding to measurement uncertainties. It should therefore not be surprising that experimental results and interpretation varies significantly between past experiments. As a first approximation, several of these models were previously compiled and are summarized in Table 2.2.

Table 2.2: Solubility and diffusivity constants of TF and T_2 in flibe as a function of temperature [9]

	T_2	TF
Henry's constant $k\ [\mathrm{mol\ m^{-3}Pa}]$	$2.714 \cdot 10^{-8} \exp(4.235 \cdot 10^{-3}T)$ [42]	$1.707 \cdot 10^{-3} \exp(-4.260 \cdot 10^{-3}T)$ [43]
Diffusivity $D\ [\mathrm{m^2 s^{-1}}]$	$9.3 \cdot 10^{-7} \exp(-42 \cdot 10^3/RT)$ [44]	$6.4854 \cdot 10^{-26} T^{5.7227}$ [45]

The concentration of a dissolved gas is given by Henry's law where the concentration is equal to Henry's constant multiplied the partial pressure of that gas. Hence, Henry's constant is a direct measure of the solubility of TF and T_2. From the coefficients in table 2.2, the solubility of TF is roughly 1000 times greater than that of T_2 at the same partial pressure. The diffusivity is directly proportional to the mass flux, which is calculated with the Equation (2.15).

$$j_{T_i} = D \frac{Sh}{L} \Delta C_{T_i} \tag{2.15}$$

Where Sh is the dimensionless Sherwood number representing the convective mass transfer over the diffusive mass transfer, which is found using empirical closure relationships, L [m] is the characteristic length of the system (i.e. diameter of pipe), and ΔC_{T_i} is the concentration difference between two points (i.e. bulk concentration versus surface concentration). In flibe, the TF can dissociate into T+ and F- ions. Since T+ has a smaller atomic radius than T_2, the diffusive transport rate of TF is higher than that of T_2. This is in agreement with experimental data shown in Table 2.2.

2.3.2. Tritium Transport in Metal Components

It is well known that hydrogen transport in metal begins with the dissociation of diatomic H_2 at the gas-solid interface. After dissociation, the tritium movement is driven by the hopping of atomic tritium through the metallic lattice from high to low concentration areas. The solubility follows Sievert's law:

$$c_T = K_S \left(p_{T_2}\right)^{\frac{1}{2}} \tag{2.16}$$

Where K_S [mol m^{-3} MPa] is Sievert's constant and c_T is the atomic concentration of T in the metal. In stationary media, there is no convective transport, and therefore the mass flux can be found by combining Fick's first law of diffusion and Sievert's law:

$$j_{T_2} = D \cdot K_S \frac{\partial \sqrt{p_{T_2}}}{\partial x} \tag{2.17}$$

Where D is the diffusivity and p_{T_2} is the partial pressure of tritium gas at the fluid-solid interface. Here, both the diffusivity and the Sievert's constant typically follows an Arrhenius relationship and the product of these two is called the permeability, which takes the temperature dependence:

$$\phi = K_0 D_0 \exp\left(-\frac{(\Delta H_S + E_D)}{RT}\right) \tag{2.18}$$

Where ΔH_S and E_D represent the heat of solution from Sievert's constant and activation energy of diffusion from the diffusivity respectively. These constants are well tabulated for hydrogen on various metals and were given by Tanabe as shown in Table 2.3.

Table 2.3: Permeability, diffusivity, and solubility with the associated pre-exponential factors and activation energies [46]

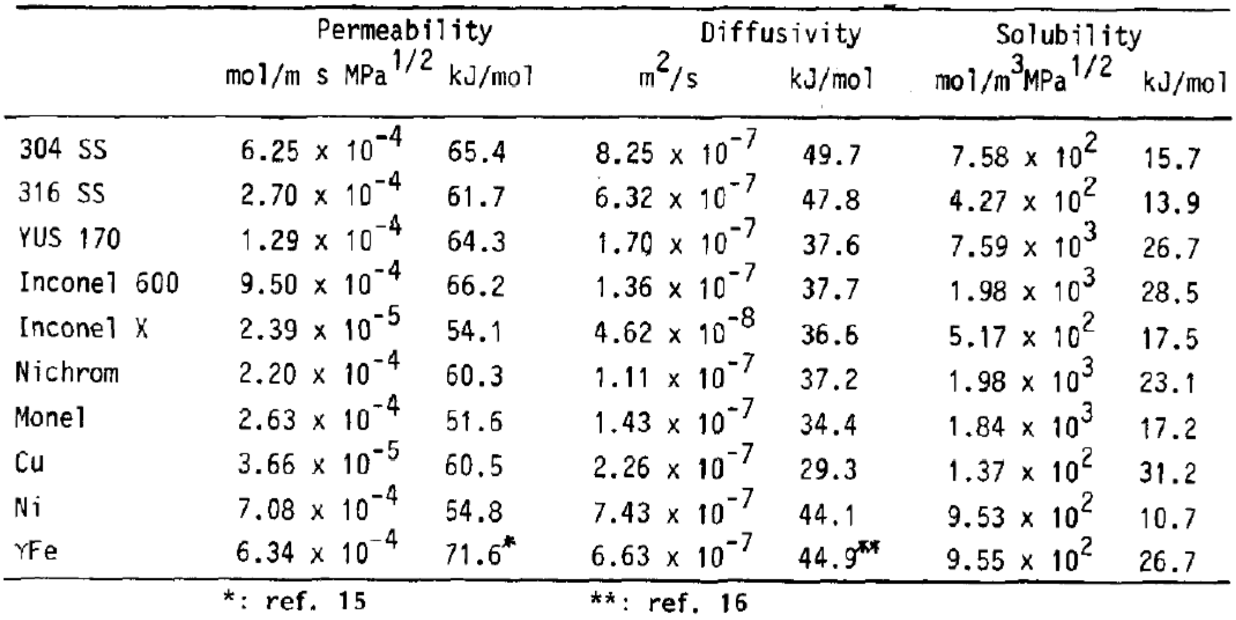

	Permeability		Diffusivity		Solubility	
	mol/m s MPa$^{1/2}$	kJ/mol	m^2/s	kJ/mol	mol/m^{3}MPa$^{1/2}$	kJ/mol
304 SS	6.25×10^{-4}	65.4	8.25×10^{-7}	49.7	7.58×10^{2}	15.7
316 SS	2.70×10^{-4}	61.7	6.32×10^{-7}	47.8	4.27×10^{2}	13.9
YUS 170	1.29×10^{-4}	64.3	1.70×10^{-7}	37.6	7.59×10^{3}	26.7
Inconel 600	9.50×10^{-4}	66.2	1.36×10^{-7}	37.7	1.98×10^{3}	28.5
Inconel X	2.39×10^{-5}	54.1	4.62×10^{-8}	36.6	5.17×10^{2}	17.5
Nichrom	2.20×10^{-4}	60.3	1.11×10^{-7}	37.2	1.98×10^{3}	23.1
Monel	2.63×10^{-4}	51.6	1.43×10^{-7}	34.4	1.84×10^{3}	17.2
Cu	3.66×10^{-5}	60.5	2.26×10^{-7}	29.3	1.37×10^{2}	31.2
Ni	7.08×10^{-4}	54.8	7.43×10^{-7}	44.1	9.53×10^{2}	10.7
YFe	6.34×10^{-4}	71.6*	6.63×10^{-7}	44.9**	9.55×10^{2}	26.7

*: ref. 15 **: ref. 16

While the transport of tritium is not explicitly tabulated, it can be calculated with an isotopic correction from diffusion theory, which states that the ratio of diffusivity of isotopes is proportional to the inverse of the square root masses shown in (2.19), which implies that the tritium diffuses at roughly 60% of the speed of hydrogen. This can be an important consideration if using hydrogen gas as a redox control mechanism since tritium removal systems that rely primarily on diffusive transport are penalized by the inadvertent, preferential withdrawal of hydrogen.

$$D_T = D_H \sqrt{\frac{m_H}{m_T}} \tag{2.19}$$

2.4. Adsorbent Material Selection

The main thrust of this thesis involves the use of adsorbent material to capture and control tritium. In literature, many studies have demonstrated a strong reactivity of rare-earth elements (group 3-5) with hydrogen [31]. The electropositive elements with the highest known affinity for hydrogen include Y, La, Zr, as well as other elements in the Ti and Va groups. Several of these have been proposed for use in fusion to remove tritium that is strongly bound to the lithium blankets at high temperatures [47]. In addition, transition metals of group 8-10 such as Ni and Pd have generally shown an ability to efficiently dissociate hydrogen, enhancing catalysis and speeding up hydrogen permeation. As a result, combining the transition metals and rare-earth metals have created intermetallic alloys that can quickly react with and store hydrogen, many of which react with hydrogen to form stable interstitial hydrides. Some of the most significant of these intermetallic alloys have been Mg_2FeH_6 and $LaNi_5$, which have reported hydrogen densities up to 150 kg/m^3 and 115 kg/m^3 respectively [48][49].

When considering the absorbent material applicable to FHRs, a primary consideration is the chemical stability in molten salt redox conditions. In flibe, the solution redox potential (in terms of Gibbs Energy), must be lower than the most stable corrosion product (CrF_2), but higher than the salt constituents (LiF and Be_2), to ensure $Cr_{(s)}$ in steel piping does not corrode and to ensure coolant species remain stable. This redox condition can therefore be referred to as the normal FHR operating zone, which limits salt degradation and material corrosion but ensures coolant stability. A simple representation of relative stabilities was previously shown using the Ellingham diagram with Gibbs free energy versus temperature in Figure 2.1. This representation was used as a first assessment of compatible metals by comparing the Gibbs free energy of the metal-fluorides to that of existing salt constituent fluorides and the fluorides of the most stable corrosion product CrF_2 in Figure 2.4. When determining suitable metals for use in the FHR, the Gibbs energy of corrosion products must 1) lie above the BeF_2 line to prevent salt degradation and 2) preferably lie above the CrF_2 line to maintain the redox limits of operation, set by chromium oxidation. The Gibbs energies of many hydrogen-getting metal fluorides were calculated using HSC Chemistry V6.0 including those of Sc, Y, Ti, Zr, Cr, La, Mg, V, Nb and Ce.

Most of these lie below the BeF_2 line, which indicates that they are not feasible for the FHR system, as they readily de-stabilize the salt. The fluorides ZrF_3 and TiF_3 lie above the BeF_3 line but lie below CrF_3 line. This shows that Zr or Ti is not stable clean salt, but significantly reduces the operating margin, which means they require tighter system redox controls to maintain stability. While HSC Chemistry does not explicitly account for solvent effects, these generally change the energies by about 5 – 10% according to experimental data [9]. Thus, the use of these metals in FHR remains unlikely.

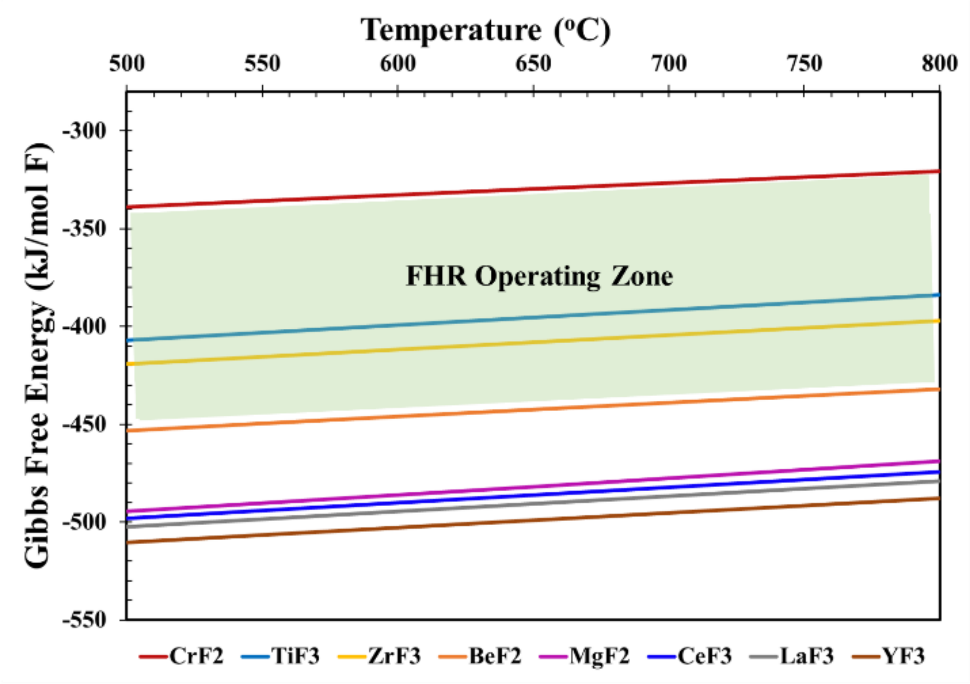

Figure 2.4: Ellingham diagram of hydride forming metals

2.5. Tritium Transport in Carbon and Graphite Materials

The most common carbon-based materials used for nuclear applications are graphite and carbon composites, which provide sufficient strength and dimensional stability under high temperature and irradiation. Graphite is used extensively in the FHR in the fuel, reflectors and structural components and it was found during the MSRE that the graphite adsorbs large amounts of tritium, making it a good candidate adsorbent for tritium control. This chapter first describes the microstructure of graphitic materials followed by a review of existing literature related to tritium transport including the solubility and diffusivity considerations.

2.5.1. Graphite Structure

Graphite is most commonly produced using the Acheson process [50]. Coke is calcined at 1300°C, then crushed, ground, and blended to size. Many properties of the graphite will ultimately depend on the size and shape of these particles, which was described in detail by Burchell [32]. Coal-tar pitch is added and the batch is heated to around 800°C – 1000°C. The process is repeated several times, which removes voids and increases the density. The final heating stage is known as the graphitization step in which the molded batch is heated at temperatures between 2500 and 2800°C over a period of around 15 days.

As an illustration of the structural complexity, Figure 2.5 shows the mesophase evolution of graphite during heat treatment from 1100K to 2200K showing the transformation from disordered defective mesogen molecules of petroleum pitch to perfectly aromatic graphite stacks. In a real process, the perfect structures are not achieved, and different graphite materials will vary greatly in their extent of graphitization.

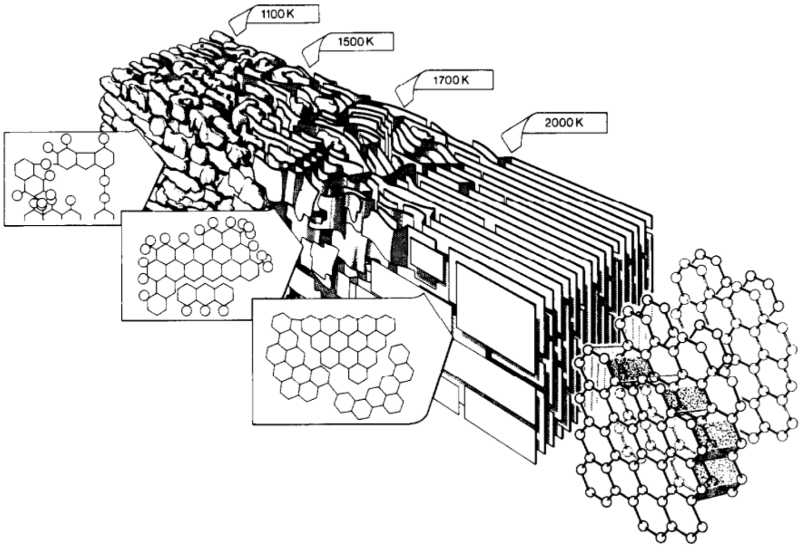

Figure 2.5: Mesophase changes during graphitization [51]

The final product graphite is relatively porous with a density around 1.8 – 1.9 g cm^{-3} and a BET surface area of 0.5 – 1.0 m^2 g^{-1}. Graphite is made up of grains derived from the original coke particles, which are around 5 – 50 μm in diameter. These grains are composed of sub-grains with a size of 5 nm or less.

2.5.2. Tritium Solubility and Diffusivity in Carbon Materials

The most applicable data for hydrogen adsorption on graphite comes from the MSRE and MSBR experiments where tritium adsorption measured on nuclear graphite [52][19]. The MSRE was in operation for 1786 hours after which the tritium uptake on the graphite components was measured. It was found that the total graphite in core adsorbed approximately 8 Ci/day for the 7.3 MWt test reactor.

Most of the current available data on hydrogen adsorption on carbon comes from studies aimed at investigating energy storage materials at low temperatures, industrial catalysis [48][53] at temperatures below 300°C or fusion applications at temperatures greater than 700°C [54]. While it is generally accepted that hydrogen is chemisorbed to graphite by a chemical bond at high temperatures, the general mechanism suggested is not consistent amongst different studies and different types of graphite [55][56][57]. Analyzing IG-110U and POCO AXF-5QBG graphite materials at 700 - 1000°C and pressures below 20, 000 Pa, Shirasu found that solubility followed Sievert's law with a square root dependence on pressure proposing a simple dissociative adsorption process [58]. This result is confirmed by Strehlow who analyzed A681, CGB, POCO AXF-5QBG [28]. In contrast, Atsumi analyzed 18 different graphite materials under similar conditions and found that the square root dependence was not necessarily followed. He proposed a mechanism involving both molecular diffusion and dissociative adsorption, in which hydrogen could only bind to a limited number of activate sites designated C* in the reactions below [30]:

$$\mathrm{H_2} \leftrightarrow 2\mathrm{H}\ \text{(transient)} \tag{2.20}$$

$$\mathrm{C}^* + \mathrm{H} \leftrightarrow \mathrm{C-H} \tag{2.21}$$

Thus, the solubility equation can be expressed as follows:

$$[\mathrm{C-H}] = \frac{\mathrm{K_0}\sqrt{\mathrm{P_{H_2}}}}{1 + \mathrm{K_0}\sqrt{\mathrm{P_{H_2}}}}\mathrm{N_0} \tag{2.22}$$

Where $\mathrm{K_0}$ is a combined rate constant, $\mathrm{P_{H_2}}$ is the hydrogen partial pressure, [C-H] is the concentration of H adsorbed on C, and N_0 is a characteristic of the material which represents the total number of available active sites. At the limit of low pressure and hydrogen occupancy on graphite, Atsumi's solubility relation converges to Strehlow's and Shirasu's observation. A large variance of hydrogen solubility and diffusivity exists amongst different graphite materials shown in Figure 2.6 and Figure 2.7. The vast differences may be explained by the complexity of the graphite structure and variation between different types of graphite explained in Chapter 2.5.

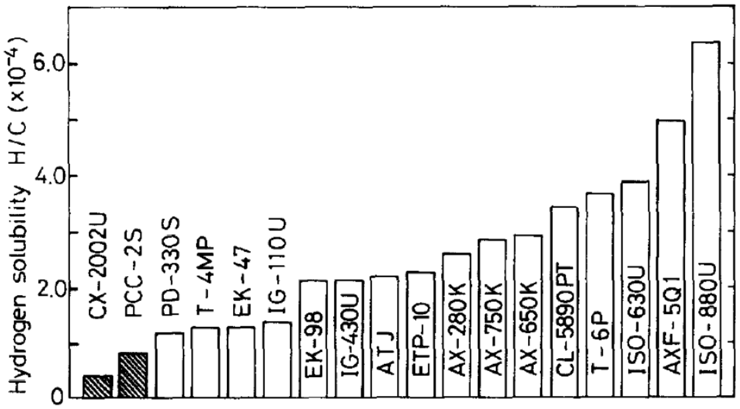

Figure 2.6: Hydrogen solubility in graphite materials at 1000°C & hydrogen pressure of 101 kPa [30]

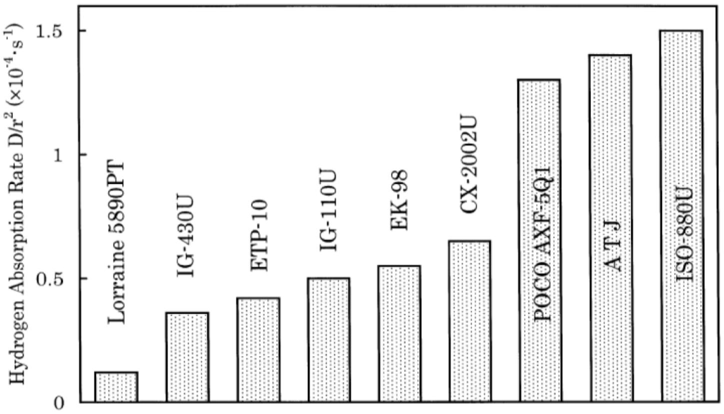

Figure 2.7: Hydrogen diffusion rates in graphite at 1000°C under hydrogen pressure of 10 kPa [59]

Only a few studies have been conducted at high temperatures of 750°C - 1000°C, which found correlations between hydrogen adsorption and material properties. As mentioned earlier, Strehlow showed that for oxidized graphite, the hydrogen adsorption increased roughly linearly with BET surface area [28]. Atsumi and Tanabe obtained similar findings but also found a positive correlation with both the crystalline edge surface area and the degree of graphitization [29][30]. Less data has been collected for the kinetics of adsorption. Atsumi and Iseki analyzed different graphite materials in Figure 2.7 and postulated that the diffusion rates correlated roughly with size of the graphite filler grains.

Atsumi proposed two trapping sites that contribute to solubility at temperatures greater than 1000K: 1) high energy interstitial clusters at dislocation loop edges (type 1) and 2) graphite filler grain edge sites with low adsorption energy (type 2). Graphite materials with smaller grain sizes have higher total grain edge surface area and thus a greater number of available type 1 site. This explains the observation of increased solubility with grain edge surface area and the increased diffusion rates due to inter-granular motion. The general transport model is described in the illustration of Figure 2.8.

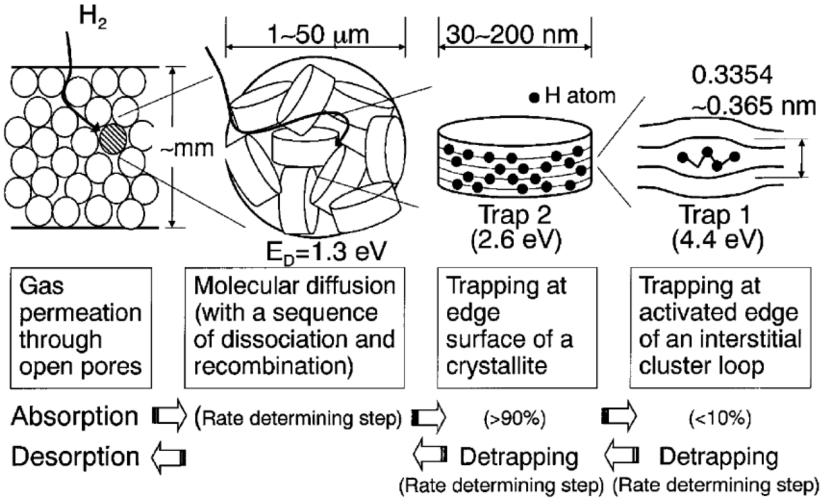

Figure 2.8: Illustration of proposed model of hydrogen transport and trapping in graphite material by Atsumi [60]

In Atsumi's model, the hydrogen readily migrates through open pores to the surface of the graphite grain. The hydrogen molecule can penetrate deeper into the graphite by diffusion along grains boundaries. Movement along the grain edge is dominated by diffusion with a relatively low activation energy of 1.3 eV during which dissociation and recombination can occur. The edge of the grains contain carbon dangling bonds on which the hydrogen can form a covalent bond with an adsorption enthalpy of 2.6 eV. A smaller fraction (~10%) of the hydrogen will interact with an interstitial loop, which forms a higher energy trap at 4.6 eV. The various modes of transport outlined here suggests a multi-process model whereby the tritium adsorption and migration depend on many operating variables (temperature, pressure) and material parameters (grain size, degree of graphitization, porosity, etc.). Consequently, the choice of specific material for optimal control and capture in the FHR is not obvious given current knowledge.

The studies that have been conducted provide insight into possible mechanisms that dictate the hydrogen solubility, but cannot be directly applied to the FHR system, which operates at temperatures of 600-700°C and low tritium partial pressures. While the literature provides suggestions for postulated relationships between hydrogen uptake and different material parameters, the inferences often lack unity and quantification and thus are difficult to apply to specific thermodynamic ranges, and to specific graphite materials that have not been tested experimentally. The solubility relationship used in the calculations of the next chapter for tritium solubility in nuclear graphite come from Atsumi [61] and was re-formulated by Stempien [9] in the equation below:

$$S[\mathrm{cm}^3 \mathrm{D} \mathrm{g}^{-1} \text{ graphite}] = 2 \cdot 1.9 \cdot 10^{-4} \sqrt{P[\mathrm{Pa}]} \exp\left(\frac{19[\mathrm{kJ\ mol}^{-1}]}{RT}\right) \tag{2.23}$$

The solubility data collected by Atsumi was for ISO - 88, which is assumed to exhibit a similar hydrogen uptake to the IG - 110U that is used in the FHR. Also, the solubility relationship was determined for D_2, but is assumed applicable to T_2. The tritium penetration in graphite strongly depends on the porosity of the graphite. In the MSRE moderator stringers, they found that tritium penetration into graphite was relatively low. At the surface, the POCO graphite sample tritium concentration was 0.0156 cm^3 STP/g, which decreased to 3.4×10^{-5} cm STP/g just 1.6 mm deep. Thus, it was inferred that reaction on the surface was much quicker than the diffusion into the bulk graphite. The code used in this thesis makes the assumption that the adsorption rate of hydrogen on graphite is not surface-reaction limited.

2.5.3. Effects of Irradiation

As highlighted in the Chapter 2.5.2, previous studies found that the uptake of tritium generally trends with various graphite properties. Hydrogen solubility was found to increase with increasing BET surface area, decreasing grain size and decreasing degree of graphitization. During the operation of a reactor, irradiation of graphite can change all of these properties, which will likely result in a change in the hydrogen uptake behavior. In idealized graphite, perfect sheets of sp^2 bonded graphene are stacked in a hexagonal lattice network with a sheet separation of 0.335 nm held together by Van der Waals interactions [50]. As examined in Chapter 2.5.1, real manufactured graphite is far from this with as many as one stacking fault in every six layers. During neutron irradiation, primary and secondary knock-on of carbon causes structural deformation of the crystal lattice, and the creation of more defects. Dislocation loops and trap sites can form, and it has been speculated that the deformation of the lattice can cause sp^3 bonding between basal planes [62]. While the exact mechanisms of displacement still lack fundamental understanding, the clear effect of irradiation is a change in dimensionality of the crystallite structure.

In a simplified format, the damage-induced dimensional change is shown in Figure 2.9, where the irradiation damage causes a contraction in the a-axis (parallel to basal plane) and an expansion of the c-axis. The magnitude of the change can be significant and increases with neutron dose, measured in displacements per atom (dpa). The dimensional change experienced is also dependent on the graphitization temperature during the manufacturing process of the graphite. Burchell showed that graphite materials graphitized at high temperature will exhibit a lower relative dimensional change under irradiation [62]. During the manufacturing process, higher temperatures results in a product with a higher degree of graphitization and fewer defects and trapping sites.

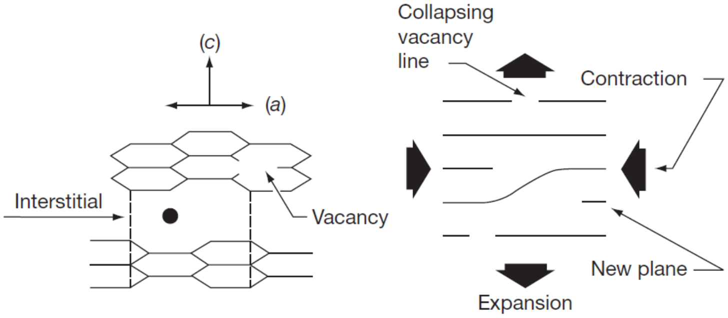

Figure 2.9: Neutron irradiation damage mechanism illustrating the induced crystal dimensional strains [62]

It has been observed in many studies that neutron irradiation greatly enhances hydrogen uptake in graphite materials and CFCs [63][64][65][66][67]. From Atsumi, one example showed an increase in the hydrogen retention by more than two orders of magnitude (140X) at a temperature of 1273K and a hydrogen partial pressure of 10 kPa [64].

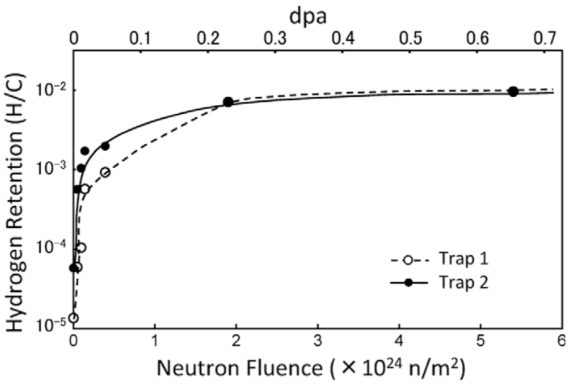

Figure 2.10: Hydrogen retention in irradiated graphite at several neutron fluxes. Two lines represent the two trapping sites postulated by Atsumi. Experiment conducted at 1273 K and at a pressure of 10 kPa

Figure 2.10 shows that for isotropic graphite IG-430U, hydrogen retention increases sharply initially with increasing fluence and dpa, which is likely caused by an increase in the number of defects. The concentration of these defects eventually saturates and reaches an equilibrium where the hydrogen uptake no longer increases. The effect of fluence is also shown at different temperatures in another similar isotropic graphite ISO-880U in Figure 2.11. Here, both the graphite materials showed a 2-3x increase in hydrogen retention after irradiation. Further, the slope of the plot of adsorbed hydrogen versus 1/T can be used to determine the adsorption energy. Comparing the irradiated to the non-irradiated graphite, the activation energies increased from 0.115 and 0.136 eV to 0.333 and 0.231 eV for ISO-880U and IG-430U respectively.

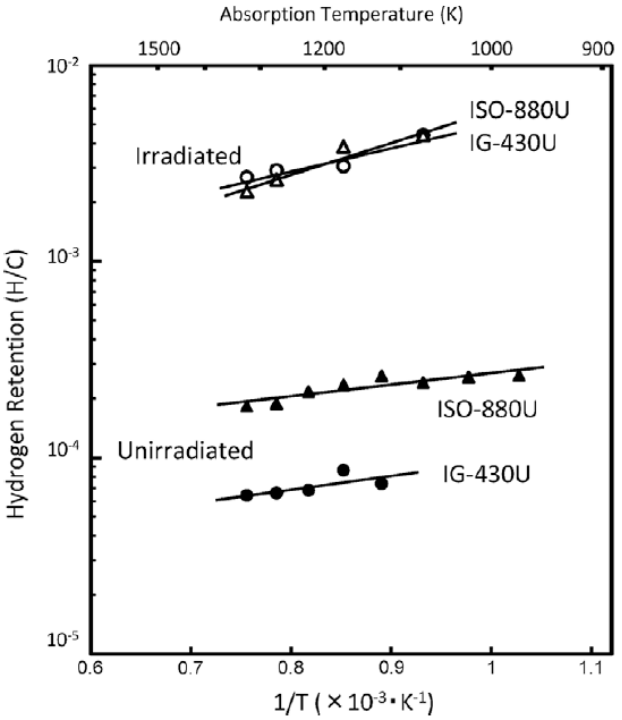

Figure 2.11: Temperature dependence on hydrogen retention in graphite before and after neutron irradiation at fluence of $3.9x10^{23}$ n/m^2 (0.047 dpa), temperature of 1273K and pressure of 10 kPa

The authors ascribe the increase in average adsorption energy to a shift in the concentration of the type of trapping sites available. Pertaining to the same trapping sites postulated in 2.5.2, Atsumi asserts that the un-irradiated graphite trapping is dominated largely by type 2 sites where the hydrogen can bind to grain edge sites, while irradiation causes a larger relative production of high-energy type 1 sites, where hydrogen binds to interstitial loops.

In addition to the tritium solubility changing with irradiation, the authors noticed a change in the diffusivity of hydrogen with respect to irradiation, which is shown in Figure 2.12. The diffusivity shown here is an estimation of migration in a grain and should not be taken as the true diffusivity of the material. The figure shows that the diffusion rates are strongly influenced by the presence of trapping sites where the apparent diffusivity drops quickly for both graphite materials and reaches a minimum between 0.1 – 0.2 dpa. The diffusivity then slowly increases with fluence, which is potentially due to the short-circuiting of hydrogen migration due to the continued formation of micro-cracks with increasing irradiation.

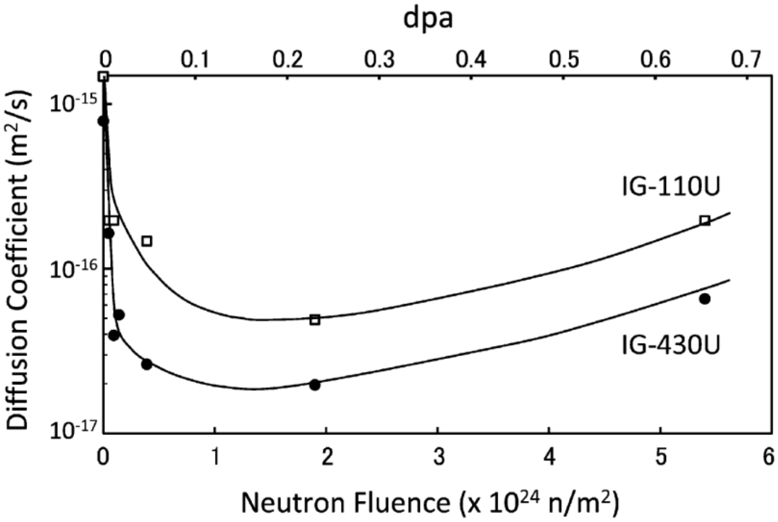

Figure 2.12: Change of diffusion coefficients of hydrogen in graphite irradiated with neutrons at various fluences at a temperature of 1273K and pressure of 10 kPa

The information of this section is meant to provide qualitative understanding of the effects of irradiation on tritium transport. To date, the exact mechanisms which cause irradiation-induced microstructural reconstruction still lack a widely accepted understanding although much progress has been made with irradiation experiments [62]. In TRIDENT calculations, the effect of irradiation in the core is not explicitly accounted for, reducing the total uptake that may be possible in the reactor core. This simplification is therefore conservative as it increases the concentration in the primary system and the potential release, which must be mitigated. Additionally, considering the use of graphite materials for adsorption in an out-of-core tower has advantages, which include not only improved performance consistency over time (no irradiation), but also an increased selection of materials that need not have the same stability requirements as nuclear-grade graphite.

Chapter 3.

System Modeling and Simulation

This chapter provides a brief overview of the code used for system-level simulation and the results of these preliminary simulations, which precede and provide a basis for experimental studies in Chapter 4. Simulation work will again be revisited in the last Chapter of this thesis.

3.1. Tritium Transport Code: TRIDENT

The purpose of this section is to provide context and a general overview of the functionality of the code and not designed to be a complete description of the code details which have already been provided elsewhere [27]. While various codes existed for tritium transport in HTGRs and SFRs, none were available for FHRs, which drove the development of TRIDENT (TRItium Diffusion EvolutioN and Transport) in 2015. An illustration of code's workflow is shown Figure 3.1.

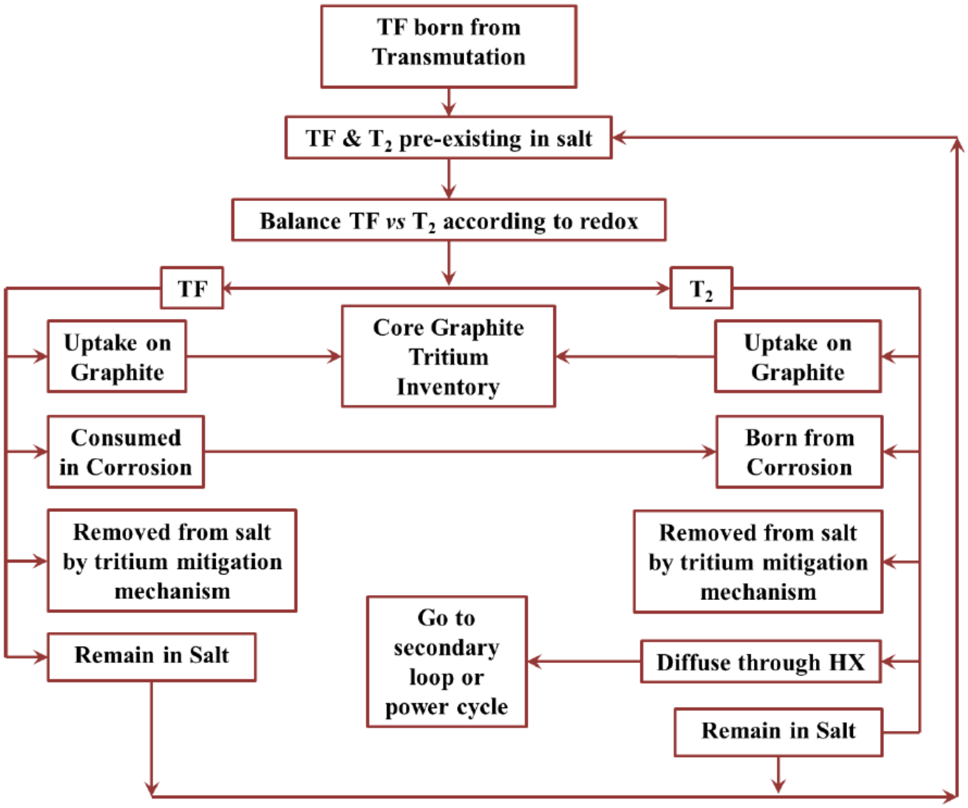

Figure 3.1: TRIDENT modeling workflow schematic

The main purpose of TRIDENT is to track the migration of tritium through the system while accounting for the reactions which act as tritium sources and sinks. First, the tritium is generated as TF as per Equation (2.1) in Chapter 2. Tritium generation due to impurities in the graphite and structural materials is neglected as it is relatively small compared to the tritium generated in the flibe. Globally, a redox potential in the system can be imposed as a user input by fixing the fluorine potential described in Chapter 2.2.2, or allowed to be transient in the system based on the natural un-controlled tritium speciation in the system. Tritium is generated in the core from neutron reactions, and simultaneous uptake and release from the graphite and structural components occur in the core. At each point in the system, the corrosion and deposition of structural metals is accounted for, which causes transformation of TF into T_2 and vice versa. The corrosion is based on selective attack of chromium, in which the equilibrium condition is set by the solution redox potential and the kinetics are limited by chromium diffusion along grain boundaries of the metallic structural components. The code allows a user option to input one of three different mechanisms that remove tritium: 1) transfer to gas in a multi-stage absorption column, 2) diffusion through a tritium-permeable window, and 3) uptake by graphite material in a solid adsorption column. Finally, the code calculates the tritium flux and mass lost through the heat exchangers by diffusion of T_2 across the tubing. The flibe coolant circulates through the system and returns any remaining tritium to the reactor core.

3.1.1. System Model and Calculation Structure

The FHR system that is modeled in TRIDENT is shown in Figure 3.2 and Figure 3.3. This includes the core where the tritium is produced, the hot and cold legs of the system where tritium causes corrosion/deposition based on the local thermodynamic potential, and the primary heat exchanger where corrosion/deposition occurs and the T_2 is allowed to diffuse out of the primary system. Additionally, the code has the option of simulating a secondary loop, which is shown in Figure 3.3. The secondary loop provides an additional barrier to tritium diffusion and prevents the radioactive primary salt from making direct contact with the power-cycle fluid. However, this would increase the system complexity, increase the cost of the system and reduce its thermal efficiency. Thus, the final designs previously proposed have included the addition of the secondary loop and this is simply allowed as an option in TRIDENT. The Table 3.1 summarizes the components that are simulated by TRIDENT along with the associated physics and dimensionality. TRIDENT uses explicit finite difference methods to solve the time-dependent tritium conservation equations in the system, which include the phenomena of generation, diffusion, absorption, corrosion, and permeation. Many of these phenomena have been discussed in Chapter 2.

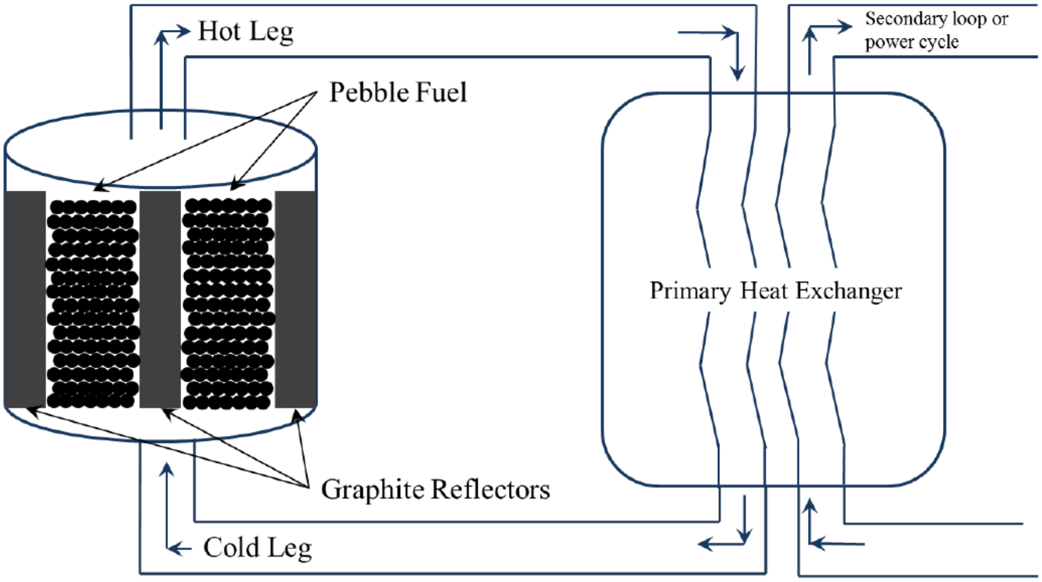

Figure 3.2: Schematic of FHR primary coolant system in TRIDENT

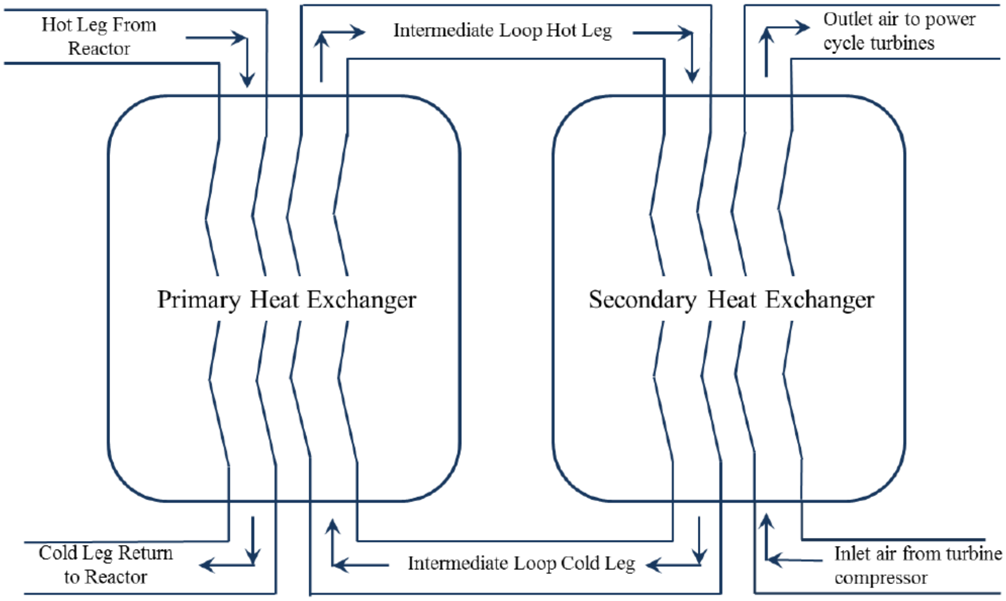

Figure 3.3: Schematic of optional secondary system modeled in TRIDENT

Table 3.1: TRIDENT simulated components with tritium-related physics that are simulated and the spatial dimensions of the simulation

Component	**Physics Options**	**Spatial Dimensionality**
Core	Generation, corrosion, deposition, adsorption	1D in coolant 1D in structures
Hot Leg / Cold Leg	Corrosion, deposition	0D in coolant
Heat Exchanger	Corrosion, deposition, absorption, permeation	1D in coolant 3D in tubing (isotropic in polar coordinate)
Optional: Permeation Barrier	Adsorption, permeation	3D in oxide layer (isotropic in polar coordinate)
Optional: Adsorption Tower	Adsorption	0D in coolant 0D in adsorbent

Continuous generation of tritium is driven by the neutron reactions in flibe. The corrosion of structural metals is enabled by the local temperature-dependent fluorine potential and driven by chromium diffusion along grain boundaries. Adsorption is driven by tritium diffusion from the bulk of the molten salt to the solid surface and limited by the pressure and temperature-dependent tritium solubility. Permeation is driven by transport in molten salt, diffusion in static media and transport in power cycle fluid. In addition to the default FHR components, two optional simulation parameters are shown in Table 3.1. The first is the permeation barrier, which is a coating or cladding applied to the outside tubing of the primary HXs. This coating is a material with a low hydrogen diffusivity, which serves as a barrier to limit the radiological tritium release to the atmosphere. In literature, some have defined the permeation reduction factor below:

$$\mathrm{PRF} = \frac{j_{\text{bare material}}}{j_{\text{with barrier}}} \tag{3.1}$$

Where $j_{\text{bare material}}$ is the permeation rate of tritium with in bare material, and $j_{\text{with barrier}}$ is the permeation rate of tritium with a barrier applied. Studies in fusion for tritium permeation at high temperatures have shown that permeation reduction factors of 1000 or greater can be achieved with oxide coatings of just a few μm in thickness [68][69]. While this may limit the rapid release by retaining more tritium in the system, the permeation rate increases with increasing tritium concentration in the system and increasing concentration gradient between opposite sides of the barrier. Thus, the barrier by itself is insufficient to limit long-term tritium release and a tritium capture technology must still be established.

The second option listed in the Table 3.1 is the adsorption mechanism. Previously, first-order approximate calculations were done for three tritium control technologies: 1) release through permeation window, 2) removal by gas stripping and 3) adsorption with a graphite pebble-bed, where the most promising of the 3 was the pebble-bed. Each of these mechanisms were placed in the primary loop hot leg to capture tritium in the salt prior to entering the heat exchangers. Typical engineering design parameters were used. For the stripping column, 50% of primary molten salt flow was processed in a gas-liquid contactor with 10 equilibrium stages and 20,000 L/hr at STP of counter-current inert gas flow to strip the tritium. This removed 80% of the tritium that would otherwise be released. For the permeation window, a shell and tube exchanger was used with nickel tubes in which 100% of the primary molten salt would flow through. The other sides of the tubes were maintained at hydrogen vacuum by flowing an inert sweep gas. The total mass transfer area used was 20, 164 m^2, window thickness was 8.89 x 10^{-4} m, tube outer diameter was 0.00635 m, and the total number of tubes was 27, 360. With the permeation window, removal was approximately 65%. The adsorption column received full flow of primary coolant and used nuclear graphite (ISO-88) spheres with a diameter of 3 cm. The bed size was 1.2 m R x 3.6 m H, the packing fraction was 0.6 and the graphite pebbles were regenerated continuously at an average rate of one full replacement every 30 days. For this arrangement, the radiological peak release was reduced by greater than 99%. The adsorption bed is the most relevant to this thesis, and the calculations have been modified and expanded in the next section.

3.1.2. Mitigation Mechanism: Graphite Adsorption Column

Ultimately, the design of an adsorption column requires the accurate accounting of various physical phenomena:

- Material and fluid densities
- Void Fraction: arrangement of pebbles in bed
- Adsorption Isotherms: solubility limits
- Kinetics: overall mass transfer resistances leading to breakthrough
- Dynamics: pebble-fluid interactions yielding mass transfer coefficient data

The graphite adsorption column was modeled in 0D in the hot leg of the primary loop, as shown in the Figure 3.4. The adsorbent used was ISO-88, with the equilibrium isotherm given in Equation

(2.23). The mass transfer to the graphite was assumed to be limited by transfer in the salt where empirical correlations for forced convection in packed beds were used [60][70] to determine the mass transfer coefficient and the mass flux of tritium species i to the pebble surface. The Equations (3.2) to (3.4) show the mass transfer coefficient and rate calculations.

$$\begin{aligned} k_{T_i,\mathrm{pebble}} &= \frac{D_{T_i,\mathrm{flibe}} * Sh_{T_i,\mathrm{pebble}}}{d_{\mathrm{pebble}}} \\ &= \frac{\mu}{\rho d_{\mathrm{pebble}}}\left[\left(1.18\left(\frac{\rho v_s d_{\mathrm{pebble}}}{\mu(1-\epsilon)}\right)^{0.58}\right)^4 + \left(0.23\left(\frac{\rho v_s d_{\mathrm{pebble}}}{\mu(1-\epsilon)}\right)^{0.75}\right)^4\right]^{0.25} \end{aligned} \tag{3.2}$$

$$j_{T_i,\mathrm{pebble}} = k_{T_i,\mathrm{pebble}}(c_{T_i,\mathrm{bulk}} - c_{T_i,\mathrm{surface}}) \tag{3.3}$$

$$\dot{n}_{T_i} = j_{T_i,\mathrm{pebble}} * A_{\mathrm{graph}} = j_{T_i} * \pi d_{\mathrm{pebble}}^2 * N_{\mathrm{pebbles}} \tag{3.4}$$

The subscript T_i represents an association with the tritium species i (TF or TF₂), $k_{T_i,\mathrm{pebble}}[\mathrm{m\ s^{-2}}]$ is the mass transfer coefficient, $D_{T_i,\mathrm{flibe}}[\mathrm{m^2 s^{-1}}]$ is the diffusivity in flibe, $Sh_{T_i,\mathrm{pebble}}$ is the Sherwood number, d_{pebble} [m] is the diameter of the pebble, ρ [$\mathrm{kg\ m^{-3}}$] is the density of the flibe coolant, v_s [$\mathrm{m\ s^{-1}}$] is the superficial velocity, μ [$\mathrm{Pa \cdot s}$] is the viscosity of flibe, ϵ is the void fraction of the pebble bed, $c_{T_i,\mathrm{bulk}}[\mathrm{mol\ m^{-3}}]$ is the concentration in bulk coolant, $c_{T_i,\mathrm{surface}}[\mathrm{mol\ m^{-3}}]$ is the concentration on the surface of the graphite, $j_{T_i,\mathrm{pebble}}[\mathrm{mol\ m^{-2} s^{-1}}]$ is the average molar flux to the surface of a pebble, $n_{T_i}[\mathrm{mol\ s^{-1}}]$ is the molar transport rate to graphite surfaces, $A_{\mathrm{graph}}[\mathrm{m^2}]$ is the total area of all graphene pebbles, and N_{pebbles} is the number of pebbles in the bed. Thus from Equations (3.2) - (3.4), it can be shown that the amount of tritium transferred and absorbed by the graphite surface increases with decreasing pebble diameter, which increases the mass transfer coefficient and increases transfer area.

The reaction on the surface of the graphite was assumed to be relatively fast and therefore non-limiting, which is an assumption that has been made in previous studies [19][52], although this should be verified in future experimental studies. The uptake onto the graphite surface was allowed to progress at the rate of bulk diffusion in flibe until the solubility limit (defined by the adsorption isotherm) was met. The user is allowed to input a bed regeneration rate in which a fraction of the bed containing adsorbed tritium is replaced with freshly regenerated adsorbent material.

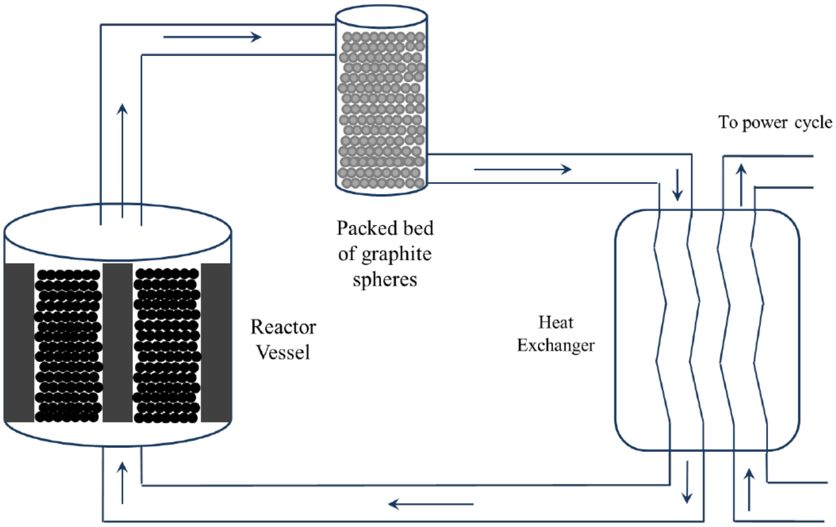

Figure 3.4: schematic of pebble bed simulation

Without mitigation, the total tritium inventory and release rates were calculated and the results are shown in Figure 3.5 a) and b) respectively. The inventory stabilizes at 68, 365 Ci, with the majority of this made up by the inventory in the graphite, which is 2-3 orders magnitude larger than the tritium in the heat exchanger and 4-5 orders of magnitude larger than the tritium in the molten salt. The maximum release rate occurs at approximately 2400 Ci/day.

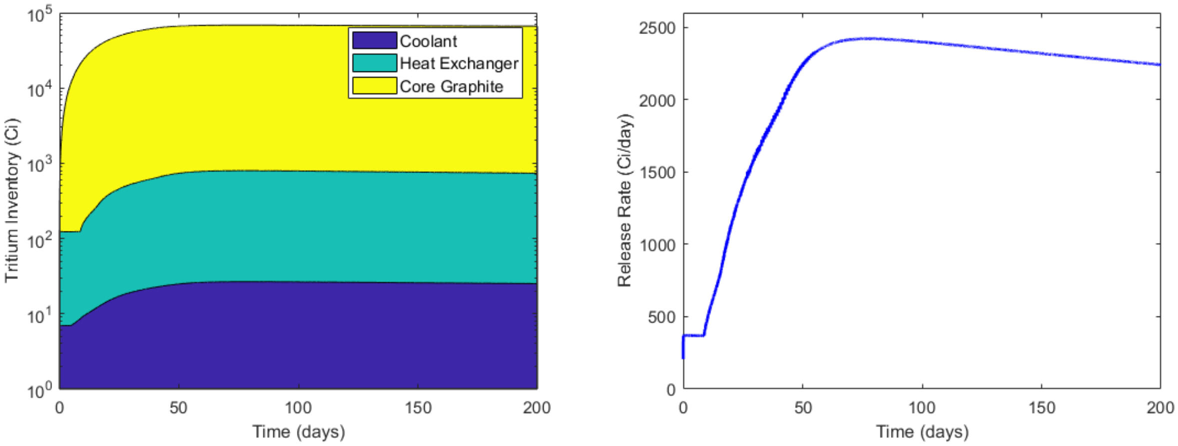

a) **b)**

Figure 3.5: Baseline simulation with no mitigation mechanism in place. a) The tritium inventories in the coolant, heat exchanger and core graphite and b) the release rate during a 200 simulation.

As mentioned at the end Chapter 3.1.1, Stempien previously calculated that the release rate could be reduced to 7.5 Ci/day. Since then, the calculation has been updated with new results based on the work of this thesis. In TRIDENT v1.0, it was found that the adsorption column was nested in the loop that numerically solved for tritium transport in the hot leg, resulting in an over-estimation of graphite bed capacity. Secondly, the code assumed that the concentration of tritium in the salt at the surface of the graphite was 1% of the bulk value. While this assumption is valid if the adsorbent is instantaneously regenerated, it can lead to considerable inaccuracy if the graphite concentration changes significantly before it is regenerated due to incorrect modeling of the approach to saturation; a conditions that is true under the simulation base case. Classically, an equilibrium condition between the salt and graphite is assumed at the graphite interface [71]. The equilibrium concentration in the bulk fluid can be related to the concentration in the graphite pebble using Henry's law with coefficients in Table 2.2 and the solubility relation for tritium in graphite in Equation (2.23). These changes have now been implemented in TRIDENT.

Using the same column specifications as in Chapter 3.1.1 but with the updated code, the release rate was found to be significantly higher at approximately 600 Ci/day shown in Figure 3.6 b). Additionally, the tritium inventory is also shown in Figure 3.6 a). This tritium inventory has a maximum occurring at 40, 938 Ci, which is 40% less than the unmitigated case shown in Figure 3.5.

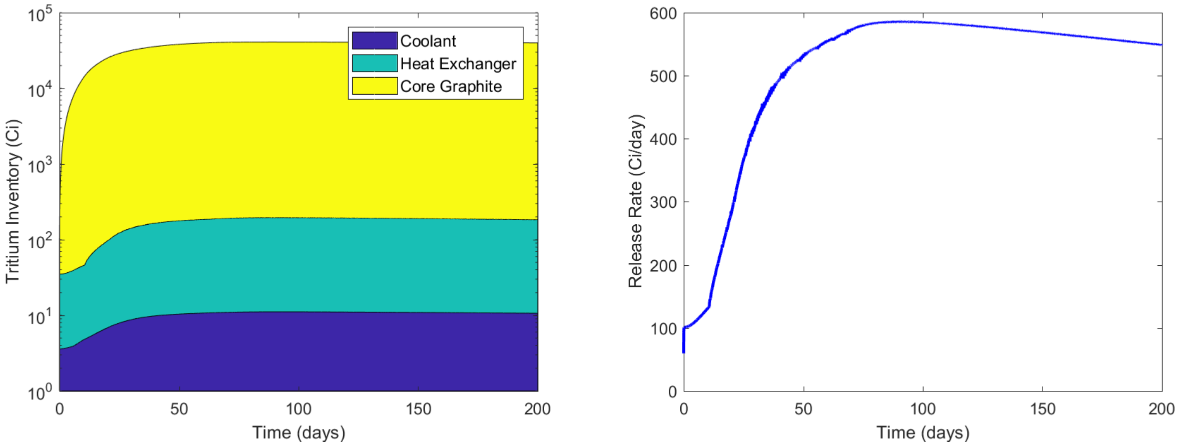

a) **b)**

Figure 3.6: Baseline simulation with standard IG-110U adsorption column. a) System tritium inventory b) total tritium release

In order to understand the limitations of this material and configuration, the average pebble concentration in the adsorption column was calculated and compared to the solubility limit as shown in Figure 3.7.

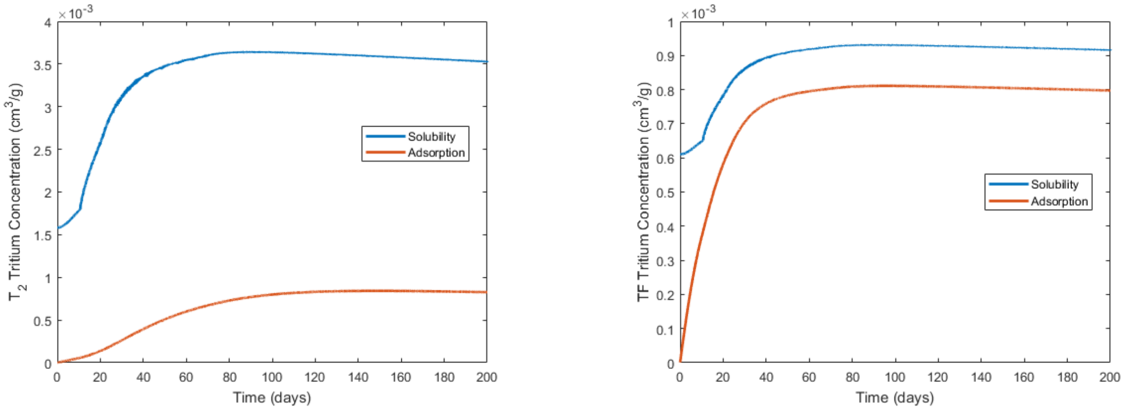

a) **b)**

Figure 3.7: a) T_2 and b) TF concentration adsorbed on graphite pebble bed versus the solubility limit

In both the TF and T_2, the increase in concentration in the graphite pebbles was the fastest initially. The solubility limit increases with the increase in partial pressure in the system. As the concentration rises, the mass transfer rate slows down due to the increase in concentration at the interface of the salt and pebble. For TF, the concentration in the pebble approached solubility limit very quickly and stabilized at a value that was approximately 90% of the solubility limit. This indicates that the total removal of TF is significantly limited by the solubility in the material. The bed was regenerated at each time step thus continuously removing TF tritium before the solubility limit was reached. In contrast, the increase in concentration was much slower for T_2 and the equilibrium value was near 20% of the saturation limit. This suggests that the removal of T_2 was limited by a slow transfer rate, rather than solubility. While 600 Ci/day is significantly more than current water reactors, various engineering parameters can be changed to improve the performance of the packed bed. In designing a column, numerous configurations and design parameters are possible. Some of these include the following:

- Placement of the adsorption tower: primary loop, secondary loop, hot leg, cold leg
- Number of adsorption columns
- Capital and operating cost
- Adsorbent size and shape
- Size and dimension of column: vessel radius and height
- Regeneration rate of adsorbent
- Selection of adsorbent materials

In this section, to limit the scope of preliminary analysis, the focus will be on the last 4 points listed above. As before, one adsorption column will be placed in the primary loop of the hot leg. Both the height and the diameter of the vessel are variable depending on the demands of the process. In this case, the minimum size is desirable since the placement of the tower in the primary loop and the concentration of radiological tritium on graphite may require the system to be placed in primary containment. Here, the size of the reactor vessel itself was used as a reference point. As per the technical description for the 236 MWt FHR, the reactor vessel height is 12.0 m and vessel radius of 1.75 m. One important limiting conditions that must be considered is the pressure drop in the bed, which is determined with the Ergun equation below:

$$-\frac{\Delta P}{H} = \frac{150\mu U(1-\epsilon)^2}{r^2\epsilon^3} + \frac{1.75\rho_f U^2(1-\epsilon)}{r\epsilon^3} \tag{3.5}$$

Where ΔP [Pa] is the pressure drop, H [m] is the height of the column, r [m] is the pebble radius, μ [Pa · s] is the dynamic viscosity of molten salt, ϵ is the void fraction, and ρ_f [kg m^{-3}] is the density of flibe. The superficial velocity U is simply the total flow rate of the molten salt in the primary system divided by the total cross-sectional area inside the adsorption column. The pressure drop per unit length is shown as a function of vessel radius and pebble radius in Figure 3.8.

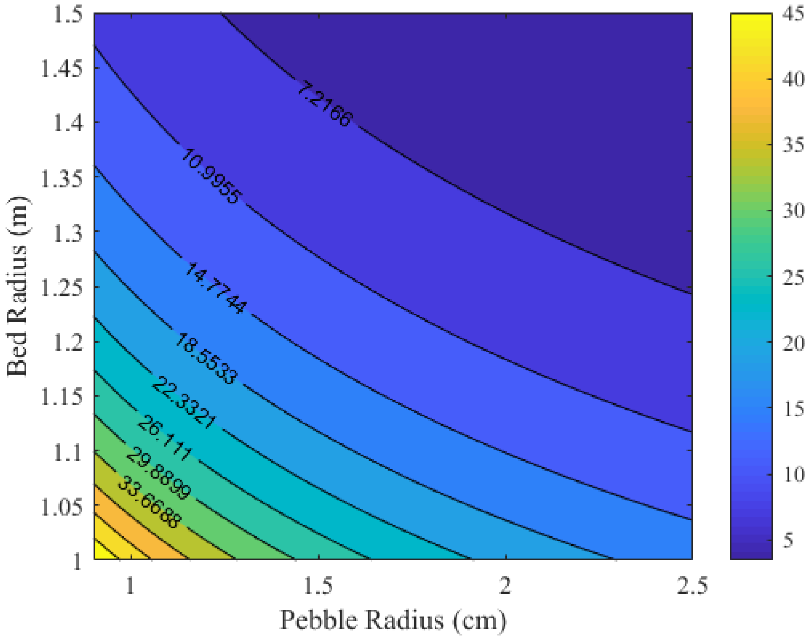

Figure 3.8: Pressure drop in color shown as a function of pebble radius (m) and bed radius (m) calculated using the Ergun equation

One of the design goals of the FHR is to limit the total pressure drop in the system to roughly 2 or 3 m of head [5]. This corresponds to a pressure drop of roughly 40 – 60 kPa. Increasing the pressure drop in the system can significantly increase the pumping demand, creating increased wear on components and increasing the cost of operation. The target used here for total pressure in this column will therefore be < 50 kPa. In addition to the total pressure drop, the pressure drop per unit length is also an important consideration in the column. Excessive pressure drops over a short distance can cause excessive wear on the absorbent material. Typically, ΔP in adsorption columns with carbon material are limited to around 3 – 10 kPa per meter. Increasing the diameter of the bed has the effect of increasing the total surface area for mass transfer, which higher tritium retention. This is limited however, by the space available. Using a bed radius of 1.5 m and a height of 4.5 m, Figure 3.8 shows that the pressure drop does not exceed 10 kPa/m (for pebble radius >1 cm) or 50 kPa total across the adsorption bed. This provided a starting point with dimensions that are of similar scale to those of the reactor vessel. Varying the pebble size and the regeneration rate with the above parameters, the sensitivity to these operating parameters was determined.

3.1.3. TRIDENT User Inputs

In these simulations, the standard configuration of the baseline FHR was used [9]. The inputs are recorded in Table 3.2, Table 3.3 and Table 3.4. Table 3.2 shows the general parameters of simulation of the FHR including core inlet temperatures, reactor power, and more. Table 3.3 shows the simulation options including number of simulation days, redox control scheme, permeation reduction, core refueling etc. Table 3.4 includes the additional simulation options for the simulation of an adsorption column.

Table 3.2: Baseline simulation input parameters for the FHR in TRIDENT from Ref [9]

Parameter	**Input Variable**	**Value**	**Units**
Core inlet temperature	`T_in`	873.15	K
Core outlet temperature	`T_out`	973.15	K
Reactor power	`Rx_power`	236	MWt
Axial peak linear heat generation rate*	`qo`	79.72*	MWt
Redox potential specified as the ratio PTF/(PT20.5)*	`Ratio_TF_T2`	9.2×10^{-5}	-
Li-7 enrichment in flibe	`Li7_enrichment`	99.995	wt.%

Number of un-fueled graphite pebbles in the core	`N_CoreGraphPebbles`	2.18x105	-
Volume-averaged one-group flux* [62]	`flux`	3.41 x 10^{14}*	n/cm2-s
TRISO fuel kernel diameter	`Kernel_d`	400 x 10^{-6}	m
TRISO fuel buffer thickness	`Buffer_t`	100 x 10^{-6}	m
TRISO fuel IPyC thickness	`IPyC_t`	35 x 10^{-6}	m
TRISO fuel SiC thickness	`SiC_t`	35 x 10^{-6}	m
TRISO fuel OPyC thickness	`OPyC_t`	35 x 10^{-6}	m
Number of TRISO particles per fuel pebble	`TRISOperPebble`	4730	-
Fuel pebble radius	`Pebble_radius`	0.015	m
Pebble packing fraction in the core	`PF`	0.60	-
Core height*	`Core_height`	4.65*	m
Radius of core central graphite reflector	`CentralRef_radius`	0.35	m
Outer reflector outer radius*	`OuterRef_inradius`	1.69*	m
Outer reflector inner radius	`OuterRef_inradius`	1.25	m
Inner radius of fuel pebble zone	`Fuelzone_innerradius`	0.35	m
Outer radius of fuel pebble zone	`Fuelzone_outerradius`	1.05	m
Hot leg pipe wall thickness	`pipe_thick1`	0.02	m
Hot leg pipe inner diameter*	`pipe_d`	0.792*	m
Hot leg pipe length*	`pipe_l`	29.74*	m
Cold leg pipe wall thickness	`pipe_thick2`	0.02	m
Cold leg pipe inner diameter*	`pipe_d2`	0.495*	m
Cold leg pipe length*	`pipe_l2`	35.44*	m
Number of tubes in primary heat exchanger*	`Hx1tubes`	2.736 x 10^{4}*	-
Heat exchanger tube outer diameter	`Hx_tube_od`	0.00635	m
Heat exchanger tube wall thickness	`Thick`	8.89 x 10^{-4}	m
Primary heat exchanger tube outer surface area*	`A1`	10082*	m^2

*Represents values that have been calculated ore extrapolated

Table 3.3: Table of simulation options in TRIDENT for baseline PB-FHR simulation

Input Variables	**Value and Explanation**
`Days`	200
`Hour_Fraction`	0.1
`Elements`	6
`T_uptake`	2 (On, tritium uptake on graphite is simulated)

`CoreRefuelFrac`[a]	1/30 (Pebble refueling is accounted for with a 30 day cycle)
`CoreGeometryAdjust`	2 (On)
`Redoxflag`	2 (TF and T2 may exist subject to the redox option `Feedbackflag`)
`Feedbackflag`	2 (Redox potential is fixed to baseline at -700.5 kJ/mol-F_2)
`Oxideflag`	2 (oxide layer on air-side of HX is accounted for)
`PRFinput`	10 (permeation reduction factor)
`Corrosionflag`	1 (corrosion is not simulated)
`Core_mesh`	10
`Hot_mesh`	10
`HX_mesh`	10
`Cold_mesh`	10
`Tritiumproductionflag`	3 (the tritium production rate varies with time according to (2.1))

[a] Regeneration rate of the bed is based on a continuously-stirred tank reactor (CSTR)

The specifications above includes the use of a permeation barrier with a PRF of 10, redox control set to a fixed fluorine potential, disabling of the corrosion simulation, and definition of finite difference space and time step sizes. The baseline simulations in Table 3.2 and Table 3.3 above were fixed for the analyses of this chapter and in the calculations of Chapter 6. In these analyses, only the additional specifications shown in Table 3.4 were varied.

Table 3.4: TRIDENT inputs for simulating optional adsorption column

Input Variables	**Value and Explanation**
`Tritiumproductionflag`	3 the tritium production rate varies with time according Eqn. (2.1)
`Tritiumcapturebedflag`	2 (on)
`Bed_frac_rep`	1/7, 1/13, 1/19, 1/25, 1/31 [fractional bed regeneration per day]
`Bed_vessel_radius`	1.5 (Inner radius of the packed bed [m])
`Bed_height`	4.5 (Height of the adsorbent zone in the bed [m])
`Particle_radius`	0.009, 0.013, 0.017, 0.021, 0.025 ([m])
`Particle_density`	$1.77\text{x}10^{6}$ (Density of graphite [g/m3])
`Bed_packingfraction`	0.60 (Packing fraction in the bed)

For the simulations, the bed replacement fraction was varied as well as the pebble radius shown by the range of inputs above. Previously, TRIDENT accepted input for the total surface area of the adsorbent, packing fraction, pebble radius and bed radius and then used these inputs to calculate the required height. The code now accepts the input of bed height instead and then calculates the surface area for mass transfer as needed. The total size of the column is set to 1.5 m in radius and 4.5 m in height, which is dimensionally similar to the core (1.69 m outer reflector radius x 4.69 m H), and ensures that the pressure limitations are not exceeded.

3.1.4. Tritium Release Rates and Inventory

Regeneration Rates

The pebble bed was regenerated continuously at a rate of one bed every 7, 13, 19, 25 and 31 days. The maximum pebble size of 2.5 cm was used. The effect of varying the regeneraetion rate on the release rate to the power cycle is shown Figure 3.9.

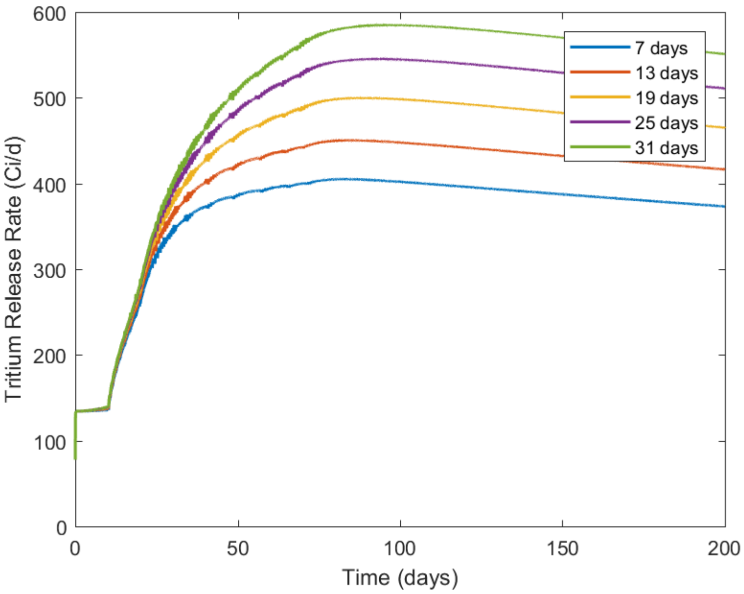

Figure 3.9: Release rates (Ci/EFPD) at different bed regeneration rates (days per bed replacement) with ISO-88 pebble radius R = 2.5 cm and bed size of 1.5 m R x 4.5 m H

The upper limit of regeneration rate was set to a rate of 1/7 of a bed per day. Ultimately, the rate is limited by the practical physical limits of operation. This includes the limitations of speed and size of the regenerative process, as well as mechanical limitations of the material. In comparison, the fuel in the core was regenerated once every 30 days. As shown in Figure 3.9, the total release was supressed with an increasing regeneration rate. When the bed was only regenerated once every 31 days, the release rate peaked at 600 Ci/day. When the regeneration rate was increased a to a replacement every 7 days, the release rate was supressed to under 400 Ci/day, as more of the tritium was captured in the adsorption column. In addition to the net release rates, one goal of tritium control is the minimization of tritium inventory, which is shown for various regeneration rates in Figure 3.10 to Figure 3.13.

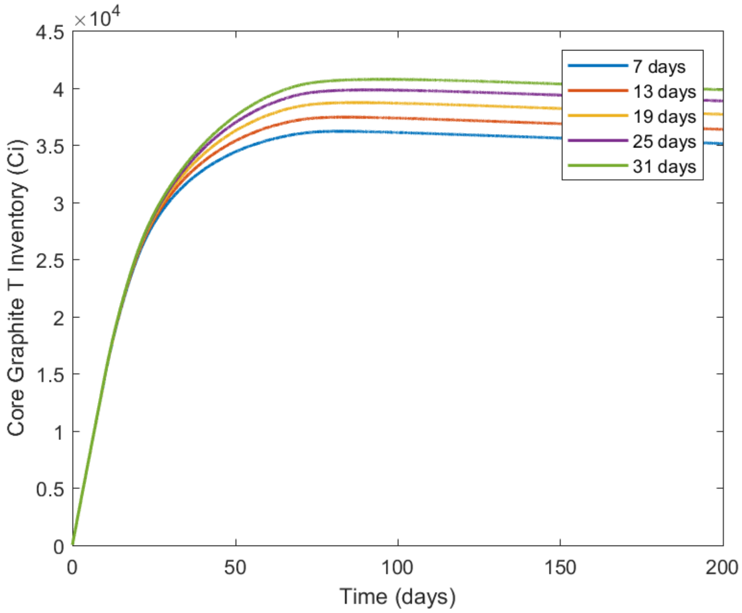

Figure 3.10: Tritium inventory in Ci in core graphite versus adsorbent bed regeneration rate with ISO-88, pebble radius R = 2.5 cm and bed size of 1.5 m R x 4.5 m H

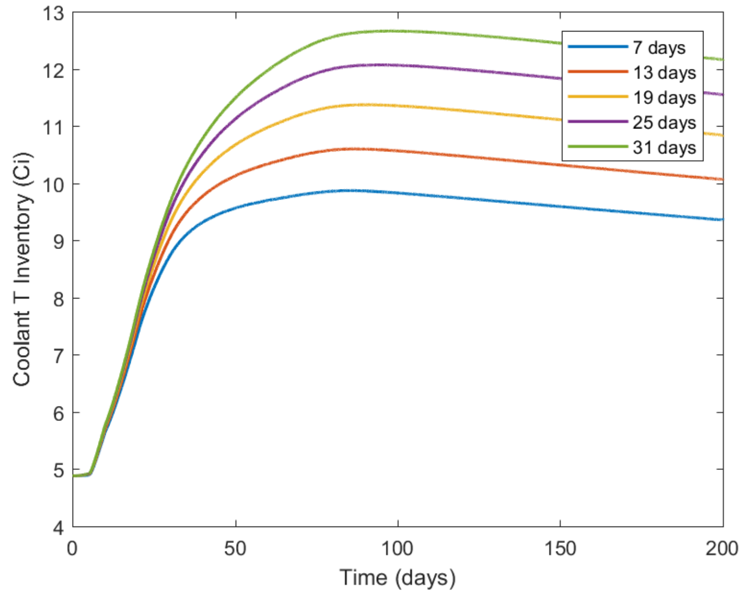

Figure 3.11: Tritium inventory in Ci primary flibe coolant versus adsorbent bed regeneration rate with ISO - 88 pebble, radius R = 2.5 cm and bed size of 1.5 m R x 4.5 m H

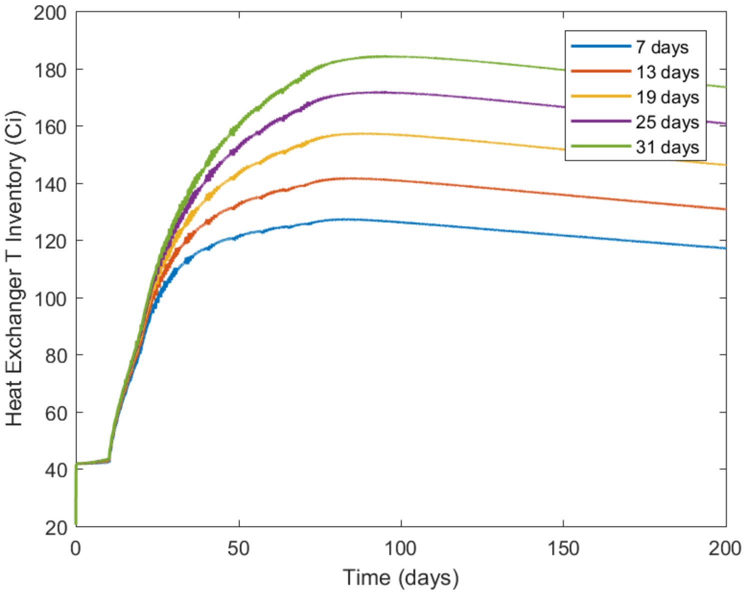

Figure 3.12: Tritium inventory in Ci in primary heat exchanger tubes versus adsorbent bed regeneration rate with ISO-88, pebble radius R = 2.5 cm and bed size of 1.5 m R x 4.5 m H

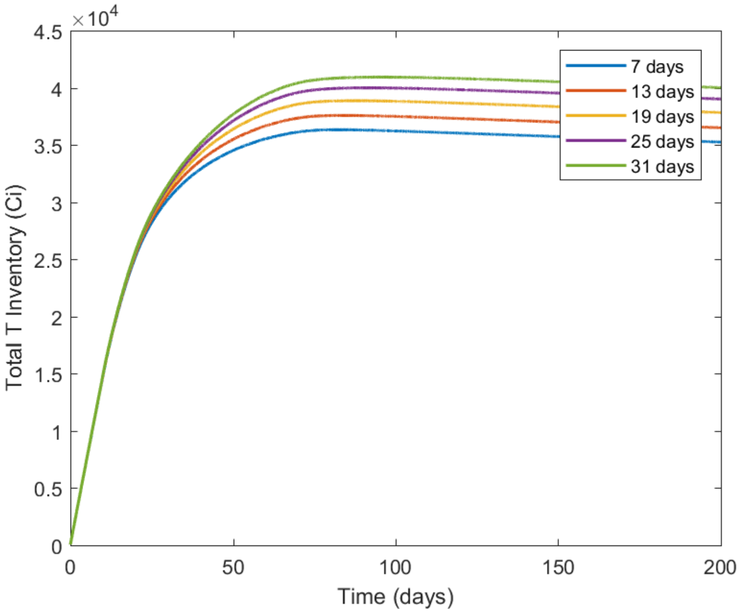

Figure 3.13: Total tritium inventory in the primary system (excluding column) versus bed regeneration rate with ISO-88, pebble radius R = 2.5 cm and bed size of 1.5 m R x 4.5 m H

The largest sink in the system excluding the removal system was the graphite of the core, which held orders of magnitude higher activity than the coolant, and HX metal tubing. Increasing the regeneration rate reduced the inventory from 4.2 to 3.6 x 10^4 Ci in the core graphite, 180 to 120 Ci in the primary heat exchanger tubing and 13 to 10 Ci in the flibe coolant. In total the tritium in the inventory can be reduced by an additional 12% by varying the regeneration rate. By minimizing the tritium inventory, the total amount that can be released is minimized in a reactor transient, increasing the safety margin. In order to accurately quantify transient release, both the absorption and desorption characteristics of the material must be known.

Radius of Adsorbent Particles

Using the same column dimensions, the adsorbent particle radius was varied between 0.9 and 2.5 cm. The upper limit of regeneration rate was used with an average full bed replacement every 31 days. The release rates are shown in Figure 3.14.

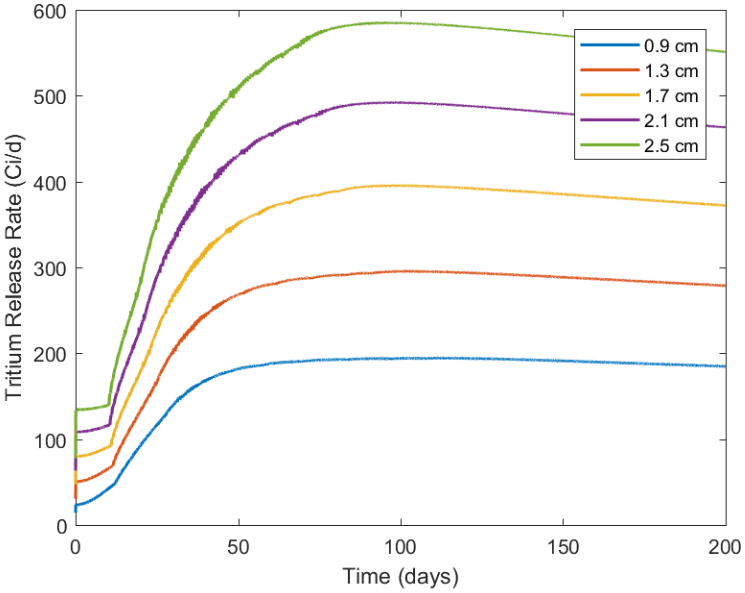

Figure 3.14: Tritium release rate (Ci/d) versus pebble radius in a 1.2 m R x 4.5 m H adsorption column with ISO-88 and on average 1 bed full regeneration every 31 days

At the maximum pebble size of 2.5 cm, the release rate peaks near 600 Ci/day and is suppressed to under 200 Ci/day if this pebble size is reduced to 0.9 cm. Figure 3.14 shows that as the pebble size decreases, the release rate decreases as expected due to increased surface area for mass transfer to the bed. In this configuration, varying the pebble size proves to be an effective method of reducing the release rates with a decrease of more than 70% between the pebble sizes of 2.5 cm and 0.9 cm. The tritium inventory while varying the pebble size is shown in Figure 3.15 to Figure 3.18.

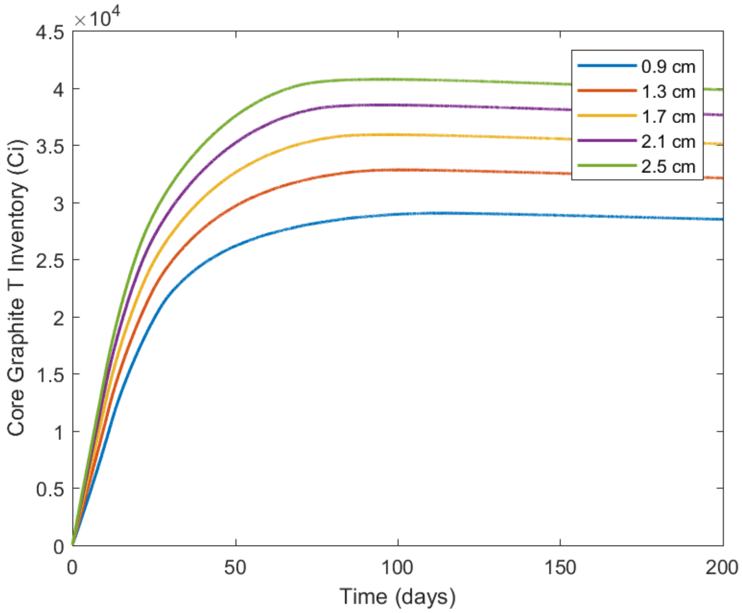

Figure 3.15: Tritium inventory in core graphite (Ci) versus pebble radius in a 1.2 m R x 4.5 m H adsorption column with ISO-88 and on average 1 bed full regeneration every 31 days

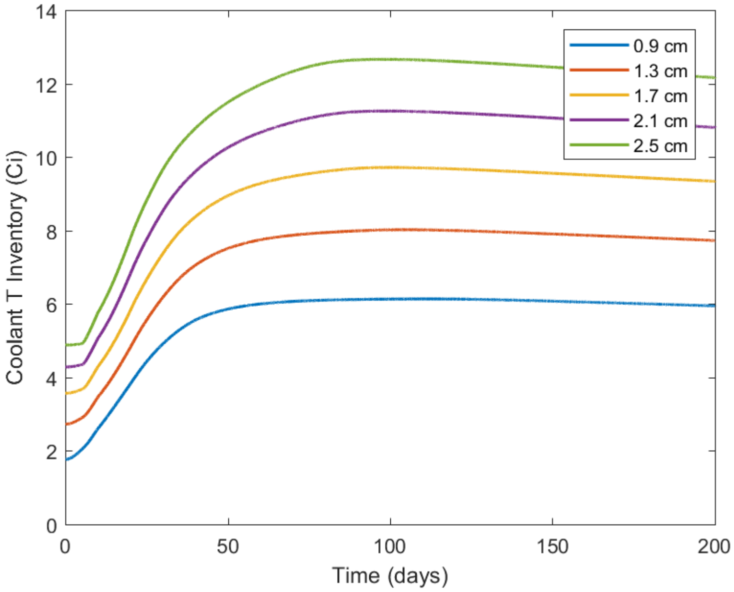

Figure 3.16: Tritium inventory in coolant versus pebble radius in a 1.2 m R x 4.5 m H adsorption column with ISO-88 and on average 1 bed full regeneration every 31 days

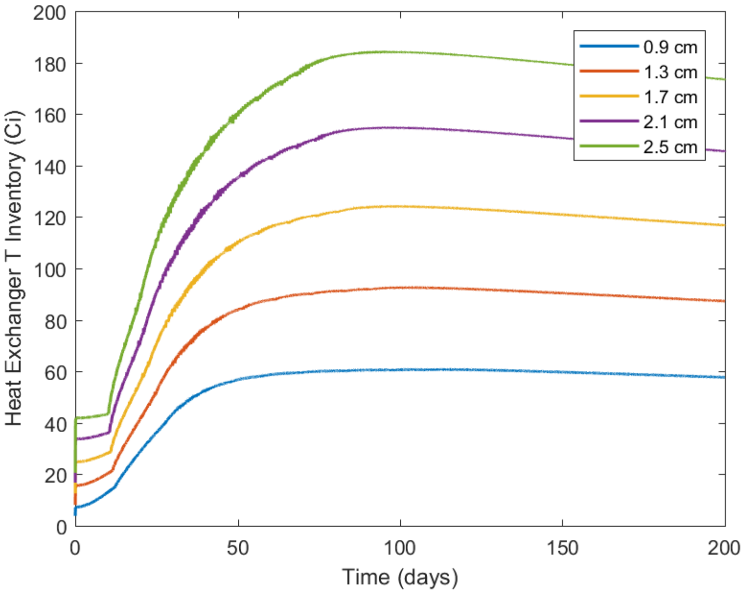

Figure 3.17: Tritium Inventory (Ci) in heat exchanger tubing versus pebble radius a 1.2 m R x 4.5 m H adsorption column with ISO-88 and on average 1 bed full regeneration every 31 days

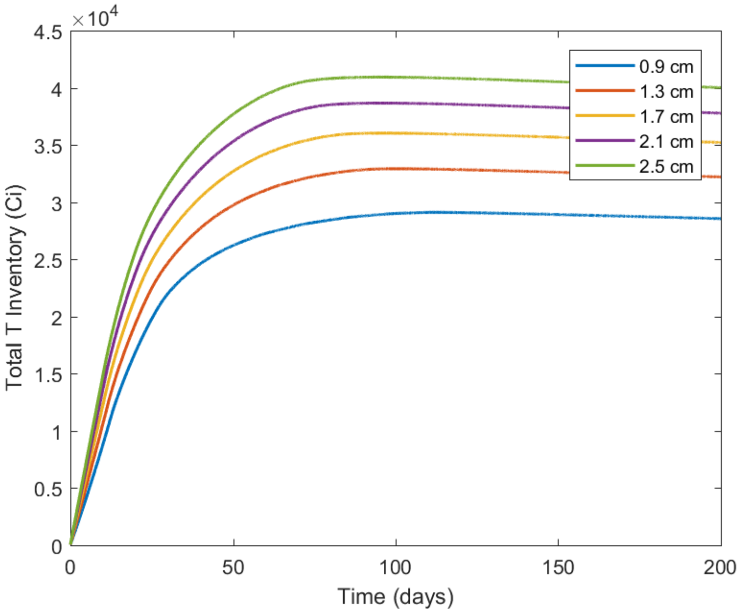

Figure 3.18: Total tritium inventory in primary loop (Ci) versus pebble radius a 1.2 m R x 4.5 m H adsorption column with ISO-88 and on average 1 bed full regeneration every 31 days

As expected, the tritium inventory in the core graphite, heat exchangers tubing and the flibe coolant decreased with decreasing pebble size. Graphite is available in large quantities in the core and also has a much higher tritium solubility compared to both flibe coolant and the metal heat exchanger tubes. Decreasing the pebble radius from 2.5 cm to 0.9 cm, the core graphite inventory decreased from a maximum of 4.1 x 10^4 to 2.75 x 10^4 Ci, the coolant inventory decreased from 12 to 6 Ci and the heat exchanger tubing inventory decreased from 180 Ci to approximately 60 Ci. This shows that significant reductions in inventory can be achieved by adjusting the surface area.

In the event of a transient, the heat exchanger tritium is released first, followed by the molten salt and the graphite due to proximity to the environment. Thus, the 60%+ tritium reduction in the heat exchanger tubing is very desirable. In both the release and inventories of reactor materials, a greater relative reduction is achieved by reducing the pebble radius than by increasing the regeneration frequency up to the limits allowed by pressure drop and handling rate. The pebble size is inversely related to the total surface area of transfer, and therefore the total mass transfer rate to the pebble surface increases sharply at low pebble sizes, while the uptake rate on the adsorbent surface will increase proportionally with the rate of regeneration. The relationship between these two parameters can be shown in further detail by varying them both simultaneously shown in

Figure 3.19, which is a surface plot of the release rate from the power cycle.

This plot suggests regions where the process can be optimized by varying either regeneration cycle or pebble radius. For example, on the right side, the plot demonstrates that decreasing the regeneration cycle from 31 days to 7 days can reduce the release rate by about 200 Ci /day. On the left side, the decrease is less than 150 Ci/day when changing the cycle from 31 to 7 days. The small difference is due to the difference in mass transfer rates between the small (left side) and large pebbles (right side). In large pebbles, the mass transfer rate is lower due to the lower surface area, and thus, the regeneration rate can play a larger role. In the middle of the plot, the contour lines show a slight inflection, where the slope of the line is largest (less negative). In this case, either increasing regeneration rate or decreasing pebble size can result in a significant reduction in release rate. This means, that the transfer is dominated neither by area or solubility limitations, in comparison to places on the plot where the slope becomes more vertical.

Overall, within the defined bounds of the problem, it can be shown that reducing the pebble size decreases the release rate to a greater extent than the reduction in cycle length. Reducing the pebble size from 2.5 to 0.9 cm reduced the release rates from 600 to 200 Ci/day even for a long 31 day regeneration cycle. At any regeneration cycle length between 7 and 31 days, the fastest descent in release rate is generally achieved by reduction in pebble size. However, significant reductions in release can still be made by modifying the cycle length, which is an operating parameter that is easier to adjust than pebble size.

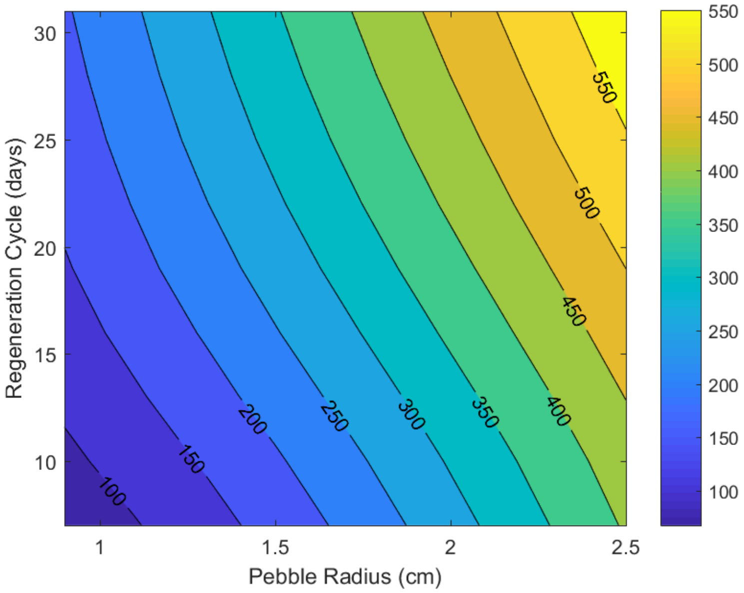

Figure 3.19: Maximum release rates (Ci/EFPD) at different regeneration rates (days per full bed replacement) and pebble radius in a 1.2 m R x 4.5 m H adsorption column with ISO-88

In all cases, the optimization between these two engineering parameters given any point in the plot can be determined simply by taking the path along the surface plot which yields the fastest reduction in release rate. The eventual limits of these parameters depend not only on the major constraints discussed in this section but also on the choice of material and the specific systems employed, which must be informed by further research. Further, dozens of optimizations can be performed on the various parameters discussed in 3.1.2 based on specific system constraints. These calculations show just a couple of variables that can be changed.

It has been shown that with just graphite ISO-88, large performance improvements can be achieved. Without mitigation, the release rates reach a peak at approximately 2410 Ci/day while it has been estimated here that adjustment of operating parameters has the potential to decrease this to less than 100 Ci/day, a reduction of greater than 95%. In all these calculations, nuclear graphite ISO-88 was used based on its stability in FHR conditions and past experience in the MSRE. However, there are other materials that potentially adsorb high quantities of hydrogen, which are considered in the next section.

3.2. Consideration of Alternative Adsorbents

Intermetallic compounds containing hydrogen-getting rare-earth metals that would typically be used for hydrogen storage was discussed briefly in Chapter 2.4, where the majority of these materials were found to be inherently unstable in flibe. Due to the complexity in the structure of graphite and in the transport of hydrogen on graphite, a unified model for hydrogen adsorption does not exist. However, various experiments have been conducted on a limited set of graphite materials for fusion applications at high temperatures, which suggest that the total solubility of hydrogen generally correlates with increasing available surface area, decreasing grain size, and decreasing degree of graphitization. Meanwhile, the processing of graphite required for typical nuclear applications results in changes to these features that ultimately reduce the total hydrogen uptake. Due to the requirement of nuclear graphite to be dimensionally stable under irradiation and to contain few neutron absorbers, high purity graphite is required. The manufacture of high purity graphite however, requires thermal cycling at high temperatures often exceeding 2800°C, which results in the annealing of the graphite surface and thermal closure of pores. This results in a less-permeable and less-accessible material and increased graphitization, which reduces the defects where hydrogen can become adsorbed and trapped [32].

In using the adsorption column as shown in Figure 3.4, the adsorbent does not need to be nuclear-grade graphite since the goal is for hydrogen adsorption to occur outside of the reactor core. Therefore, the same limitations for nuclear graphite do not apply to materials that are used for adsorption. In fact, many carbon-based materials that would be stable in salt exhibit the desired qualities that would theoretically yield a high uptake. Activated carbon and graphene nanomaterials exhibit high surface area, and porosity, and unlike graphite is amorphous, allowing faster hydrogen permeation to occur. However, almost all studies of these materials have been conducted at room temperatures for the purpose of hydrogen energy storage and therefore requires more experimental data [72]. Consistent with the understanding in graphite, it was found that at ambient conditions that hydrogen uptake correlates well with specific surface area, micropore surface area, total pore volume and micropore volume [72]. In another study, it was been found that graphite materials exhibiting a mix of both sp^2 and sp^3 bonded carbons can readily adsorb/desorb hydrogen reversibly [73]. In addition, while the rare-earth metals may be unstable in the flibe, the transition metals (such as Ni) are not. The transition metals themselves do not have high adsorption capacity but catalyze the surface dissociation of hydrogen. Thus, depending on the kinetics of bare carbon material, transition metals supported by the graphite matrix could be a promising path forward. Such proposals have been made for the purpose of hydrogen storage where activated carbons supporting palladium catalysts have shown high hydrogen uptake at ambient conditions [74][75]. Another option could involve designing a pebble composed of graphite and highly absorbing intermetallic compounds where the graphite provides a barrier layer to direct contact between the intermetallic and molten salt. The hydrogen adsorbed on graphite could then spillover to the shielded intermetallic, resulting in a high uptake in both the intermetallic and graphite layer. Many materials and material combinations exist with only a limited body of experimental research. The next couple of chapters of this thesis focuses on experimental work conducted on high surface area, porous carbons.

Chapter 4. Experimental Methods

The experimental work can divided into three sections: 1) characterization of materials using N_2 and CO_2 gas physisorption, 2) hydrogen solubility measurement at 700°C, and 3) morphological study using scanning electron microscopy. In this section, all the experimental methods, parameters and analyses are explained. The information and data obtained from each method is also discussed.

4.1. Material Procurement and Preparation

Isotropic graphite IG-110U is of interest since it is a major reflector and structural material used in the FHR core as discussed in Chapter 1.1.2. Additionally, powdered activated carbons (PACs) Cabot PAC-200 and Maxsorb MSC-30, granular activated carbons (GACs) Cabot Norit Vapur 612, CalgonCarbon OLC12x40, Cal-TR 12x40 and OVC 4x8, extruded activated carbon (EAC) Cabot Norit RB-40, and graphene nanoplatelets (GNP) Graphenit-OX were all examined. Many of the activated carbon (AC) samples were donated from Cabot and CalgonCarbon.

Prior to analysis, each of these were rinsed and decanted under acetone ultrasonication to remove fine particulates and dust. The rest of the sample preparation was conducted with the Autosorb IQ-C-XR by QuantaChrome Inc. For the physisorption experiments described Chapter 4.2, the samples were heated to 350°C and held under a vacuum of 10^{-8} Pa for at least 3 hours in a sample cell prior to analysis to remove moisture and other volatile impurities, which interact with the adsorbate. At the end of the out-gassing step, the change of pressure in the cell over time was measured to ensure there were no adsorbates still being released. If the pressure in the cell changed more than 3 Pa/min during evacuation, the evacuation time was extended. The sample was placed in the smallest cell possible with a glass filler rod to reduce the void volume in the sample cell.

For chemisorption analyses, the samples were purged with helium gas to remove impurities while the temperature of the sample cell was increased to 1000°C. The samples were held at 1000°C under a 5×10^{-8} Pa vacuum for 2 hours and then ramped temperature of 700°C and analyzed. The samples were held in place by quartz wool to prevent elutriation from the sample cell. Quartz is generally considered to be non-adsorptive and impermeable to hydrogen.

4.2. Gas Adsorption Experiments

4.2.1. Fundamentals of Gas Adsorption

Adsorption of gas onto a solid surface can be divided into two groups: physical interactions, namely physisorption, and chemical reaction, known as chemisorption. Physisorption is a reversible process and describes the general phenomena when an adsorptive is brought to the surface of a solid. The process is driven by attractive dispersion forces, short-ranged atomic repulsion and adsorptive-adsorbate specific interactions such as dipole or quadrupole fields [76]. At low temperatures near the boiling point of the gas, the adsorbed gas on solid surface forms a dense layer of adsorbate at the fluid-solid interface where the total number of gas molecules can be described by the two-phase model [77]:

$$n^g = n_{ads} + n_{bulk} \tag{4.1}$$

$$V^g = V_{ads} + V_{bulk} \tag{4.2}$$

Where the n^g is the total number of gas molecules, n_{ads} is the number of gas molecules adsorbed on the solid surface and n_{bulk} is the number of molecules in the bulk gas. As the temperature increases, the theoretical boundary between the adsorbed phase and gas phase disappears as the physical attraction between adsorbed molecules decreases. Thus, the density of the gas phase is no longer insignificant relative to the adsorbed phase. The potential well of the molecule near the solid surface and the fluid density profile ρ(z) from the pore wall are schematically shown in Figure 4.1.

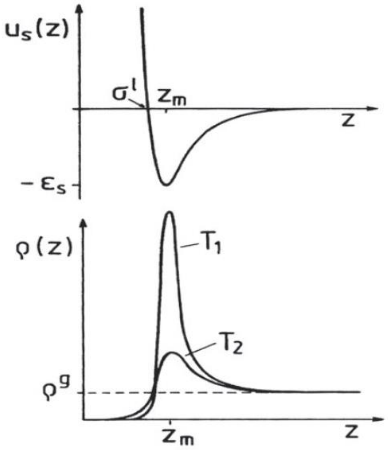

Figure 4.1: Gas-solid interaction potential U(z) (upper graph) and density profile ρ(z) of an ideal adsorbed gas at a flat, homogeneous surface for two temperatures $T_2 > T_1$ [78]

The density profile of the fluid adsorbed onto the wall begins to flatten at higher temperatures, in which case the two-phase model description becomes problematic. Further, the adsorbed phase n_{ads} is not actually the physical quantity that is measured in volumetric experiments. More accurately, the surface excess n^{σ} is defined as the number of gas molecules adsorbed onto the solid surface subtracted by the number of gas molecules in the bulk gas phase that would otherwise occupy the adsorption volume V_{ads}. The surface excess is found with the simple expression:

$$n^{\sigma} = n_{ads} - \rho^{g} V_{ads} \tag{4.3}$$

Where ρ_g is the gas phase density and V_{ads} is the volume of the adsorption layer. The excess adsorption as a function of pressure at a constant temperature is called an isotherm.

4.2.2. Gas Adsorption Isotherms

In real materials, the potential and density profile on a solid surface differs than the depiction shown in Figure 4.1 due to the presence of other nearby surfaces that interact with the adsorbate. In addition to the physical description of gas adsorbing on an isolated surface, models accounting for adjacent wall interactions must be used. A schematic representation of the interaction potentials is shown Figure 4.2.

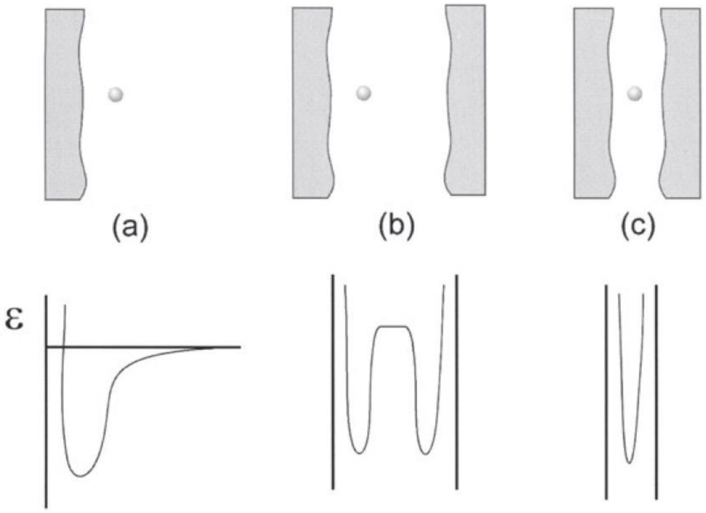

Figure 4.2: Schematic provided by Lowell and Thommes [77] showing a) adsorption potential on a planar non-porous surface, b) adsorption potential inside a meso-pore 3) adsorption potential in a micopore

The International Union of Pure and Applied Chemistry (IUPAC) broadly proposed the classification of pores into 3 sizes: 1) micropores which have an internal width of less than 2 nm, 2) mesopores with a width of greater than 2 nm but less than 50 nm and 3) macropores which have a width larger than 50 nm [76]. Additionally, it has often been found useful to add the narrow micropore sub category, which is simply defined by micropores of widths less than 0.7 nm. The characteristic of the adsorption isotherm is determined by the thermodynamics of the adsorption process, which are dependent on fluid-solid interactions, fluid-fluid interactions and the geometry of the surface. In 1985, IUPAC published a convention for classifying 6 different types of isotherms shown in Figure 4.3.

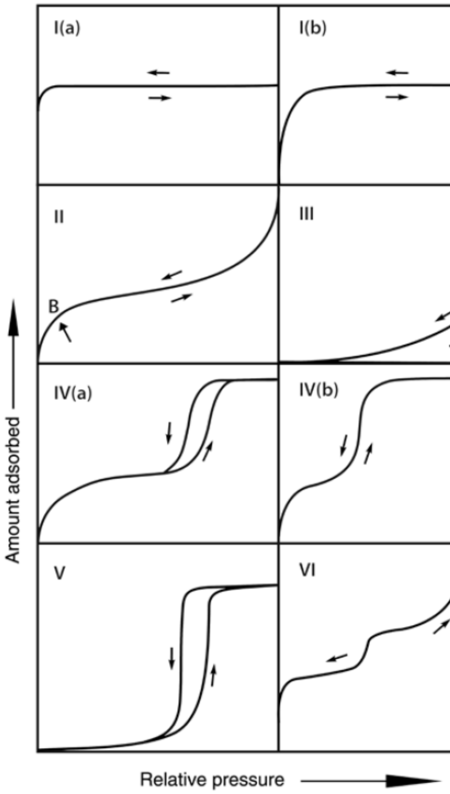

Figure 4.3: IUPAC classification of sorption isotherms [76]

Type I isotherms are concave with respect to the relative pressure axis and approach a saturation limit with higher pressures. These isotherms are common for microporous materials, which have a high uptake at low pressures during micropore filling and in chemisorption where the adsorption occurs on a single layer and limited by the available reactive sites on the solid surface. Type II isotherms are exhibited by nonporous or macroporous materials. The knee labelled point ‘B’ represents the point where the solid surface is covered with a single monolayer, after which fluid multilayers develop, demonstrated by the continued increase in adsorbed volume with pressure. Type III isotherms are convex relative to the pressure axis and are exhibited by materials where the adsorbate-adsorbent interactions are weak and thus the measured adsorption is low at low pressures. Type IV isotherms are typical of mesoporous materials, in which the mesopores fill with fluid exhibited by the final plateau at high relative pressure. Similar to Type II isotherms, these also have an initial knee that represents the monolayer adsorption. In Figure 4.3, two curves in each plot represent the adsorption and desorption isotherms. Hysteresis can exist due differences in the thermodynamics of condensation and evaporation in pores, which will be further discussed in later sections. Type V isotherms are a combination of type III and IV isotherms where a weakly interacting solid also exhibits mesoporous condensation. Finally, type VI represents stepwise layer-by-layer adsorption on materials that are uniform, non-porous, and non-polar. Various types of isotherms are examined in the results section of this thesis. Using physisorption at low temperature, materials can be characterized using various kinetic and molecular models discussed in the sections below. Further, chemisorption at high temperatures with hydrogen gas can be used to probe the nature of the surface reaction at the FHR operating conditions.

4.2.3. Adsorption Experimental Setup and Method

Figure 4.4 shows the experimental setup for vacuum volumetric adsorption. Various techniques can be employed using in the experimental setup shown but here we describe only the physisorption and chemisorption capabilities that were used for this work. The physisorption and chemisorption experiments were conducted using an Autosorb IQ-X-CR and the data was reduced in ASIQWin v.4.01 software, which use methods outlined in this chapter [77]. The setup consists of a series of control valves, pressure transducers, a temperature controlled furnace, sample cell, and analyzers such as a thermal conductivity detector or mass spectrometer.

Many versions of the apparatus used for vacuum volumetric adsorption exist [77], designed based on the needs of the application, but mostly use the same general methods. Gas is injected into the sample chamber, which is heated or cooled during analysis. Gas injections are staged through the manifold shown in Figure 4.4 over a desired pressure range. At each stage, the pressure in the system is allowed to equilibrate while the gas adsorbs onto the surface. After equilibrium is reached, the cell pressure is measured with transducers and using gas equations, the adsorbed volume on the sample surface is calculated. The output data of this process produces isotherms, such as those shown in Figure 4.3.

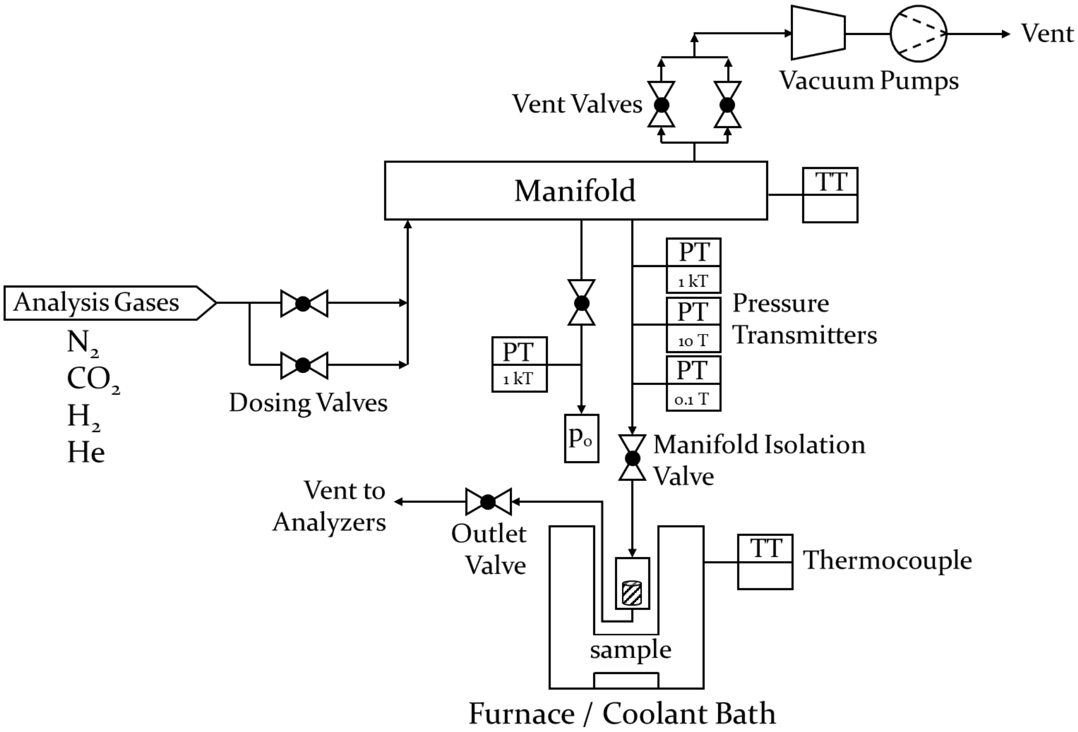

Figure 4.4: Piping schematic of experimental setup used for performing adsorption analyses

In order to calculate the amount of gas adsorbed onto the sample at each stage after equilibration with the manifold, the effective void volume in the sample cell must be known. The void volume must be measured since the space occupied by individual samples is unknown. This is done prior to analysis by evacuating the system, by dosing with helium, a non-adsorbing ideal gas, and equilibrating the pressure into the sample cell. Thus, the void volume in the system is calculated using the equation of state:

$$V_{void}(P_2) = \left[\frac{P_1 V_{man}\left(T_{man,2} - T_{man,1}\right)}{T_{man,1} T_{man,2}}\right] \cdot \frac{T_{void}}{P_2} \tag{4.4}$$

Where the volume of free space in the sample cell is V_{void}, P_1 and P_2 are the initial and final pressures, V_{man} is the known geometric volume of the manifold, $T_{man,1}$ and $T_{man,2}$ are the initial and final temperatures in the manifold, and T_{void} is the analysis temperature in the sample cell. It is important to note that the temperature profile in the cell changes with increasing pressure in the system since convective and conductive heat transfer increases. Thus, the effective void volume calculation is performed at several pressures over the desired analysis range prior to the start of the analysis. Knowing the effective void volumes, the adsorbed gas at each stage is calculated by the following balance equation:

$$V_{ads}[\mathrm{std.\,cm}^3] = \left(\left[\frac{P_i V_{man}}{T_{man,i}} - \frac{P_{i+1} V_{man}}{T_{man,i+1}}\right] - \left[\frac{P_{i+1} V_{void}(P_{i+1})}{T_{void}}\right]\right)\left[\frac{T_{std}}{P_{std}}\right] \tag{4.5}$$

Where P_i and P_{i+1} are the initial and final pressures of the manifold at stage i, $T_{man,i}$ and $T_{man,i+1}$ are the initial and final temperatures in the manifold, $V_{void}(P_{i+1})$ is the void volume calculated in Equation (4.4).

4.3. Characterization with Gas Physisorption

The process of physisorption occurs in three distinct stages. Firstly, the gas adsorbs as a monolayer whereby each adsorbed molecule makes direct contact with the solid. As the surface coverage increases, gas molecules begin to form multi-layers where some of the gas molecules are in contact with an underlying adsorbed layer but are separated from the material surface. Finally, with sufficient multilayer build-up, gas begins to condense in mesopores creating a liquid-like state through the process of capillary condensation. By applying thermodynamic models to experimental isotherms, physical characteristics of the materials can be determined including the surface area, total pore volume, and pore size distribution. Since gas physisorption occurs at low temperatures, adsorbate gases N_2 and CO_2 exhibit non-ideal behavior that needs to be corrected. To do this, the sample cell is divided into two theoretical regions: the cold zone and the warm zone, separated by the point where the sample is immersed in coolant.

$$V_v = V_w + V_c \tag{4.6}$$

The total void volume represented by V_v in (4.6) describes the total void volume in the sample cell plus the manifold volume measured using the non-ideal adsorbate. Considering that the gas behaves ideally at ambient conditions, compensation only needs to be applied to the cold zone. The difference between the ideal volume calculated in Equation (4.4) and the apparent non-ideal volume V_v is therefore equal to the difference between the cold zone calculated at ambient temperature versus the cold zone calculated at the cryogenic conditions expressed in (4.7):

$$V_c = \frac{V_{void} - V_v}{\left(1 - \frac{T_{cold}}{T_{ambient}}\right)} \tag{4.7}$$

Which is an expression for the volume of the cold zone when a sample cell is immersed in the coolant bath at temperature T_{cold}. Finally, the void volume V_{void} correction is made by using non-ideality factors α applied to the Equation (4.5) [77]:

$$V_{ads}[\mathrm{std.\,cm}^3] = \left(\left[\frac{P_i V_{man}}{T_{man,i}} - \frac{P_{i+1} V_{man}}{T_{man,i+1}}\right] - \left[\frac{P_{i+1} V_{void}(P_{i+1})}{T_{void}} + \frac{P_{i+1}^2\, V_c \alpha}{T_{void}}\right]\right)\left[\frac{T_{std}}{P_{std}}\right] \tag{4.8}$$

These non-ideality factors were determined by Emmett and Brunauer [5] and is 6.58 x 10^{-5} torr^{-1} for N_2 at 77K. With N_2 analysis at 77K, another effect is accounted for is thermal transpiration, which is the thermal force on a gas due to temperature difference[79]. The result of this effect is an increased pressure on the cold zone where the sample is held compared to warm zone, where the pressure transducer measures the system pressure. At low pressures, Knudsen postulated the relationship between point two points at different temperatures follows Equation (4.9).

$$P_1 = P_2 \sqrt{T_1/T_2} \tag{4.9}$$

At higher pressures, the model given by Liang[80], [81] is used:

$$\frac{P_1}{P_2} = \frac{\alpha\phi^2 x^2 + \beta\phi + \sqrt{\frac{T_1}{T_2}}}{\alpha\phi^2 + \beta\phi x + 1} \tag{4.10}$$

Where $x = 0.133 \cdot P_2 \cdot d$, d = diameter of the connecting tube (m), α and β are constants dependent on the gas, and ϕ is the pressure shift factor:

$$0.27 \log \phi = \log D + 9.59 \tag{4.11}$$

Where D is the molecular diameter of the gas molecule.

4.3.1. Choice of Adsorptive

The ideal choice of adsorptive depends mostly on the material being studied. N_2 at 77K has been the most widely applied to study the surface area, pore topology and morphology of carbon materials due to its ability to produce full adsorption and desorption isotherms from partial pressures of 10^{-7} to 1. However, the diffusion of N_2 at low relative pressure below 10^{-5} is slow, resulting in extended analysis times. Furthermore, the statistical thickness of a condensed nitrogen bilayer is 0.7 nm. Thus, for the analysis of narrow micropores, the blockage of the entrance of a pore can restrict further access, causing underestimation of the pore volume [82]. To resolve these issues, alternatives to N_2 have been proposed including Ar and CO_2. While the kinetic diameter of Ar and CO_2 are 0.34nm and 0.33 nm, which is similar to that of nitrogen (0.36 nm), differences in the adsorption characteristics allow for a more accurate probe of microporous materials.

Studies comparing the use of Argon at 87K to N_2 on activated carbon found that Argon adsorption branches were delayed. This demonstrates that the pores fill at higher pressures than they empty due to a weaker adsorption potential [83]. The difference between Argon and other gases can become more pronounced on functionalized surfaces. The presence of a quadrupole moment in N_2 and CO_2 results in surface interactions with functional groups, which can cause a shift in the adsorption isotherm towards lower pressures [84]. This means that low pressure transducers with higher accuracy are required to collect and calculate pore data if N_2 is used compared to Ar. Additionally, Ar is generally used at a higher temperature (+10K) than N_2, and so the diffusion rate is faster and the equilibration time is shorter. These combined effects all contribute to a more accurate micropore characterization using argon gas.

Even with these improvements, condensation and pore blocking has been observed at low pressures using Argon at 87K, limiting the pore size analysis to >0.45 nm. However, studies have shown that using CO_2 at 273K can effectively eliminate this problem [85][86]. CO_2 has a high saturation pressure of 3.5 MPa at 273K, which is 32K above the critical point. This enables the use of moderate pressures (near atmospheric) to adsorb CO_2 onto a surface at 273K while maintaining a very low relative pressure, operating far from the point where pore blocking would occur. While CO_2 cannot be used for characterizing the full pore size distribution range at moderate pressures, CO_2 adsorption is often combined with N_2 or Argon adsorption isotherms, where CO_2 is used for the narrow micropores < 1nm and the other gas accurately characterizes the micropore to macropore range [82].

In the experiments conducted in here, N_2 was used widely used for the determination of surface area, total pore volume and average pore size, and the pore distribution of pores > 1 nm. CO_2 adsorption and desorption will be used just to determine the pore size distribution in the micropore region of < 1 nm.

4.3.2. Liquid Density Functional Theory

Using statistical mechanics-based descriptions of the nano-phase, many studies combining molecular modeling and experiments have demonstrated that density functional theory allows the reliable calculation of pore size distributions. Macroscopic approaches such as the Dubinin-Radushkevich (DR), approximate the adsorptive as a constant-density, bulk fluid independent of pore morphology. It has been demonstrated that significant error is caused by such approximations and the applications of liquid DFT and molecular simulation have greatly improved estimation of pore size distributions [87][88][89].

The method of non-local density functional theory (NLDFT) was first proposed by Seaton [90]. In DFT, the experimental adsorption isotherm $N_{exp}(P/P_0)$ is used to calculate the pore size distribution f(D) using mean field approximation methods. The experimental isotherm is fit to a set of theoretical isotherms that are calculated for different pore sizes. Mathematically, this fit is expressed by the equation of the experimental isotherm and the integral of the product of the theoretical isotherm of pore diameter D and the pore size distribution function f(D), integrated over the applicable pore diameter range:

$$N_{exp}\left(\frac{P}{P_0}\right) = \int_{D_{min}}^{D_{max}} N_{DFT}\left(\frac{P}{P_0}, D\right) f(D)dD \tag{4.12}$$

The theoretical isotherms are represented by N_{DFT}, which are calculated by spatial integration of the fluid density $\rho_f(r)$ inside the pore of radius r. This density is calculated using the two methods: Non-Local Density Functional Theory (NLDFT) and Quenched-Solid Density Functional Theory (QSDFT), which are discussed below.

Non-Local Density Functional Theory (NLDFT)

In NLDFT, the solid surface is assumed to be smooth with no surface functional groups present, eliminating the effects of surface heterogeneity. In the volumetric experiment, the nitrogen is adsorbed onto the material surface and held in isothermal equilibrium at each pressure step, which corresponds to the minimization of the grand canonical thermodynamic potential with a fixed chemical potential μ, volume V and temperature T. The potential for a fluid confined in a pore can be expressed solely as a function of the fluid density ρ_f, and is given by the Equation (4.13) [91].

$$\Omega_f[\rho_f(r)] = F_f[\rho_f(r)] - \int dr\, \rho_f(r)[\mu_f - V_{ext}(r)] \tag{4.13}$$

In (4.13), F_f is the Helmholtz free energy of the fluid, V_{ext} is the external potential imposed by the solid wall of the pore and r is the radial position inside the pore. The Helmholtz free energy can then be subdivided into the ideal component of energy F_{id}, excess hard sphere repulsion of the fluid F_{ex} and the attractive energy terms shown in (4.14):

$$F_f[\rho_f(r)] = F_{id}[\rho_f(r)] + F_{ex}[\rho_f(r)] + \frac{1}{2}\iint dr\, dr'\rho_f(r)\rho_f(r')u_{ff}(|r - r'|) \tag{4.14}$$

Where $u_{ff}(r)$ is the attractive term of the pair-wise fluid-fluid potential considered at positions r and r′. The simplest model assumes that the shapes of the pores are infinite slits. The equation (4.14) above can be further expanded. The ideal free energy is the energy of an ideal gas and given by the exact expression:

$$F_{id}[\rho_f(r)] = k_B T \int dr \rho(r)[\Lambda^3 \rho(r) - 1] \tag{4.15}$$

Where $k_B T$ is Boltzmann's constant multiplied by the temperature and $\Lambda = \sqrt{2\pi m k_B T / h^2}$ is the thermal de Broglie Wavelength. The external potential is calculated by integrating the hard sphere excess energy function:

$$F_{ex}[\rho_f(r)] = \int dr \rho_f(r) f_{ex}[\bar{\rho}_f(r); d_{HS}] \tag{4.16}$$

Where the $\bar{\rho}_f$ is given by the smoothed density approximation of Tarazona [92]:

$$\bar{\rho}(r) = \int dr' \rho(r') \omega\big(|r - r'|, \rho(r)\big) \tag{4.17}$$

And the $f_{ex}[\bar{\rho}_f, d_{HS}]$ is calculated by the Carnahan-Starling equation of state for non-attracing rigid spheres. The weighting function ω is chosen to match the Percus-Yevick approximation [93]. Lastly, the attractive potential is modeled by the Lennard-Jones 6-12 with the Weeks-Chandler-Anderson (WCA) perturbation scheme:

$$u_{ff} = \begin{cases} -\epsilon_{ff} & r < r_m \\ 4\epsilon_{ff}[\left(\frac{\sigma_{ff}}{r}\right)^{12} - \left(\frac{\sigma_{ff}}{r}\right)^{6} & r_m < r < r_c \\ 0 & r > r_c \end{cases} \tag{4.18}$$

Where ϵ_{ff} is the depth of the potential well, r_m is the position of minimum potential, and r_c is the cutoff distance of the potential.

The minimization of the grand potential in Equation (4.13) yields the fluid density$\rho_f(r)$, which is then used to calculate the theoretical isotherm $N_{NLDFT}(P/P_0, D)$. Theoretical isotherms are calculated over a specified pore range, for a chosen temperature, pore geometry and adsorbate-adsorbent pair. These isotherms are packaged into kernels, which are then conveniently used to then calculate the statistical pore distribution of a real material by fitting them to the experimental data as shown in Equation (4.12) with least squares minimization. It should be noted further that the minimization of the canonical potential Ω can yield two minima, which represent the adsorption and desorption isotherms [94]. Thus, DFT can generally be applied to either adsorption or desorption branches. In materials that exhibit specific types of hysteresis, only the adsorption branch can be used due to limitations of the thermodynamic methods that do not capture complex desorption processes [95]. Specifically, the NLDFT kernel used for the work of this thesis was for slit-pore geometry with CO_2 adsorbent at 273K developed for carbon materials. The details can be found in Ref, [91] and the isotherms are shown in Figure 4.5.

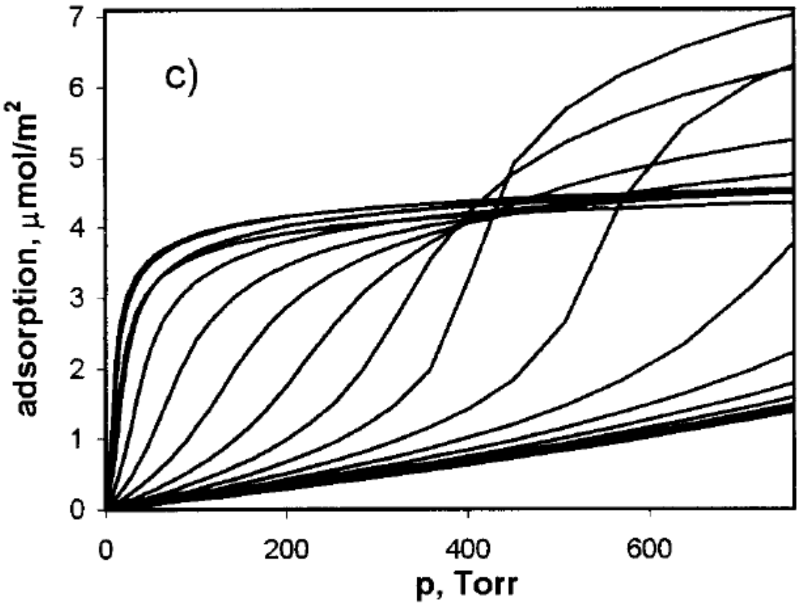

Figure 4.5: NLDFT kernel of CO_2 adsorption isotherms on carbon in slit pores at 273 K [91]

Quenched Solid Density Functional Theory (QSDFT)

Due to the treatment of the solid surface as a smooth plane, NLDFT isotherms exhibit jumps in the adsorption isotherm and consequently gaps in the calculated pore size distribution near the

1 nm range. In order to model these pore ranges more accurately, Quenched Solid Density Functional Theory (QSDFT) was developed [88]. This method accounts for the heterogeneity of the solid surface by modeling the solid as hard spheres interacting with the liquid. Thus, the solid density is included in the grand canonical potential [88]:

$$\begin{aligned}\Omega_{\mathrm{sf}}[\rho_{\mathrm{s}}(\mathrm{r}), \rho_{\mathrm{f}}(\mathrm{r})] \\ &= \mathrm{F}_{\mathrm{id}}[\rho_{\mathrm{f}}(\mathrm{r})] + \mathrm{F}_{\mathrm{id}}[\rho_{\mathrm{s}}(\mathrm{r})] + \mathrm{F}_{\mathrm{ex}}[\rho_{\mathrm{s}}(\mathrm{r}), \rho_{\mathrm{f}}(\mathrm{r})] \\ &+ \frac{1}{2}\iint \mathrm{drdr}'\rho_{\mathrm{f}}(\mathrm{r})\rho_{\mathrm{f}}(\mathrm{r}')\mathrm{u}_{\mathrm{ff}}(|\mathrm{r}-\mathrm{r}'|) \\ &+ \frac{1}{2}\iint \mathrm{drdr}'\rho_{\mathrm{s}}(\mathrm{r})\rho_{\mathrm{s}}(\mathrm{r}')\mathrm{u}_{\mathrm{ss}}(|\mathrm{r}-\mathrm{r}'|) \\ &+ \frac{1}{2}\iint \mathrm{drdr}'\rho_{\mathrm{f}}(\mathrm{r})\rho_{\mathrm{f}}(\mathrm{r}')\mathrm{u}_{\mathrm{sf}}(|\mathrm{r}-\mathrm{r}'|) - \mu_{\mathrm{f}}\int \mathrm{dr}\rho_{\mathrm{f}}(\mathrm{r}) \\ &- \mu_{\mathrm{s}}\int \mathrm{dr}\rho_{\mathrm{s}}(\mathrm{r})\end{aligned} \tag{4.19}$$

There two key differences between the NLDFT potential function in Equation (4.13) and the QSDFT potential function in Equation (4.19). Firstly, the excess hard sphere free energy $\mathrm{F}_{\mathrm{ex}}\,[\rho_{\mathrm{s}}(\mathrm{r}), \rho_{\mathrm{f}}(\mathrm{r})]$ now accounts for both solid and liquid density and is calculated by Rosenfeld's theory [96]. Secondly, the solid, modeled as a secondary component of hard spheres interacting with the liquid, requires additional terms to capture all pairwise attractive potentials. Similar to in NLDFT, the grand canonical potential is minimized with respect to the fluid. During this minimization, one important simplification made is that the solid density ρ_{s} is constant:

$$\frac{\delta\Omega_{\mathrm{sf}}}{\delta\rho_{\mathrm{f}}(\mathrm{r})} = 0 \tag{4.20}$$

Which yields the Euler-Lagrange formulation. The solid fluid interactions are modeled with the Lennard Jones WCA scheme:

$$\mathrm{u}_{\mathrm{ij}} = \begin{cases} -\epsilon_{\mathrm{ff}} & \mathrm{r} \leq 2^{\frac{1}{6}}\sigma_{\mathrm{ij}} \\ 4\epsilon_{\mathrm{ff}}[\left(\frac{\sigma_{\mathrm{ff}}}{\mathrm{r}}\right)^{12} - \left(\frac{\sigma_{\mathrm{ff}}}{\mathrm{r}}\right)^{6} & \mathrm{r} > 2^{\frac{1}{6}}\sigma_{\mathrm{ij}} \end{cases} \tag{4.21}$$

Where the i and j represent the fluid-fluid and fluid-solid interactions. The density of the solid can be modeled with a 1D density profile of carbon atoms using a linear ramp towards the solid-fluid interface. The shape of the pores is an important consideration and is dependent on the known properties of the material of interest and the fitting errors of the applied model. The most typical shapes for carbon material are slit-shaped in the nanopores < 2nm and cylindrical in pores > 2 nm, which were used in this thesis. The kernels for these models have been calculated by Neimark et al, [88][87], and are shown in Figure 4.6 and Figure 4.7.

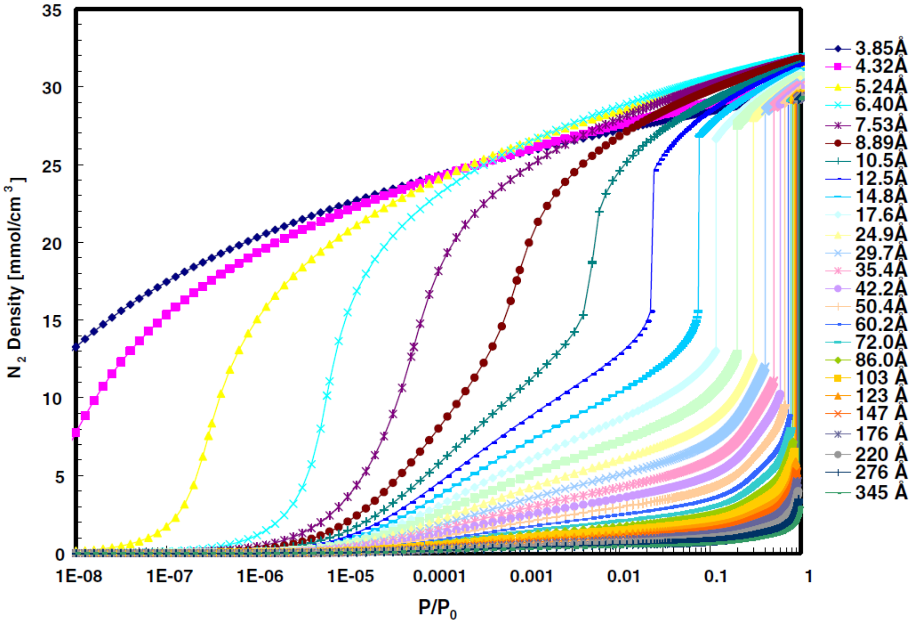

Figure 4.6: QSDFT kernel of N_2 adsorption isotherms on carbon at 77.4 K in slit pores [88]

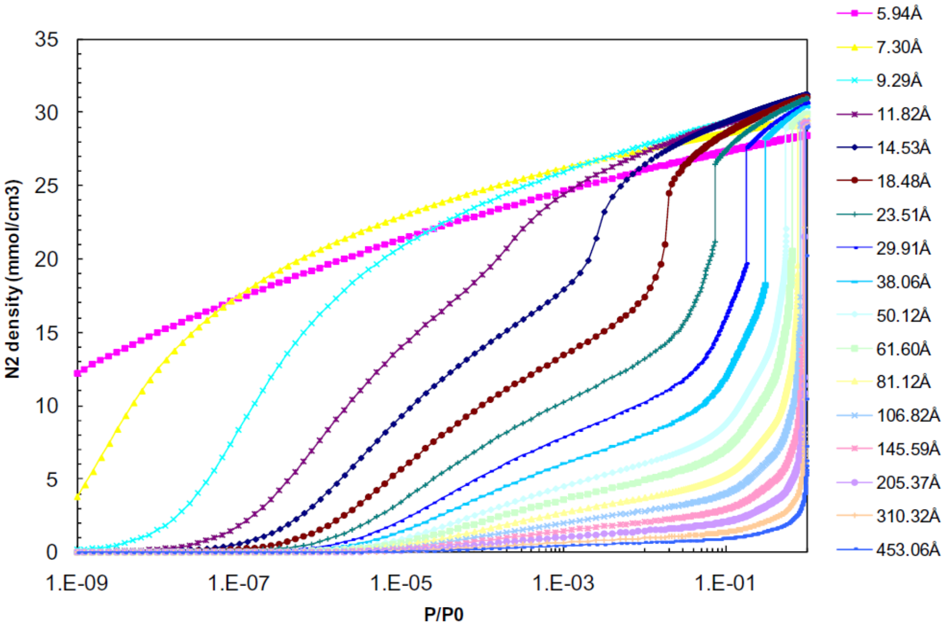

Figure 4.7: QSDFT kernel of N_2 adsorption on carbon at 77.4 K in cylindrical pores [87]

4.3.3. BET Surface Area Measurement

BET theory [97] allows for an approximation of the surface area by applying thermodynamic equilibrium between the adsorbed layer of molecules and the molecules of adsorbate in the gas phase. For the first layer, the equilibrium is defined:

$$N_m \theta_1 v e^{-\frac{E_1}{RT}} = kP\theta_0 A_1 \qquad (4.22)$$

Where the left side of the equation above represents the rate of desorption from the surface defined by the number of molecules that cover one monolayer on the surface N_m, the fraction of surface that is occupied by a single layer of adsorbate θ_1, the vibrational frequency v, the energy of adsorption E_1 and the temperature T. This desorption rate is set equal to the adsorption onto the surface which is defined by a collision constant k, pressure P, uncovered surface fraction θ_0 and the condensation coefficient A_1, which represents the probability that a molecule striking the surface will become adsorbed. The thermodynamic equilibrium of the first layer can be extended to multi-layers by applying the generalized form of the same equation:

$$N_m \theta_i v e^{-\frac{E_m}{RT}} = kP\theta_{i-1} A_m \qquad (4.23)$$

In the Equation (4.23), E_m is now the adsorption energy of an adsorbate molecule on an underlying layer of adsorbate, A_m is the adsorption probability coefficient of the new layer. The total number of adsorbate molecules is given by the sum of all layers:

$$N = N_m \sum_{n=1}^{\infty} i\theta_i \qquad (4.24)$$

Since $V/V_m = N/N_m$, the total adsorbed amount can be expressed as a function of the pressure and the volume of the adsorbed monolayer in the BET equation:

$$\frac{1}{V\left[\frac{P}{P_0} - 1\right]} = \frac{1}{V_m C} + \frac{C-1}{V_m C}\left(\frac{P}{P_0}\right) \qquad (4.25)$$

Where V is the adsorption volume, V_m the monolayer adsorption volume, and C is a constant term. By applying linear regression of the BET equation taking $\frac{1}{V\left[\frac{P}{P_0}-1\right]}$ versus $\left(\frac{P}{P_0}\right)$, the constants $\frac{1}{V_m C}$ and

$\frac{C-1}{V_m C}$ can be determined, which can be solved simultaneously, to give the monolayer volume V_m. With the monolayer volume, the surface area can then be calculated:

$$S_{BET} = \frac{V_m N s}{v_{gas}} \tag{4.26}$$

Where, N is Avagadro's number, s is the cross-sectional surface area covered by a single molecule and v_{gas} is the specific molar volume of the gas in the adsorbed state. For N_2 used in our experiments, the surface area of 16.2 $Å^2$ was used.

A fundamental assumption and known criticism of BET theory is that adsorption of layers above the first are kinetically similar and that the adsorption energies E_m of a molecule adsorbing on an existing adsorbate layer is constant. This has resulted in the finding that the equation agrees best within a relatively narrow range of relative pressures where the experimental isotherms can be fit to the linearized BET equation. This pressure range typically occurs between ($0.05 < P/P_0 < 0.3$). For each experiment where the BET surface area is determined, only the linear portion of the isotherm was used for regression. Another important note to make is that BET theory does not explicitly treat micropores. The kinetic equations used to derive the BET equation simply treats an isolated surface in thermodynamic equilibrium with the gas, does not account for the multi-wall effects on adsorbate molecules and thus is strictly-speaking, only applicable to non-porous or mesoporous materials. Further, it is found that for microporous materials, pores begin filling at low partial pressures typically below relative pressures of 0.1, before monolayer coverage occurs due to the strong potential well inside the micropores [77]. In the case of narrow micropores, using the BET equation substantially underestimates the geometric surface due to the size of the channels being relatively small in comparison to the diameter of the probe molecule. Therefore, the surface cannot be accurately probed and the area calculated from BET on microporous materials should only be taken as a relative measurement. On the other hand, in mesopores around 4 nm, it was found that pore condensation occurs in the same range as the mono-multilayer transition regime, causing a significant overestimation [77].

In order to standardize the process of calculating the BET linear applicability range, Rouquerel et. Al. [98] proposed a procedure based on 2 criteria:

1) The value of C in the BET equation must be positive in order to be within the applicability range of the derived BET equation

2) The application of the equation must be limited to the range where the $\ln(P_o - P)$ increases continuously with relative pressure P/P_o, which has been suggested by ISO standard 9277:2010.

The two criteria are widely used in BET surface area determination and thus was used for each measurement of the BET surface area in this thesis.

4.3.4. Total Pore Volume and Average Radius

The pore size distribution and volume was calculated using DFT based methods in the earlier sections discussed, which are applicable up to a pore size of up to 40 nm. To measure total overall pore volume, the saturation point of the isotherm was used. For N_2 at 77K, the relative pressure was taken near 0.95, and the adsorbed liquid volume V_{liq} was calculated with (4.27):

$$V_{liq} = \frac{PV_{ads}v_m}{RT} \tag{4.27}$$

Where V_{ads} is the adsorbed volume of gas determined experimentally and v_m is the molar volume of N_2 in the liquid state (34.7cm^3/mol). Various studies have shown that near the saturation point, the density (and thus molar volume) of the liquid almost constant and approximately the bulk density of liquid nitrogen [99]. The application of constant density is known as the Gurvich rule [100]. The pore radius was calculated assuming cylindrical pores with Equation (4.28):

$$r_p = \frac{2V_{liq}}{S} \tag{4.28}$$

Where S is the surface area which can be determined by the BET equation. It should be noted that the assumption was made that the surface area of the material external to the pore is negligible compared to the pore surface area, since the surface area is completely allocated to the pores in this calculation. Secondly, it must be noted that the method is only applicable in isotherms where a plateau is observed after the condensation point, since a saturation point must be assigned in the analysis. Using the Kelvin equation [77], it was shown that the largest meaningful pore radius evaluated with this method using N_2 at 77K is 95 nm.

4.4. Chemisorption Analysis

While low concentrations of tritium relevant to FHR operating conditions can be measured with various radiographic techniques [22], the handling of tritium requires complex facilities and procedures, which limits the flexibility of data that can be collected. For ease of experimentation, a hydrogen surrogate was used.

Two techniques are available for this analysis: 1) vacuum volumetric manometry and 2) dynamic flow adsorption with thermal desorption spectroscopy. Static volumetric chemisorption was described in 4.2. The dynamic flow method involves injections of small volumes of reactant gas into the inlet stream until saturation is reached. Injections are staged sequentially and the outlet stream is coupled to a thermal conductivity detector that measures the outlet concentration. While the dynamic method can be faster and is commonly used in industry, it does not afford the same accuracy, resolution and information as the static method that has been described. The use of static adsorption allows the strong and weak interactions of the reactant gas on the adsorbate to be decoupled as discussed in the next section. Thus, for the studies presented in this thesis, the isotherms were all determined using static volumetric adsorption.

4.4.1. Strong versus Weak Chemical Bonding

The first isotherm measured by methods described in Chapter (4.2) is known as the combined isotherm, which is the total adsorption isotherm. Using static chemisorption, two broad categories of adsorption can be identified, namely as the ‘strong’ and the ‘weak’ adsorption, which represent strength of the bond between the H atom and the solid atom on the material surface. These interactions were decoupled after completing the combined adsorption isotherm by applying a 10^{-8} Pa vacuum using a turbo-molecular and diaphragm pump until equilibrium in the sample cell was reached at the analysis temperature. Adsorbed hydrogen atoms which had a significant activation barrier to release remained on the material surface during this step. After vacuuming, hydrogen was re-introduced to the system and the chemisorption analysis was repeated, which gave the weak adsorption isotherm. Taking the difference between the combined and the weak therefore yields the strong isotherm. For example, these three isotherms were calculated for an activated carbon used in these experiments is shown Figure 4.8:

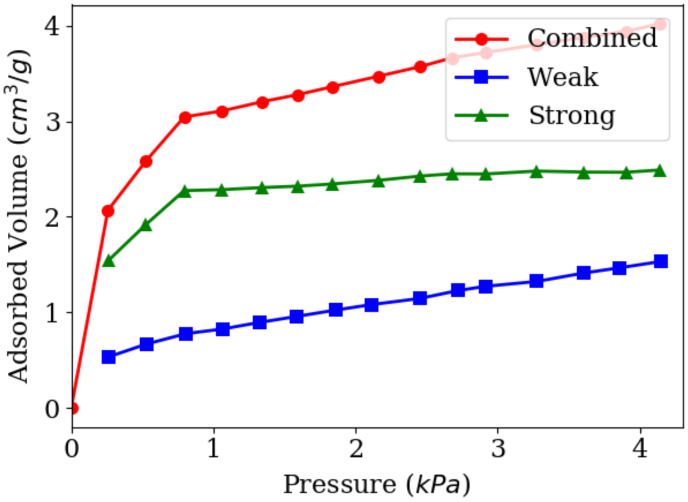

Figure 4.8: Chemisorption isotherms a) combined isotherm b) weak isotherm c) strong isotherm collected for CalgonCarbon OLC 12x40 granular activated carbon at 700°C

The strong and weak isotherms represent a difference in reaction energy and adsorbate stability. By extracting separate isotherms, insights to the nature of these interactions were gained. Thermodynamic models, which is discussed in Chapter 6 were applied to determine for example, whether the hydrogen atoms were bonding atomically or in the molecular form to carbon.

4.5. Scanning Electron Microscopy

Images were obtained on a JEOL 5910 General Purpose Scanning Electron Microscope.

4.6. Experimental Uncertainty and Error

Random error in the in the volumetric experiments conducted was primarily the result of the measurement error of the instruments used. In the calculation of the adsorbed volume at each step in Equations (4.3) and (4.4), cumulative errors propagate through staged equilibrations. The main experimental measurement was the pressure of the manifold and sample cell system with the 0.1 torr, 10 torr and 1000 torr transducers. The error provided by QuantaChrome for these transducers is shown in Table 4.1.

Table 4.1: Errors of pressure transducers used in adsorption experiments

Absolute Error (torr)	**Pressure Range (torr)**
0.0015*MV[a]	$P < 0.1$
0.0015*MV[a]	$1 < P < 10$
1	$P > 10$

[a]MV is the measured value of pressure in the range

The determination of void volume can be a significant source of error since it must be estimated indirectly using Helium. The assumptions made in the void determination using helium was that 1) the helium was non-adsorbing on the solid surface and 2) helium did not penetrate into locations in the solid, which would be inaccessible to the bulk gas. These requirements however, are not always met, and particularly, it has been found that certain microporous materials absorb amounts of He that are not be absorbed by N_2. One technique that has been developed is called NOVA, which measures the void space outside the adsorption setup without gas adsorption [101]. In order to limit the random error in the experiments, the setup was calibrated against known samples with standardized procedures. For chemisorption, a platinum catalyst standard was used with method in accordance to ASTM D3908-03(2015). For physisorption experiments, the BET surface area was measured with 5 Å molecular sieves with methods in accordance with ASTM D3663-03(2015) and ISO 18852:2015.

Another contribution to random error came from sampling. Depending on the homogeneity of the material, significant misrepresentation can occur from improper sampling. Given the wide range conditions and processes under which carbon materials such as graphite are produced and manufactured [32], structural and chemical homogeneity is hardly guaranteed even within the same batch, let alone across different lots of the same material. Thus, an extensive sampling study should be conducted to accurately predict performance in FHRs and is not the focus of this work. Rather, the systematic errors are discussed in detail for each analysis type and calculation. These systematic errors arose from the application of certain models and calculations, which led to biases that were quantified by the residuals between the applied models and the experimental data. This is discussed with the results in Chapter 6 and helped motivate the choice of model recommended.

Chapter 5.

Experimental Results

This section outlines the results of experimental work, which can be divided into two parts: 1) material characterization including the assessment of BET surface area, pore size distribution, average pore size and average pore volume, and 2) the measurement of hydrogen chemisorption on material surfaces including the strong, weak and combined interaction.

5.1. Carbon Characterization

The materials considered in thesis are grouped into three categories: 1) graphitic carbon, 2) activated Carbon (AC) and 3) Graphene nanoplatelets (GNP). The known properties of these materials as well as new data collected from characterization are discussed in this chapter.

Graphitic Carbon

The material tested in this category is IG-110U, which is an ultra-purified, fine-grained grade of graphite that has been tested and studied extensively for use in HTGRs [102] as a moderator, and in fusion applications as a low-atomic-number plasma-facing material [103]. The use of IG-110U is a desirable in the FHR because it has isotropic properties, which results in stability under irradiation, and a high strength, which allows increased loading, making it a good candidate for moderator, fuel and structural materials [62]. IG-110U has a bulk density of 1770 kg/m^3, flexural strength of 39 MPa and a compressive strength of 78 MPa (manufacturer specification). In comparison to other carbon materials, nuclear graphite is treated at a much higher temperature between 2500 - 3000°C under which crystallographic planes form, open pores are annealed and impurities are removed.

Activated Carbon (AC)

Materials with large surface areas and micropore volumes are expected to adsorb more tritium even at high temperatures. This drove the motivation for testing activated carbons, which make up the bulk of the experiments conducted in this thesis. Activated carbons are amorphous materials, which come in many forms with highly developed porous networks, high surface area reactivity and therefore serve as highly effective adsorbent materials in many other industries. They are derived from industrial or agricultural waste materials, which are ground into smaller particles. It is generally found that smaller particles produced larger measurable surface area and to a lesser extent a greater fraction of microporosity.

The particles are then activated in one of two processes: 1) chemical activation with mineral salt or 2) physical activation with oxidizing agent and high temperatures [104]. In chemical activation, the carbon is impregnated with an activating agent (i.e. KOH, NaOH, etc.), then heated in an inert atmosphere to temperatures between 400 and 800°C. After this, the activated product is washed, filtered and dried. Physical activation on the other hand involves pyrolysis of the raw material (< 700°C) followed by a high temperature (600 -1200°C) oxidation with steam, CO_2 or an air mixture. ACs typically contain roughly 90% elemental carbon with the balance made up by oxygen, nitrogen and hydrogen atoms, which form a variety of acidic surface functional groups, such as carboxyls, hydroxyls or phenols that can, depending on the adsorbate, significantly impact adsorption behavior [105][106]. The properties of AC depend on many parameters including the raw material, pre-treatment (particle size), the activation method and agents, and the manufacturing conditions (time, temperature, heating methods). This results in a great diversity amongst ACs.

Three types of ACs were investigated in this thesis: 1) Granular activated carbon (GAC) 2) powdered activated carbon (PAC) and 3) extruded activated carbon (EAC). The published properties of the GACs used are shown in Table 5.1.

Table 5.1: Summary of granular activated carbon properties

Material	Bulk Density (g/mL)	Mesh Size	Iodine Number (mg/g)	Hardness
OVC 4x8	0.45	4x8	-	97
NV 612	0.51	6x12	920	90
CTR 12x40	0.54	12x40	1100	75
OLC 12x40	0.48	12x40	1050	95

Mesh size refers to the particle size range determined by sieve retention. The two numbers represent the passage and retention rate (typically 95 - 95% wt.) through sieves sized with ASTM E11-87 designation. For example, a mesh size of 4 refers to a sieve size of 4.75 mm, and 8 refers to a size of 2.36 mm, which means that for a 4x8 mesh material, 95% of the particles will be smaller than 4.75 mm (size 4), but larger than 2.36 mm (size 8). The iodine number is capacity to adsorb iodine, which is an indicator of surface area. The hardness is a qualitative measure of resistance to abrasion and is a desirable property, which can limit the amount of particulate dust in the system.

PACs have sizes less than 1 mm. Two of these were studied; Norit PAC 200, and MSC-30. While PACs can provide a high surface to volume ratio, they create a high pressure drop in the system and so are used primarily in batch processing. For Norit PAC 200, 96% of the particles are less than 150 μm, 88% are less than 75 μm and 50% are less than 45 μm in diameter. PAC 200 is derived from coal and has a published iodine number of 900 mg/g. MSC-30 (Maxsorb) is a KOH super-activated carbon of type 'AX-21', which is synthesized from petroleum coke, has a surface area > 3000 m^2/g and median D50 diameter of 6 - 50 μm.

The last type of activated carbon that was evaluated in this thesis is an EAC named Norit RB 40M. The extrusion process results in a high strength product, which has a low dust content and low pressure drop. The diameter of RB 40M pellets is 4 mm, the iodine number is 900 - 1000 mg/g and the apparent density is 0.51 g/mL.

Graphene Nanoplatelets

The last group of materials tested was graphene nanopolatelets (GNP), namely Graphenit-OX. Dillon et. Al [2] first showed using temperature programmed desorption that graphene materials (single-walled carbon nanotubes) were capable of storing significant amounts of hydrogen; more than 5 wt. % at 40 kPa and 133K. Subsequently hydrogen dissociation on both the surface and edge sites of graphene materials was found to be possible in various studies [107][108][109] and the adsorption was further found to be reversible through temperature cycling with minor loss in capacity [110]. Graphenit-OX platelets have a lateral dimension of 2 -3 microns, are usually several graphene layers thick and have high chemical stability. These GNPs are slightly oxidized with a carbon content of 96.45 %, oxygen content of 2.28%, balanced by hydrogen, nitrogen and sulfur impurities. The bulk density is 0.21 g/mL and the surface area provided by the vendor is 110 m^2/g.

The material names and manufacturers of all materials used in this thesis are shown in Table 5.2 and further details can be found in published data sheets.

Table 5.2: Material name and manufacturer summary

	Material Name	**Manufacturer/Vendor**
Nuclear Graphite	IG-110U	Toyo Tanso Inc.

Granular AC	CAL TR 12x40 (CTR 12x40)	CalgonCarbon
GAC (continued)	OLC 12x40	CalgonCarbon
	OVC 4x8	
	Norit Vapur 612 (NV 612)	Cabot Corporation
Powdered AC	Norit PAC 200 (PAC 200)	Cabot Corporation
	MAXSORB (MSC-30)	Kansai Coke and Chemicals Co. Ltd.
Extruded AC	Norit RB 40M (NRB 40M)	Cabot Corporation
Graphene Oxide	Graphenit-OX	Nanoinnova Technologies SL

5.1.1. N_2 and CO_2 Physisorption Isotherms

This section shows the results of CO_2 and N_2 physisorption. The CO_2 adsorption was performed at 273K and was used to determine the pore size distribution of micropores in the range of 0.35 nm to 1.0 nm. The pressure range of analysis spanned from 0.1 kPa to atmospheric pressure. Since the saturation pressure of CO_2 at 273K is 3485.2 kPa, pore condensation did not occur under the analysis conditions and the desorption isotherms matched the adsorption isotherms. Since the errors from the experiment accumulate with the progression of the experiment, the adsorption isotherm is slightly more accurate and was used for pore size distribution (PSD) calculations. All of the CO_2 isotherms are shown in Figure 5.1.

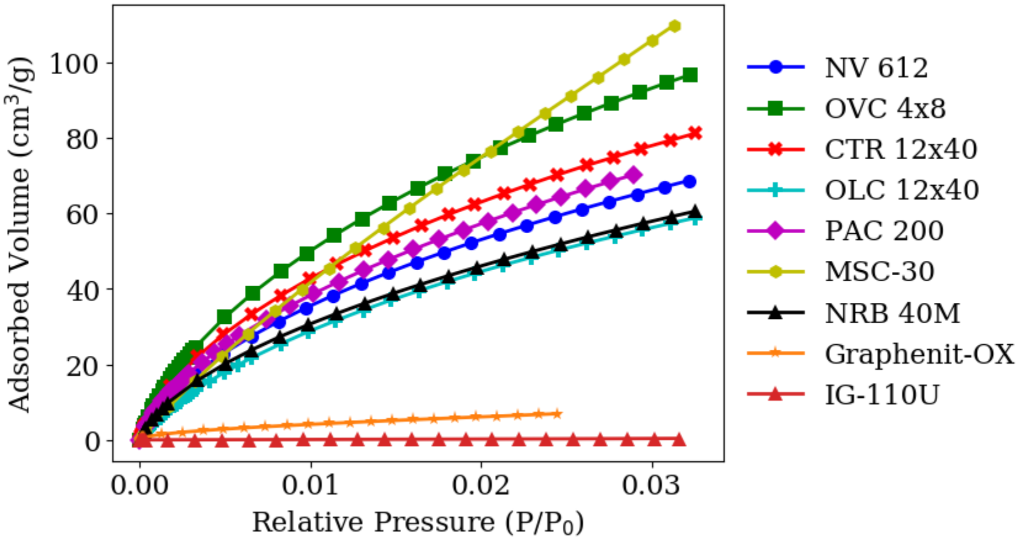

Figure 5.1: CO_2 adsorption isotherms at 273K for various activated carbons taken relative to the CO_2 saturation pressure P_o = 3485.2 kPa

In comparison to the N_2 adsorption, CO_2 isotherms were collected at higher temperatures, which resulted in short analysis durations. All the curves in Figure 5.1 show a type I or similar isotherm since CO_2 is far from saturation and adsorbs onto the surface by monolayer coverage. Since CO_2 was only used for the pore regime of < 1 nm, the N_2 isotherms were also measured for analysis of pores > 1 nm and < 40 nm shown in Figure 5.2 to Figure 5.5.

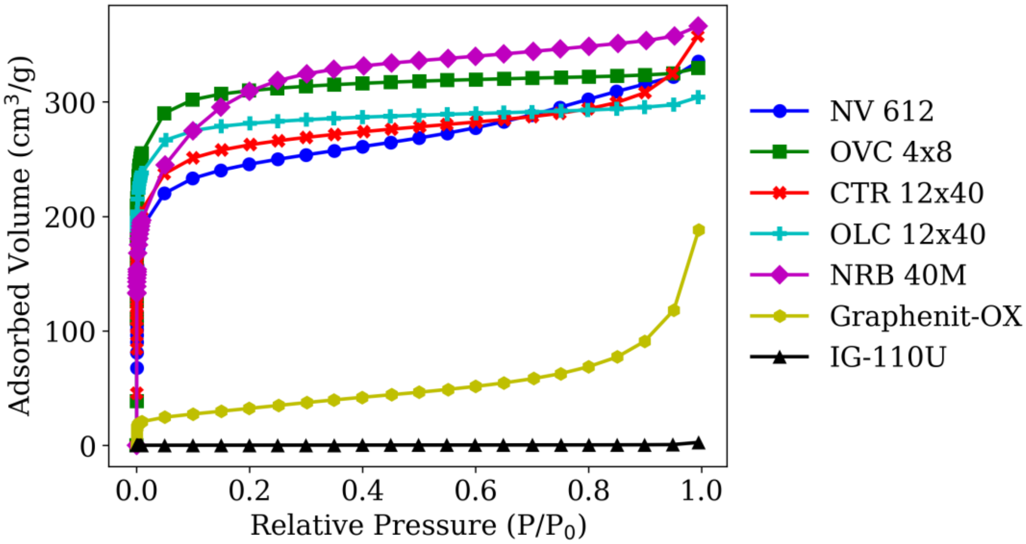

Figure 5.2: N_2 Adsorption isotherms taken at 77K of GAC, EACs, graphite, and graphene nanoplatelet materials relative to the N_2 saturation pressure P_0 = 97.07 kPa

Figure 5.2 shows the adsorption isotherms and Figure 5.3 shows both adsorption and desorption isotherms for GACs, EAC, GNP and the nuclear graphite. Figure 5.4 and Figure 5.5 show both the adsorption and desorption curves for the graphite and PACs, which are separated from the other isotherms for clarity. Most of the granular and activated carbons showed a type 1 isotherm, which is indicative of high uptake in the micropores at the lower pressures. Two of these, namely NV 612 and CTR 12x40 showed a gradual increase after the knee, which indicates the presence of mesoporosity. This was also true but to a lesser extent for the EAC NRB 40M. In contrast, the GNPs Graphenit-OX adsorbs much less nitrogen than ACs. Graphenit-OX showed a type II isotherm, which is common in non-porous or macroporous materials. The perceived 'macropores' were likely due to the inter-particle spacing of the nano material. The IG-110U adsorption is shown by itself in Figure 5.4. Here the knee occurred very early at a relative pressure of approximately 0.001 P/P_0 indicating a very low capacity for the monolayer, which would imply a low surface area. The large increase in adsorbed volume was a product of rapid condensation near saturation point, which occurs on non- or macro-porous materials since there is no pore filling.

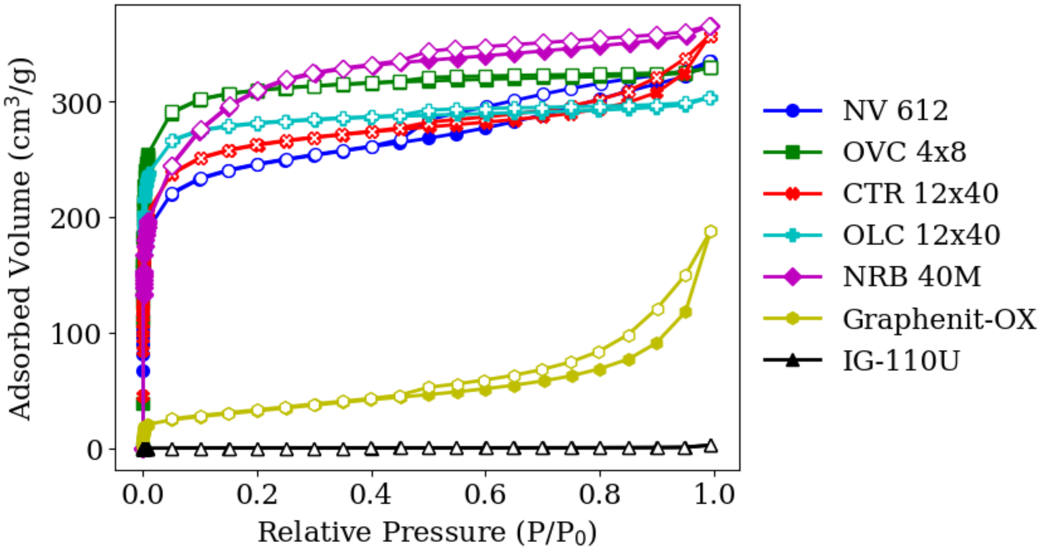

Figure 5.3: N_2 Adsorption and desorption isotherms taken at 77K of various graphite, activated carbon and graphene materials. Adsorption isotherms shown with filled symbols, and desorption curves shown with open symbols

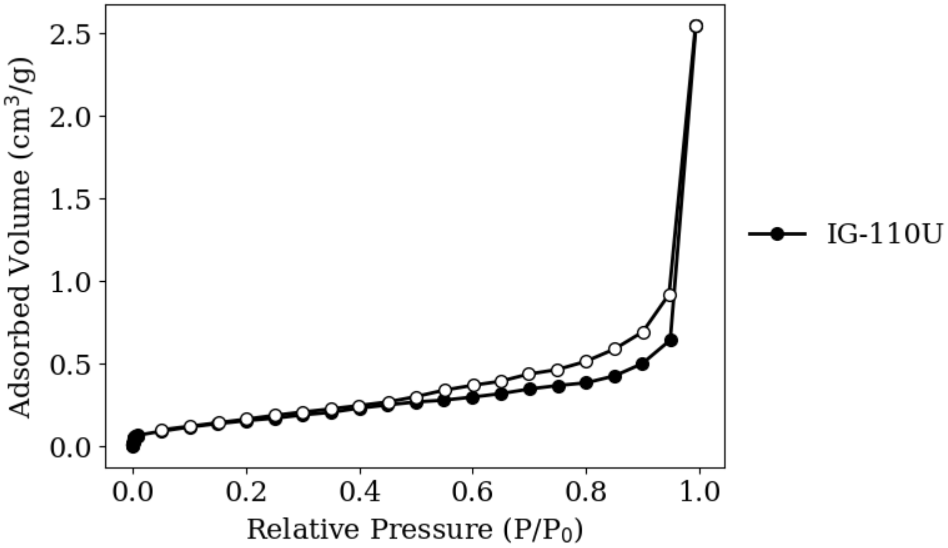

Figure 5.4: Expanded N_2 adsorption and desorption isotherms taken at 77K of graphite IG-110U. Adsorption shown with filled symbols and desorption shown with open symbols

The PAC adsorption curves in Figure 5.5 were both similar to type I isotherms. The MSC-30 material showed a much higher adsorption capacity for N_2 in comparison to PAC 200 (1100 cm^3/g versus 300 cm^3/g), and in comparison to all other materials, which indicates a higher surface area.

In examining the desorption curves of each material, most followed their corresponding adsorption curves with IG-110U, Graphenit-OX, NRB 40M and CTR 12x40 showing a slight hysteresis. The hysteresis was most pronounced in NV 612. This hysteresis was similar to the H4 type described by IUPAC [76], which is indicative of capillary condensation in mesopores. This hysteresis is typically caused by meta-stable film formation during adsorption causing a delay in the adsorption curve. At low pressures near 0.4 – 0.5 P/P_0, cavitation induced evaporation can occur at the pore, and the hysteresis loop can quickly collapse as shown in NV 612 [111]. If the effect is pronounced, the desorption curve cannot be used to calculate the pore size distribution due to limitations of the thermodynamic models. However, current Quenched Solid DFT (QSDFT) methods can accurately account for delay in the adsorption isotherm [101].

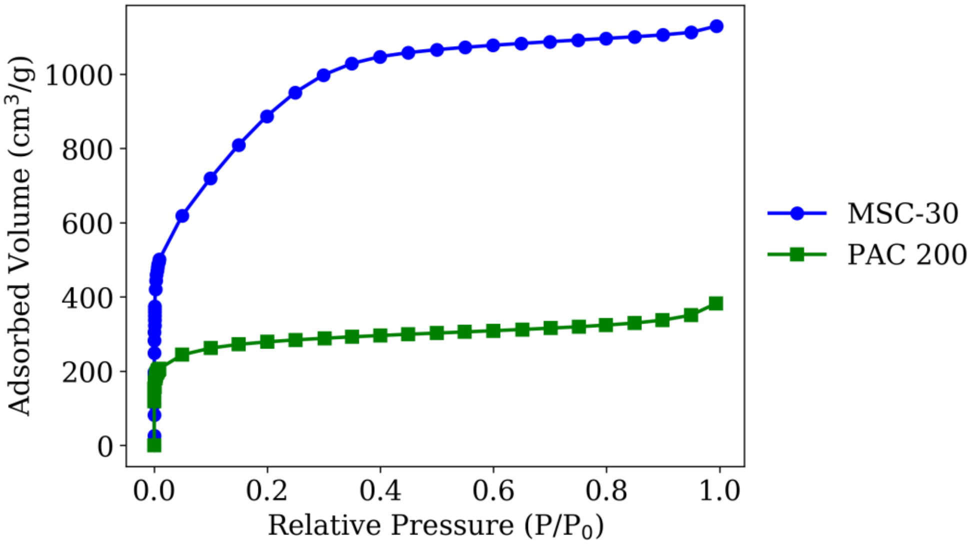

Figure 5.5: Powdered activated carbon adsorption and desorption curves

5.1.2. BET Surface Area

The BET surface area was calculated with the methods described in Chapter 4.3.3. Although the equation was not strictly developed for microporous material, the suggested criterion in ISO 9277 was used where the BET points are taken for the region in which the plot of $\ln(P_0 - P)$ vs. P/P_0 is continuously increasing and the regression parameter C is positive. The results of the BET calculations can thus provide a general idea of the total available surface area of each material shown in Table 5.3.

Table 5.3: BET surface areas of tested materials

Material	BET Surface Area	C-Value in Eqn. (4.25)
IG-110U	0.588	38.865
OVC 4x8	1153.531	2201.599
NV 612	923.641	983.921
CAL TR 12x40	993.224	1026.43
OLC 12x40	1113.998	1449.539
PAC 200	1033.576	783.873
MSC-30	3125.557	145.390
RB-40M	1094.006	386.397
Graphenit OX	113.041	263.315

As expected from the N_2 adsorption isotherms, the superactivated carbon MSC-30 exhibited the highest surface area at 3126 m^2/g while the nuclear graphite IG-110U showed the lowest surface area at 0.588 m^2/g. Nearly all other types of activated carbons showed similar surface areas between 900 – 1200 m^2/g independent of type (granular, powder or extruded), form or particle size, which suggests that the contribution to surface area lies largely in the accessible microporosity and not in the apparent bulk area of the particle. The GNP showed a higher surface area than the IG-110U at 113 m^2/g, but significantly lower surface area than the AC materials.

5.1.3. Total Volume and Average Pore Size

Using the total adsorbed N_2, the average pore size and the total pore volume were simply calculated from the methods presented in 4.3.4. The data is shown in Table 5.4. The observations for total pore volume were similar to that of BET surface area shown in the previous section. The MSC-30 material had the highest (by more than 3X) volume compared to all other materials at 1.7 cm^3/g in comparison to the ACs which had volumes close to 0.5 cm^3/g. The GNP had a pore volume of 0.1828 cm^3/g. The average pore size was also calculated. The calculation of the average pore size assumed a constant bulk density, which has been shown by theory and simulation to be a non-rigorous simplification. Further, the average pore size calculation used the BET surface area, which does not apply strictly apply to porous material.

Table 5.4: Average pore radius (Å) and pore volume for pores smaller than 200 Å, taken at a relative pressure of 0.95 P/P_o

Material	Average Pore Size (A)	Average Pore Volume (cm³/g)
IG-110U	33.7038	$0.9909*10^{-3}$
OVC 4x8	8.71103	0.5024
NV 612	10.9385	0.5052
CAL TR 12x40	10.1126	0.5022
OLC 12x40	8.25987	0.4601
PAC 200	10.7479	0.554
MSC-30	11.0156	1.721
RB-40M	10.1082	0.5529
Graphenit OX	32.0211	0.1828

The average pore sizes were largest for IG-110U and Graphenit-OX both at ~33 Å. This makes sense based on the adsorption isotherms of these materials that suggested significant meso and macroporosity. Most of the activated carbons had average pore sizes near 10 Å, while OLC 12x40 and OVC 4x8 had the lowest average pore sizes of 8.26 and 8.7 Å respectively. Pore size distribution and volumes were calculated using liquid density functional theory.

5.1.4. Pore Size, Surface Area, and Volume Distribution

The pore size distributions from the microporous to mesorporous regime are shown from Figure 5.6 to Figure 5.9 for all 9 materials that were tested. These plots show from the combined methods of NLDFT with CO_2 adsorption at 273K (for pore sizes 0.35 nm to 1.0 nm), and QSDFT with N_2 adsorption at 77K (up to a pore size of 40 nm). The two methods were merged at a pore size of 1 nm to analyze the full range where the left shown in blue is the microporous content (<1 nm), and the red is the micro-meso porous content (1 nm to 40 nm). The graphite IG-110U showed almost no mesoporosity with a small fraction of microporosity. In contrast, the graphene showed approximately an order of magnitude larger volume in the microporous region than IG-110U in Figure 5.6 and also a higher mesoporosity in the size range between 5 – 40 nm. We believe that the mesoporosity observed in the graphene nanoplatelet is due to the space between nanoparticles, since the platelets can consist of just several stacks of graphene sheets, and are on the nanometer scale in thickness.

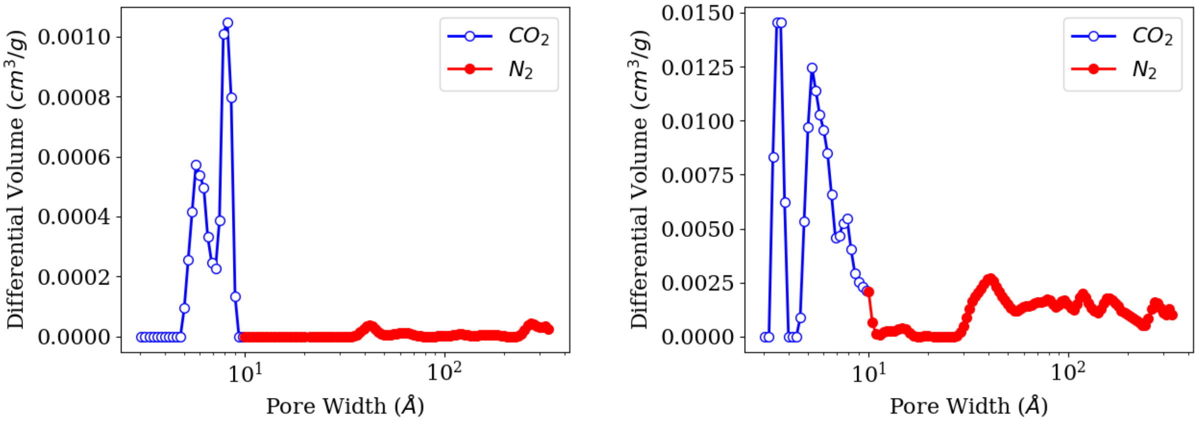

a) IG-110U **b) Graphenit-OX**

Figure 5.6: Pore size distribution determined by CO_2 adsorption at 273K and N_2 adsorption at 77K for graphite and graphene oxide nanoplatelets: a) IG-110U, b) Graphenit-OX

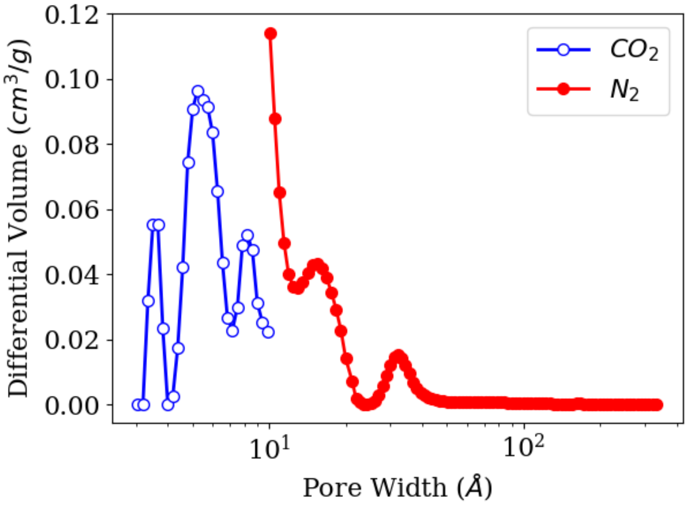

Figure 5.7: Extruded activated carbon NRB 40M pore size distribution determined by CO_2 adsorption at 273K and N_2 adsorption at 77K

The EAC in Figure 5.7 showed a larger adsorption in both micro and mesoporous regions compared to the graphite and GNP and showed comparable volumes to the GACs in Figure 5.8. The discontinuity between the fits in N_2 and CO_2 comes from the application of different models, which were based on different assumptions. Overall, the peak of the N_2 at 1 nm contributes only a small amount to the total pore volume.

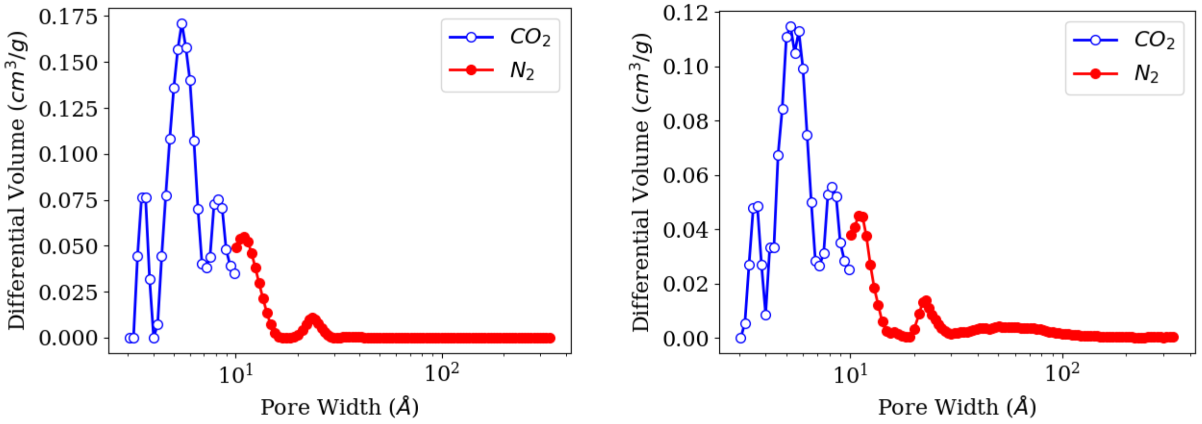

a) OVC 4x8 **b) NV612**

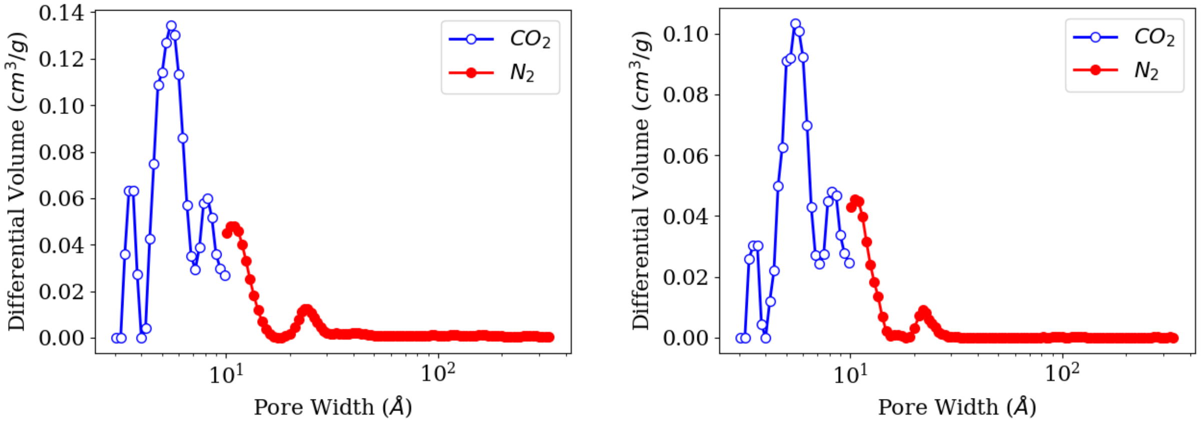

c) CTR 12x40 **d) OLC 12x40**

Figure 5.8: Pore size distribution determined by CO_2 adsorption at 273K and N_2 adsorption at 77K for granular activated carbons: a) OVC 4x8, b) NV 612, c) CTR 12x40 and d) OLC 12x40.

Most of the activated carbons showed similar profiles with a large portion of microporosity followed by mesoporosity. These curves show three peaks in the narrow micropores, which are believed simply to be an artifact of the mathematical fit since real materials generally show a more gradual distribution unless porosity is specifically tuned by design. These all showed roughly the same order of magnitude of absorption with the CO_2 peak being highest for OVC 4x8 and lowest for NV 612 shown in Figure 5.8.

The PAC isotherms are shown in Figure 5.9. The superactivated MSC-30 showed significantly more mesoporosity than the other activated carbons. Meanwhile, the other powdered carbon PAC 200 was similar to all other forms of ACs. These pore size distribution is quantitatively described and grouped into narrow micropores (< 0.7 nm), micropores (< 2 nm) and mesopores (> 2 nm) in Table 5.5 and Table 5.6.

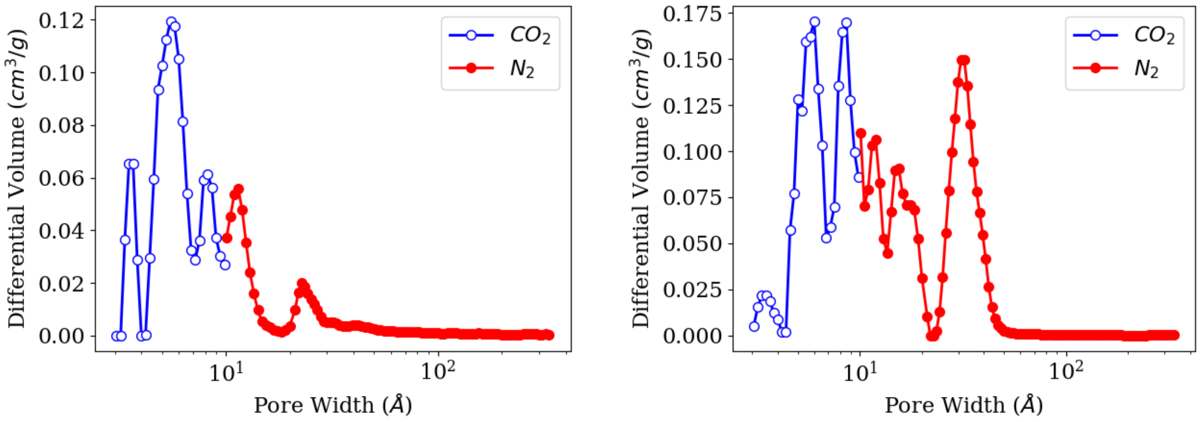

a) PAC 200 **b) MSC-30**

Figure 5.9: Pore size distribution determined by CO_2 adsorption at 273K and N_2 adsorption at 77K for powdered activated carbons a) PAC 200 and b) MSC-30

The measured surface area in narrow micropore region ranged from 1.34 m^2/g for IG-110U to 642.89 m^2/g for the GAC OVC 4x8. Graphenit-OX had a relatively low surface area of 54.84 m^2/g while most of the ACs showed high narrow micropore surface areas between 400 – 600 m^2/g. MSC-30 has the highest surface area overall. In the micropore region, the surface areas ranged from 2.88 again for IG-110U to 1462.99 m^2 /g for MSC-30. More variation was observed in the micropores compared to the narrow micropores in the other activated carbons ranging from 602.35 m^2/g for OLC 12x40 to 965.91 m^2/g for OVC 4x8. Graphenit-OX had a relatively low microporous area again at 68.60 m^2/g. The variation was again larger when comparing different materials' mesopore distributions. IG-110U also had the lowest mesopore surface area at 0.51 m^2/g while MSC-30 had the highest surface area again at 1021.10 m^2/g. Graphenit-OX had more mesoporosity at 71.29 m^2/g than some other activated carbons such as OLC 12x40 and OVC 4x8, which had areas of 38.9 and 45.10 m^2/g respectively. The other activated carbons had surface areas between 100 to 200 m^2/g.

The volumetric pore size distributions were similar to the surface area distributions. In the micropore region, IG-110U had the lowest at 0.0004 cm^3/g followed by Graphenit-OX at 0.0136 m^3/g. The ACs had about an order of magnitude more narrow micropore volume between 0.1 to 0.167 cm^3/g. For micropores under 2 nm, the IG-110U had the lowest volume again at 0.001 cm^3/g followed by graphene at 0.0196 cm^3/g, while the MSC-30 had the largest at 0.6834 cm^3/g. The mesopore volumes ranged from 0.0021 cm^3/g for IG-110U to 0.864 m^3/g for MSC-30.

Table 5.5: Surface area (m^2/g) contribution of narrow micropores (<0.7 nm), micropores (<2 nm) and mesopores (> 50 nm)

Material	Narrow Micropore (< 0.7 nm)	Micropore (<2 nm)	Mesopore (2 – 50 nm)
IG-110U	1.34	2.88	0.51
OVC 4x8	642.89	965.91	45.10
NV 612	479.76	717.18	139.95
CAL TR 12x40	540.90	807.39	104.51
OLC 12x40	381.53	602.35	38.90
PAC 200	490.25	770.08	170.37
MSC-30	571.65	1462.99	1021.10
RB-40M	397.11	801.84	102.30
Graphenit OX	54.84	68.60	71.29

Table 5.6: Volume contribution (cm^3) of narrow micropores (<2 nm), mesopores (2 – 50 nm) and mesopores (> 50 nm)

Material	Narrow Micropore (< 0.7 nm)	Micropore (<2 nm)	Mesopore (2 – 50 nm)
IG-110U	0.0004	0.0010	0.0021
OVC 4x8	0.1676	0.3280	0.0332
NV 612	0.1239	0.2418	0.1812
CAL TR 12x40	0.1404	0.2743	0.1566
OLC 12x40	0.1014	0.2112	0.0340
PAC 200	0.1270	0.2689	0.2039
MSC-30	0.1579	0.6834	0.8640
RB-40M	0.1027	0.3504	0.1080
Graphenit OX	0.0136	0.0196	0.2030

In general, the graphite material IG-110U had both the lowest surface area and volume in narrow micropores, micropores and mesopores. The superactivated carbon MSC-30 had the largest surface area and volume (2-3X) in the micropores and mesopores but not in the narrow micropore regime, where the granular activated carbon OVC 4x8 showed the highest surface area and volume. Aside from MSC-30, most activated carbons showed surface areas and volumes of similar magnitude in narrow micropore and micropores. A larger variation was observed for mesopores in ACs where OVC 4x8 and OLC 12x40 had almost an order of magnitude lower mesoporosity than other types of activated carbons.

5.1.5. Systematic Modeling Errors of Density Functional Theory

The modeling errors addressed in this thesis are primarily systematic. With respect to DFT calculations, these come from the choice of model used. Firstly, as discussed in Chapter 4.3.2, either NLDFT or QSDFT can be used for pore size calculation. NLDFT approximates the adsorbent surface as a smooth plane, while QSDFT accounts for surface chemical and geometrical heterogeneity, making it more suitable and theoretically accurate than NLDFT for the disordered carbon materials that have been tested in this thesis. Currently, only the NLDFT method is available in ASIQ V4.0 for CO_2 adsorption, which was used to probe the micropore regime < 1 nm. For N_2, both NLDFT and QSDFT methods have been developed.

Secondly, a choice must be made for the pore geometry that is modeled. Possible geometry methods include slit pores, which were developed first, followed by cylindrical and spherical pores for carbon materials. In literature, the pore morphology of carbon materials has been studied extensively by combination of experimental probe and molecular simulation [112]. Generally, micropores in carbons ($<$ 2nm pores) are considered to be slit-shaped, while the mesopores have been found to be predominately cylindrical [113][114][115]. In the absence of further experimental evidence such as an atomic probe data, the assumption of combined slit/cylindrical pore geometry where pores $<$ 2nm are considered slits, and pores greater than 2 nm are considered as cylinders is acceptable and consistent with most studies.

The third consideration is whether the DFT models should be applied to the adsorption or desorption branch of the experimental data. It was found in Chapter 5.1.1 that various isotherms exhibited Type H4 hysteresis indicating potential pore blocking or cavitation due to a restricted pore entrance during desorption. In this circumstance, it is only acceptable to use the adsorption branch, which corrects for the adsorption delay that results from meta-stable film formation. These models have been applied to each material and an example of the fit of experimental data is shown in Figure 5.10 a) and b), which show the CO_2 and N_2 adsorption modeling for NV612.

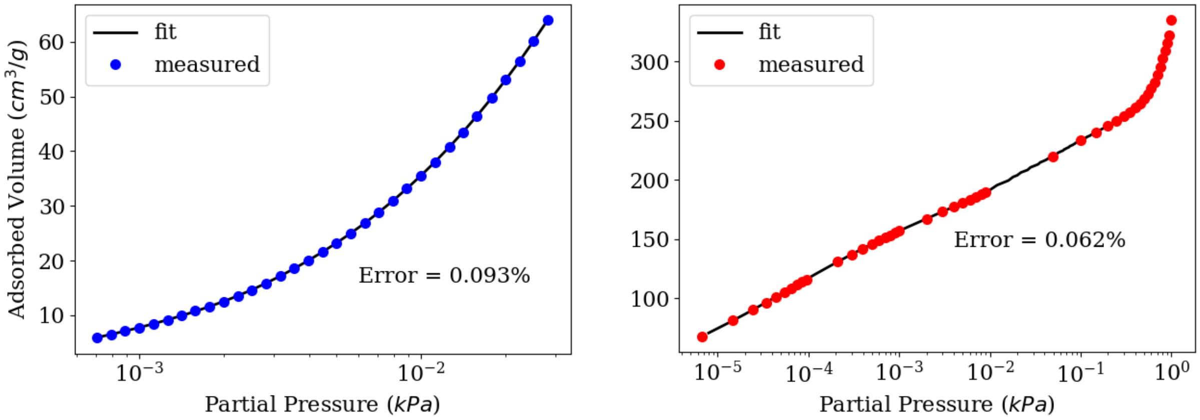

Figure 5.10: Fitting errors for: a) left - NLDFT slit pore with CO_2 at 273K and b) right - QSDFT slit/cylindrical pores with N_2 at 77K fitting errors for NV 612.

In addition to the theoretical basis for selection of DFT kernels, the total fitting error should be a secondary condition for model choice, which is shown in the Figure 5.10. While a better fit does not necessarily indicate a better physical model, large errors in the model should be noted as a failure of a model in representing the system. For practically all carbon materials, the slit NLDFT CO_2 adsorption model combined with the slit/cylindrical QSDFT N_2 model had the lowest fitting error. For these DFT calculations, the summary of errors is provided in Table 5.7.

Table 5.7: NLDFT and QSDFT fitting errors in percentages (%). NLDFT slit pore model for carbon for pores < 1 nm, and QSDFT slit/cylindrical pore model for pores > 1 nm.

Material	**CO_2 NLDFT (<1 nm)**	**N_2 QSDFT (>1 nm)**
IG-110U	0.2	2.431
OVC 4x8	0.117	0.323
NV 612	0.093	0.062
CAL TR 12x40	0.622	0.260
OLC 12x40	0.062	0.024
PAC 200	0.279	0.058
MSC-30	0.025	0.219
RB-40M	0.403	1.135
Graphenit-OX	6.219	0.339

The largest errors were found for Graphenit-OX for micropores < 1 nm with CO_2 adsorption and IG-110U N_2 QSDFT for pores > 1 nm. For Graphenit-OX, it is believed that the 6.2% error arises due to challenges in modeling the inter-particle porosity, which are perceived as pores since the diameter of the nanoparticles are only a few sheets of graphene thick. Thus, the pore shape does not adhere as well to the standard forms (cylindrical, slit, sphere). For IG-110U, the error of 2.4% is higher than most, likely due to the general absence of porosity in general. In all other carbons, the modeling errors are relatively low at 1% or less.

5.2. Hydrogen Chemisorption

In this section, chemisorption data that was collected at 700°C for each material is shown and related to the characterization data from Chapter 5.1. The experimental pressures ranged from 0 to 4 kPa. The total hydrogen solubility is presented as well as the contributions from strong and weak interactions described in Section 4.4.1

5.2.1. Combined Isotherms for Various Carbon Types

The total (i.e. combined) solubility of all the materials is shown in Figure 5.11. As expected, all of the isotherms were type I where the adsorbed volume rises fast initially and then begins to reach saturation as the active surface sites become occupied at higher pressures. The material with the lowest solubility was the nuclear graphite IG-110U, which can barely be seen in the figure. A closer examination of the IG-110U in Figure 5.12 shows that the measured value is actually negative. The negative measurement was found to be consistent and repeatable. As such, there are at least two possible reasons for this observation. The first possibility is that when the adsorbed volume was calculated with Equation (4.5), the effective void volume that corrects for convection effects was overestimated, resulting in apparent negative adsorption. The second possibility is that a reaction occurred between the graphite material and hydrogen, resulting in liberation of a gaseous product in the cell, which caused the pressure to increase and the calculated adsorption to be negative. For the first, an analysis can be run with a blank cell and non hydrogen-adsorbing material (such as quartz) in order to measure if a baseline bias exists and determine if this can be resolved by mathematical correction. To test the second hypothesis, the product stream can be fed into a TCD or MS to determine if a significant amounts of product material, such as methane CH_4, is released. The author is currently investigating these possibilities. Even if the negative signal were caused by a systematic error, it would still be a relatively insignificant contribution in isotherms determined for other materials. The amount of hydrogen that adsorbed was several orders of magnitude greater than the absolute value of that measured for IG-110U. Therefore, potential loss in accuracy in the adsorption range of IG-110U is not a generally significant concern.

With the exception of MSC-30, all the activated carbons exhibited a hydrogen solubility at 4 kPa and 700°C of between 2 – 4 cm³/g with the highest being GAC OVC 4x8 and lowest being CTR 12x40. Despite having the highest micropore and mesopore volumes and surface areas, MSC-30 was found to underperform compared to other carbons with a solubility of 1.2 cm³/g, which is almost 3x smaller than other ACs. Similarly, GNP, which had a relatively low microporous surface area and volume exhibited low hydrogen adsorption at close to 0.5 cm³/g. The adsorption isotherms of all of the materials tested appeared to show a fractional power dependence on pressure, which could suggest a contribution from hydrogen dissociation.

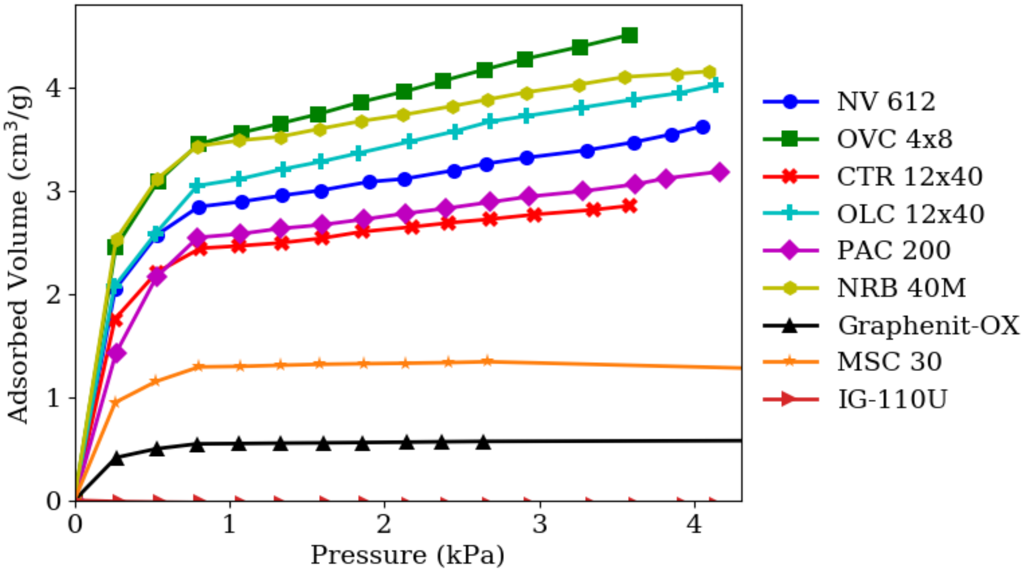

Figure 5.11: Combined 700°C isotherms for activated carbons and graphene nanoplatelets

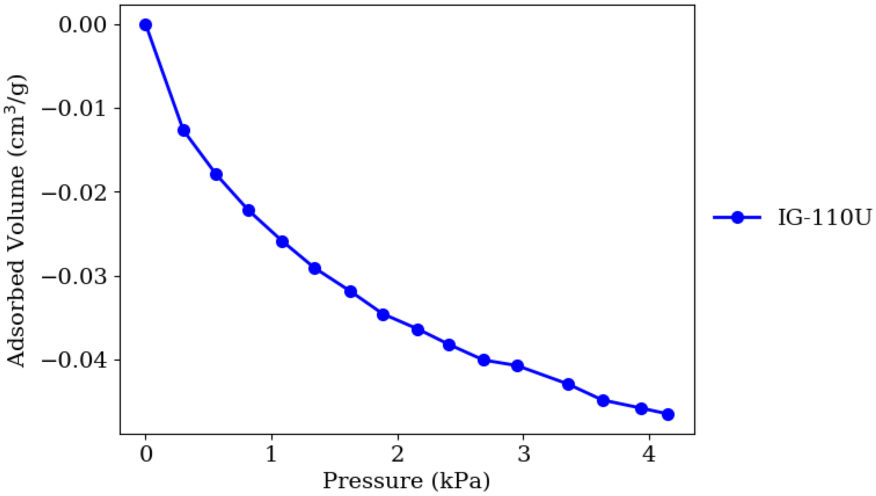

Figure 5.12: Combined 700°C isotherm for IG-110U

Additionally, the values of combined adsorption at 700°C for all the materials tested are also provided in Table 5.8 for pressures from 0.25 to 1.0 kPa (low pressures that are relevant to FHR conditions [116]). In this table, the materials are grouped into their respective types. At these low pressures, it is clear that the ACs, and specifically the GACs and EACs have a much higher hydrogen solubility than graphene and graphite.

Table 5.8: Combined chemisorption isotherm at 700°C for activated carbons, graphene and graphite materials from 0.25 to 1.0 kPa

	Adsorbed Volume (cm^3/g)[a]			
Pressure (kPa)	0.25	0.5	0.75	1.0
GAC				
OVC 4x8	2.298	2.996	3.38	3.529
NV 612	1.939	2.504	2.79	2.878
CAL TR 12x40	1.676	2.155	2.388	2.458
OLC 12x40	2.004	2.536	2.97	3.095
PAC				
PAC 200	1.328	2.078	2.478	2.571
MSC-30	0.899	1.13	1.264	1.296
EAC				
NRB-40M	2.35	3.036	3.378	3.472
Graphene				
Graphenit-OX	0.384	0.49	0.539	0.549
Graphite				
IG-110U	-0.011	-0.017	-0.021	-0.025

[a]The adsorbed volume is measured close to the target pressures listed but not exactly at these pressures. Values shown here are linearly interpolated from the measured values

5.2.2. Effect of Surface Area and Pore Volume, Pore Size Distribution on Total Hydrogen Adsorption

While some reports have suggested a correlation between BET surface area and the hydrogen adsorption at low temperatures, this did not apply at high temperatures of 700°C as shown in Figure 5.13a). Similarly, there appeared to be no correlation between the total hydrogen capacity and pore volume shown in Figure 5.13b). A clear outlier is MSC-30, which had both the highest surface area and volume but had approximately 1/3 the adsorption of some other ACs such as NRB 40M or OVC 4x8. While low temperature adsorption is driven by Van der Waals interactions between the adsorbent and adsorbate, high temperature interactions must account for other effects including impingement of hydrogen molecules, and chemical reaction of the molecule with the carbon surface. Thus, the following section discusses the effect of pore size, volume, surface area and PSD on the combined adsorption of H_2 on carbon materials.

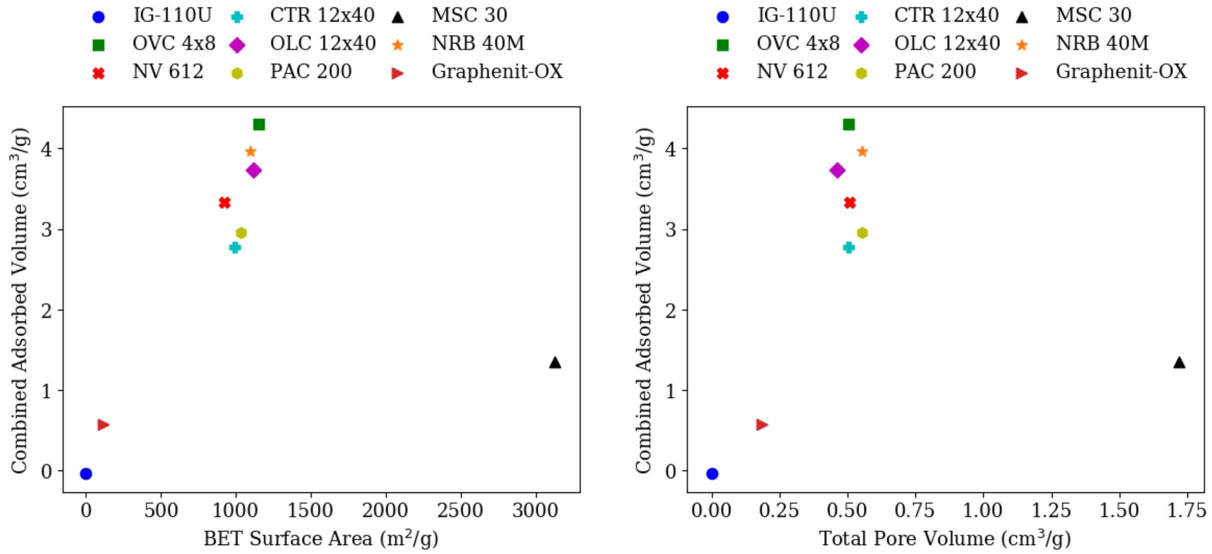

a) BET Surface Area **b) Pore Volume**

Figure 5.13: BET surface and total pore volume versus total hydrogen solubility. Temperature of 700°C and pressure of 3 kPa

The correlation between the surface area/volume of the different pore regimes (narrow micropores, micropores and mesopores) and the hydrogen capacity is shown from Figure 5.14 to Figure 5.17. Figure 5.14 a) and b) shows the correlation between the narrow micropore volume/surface area and hydrogen adsorbed at 3kPa, Figure 5.15 shows this same correlation but for micropores instead of narrow micropores, and Figure 5.17 shows this correlation for mesopores. Of the three pore regimes, narrow micropore volume/SA showed the strongest correlation with hydrogen adsorption in terms of goodness of fit and significance. Further, the incremental gain in hydrogen adsorption was largest per unit of increased narrow micropore surface area/volume. Considerable scatter exists for the data in all three cases. While the plots are shown for 3 kPa, similar trends were observed at all pressures for the combined isotherm. The summary of statistical parameters including R-value, p-value, and standard error are summarized in Table 5.9.

The narrow micropore volume and SA weakly correlated with hydrogen adsorption with R-values near 0.72. The hydrogen adsorption did not correlate well with micropore volume and SA with R-values of 0.48 and 0.33 respectively. The hydrogen adsorption did not correlate at all to mesopore volume and SA with |R-values| < 0.3. In terms of significance, the null hypothesis can only be rejected for narrow micropores if a standard significance level (α) of 0.05 is adopted.

However, the standard error of the gradient ($\Delta V_{ads}/\Delta x$) was relatively high for most values as can show both in Table 5.9. At minimum, the standard error represented roughly 35% of the gradient value for the narrow micropore surface area versus adsorbed hydrogen correlation.

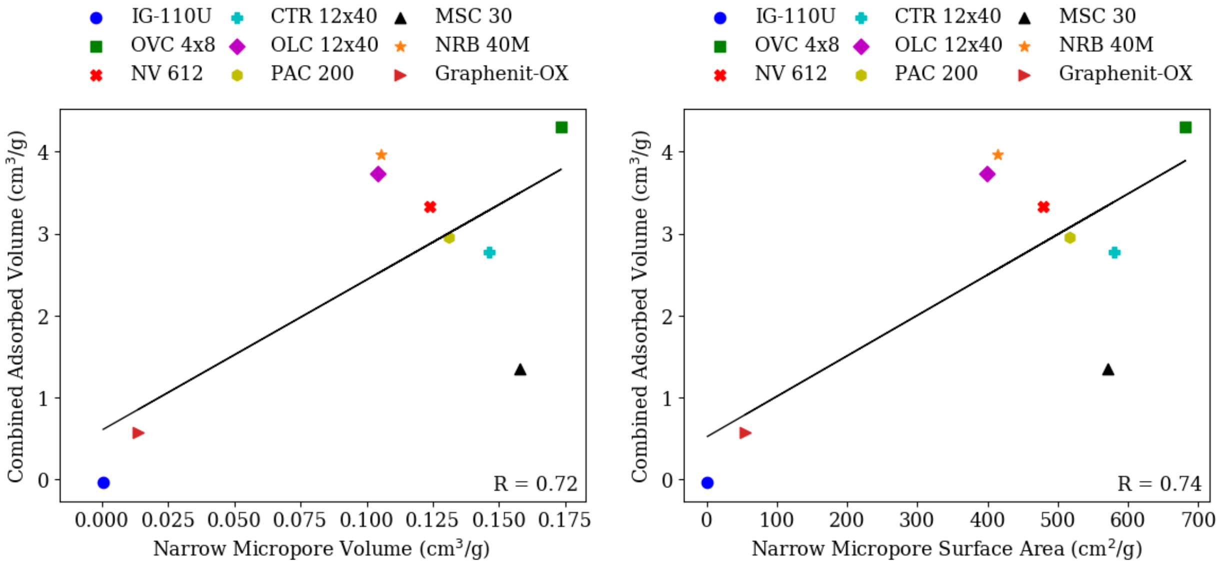

a) Volume **b) Surface Area**

Figure 5.14: Adsorbed volume of hydrogen versus narrow micropore a) volume and b) surface area. Temperature of 700°C and pressure of 3 kPa

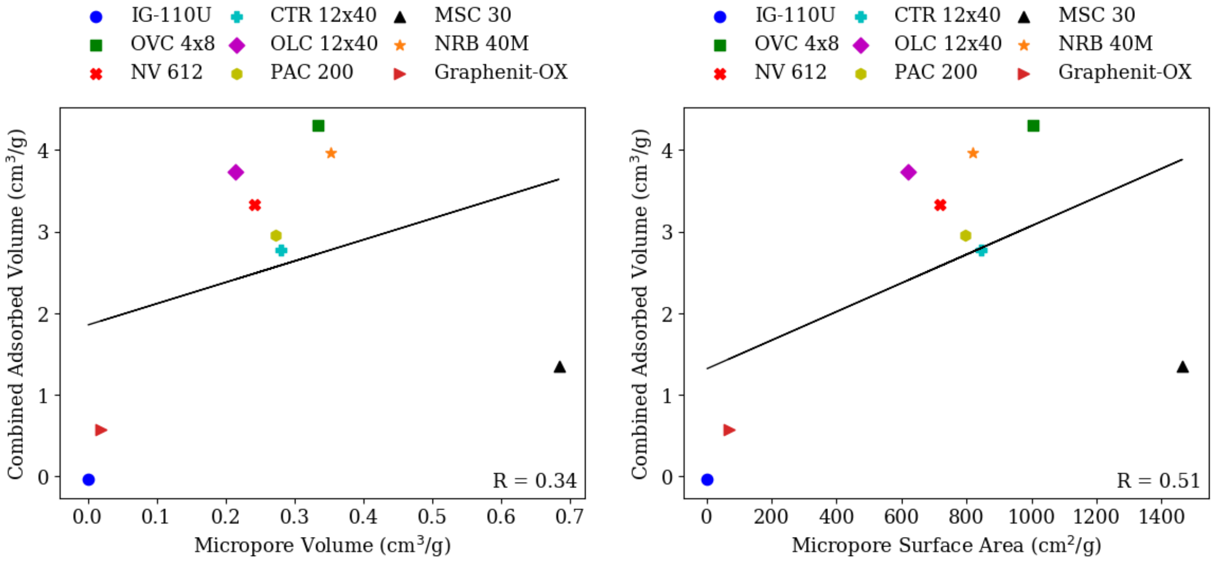

a) Volume **b) Surface Area**

Figure 5.15: Adsorbed volume of hydrogen versus micropore a) volume and b) surface area. Temperature of 700°C and pressure of 3 kPa

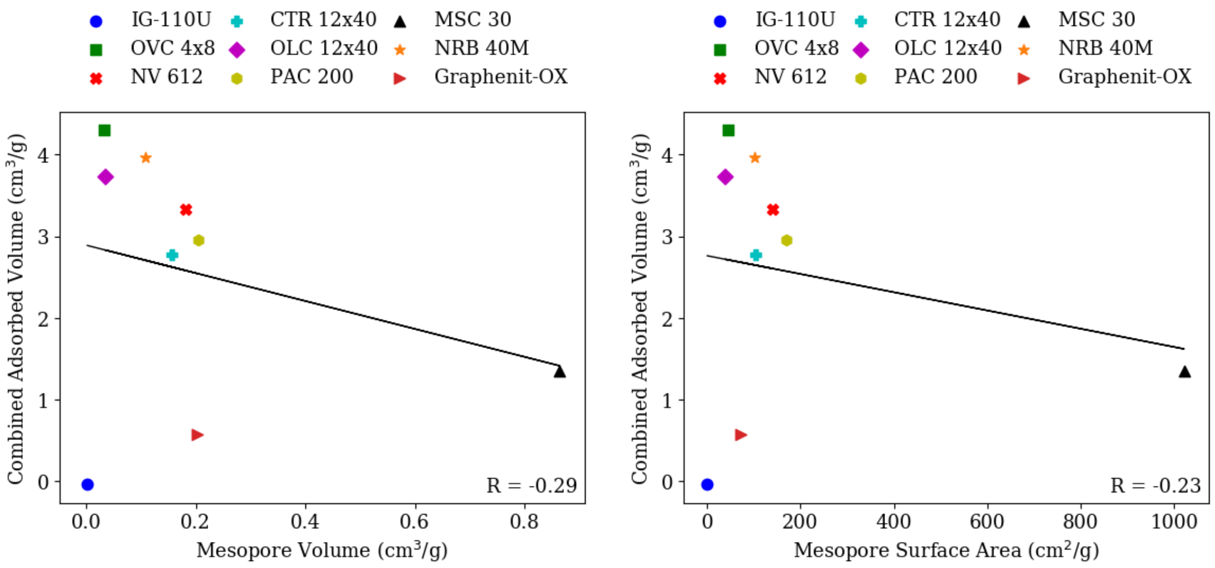

a) Volume **b) Surface Area**

Figure 5.16 Adsorbed volume of hydrogen versus mesopore a) volume and b) surface area. Temperature of 700°C and pressure of 3 kPa

Table 5.9. Statistical parameters of correlation between the specific surface area (m²/g) & pore volume (cm³/g) and the total hydrogen adsorbed in the combined isotherm at 3 kPa and 700°C for narrow micropores (< 0.7 nm), micropores (< 2 nm) and mesopores (2 – 40 nm)

		$\Delta V_{ads}/\Delta x^*$	R-value	p-value	Std. Error
Narrow Micropore	SA	0.0049	0.7361	0.0237	0.0017
	VOL	18.1341	0.7084	0.0327	6.8295
Micropore	SA	0.0017	0.5027	0.1678	0.0011
	VOL	2.6088	0.336	0.3767	2.7644
Mesopore	SA	-0.0011	-0.2244	0.5615	0.0018
	VOL	-1.6996	-0.2855	0.4564	2.1561

*x refers to the dependent variable. I.e. narrow micropore surface area, volume, micropore surface area, etc.

r pressures without saturation, although as before, the error is relatively high.

Table 5.10 shows the same statistical parameters as Table 5.9, but are provided at a lower pressure of 0.5 kPa to show the similarity in the relationships at a different pressure in the examined range. In the lower pressure case, the gradient of adsorbed hydrogen over narrow micropore SA is lower at 0.0035 cm³ adsorbed H_2 / m² of carbon surface compared to the 0.0050 cm³ / m² that was found at 3 kPa. However, the correlational strength, and significance are both of comparable magnitude. In part, the increased gradient at higher pressures may suggest that the narrow micropores continue to adsorb hydrogen at the higher pressures without saturation, although as before, the error is relatively high.

Table 5.10: Statistical parameters of correlation between the specific surface area (m^2/g) and volume (cm^3/g) and the total hydrogen adsorbed at 0.5 kPa and 700°C for narrow micropores (< 0.7 nm), micropores (< 2 nm) and mesopores (2 – 40 nm)

		$\Delta V_{ads}/\Delta x^*$	R-value	p-value	Std. Error
Narrow Micropore	SA	0.0035	0.7451	0.0212	0.0012
	VOL	12.9718	0.7191	0.029	4.7374
Micropore	SA	0.0013	0.5337	0.1389	0.0008
	VOL	2.0685	0.378	0.3158	1.9146
Mesopore	SA	-0.0006	-0.1814	0.6405	0.0013
	VOL	-0.9957	-0.2374	0.5385	1.5399

*x refers to the dependent variable. I.e. narrow micropore surface area.

5.2.3. Weak and Strong Chemisorption Isotherms

As described in 4.4.1, the total (i.e. combined) chemisorption can be separated into its component weak and strong isotherms. For IG-110U and Graphenit-OX, this is shown in Figure 5.17.

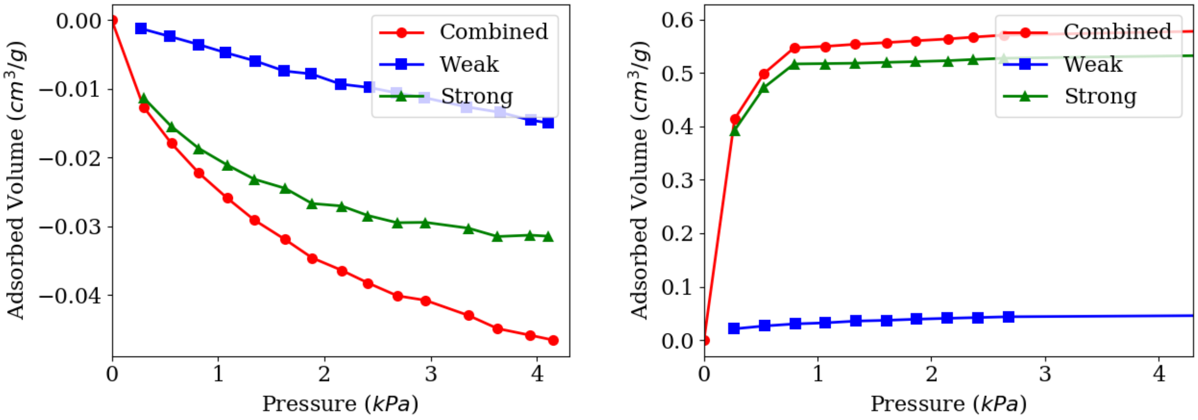

a) IG-110U **b) Graphenit-OX**

Figure 5.17: Combined, weak and strong chemisorption isotherms at 700°C for a) IG-110U and b) Graphenit-OX

In the previous section, the combined isotherm for IG-110U showed a negative signal for adsorption, which is also reflected in the weak and strong components. For the Graphenit-OX in Figure 5.17b), the figure shows that most of the adsorption came from strong interaction which trended with the combined curve and saturated early before 1 kPa, while the weak curve rose gradually. This effect was more apparent in the activated carbons. In Figure 5.18, extruded carbon NRB 40M is shown where the strong curve again saturated early below 1 kPa. Thus, the rise in the combined adsorption between 1 and 4 kPa came from the contribution of the weak curve. For NRB 40M, the contribution from weak adsorption was significantly more than for Graphenit-OX. This is likely due to the available narrow microporosity in NRB 40M where hydrogen can become trapped, compared to in graphene, where the majority of hydrogen adsorption is expected to come from strong dissociation on a graphene edge. At 4 kPa, nearly 25% of the capacity on NRB 40M is from weak adsorption.

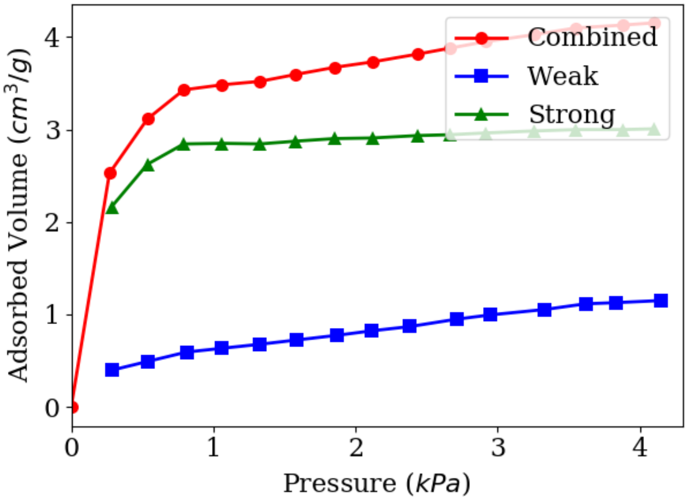

Figure 5.18: Combined, weak and strong chemisorption at 700°C for NRB 40M

The GAC isotherms are shown in Figure 5.19, which all show similar features to the NRB 40M isotherm. All of these materials had strong adsorption isotherms, which were non-linear with a quick increase to around 1 kPa followed by a gradual increase due to adsorption on the weak sites, while the strong adsorption curve was saturated. Qualitatively, the strong adsorption curves look similar to what would be observed for dissociative adsorption where the volumetric adsorption would have a square root pressure dependence [28]. Meanwhile, the weak curves are shown to be roughly first order functions, which could be potentially described by Henry's law with molecular hydrogen dissolving into a solid carbon solvent [117], or by taking the limit of the molecular adsorption Langmuir model at low pressure [118]. These models are discussed in further detail in Chapter 6. In each of these materials, the weak and strong component of adsorption contributed in varying proportions to the combined isotherm. In OVC 4x8, the weak adsorption isotherm accounted for nearly 2 cm³/g out of the total 4.5 cm³/g (>40%) at 4kPa while in CTR 12x40, the weak adsorption only accounted for 0.5 cm³/g out of the total 2.5 cm³/g (20%) at 4kPa.

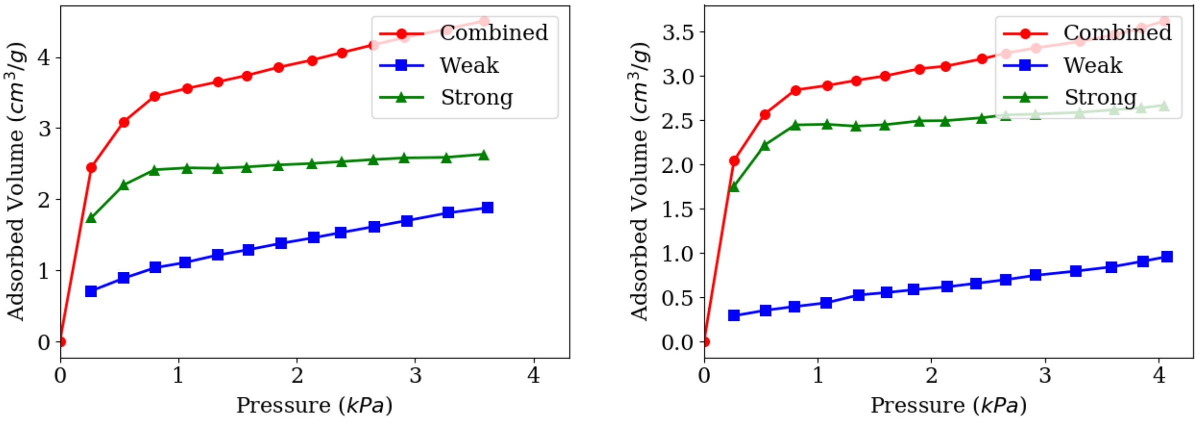

a) OVC 4x8 **b) NV 612**

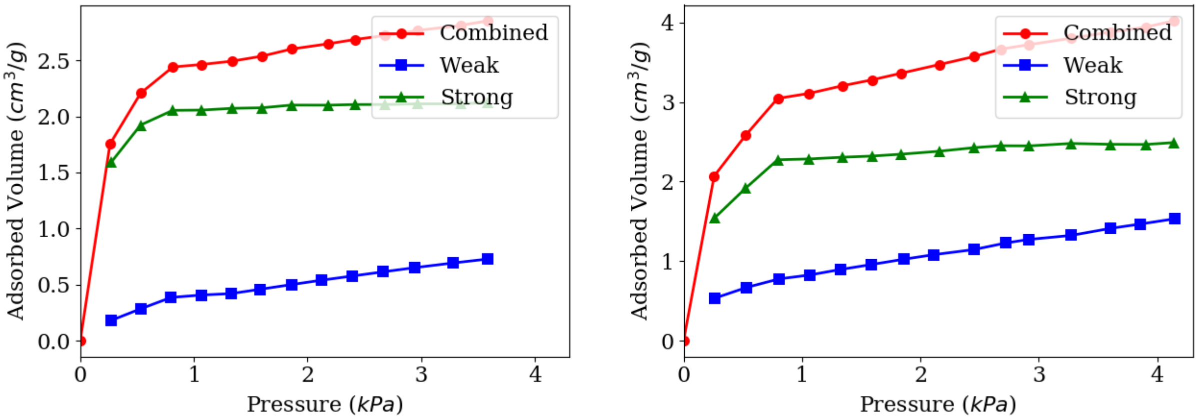

c) CTR 12x40 **d) OLC 12x40**

Figure 5.19: Combined, weak and strong chemisorption at 700°C for various granular activated carbons: a) OVC 4x8, NV 612, CTR 12x40, OLC 12x40

For the PACs, the combined, weak and strong isotherms are shown in Figure 5.20. The strong and weak isotherms of PAC 200 had similar trends to the other activated carbons. For MSC-30, the weak adsorption curve exhibited a peculiarity in that it began to actually decrease around 2.0 kPa while the strong adsorption curve stayed roughly constant. Since MSC-30 is a chemically activated carbon, the decrease in pressure was likely due to a reaction with hydrogen at 700°C, which is above the original activation temperature of the carbon. Summaries of the differences between the weak and strong interactions below 1.0 kPa for the carbon materials studied are shown in Table 5.11 and Table 5.12.

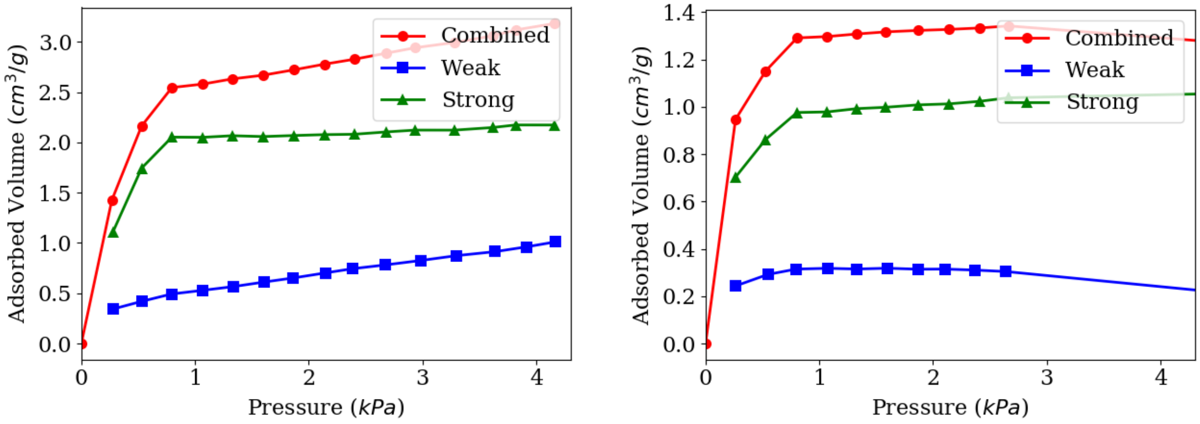

a) PAC 200 **b) MSC-30**

Figure 5.20: Combined, weak and strong isotherms at 700°C for powdered activated carbon PAC 200 and MSC-30

Table 5.11: Weak chemisorption isotherm at 700°C for activated carbons, graphene and graphite materials from 0.25 to 1.0 kPa

	Adsorbed Volume (cm^3/g)[a]			
Pressure (kPa)	0.25	0.5	0.75	1.0
GAC				
OVC 4x8	0.679	0.864	1.006	1.094
NV 612	0.274	0.343	0.387	0.425
CAL TR 12x40	0.166	0.271	0.367	0.401
OLC 12x40	0.511	0.653	0.754	0.813
PAC				
PAC 200	0.307	0.410	0.481	0.520
MSC-30	0.233	0.284	0.311	0.317
EAC				
NRB-40M	0.349	0.477	0.570	0.623
Graphene				
Graphenit-OX	0.020	0.026	0.030	0.032
Graphite				
IG-110U	-0.001	-0.002	-0.003	-0.004

[A]The adsorbed volume is measured close to the target pressures listed but not exactly at these pressures. The values shown here are linearly interpolated from the measured values

As shown in Table 5.11, ACs had a significantly higher quantities weak adsorption with the highest being in the granular activated carbons. The OVC 4x8 shows an adsorbed volume of 1.094 cm^3/g at 1.0 kPa, compared to graphene at 0.032 cm^3/g and graphite IG-110U, which could not be measured. For the strong chemisorption shown in Table 5.12, the same trends were observed with the ACs also having the highest adsorption, ranging around 2.0 - 2.5 cm^3/g at 1.0 kPa, with the exception of MSC 30, which had about half of this value. Again, graphene's strong adsorption was relatively low at 0.517 cm³/g, and graphite's adsorption could not be measured.

Table 5.12: Strong chemisorption isotherm at 700°C for activated carbons, graphene and graphite materials from 0.25 to 1.0 kPa

	Adsorbed Volume (cm³/g)[a]			
Pressure (kPa)	0.25	0.5	0.75	1.0
GAC				
OVC 4x8	1.63	2.133	2.373	2.435
NV 612	1.655	2.161	2.403	2.453
CAL TR 12x40	1.465	1.884	2.025	2.056
OLC 12x40	1.481	1.883	2.216	2.283
PAC				
PAC 200	0.997	1.668	1.998	2.051
MSC-30	0.668	0.846	0.954	0.978
EAC				
NRB-40M	1.91	2.559	2.809	2.849
Graphene				
Graphenit-OX	0.364	0.464	0.51	0.517
Graphite				
IG-110U	-0.009	-0.015	-0.018	-0.02

[A]The adsorbed volume is measured close to the target pressures listed but not exactly at these pressures. The values shown here are linearly interpolated from the measured values

The component of weak and strong interaction plays an important role in the adsorbent material choice since weakly adsorbed hydrogens are easily desorbed. This allows for a lower energy requirement in regenerating the catalyst. However, this also implies that more tritium can be released in the event of a high temperature transient. The next chapters investigate the correlation of the pore size distribution on the weak and strong isotherms to help understand the driving forces behind weak and strong interaction.

5.2.4. Effect of Pore Size Distribution on Weak Adsorption

As with the combined adsorption studied in Chapter 5.2.2, the weak interaction correlated most strongly with the available narrow micropore surface area (and volume) with R-values of 0.73 and 0.70 for 0.5 kPa and 3.0 kPa respectively shown in Figure 5.21. The pore volume correlations were almost the same as the SA correlations and are not shown here, but the regression data is provided in Table 5.13 and Table 5.14. Micropore (< 2 nm) SA showed poor correlation with the amount of weakly adsorbed hydrogen with R-values of only 0.55 and 0.41 for pressures 0.5 and 3.0 kPa respectively. Mesopore SA also showed no correlation to the weak adsorption with R-values -0.25 and -0.35 for pressures of 0.5 kPa and 3.0 kPa respectively.

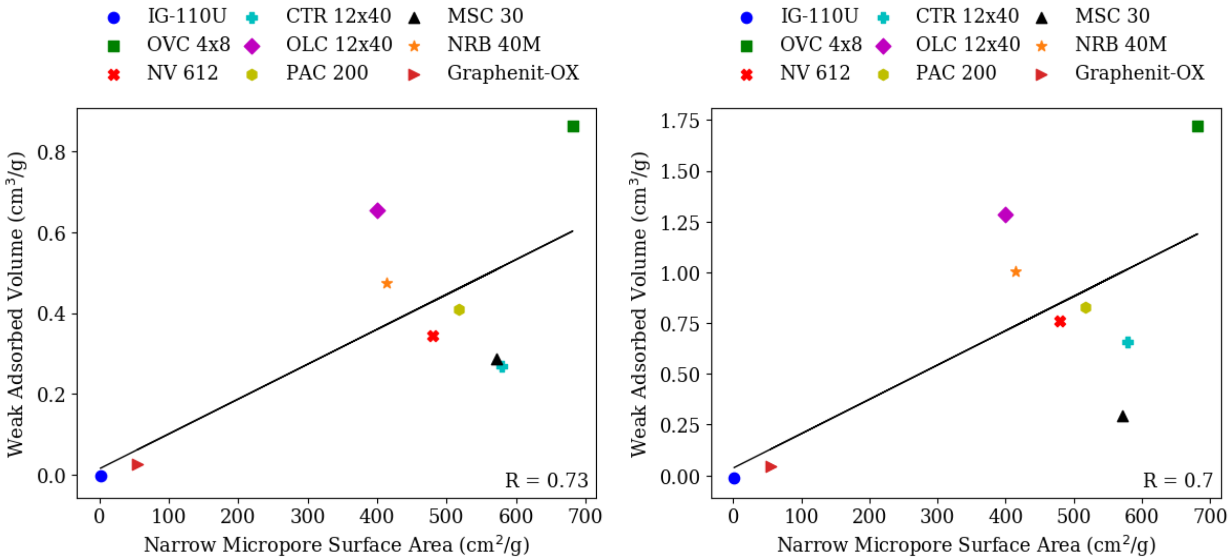

a) 0.5 kPa **b) 3.0 kPa**

Figure 5.21: Adsorbed volume of weakly adsorbed hydrogen versus available surface area of narrow micropores for a) 0.5 kPa, and b) 3.0 kPa

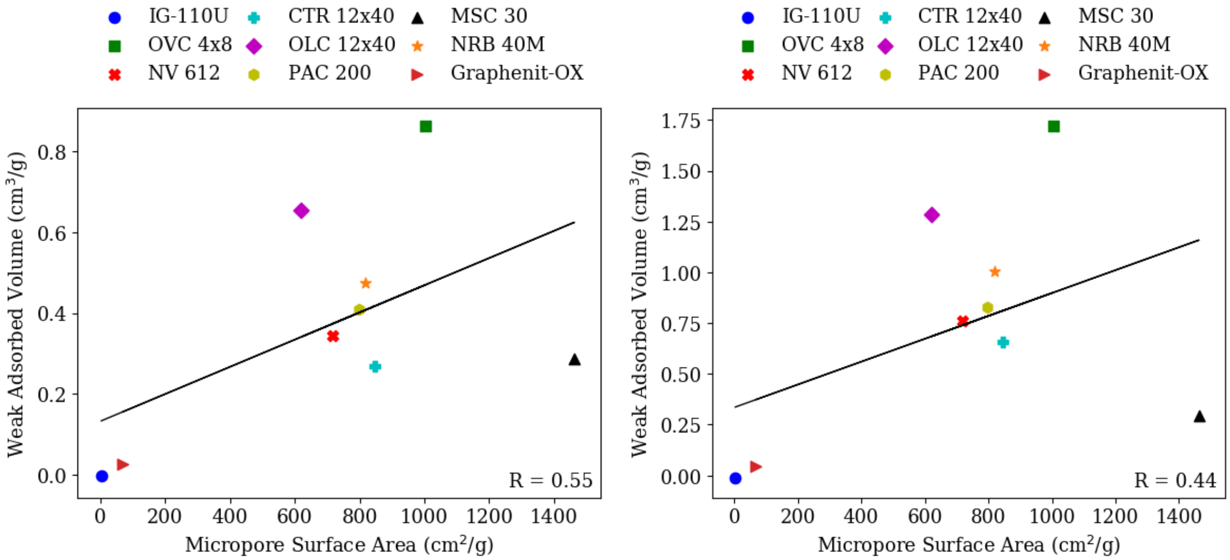

a) 0.5 kPa **b) 3.0 kPa**

Figure 5.22: Adsorbed volume of weakly adsorbed hydrogen versus available surface area of micropores for a) 0.5 kPa, and b) 3.0 kPa

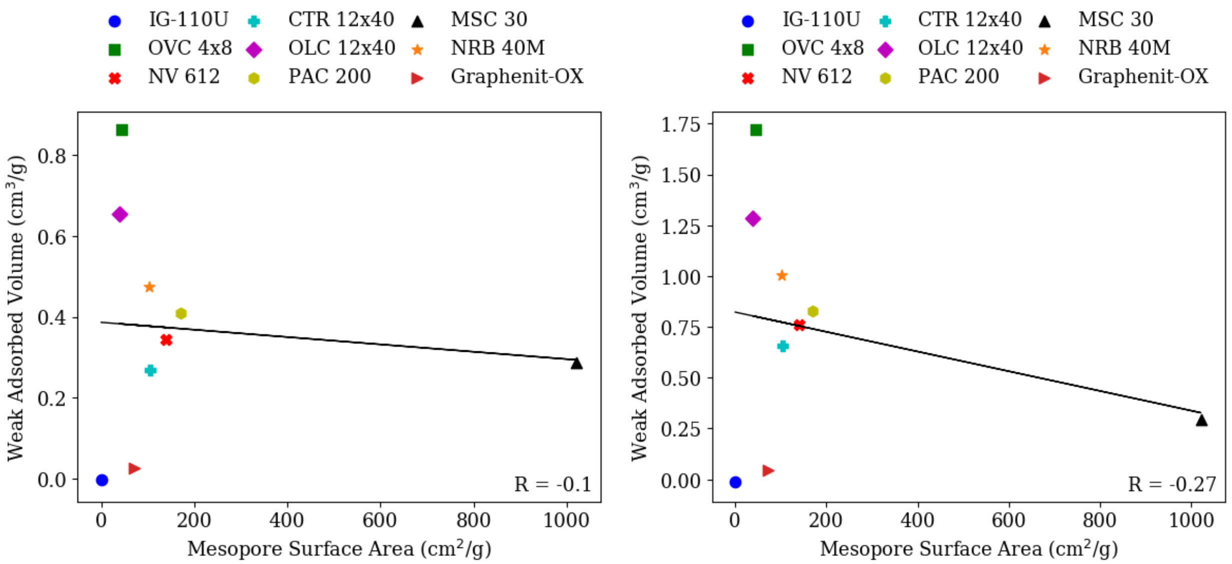

a) 0.5 kPa **b) 3.0 kPa**

Figure 5.23: Adsorbed volume of weakly adsorbed hydrogen versus available surface area of mesopores at a) 0.5 kPa, and b) 3.0 kPa

Table 5.13: Statistical parameters of correlation between the specific surface area (m^2/g) and volume (cm^3/g) and the total hydrogen adsorbed in the weak isotherm at 0.5 kPa and 700°C for narrow micropores (< 0.7 nm), micropores (< 2 nm) and mesopores (2 – 40 nm)

		$\Delta V_{ads}/\Delta x^*$	R-value	p-value	Std. Error
Narrow Micropore	SA	0.0009	0.7297	0.0256	0.0003
	Vol.	3.2473	0.7141	0.0307	1.2031
Micropore	SA	0.0003	0.5459	0.1284	0.0002
	Vol.	0.5472	0.3967	0.2904	0.4786
Mesopore	SA	-0.0001	-0.1041	0.7899	0.0003
	Vol.	-0.2145	-0.2029	0.6006	0.3913

*x refers to the dependent variable. I.e. narrow micropore surface area.

Table 5.14: Statistical parameters of correlation between the specific surface area (m^2/g) and volume (cm^3/g) and the total hydrogen adsorbed in the weak isotherm at 3 kPa and 700°C for narrow micropores (< 0.7 nm), micropores (< 2 nm) and mesopores (2 – 40 nm)

		$\Delta V_{ads}/\Delta x^*$	R-value	p-value	Std. Error
Narrow Micropore	SA	0.0017	0.6955	0.0375	0.0007
	Vol.	6.2581	0.6683	0.0491	2.6329
Micropore	SA	0.0006	0.4439	0.2313	0.0004
	Vol.	0.7614	0.2681	0.4856	1.0343
Mesopore	SA	-0.0005	-0.2699	0.4824	0.0007
	Vol.	-0.7769	-0.3568	0.3459	0.7688

If the significance level of $\alpha = 0.05$ is used, only weak hydrogen adsorption correlates to the narrow micropore SA and volume with p-values of 0.0256 and 0.0307 respectively at 0.5 kPa, and p-values of 0.0375 and 0.0491 at 3 kPa. Again however, total error is considerably high.

Further, we investigated the relationship between weak hydrogen adsorption and the SA/volume fraction of micropores and narrow micropores in each material. This allowed us to determine whether carbon materials with a higher micropore fraction also exhibited higher weak adsorption. The analysis is shown at 3 kPa, although the same conclusions are drawn at any pressure within the range of the experimental data. Both the correlations for pore volume fraction and surface area fraction versus weakly adsorbed hydrogen are shown since they differ significantly.

The strongest relationships were exhibited in Figure 5.24 a) and Figure 5.25 a) that show the volume fraction of narrow micropores and micropores correlated well to the weak hydrogen adsorption. For weak adsorption versus pore volume fraction, R-values were 0.92 for narrow micropores and 0.93 for micropores respectively. In contrast, for weak adsorption versus pore SA fraction, the R-values were significantly lower at 0.74 and 0.72 for narrow micropores and micropores respectively. The statistics for these correlations are summarized in Table 5.15. Particularly, the correlations of weak adsorption versus volume fractions of narrow micropores and micropores showed reasonable R-values, and good p-values of 0.0005 and 0.0003 respectively. This indicates that carbon materials that have a greater volume fraction of micropores are able to weakly adsorb greater amounts of hydrogen.

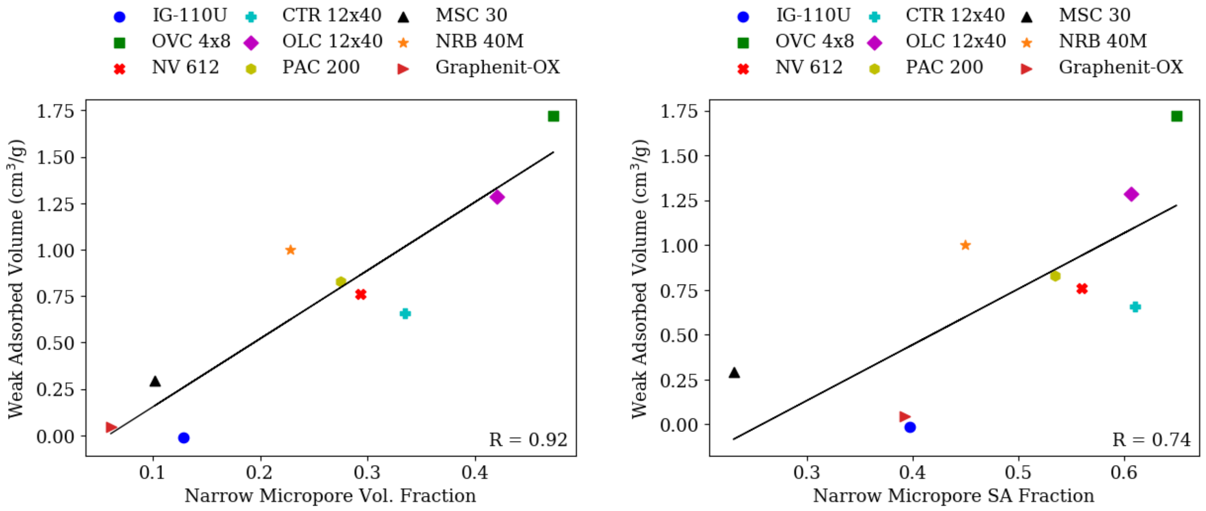

a) Volume Fraction **b) Surface Area Fraction**

Figure 5.24: Weak adsorption at 3 kPa vs. a) narrow micropore volume fraction and b) narrow micropore surface area fraction for carbon materials

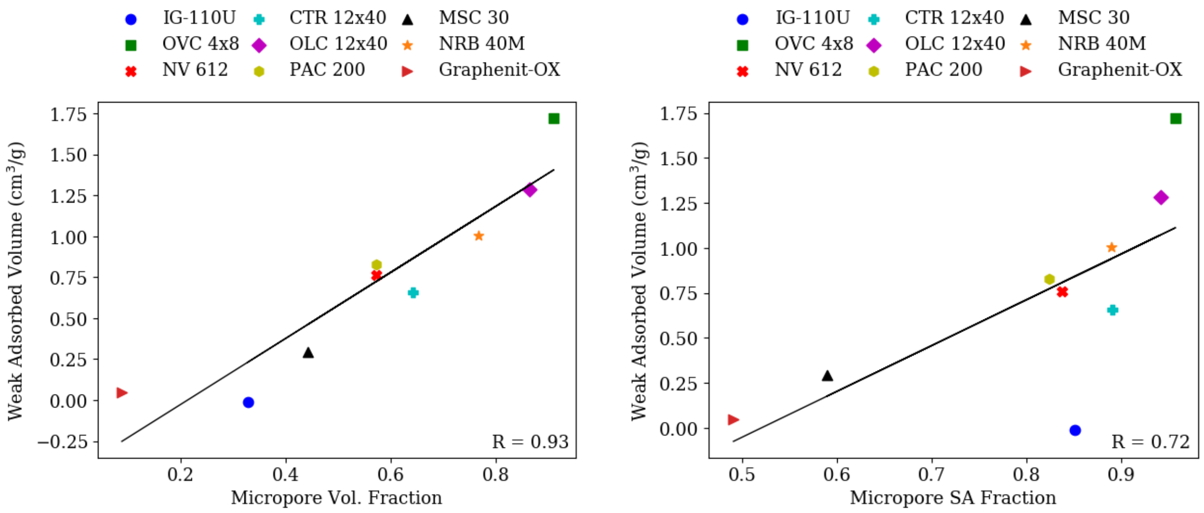

a) Volume Fraction **b) Surface Area Fraction**

Figure 5.25: Weak adsorption at 3 kPa vs. a) micropore volume fraction and b) micropore surface area fraction for carbon materials

Table 5.15: Statistical parameters of correlation between volume/SA fraction of narrow micropores and micropores versus weak hydrogen adsorption at 3 kPa

		$\Delta V_{ads}/\Delta x^*$	R-value	p-value	Std. Error
Narrow Micropore	SA	3.1110	0.7426	0.0219	1.0603
	Vol.	3.6804	0.9164	0.0005	0.6077
Micropore	SA	2.5452	0.7161	0.0300	0.9377
	Vol.	2.0178	0.9315	0.0003	0.2977

*x refers to the dependent variable. I.e. narrow micropore surface area fraction.

Finally, the volume fractions of narrow micropores/micropores were correlated against the volume fractions of weak adsorption. These correlations are shown in Figure 5.26 and Figure 5.27. By comparing these fractions, the effects of micropores and narrow micropores on weak adsorption were assessed in a more direct manner.

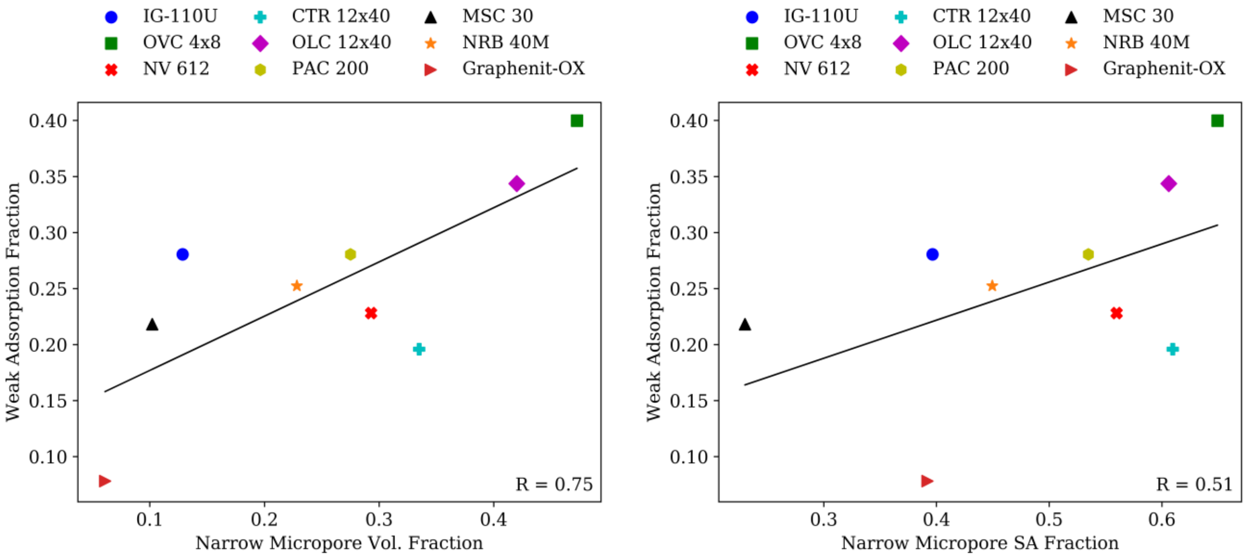

a) Volume Fraction **b) Surface Area Fraction**

Figure 5.26: Fraction of weak adsorption at 3 kPa vs. a) narrow micropore volume fraction and b) narrow micropore surface area fraction for carbon materials

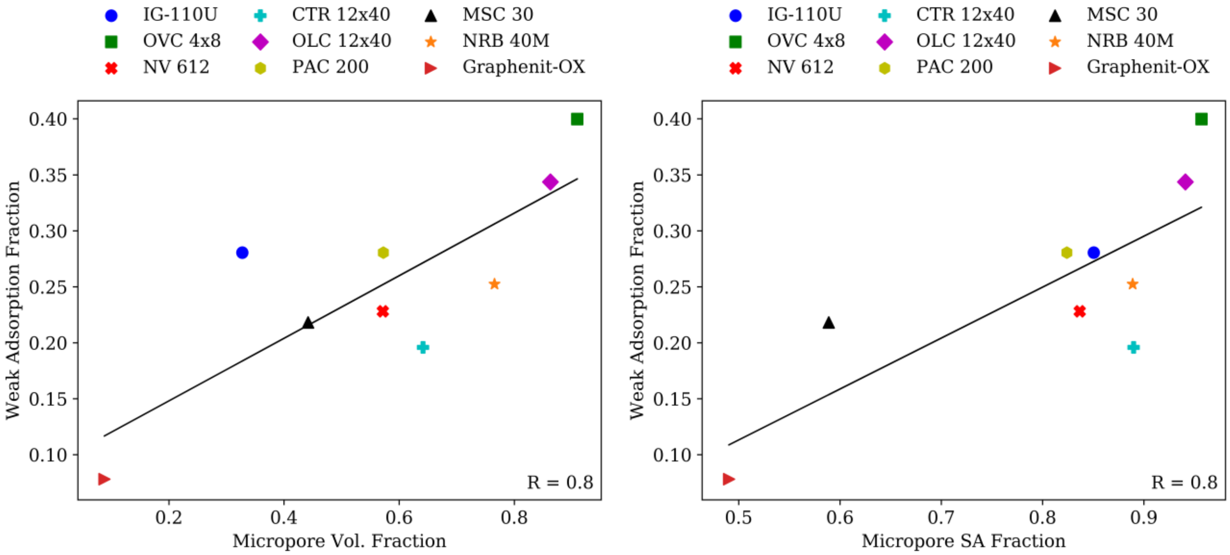

a) Volume Fraction **b) Surface Area Fraction**

Figure 5.27: Fraction of weak adsorption at 3 kPa vs. a) micropore volume fraction and b) micropore surface area fraction for carbon materials

The gradients, R-values, p-values and standard errors are summarized in Table 5.16, where good p-values were obtained at 0.02 for narrow micropore volume fraction and 0.0092 for micropore volume fraction, while being significantly higher for the surface area fraction correlations at 0.1654 for narrow micropores and 0.0103 for micropores. The surface area and volume correlations are not the same because the surface area is dependent on the pore size distribution inside a broadly defined group (micropore, mesopore). For example, if there were more pores near the upper end of the group's bounds (i.e. closer to 2 nm for micropores), then the surface area of the total group would be lower than if a larger number of pores existed near the lower end of the group bounds. This is true since smaller pores have a higher surface to volume ratio. The difference between the volume and surface area trends suggests that there may be an intermediate pore size range inside the micropore regime (< 2nm) which can optimally adsorb hydrogen. This has been suggested by a few authors in literature to be around the 0.5 to 0.7 nm range [119] for hydrogen storage at 77K and 4 MPa, and is worth deeper consideration in future studies.

Table 5.16: Statistical parameters of correlation between volume/SA fraction of narrow micropores and micropores versus weak hydrogen adsorption fraction at 3 kPa for carbon materials

		$\Delta Y_{ads}/\Delta x^*$	R-value	p-value	Std. Error
Narrow Micropore	SA	0.3401	0.5051	0.1654	0.2196
	Vol.	0.4840	0.7498	0.0200	0.1614
Micropore	SA	0.4548	0.7961	0.0103	0.1307
	Vol.	0.2795	0.8028	0.0092	0.0785

* $\Delta Y_{ads}/\Delta x$ refers to gradient of weak adsorption fraction versus variable x (I.e. micropore SA fraction).

From Figure 5.24 to Figure 5.27, it was shown that 1) materials with a larger volume of narrow micropores had the general tendency to weakly adsorb more hydrogen, and 2) materials with a high volume fraction of narrow micropores and micropores had a higher relative weak adsorption, and 3) the proportion of weak adsorption on an a material was correlated positively to the proportion of available narrow micropore and micropore volume. These three results suggest that weak adsorption occurs in the micropores and narrow micropores of a material.

5.2.5. Effect of Pore Size Distribution on Strong Adsorption

Generally, the same results that were observed for weak adsorption were also observed for strong adsorption where the strongly adsorbed volume correlates most with the narrow micropore availability. The strong adsorption was correlated with the surface areas of the narrow micropores, micropores and mesopores in Figure 5.28 to Figure 5.30. Each figure shows that the behavior at 0.5 kPa is similar to that at 3 kPa, indicating that the strong adsorption exhibits little pressure dependence over this range. This is apparent given the fact that strong adsorption saturated very early in most materials shown in Chapter 5.2.3.

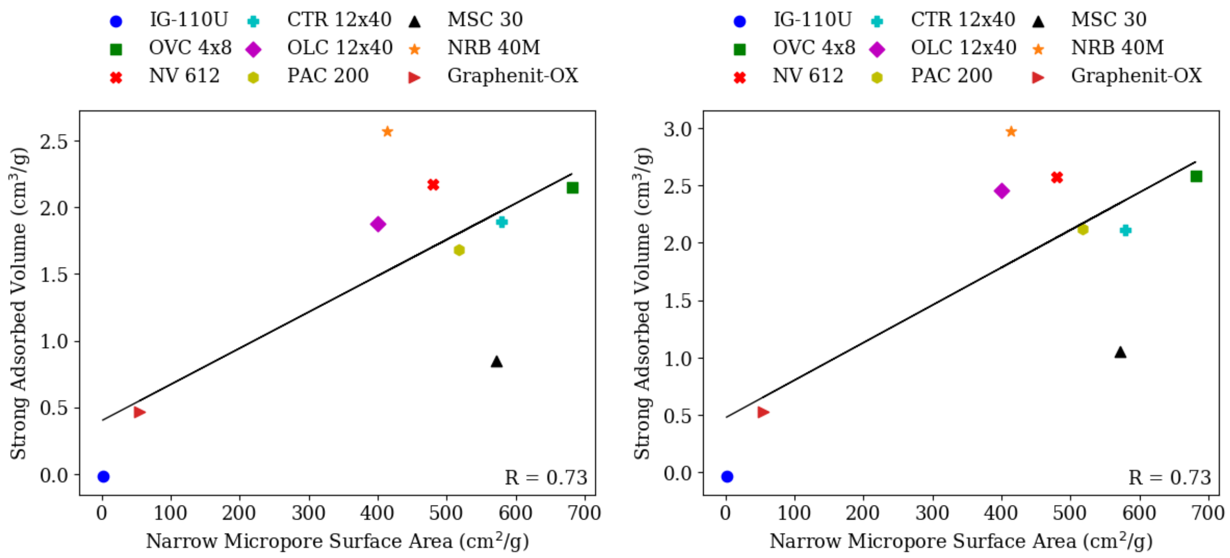

a) 0.5 kPa **b) 3.0 kPa**

Figure 5.28: Adsorbed volume of hydrogen in strong isotherm versus available surface of narrow micropores for a) 0.5 kPa, and b) 3.0 kPa

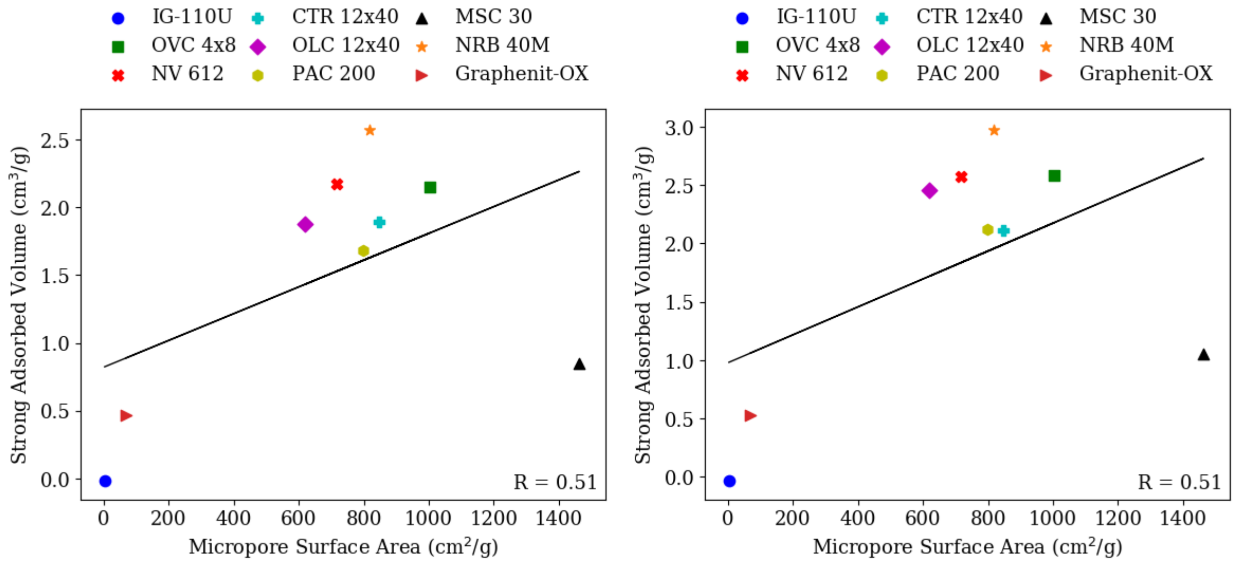

c) 0.5 kPa **d) 3.0 kPa**

Figure 5.29: Adsorbed volume of hydrogen in strong isotherm versus available surface of micropores for a) 0.5 kPa, and b) 3.0 kPa

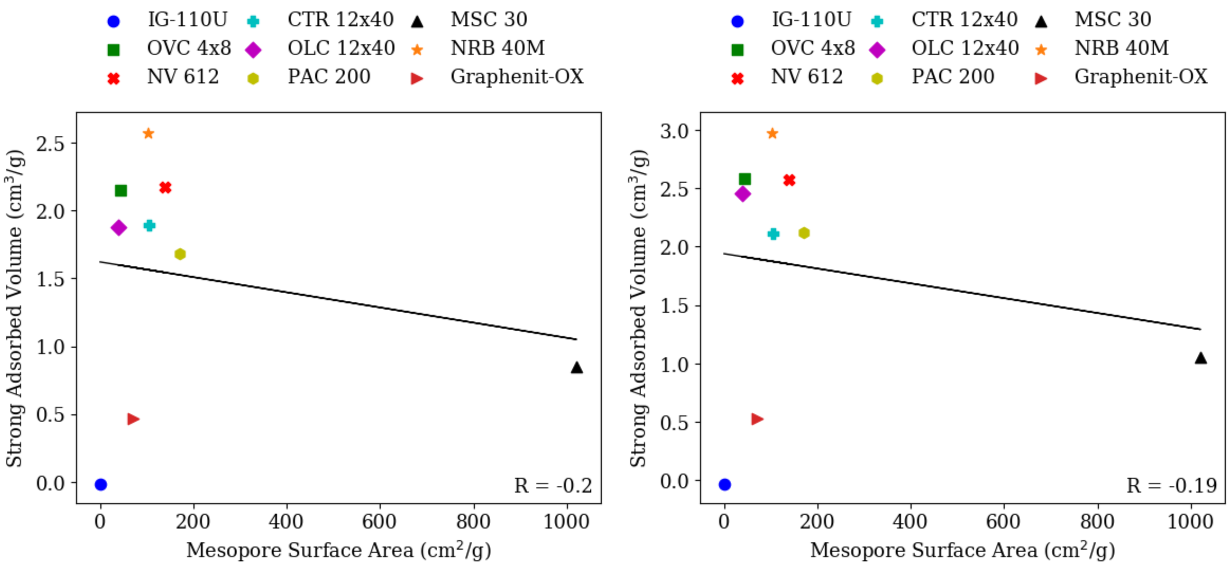

a) 0.5 kPa **b) 3.0 kPa**

Figure 5.30: Adsorbed volume of hydrogen in strong isotherm versus available surface of mesopores for a) 0.5 kPa, and b) 3.0 kPa

Quantitatively, the results are summarized by Table 5.17 and Table 5.18. These tables show the gradient of strongly adsorbed hydrogen over the SA/volume of each pore range as well as the relevant statistical parameters at 0.5 and 3 kPa. The narrow micropores showed the strongest and most significant correlation with the volume of strong hydrogen adsorption. The correlation coefficients were 0.73 and 0.70 for pore surface area and volume respectively, and were the same at both 0.5 kPa and 3 kPa. However, error was relatively high again, as they were for the correlations between combined/weak adsorption and absolute volume/surface area.

Table 5.17: Statistical parameters of correlation between the specific surface area (m²/g) and volume (cm³/g) and the total hydrogen adsorbed in the strong isotherm at 0.5 kPa and 700°C for narrow micropores (< 0.7 nm), micropores (< 2 nm) and mesopores (2 – 40 nm)

		$\Delta V_{ads}/\Delta x^*$	R-value	p-value	Std. Error
Narrow Micropore	SA	0.0027	0.7255	0.0270	0.0010
	Vol.	10.0418	0.6959	0.0373	3.9167
Micropore	SA	0.0010	0.5058	0.1648	0.0006
	Vol.	1.5317	0.3499	0.3559	1.5498
Mesopore	SA	-0.0006	-0.2024	0.6015	0.0010
	Vol.	-0.7980	-0.2379	0.5377	1.2317

*x refers to the dependent variable. I.e. narrow micropore surface area.

Table 5.18: Statistical parameters of correlation between the specific surface area (m^2/g) and volume (cm^3/g) and the total hydrogen adsorbed in the strong isotherm at 3 kPa and 700°C for narrow micropores (< 0.7 nm), micropores (< 2 nm) and mesopores (2 – 40 nm)

		$\Delta V_{ads}/\Delta x^*$	R-value	p-value	Std. Error
Narrow Micropore	SA	0.0033	0.7317	0.0250	0.0011
	Vol.	12.1006	0.7041	0.0342	4.6126
Micropore	SA	0.0012	0.5134	0.1575	0.0008
	Vol.	1.8556	0.3560	0.3471	1.8413
Mesopore	SA	-0.0006	-0.1922	0.6203	0.0012
	Vol.	-0.9342	-0.2338	0.5449	1.4685

*x refers to the dependent variable. I.e. narrow micropore surface area.

Again, as with the analyses at the end of Chapter 5.2.4, we investigated the relationship between the volume/SA fraction of micropores/narrow micropores and strong hydrogen adsorption for each material. This is shown in Figure 5.31 and Figure 5.32.

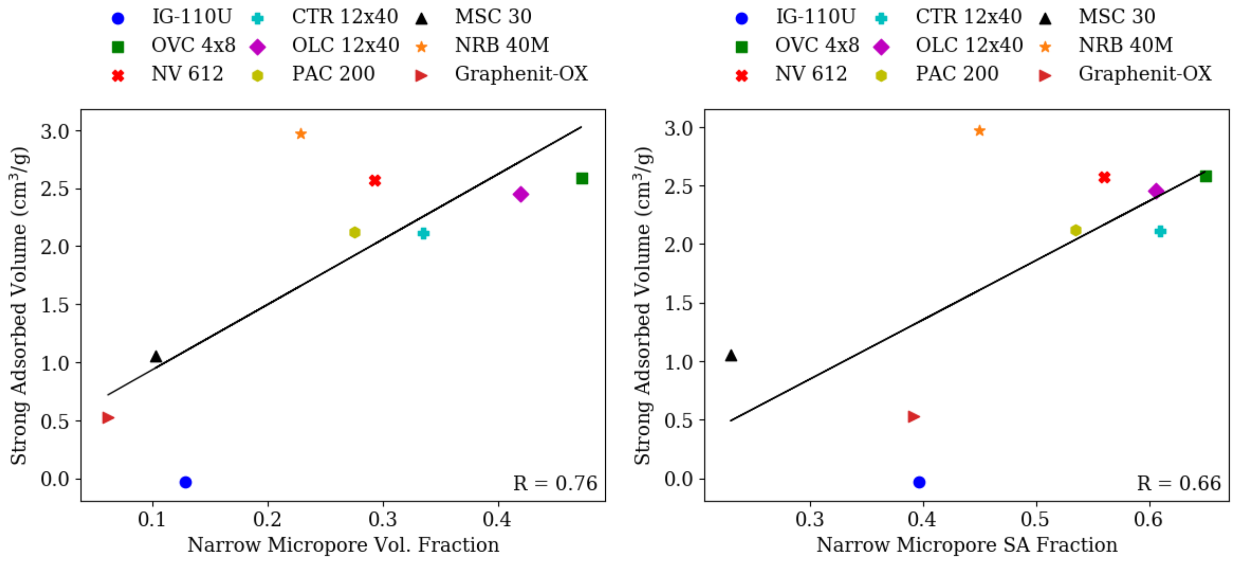

a) Volume Fraction **b) Surface Area Fraction**

Figure 5.31: Strong hydrogen adsorption at 3 kPa vs. a) narrow micropore volume fraction and b) narrow micropore surface area fraction for carbon materials

As was the case for weak adsorption, the strong hydrogen adsorption was greater for materials that had higher volume fractions of narrow micropores and micropores. Table 5.19 shows the significance parameters of these correlations. Strongly adsorbed hydrogen positively correlated with narrow micropores and micropore volume fractions with R-values of 0.76 and 0.85 respectively with relatively low p-values of 0.017 and 0.004 respectively. The gradients ($\Delta V_{ads}/\Delta x_{pore}$) were 5.6

and 3.37 with standard errors of 1.81 and 0.79 for the narrow micropore and micropore volume fractions respectively. The surface area correlations however were not as significant. This suggests that there may be an optimal pore range for strong hydrogen adsorption that lies within the broadly defined category of the micropore.

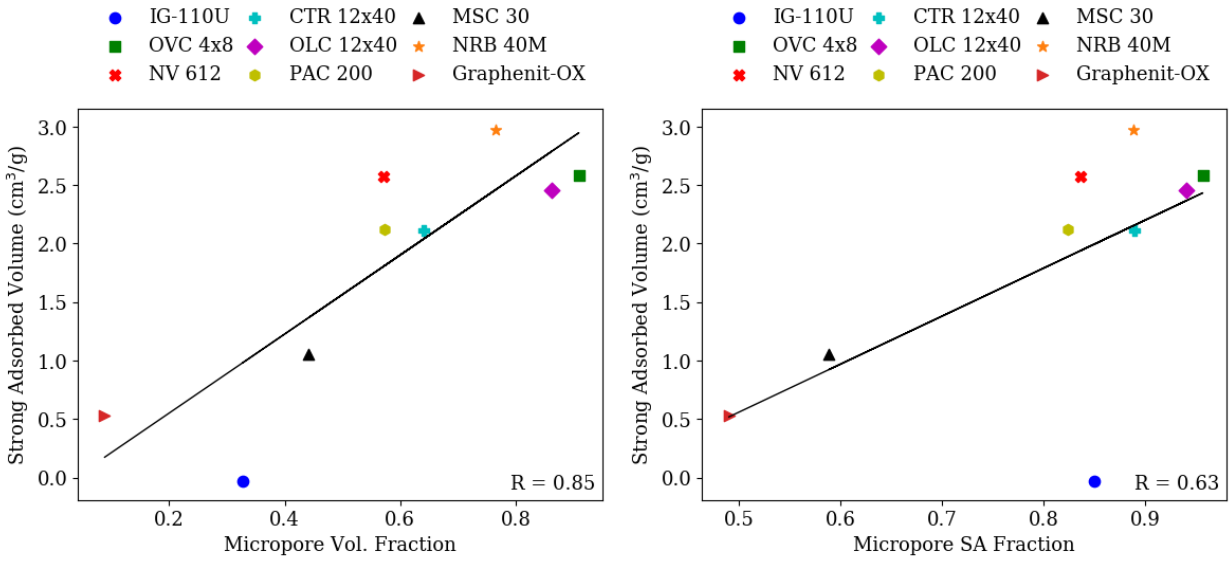

a) Volume Fraction **b) Surface Area**

Figure 5.32: Strong adsorption at 3 kPa vs. micropore a) volume fraction and b) surface area for carbon materials

Table 5.19: Statistical parameters of correlation between volume/SA fraction of narrow micropores and micropores versus the strong hydrogen adsorption at 3 kPa

		$\Delta V_{ads}/\Delta x^*$	R-value	p-value	Std. Error
Narrow Micropore	SA	5.0712	0.6596	0.0532	2.1841
	Vol.	5.6048	0.7604	0.0174	1.8095
Micropore	SA	4.1009	0.6287	0.0698	1.9174
	Vol.	3.3739	0.8487	0.0038	0.7947

*x refers to the dependent variable. I.e. narrow micropore surface area fraction.

When analyzing the weak adsorption, the fraction of weak adsorption was correlated to the fraction of narrow micropores and micropores. Since the total solubility of hydrogen is simply the sum of the weak and strong adsorption, the correlation for fractional strong adsorption versus fractional narrow micropores/micropores would just be the negative of those shown in Figure 5.26 and Figure 5.27. Thus, while carbons with higher narrow micropore and micropore volume fractions generally exhibit larger quantities of strong hydrogen adsorption, the strong interaction does not appear to be physically associated with adsorption within micropores or narrow micropores. The strong adsorption, likely arises from phenomena that are more complex. One example would be the high-energy dissociative trapping of hydrogen in interstitial cluster loops proposed by Atsumi [120] as found for graphite materials. Therefore, more data should be collected (i.e. adsorption energies) and then combined with other techniques (such as temperature programmed desorption and molecular simulation) to make proper phenomenological inferences.

5.3. Scanning Electron Microscopy

Images of various types of carbon materials used in this thesis are shown in Figure 5.33. The length scale of the images are on the orders of microns, which allows investigation into the macroporous morphology of various materials. While it is possible to use image processing and analysis to acquire quantitative values for pore size distribution [121], such methods are limited only to a small area of analysis and are best applied to two dimensional surfaces. Further, it was found that the calculated distributions were quite sensitive to user defined image-analysis threshold values. In addition, the previous section found that the chemisorption of hydrogen depended more strongly on the microporous region, and had little correlation to the larger mesopores. Thus, the images provided here act as a qualitative supplement to the results found in Chapter 5.1 and 5.2.

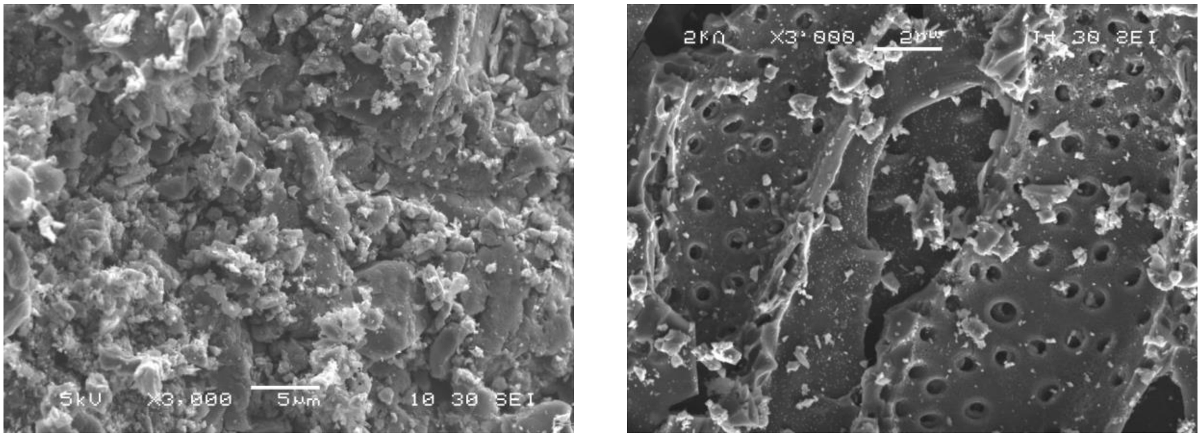

a) **b)**

Figure 5.33: Scanning electron microscopy of different carbon types at 5 kV, 3000X magnification. a) GAC CTR 12x40, b) GAC OVC 4x8, c) GAC NV 612, d) PAC MSC-30, e) Graphenit-OX, f) IG-110U

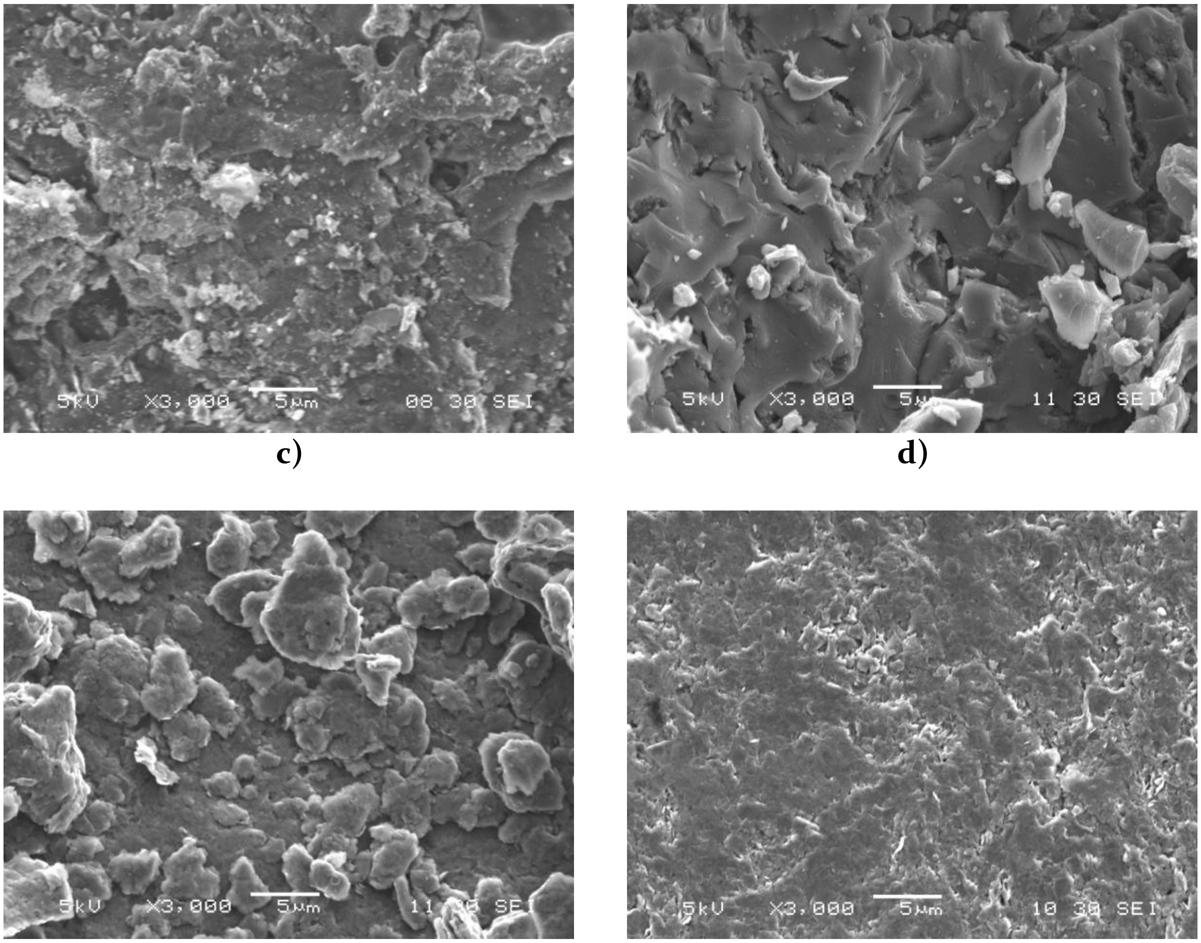

c) **d)**

e) **f)**

Figure 5.33 continued: Scanning electron microscopy of different carbon types at 5 kV, 3000X magnification. a) GAC CTR 12x40, b) GAC OVC 4x8, c) GAC NV 612, d) PAC MSC-30, e) Graphenit-OX, f) IG-110U

Figure 5.33 a) to c) show the images for granular activated carbons CTR 12x40, OVC 4x8 and NV 612, which were found to have relatively high hydrogen solubility in comparison to other types of materials. These images all show that the surfaces of granular carbons had highly three-dimensional microstructures. CTR 12x40 and OVC 4x8 both showed highly heterogeneous material grains and porosity on the surface with a high degree of roughness while the NV 612 had a more stacked planar structure with large open cylindrical pores (<1 µm), which allows direct access to the internal structure. Figure 5.33 d) shows the powdered activated carbon MSC-30, which had a much smoother surface morphology with long slit-like pores. MSC-30 had the third lowest hydrogen solubility of all the materials tested next to Graphenit-OX and IG-110U which are shown in Figure 5.33 e) and f). In the Graphenit-OX image, individual nanoplatelets can be seen on the 2-3 micron level. The surface of these platelets appear to be relatively smooth and non-porous. Figure 5.33 f) shows that IG-110U had a smooth two-dimensional surface with few meso and macropores. Of all carbons, IG-110U had the lowest hydrogen solubility by a couple orders of magnitude in comparison to the granular activated carbons. Experimentally, the carbons which had rough surfaces tended towards high chemisorption and generally appeared to obey the assumption used in DFT calculations that the mesopores were roughly cylindrical. While MSC-30 had the highest calculated BET surface area of 3000+ m^2/g, it exhibited substantially lower chemisorption (2-3X) and had a much smoother surface on the micron level. Additionally, the relatively non-porous two-dimensional structures of Graphenit-OX and IG-110U had both the lowest measured surface area and chemisorption capacity.

5.4. Data Synthesis and Summary

This section serves as a summary of key results from the adsorption studies of this chapter. Experimental data was collected which 1) characterized the materials by pore size, pore volume, surface area, and pore size distribution and 2) measured the strong, weak and combined chemisorption of hydrogen on these materials. With this data, various relationships between pore size distribution and chemisorption were determined.

In Chapter 5.1, it was found that activated carbons had the largest BET surface areas and pore volumes. The BET surface areas of the ACs generally ranged from 900 – 1200 m^2/g while it was only 0.6 m^2/g for graphite and 113 m^2/g for graphene nanoplatelets. The material with the highest surface area and pore volume by far was MSC-30, the powdered superactivated carbon with a BET surface area of 3125 m^2/g. Using DFT, the pore size distributions were also calculated. It was found that ACs generally had the highest narrow micropore and micropore SA/volume. For example, the narrow micropore SA of ACs were in the range of 400 - 600 m^2/g while it was only 1.34 m^2/g for graphite IG-110U, and 55 m^2/g for graphene platelets. The fitting errors from DFT methods were examined, where most of the models fit experimental data with errors of less than 1 % with the exception of IG-110U which had an error of 2.4% when estimating pore distribution > 1 nm, and Graphenit-OX, which had an error of 6.22 % when estimating pore distribution < 1 nm.

In Chapter 5.2, the hydrogen capacity was measured at 700°C between pressures of 0 to 4 kPa. It was found that ACs had significantly higher hydrogen chemisorption capacities ranging from 2 – 4 cm^3/g compared to Graphenit-OX, which only adsorbed a total hydrogen volume of 0.5 cm^3/g and IG-110U, in which adsorption was found to be negligible. The weak adsorption capacity varied between ACs ranging from between 0.4 to 1.0 cm^3/g, while the Graphenit-OX had a relatively low weak adsorption of 0.032 cm^3/g. The same is true for strong adsorption, which ranged from 2.0 to 2.4 cm^3/g for most of the ACs (except MSC-30), while the Graphenit-OX strongly adsorbed significantly less at 0.517 cm^3/g. Contrary to previous studies on graphite [28], the adsorbed hydrogen at 700°C showed no correlation with the BET surface area and pore volume of a material. When examined in more detail however, it was found that chemisorption was positively associated with the available narrow micropore and micropores of a material.

The total hydrogen chemisorption volumes were weakly correlated to the pore volumes and surface areas of the different pore regimes between pressures of 0.5 – 3.0 kPa. It was found that total hydrogen adsorption correlated with narrow micropore volume with an average R value of 0.72, while showing no correlation with the micropore and mesopore regimes. The same positive correlation with narrow micropore volume was found for both strong and weak interactions with average R-values around 0.72 – 0.73. Stronger and more representative correlations were found between narrow micropore/micropore volume fractions and adsorbed hydrogen in the weak and strong isotherms. The pore volume fractions are significant (as opposed to just absolute pore volumes), as they can be direct manifestations of the activation processes that are involved in producing the ACs [122]. The weak adsorption correlated well with the narrow micropore and micropore volume fractions with R-values of 0.92 and 0.93 respectively and p-values of 0.0005 and 0.0003 respectively. The strong adsorption correlations with the narrow micropore and micropore volume fractions were slightly worse with R-values of 0.76 and 0.85 respectively and p-values of 0.0174 and 0.0038 respectively. Finally, the weak adsorption fraction was correlated to the micropore volume fractions. It was found generally (R ~0.8), that materials, which contained a higher fraction of micropores and narrow micropores also exhibited larger relative volumes of weak adsorption. Thus, it was proposed that a significant proportion of weak adsorption occurs physically in the narrow micropores of carbon materials.

Chapter 6.

Discussion

This chapter discusses and expands on the results found in Chapter 3 and Chapter 5. Thermodynamic models were applied to the chemisorption isotherms measured in Chapter 5, system-level simulations with high hydrogen-solubility materials are presented, and the feasibility of these materials are discussed.

6.1. Application of Kinetic Models to Chemisorption Data

In Chapter 5, it was shown that that the strong and weak hydrogen interaction on carbon surfaces could be decoupled. For most activated carbons, the total amount of weak chemisorption accounted for 20 – 40 % of the total uptake with the remainder made up by strong adsorption. In literature, many different kinetic and thermodynamic models have been used to interpret and analyze adsorption data which has been reviewed extensively [123][77]. This thesis will focus on models that have been most widely applied for chemisorption processes in porous media [77]. These are the models derived from the theories of Langmuir, Temkin and Freundlich [124][125].

6.1.1. Langmuir, Temkin and Freundlich Methods

Langmuir Theory

Langmuir theory uses kinetic models to derive equilibrium behavior and is limited to monolayer adsorption. Since chemisorption occurs on specific sites of the adsorbent surface, monolayer adsorption is generally held to be a reasonable assumption for chemisorption. Since dynamic equilibrium is achieved when the adsorption and desorption rates are balanced, the isotherm can be found from the kinetic representation:

$$k_a P(1-\theta)^n = k_d \theta^n \tag{6.1}$$

Where θ is the volume adsorbed (V) divided to the total monolayer volume (V_m), k_a and k_d are the adsorption and desorption constants respectively, P is the pressure and n is the order of the reaction. Therefore, the left and right hand sides of this equation represent the adsorption and desorption rates respectively. Re-arranging the Equation (6.1) and substituting for the Langmuir constant $K = k_a/k_d$, the adsorption isotherm is simply:

$$V = V_m * \left[\frac{(K_L P)^{\frac{1}{n}}}{1 + (K_L P)^{\frac{1}{n}}}\right] \tag{6.2}$$

Which is known as the generalized Langmuir equation. Here the reaction coefficient K is a constant that does not depend on adsorbate loading. Thus, the assumption is made that the adsorption sites are equivalent (constant energy), and adsorbate molecules do not interact with each other on the adsorbent surface. This assumption is generally valid at low concentrations and the equation can be represented in the linearized form:

$$\frac{1}{V} = \frac{1}{V_m} + \frac{1}{V_m (KP)^{(1/n)}} \tag{6.3}$$

The order n represents the reaction type. For hydrogen dissociation, the elementary reaction would have an order $n = 2$, which gives the relationship previously found for tritium adsorption on graphite surfaces by Atsumi in Equation (2.22). Therefore, a regression on the plot of 1/V versus $P^{1/n}$ can be used to find the constants V_m and K_L at a particular 1/n value. Since the overall order (n) of the reaction is not known from other sources, it can be calculated such that the error distribution is minimized.

Temkin Method

The Temkin and Freundlich methods differ from Langmuir's equation in the treatment of the adsorption energy (ΔH_{ads}), that is found in the reaction coefficient K, which takes the general Arrhenius dependency:

$$K = K_0 \exp\left(\frac{\Delta H_{ads}}{RT}\right) \tag{6.4}$$

Instead of using a constant heat of adsorption ΔH_{ads}, Temkin derives the isotherm assuming that the heat of adsorption decreases linearly as adsorbate covers the surface where the heat of adsorption can be written in terms of the surface coverage θ as: $\Delta H_{ads} = \Delta H^{o}_{ads}(1 - \lambda\theta)$, where ΔH^{o}_{ads} is the initial heat of adsorption, and λ is the Temkin fitting parameter. In setting a linearly decreasing dependence on the heat of adsorption, the method states that the rate of adsorption slows down as the surface becomes occupied with adsorbate. This is a result of inter-adsorbate repulsion, or change to the surface as bonds are formed between the surface and gas molecules. Since the relationship is linear, Temkin effectively neglects the extremes of low and high concentrations where the forces of interactions between adsorbed molecules would change the most with incremental adsorption. By substitution of the reaction coefficient K into (6.1), the simplified linear from of the Temkin equation is shown in (6.5).

$$\mathrm{V} = \mathrm{V_m}\frac{\mathrm{RT}}{\Delta \mathrm{H^o_{ads}}\lambda}\ln \mathrm{P} + \mathrm{V_m}\left(\frac{\mathrm{RT}}{\Delta \mathrm{H^o_{ads}}\lambda}\ln \mathrm{K_0} + \frac{1}{\lambda}\right) \tag{6.5}$$

Thus, the isotherm at a particular temperature can be determined by using a plot of V versus ln P and defining the regression constants $\mathrm{A} = \mathrm{V_m}\frac{\mathrm{RT}}{\Delta \mathrm{H^o_{ads}}\lambda}$ and $\mathrm{B} = \mathrm{V_m}\left(\frac{\mathrm{RT}}{\Delta \mathrm{H^o_{ads}}\lambda}\ln \mathrm{K_0} + \frac{1}{\lambda}\right)$. If the isotherm is determined at two or more temperatures, the $\mathrm{V_m}$ can be determined at the maximum extrapolated point where the isotherm intersects, and the heat of adsorption and reaction coefficient $\mathrm{K_0}$ can be readily solved.

Freundlich Method

Similar, to the Temkin method, the Freundlich method uses a heat of adsorption that is dependent on the surface coverage, but uses a logarithmic decrease with respect to coverage where the heat of adsorption is captured by $\Delta \mathrm{H_{ads}} = -\Delta \mathrm{H_m} \ln \theta$, where $\Delta \mathrm{H_m}$ is a constant. Hence, the isotherm represents adsorption on a heterogeneous surface where the adsorption occurs on the high energy sites first, with the energy exponentially decreasing. Again, by re-writing the equilibrium relation with this energy dependence, the Freundlich isotherm can be expressed as follows:

$$\ln \mathrm{V} = \frac{\mathrm{RT}}{\Delta \mathrm{H_m}}\ln \mathrm{P} + \mathrm{V_m}\frac{\mathrm{RT}}{\Delta \mathrm{H_m}}\ln \mathrm{K_0} \tag{6.6}$$

By plotting $\ln \mathrm{V}$ versus ln P, the linear regression constants $\mathrm{C} = \mathrm{RT}/\Delta \mathrm{H_m}$, and $\mathrm{D} = \mathrm{V_m RT}/\Delta \mathrm{H_m}$ can be determined. As with the Temkin method, the $\mathrm{V_m}$ can be found at the intersection of isotherms found at different temperatures, which then allows the solution of $\Delta \mathrm{H_m}$ and $\mathrm{K_0}$. The nonlinear form of the equation (6.6) is simply $\mathrm{V} = \mathrm{K_F P^C}$, where $\mathrm{K_F} = \mathrm{e^D}$ is the freundlich constant. The regression coefficient C can therefore be interpreted as an indicator of the adsorption intensity and for chemisorption typically takes a value between 0 and 1. Unlike Langmuir's equation, Freundlich's isotherm does not saturate at high pressure when one expects all adsorption sites to be occupied [123]. Thus, the Freundlich method, although widely applied, is generally considered to be an empirical relationship for heterogeneous surfaces.

6.1.2. Combined Adsorption Isotherm Modeling

While well-motivated models should fit experimental data, the selection and screening of these models is best informed by a combination of theory, experiments and simulation, which elicit the fundamental processes that dominate the solid-adsorbate interaction. In cases where this information is not known, the models can be selected based on the minimization of a selected error functions. In literature, linearized functions are most commonly used. It is important to note during the analysis however, that linearization methods can fundamentally change the error structure and bias the data [123]. Further, many different error functions (average relative error, Mardquardt's standard deviation, Spearman's correlation, etc.) exist and the choice of this function can also have a non-trivial influence the model selection process [126][127]. For linear models, the most common measure of fit is the coefficient of determination R^2, which will be employed here. The three models discussed in the previous section were examined with the results summarized in Table 6.1.

Table 6.1: Langmuir, Freundlich and Temkin model summary of combined isotherm

Material	Langmuir*				Temkin*			Freundlich*		
	R^2	K_L	V_m	n	R^2	A	B	R^2	C	K_F
OVC 4x8	0.99	2.45	5.62	1.76	0.98	0.73	3.48	0.98	0.21	3.42
NV 612	0.98	3.88	4.11	1.66	0.97	0.50	2.81	0.96	0.18	2.77
CTR 12x40	0.98	5.93	2.94	1.10	0.96	0.37	2.38	0.93	0.16	2.36
OLC 12x40	0.99	2.15	5.01	1.72	0.99	0.66	3.02	0.97	0.22	2.96
PAC 200	0.97	2.94	3.34	1.00	0.93	0.53	2.41	0.87	0.23	2.34
MSC 30	0.69	10.12	1.36	1.00	0.19	0.05	1.23	0.21	0.05	1.22
NRB 40M	0.98	5.16	4.61	1.52	0.97	0.54	3.38	0.95	0.16	3.34
Graph-OX	0.97	8.55	0.60	1.00	0.79	0.05	0.53	0.75	0.09	0.52

*Volume is in units of cm^3 STP/g, pressure in units of kPa, and regression coefficients defined in 6.1.1

Langmuir Method

Based on the coefficient of determination, the Langmuir equation was the most applicable to the majority of the carbon materials. The n coefficient representing the overall stoichiometry was optimized between a value of 1 to 2 to maximize the R^2. In theory, the value of $n = 1$ represents molecular chemisorption on the surface while a value of 2 represents dissociative chemisorption. As shown in the Table 6.1, the optimized value of n was usually somewhere in between 1 and 2, which suggests that the combined chemisorption curve is comprised of a combination of molecular and dissociative adsorption. The Langmuir models for GACs are shown in Figure 6.1, for PACs are shown in Figure 6.2 and for EACs and GNPs are shown in Figure 6.3.

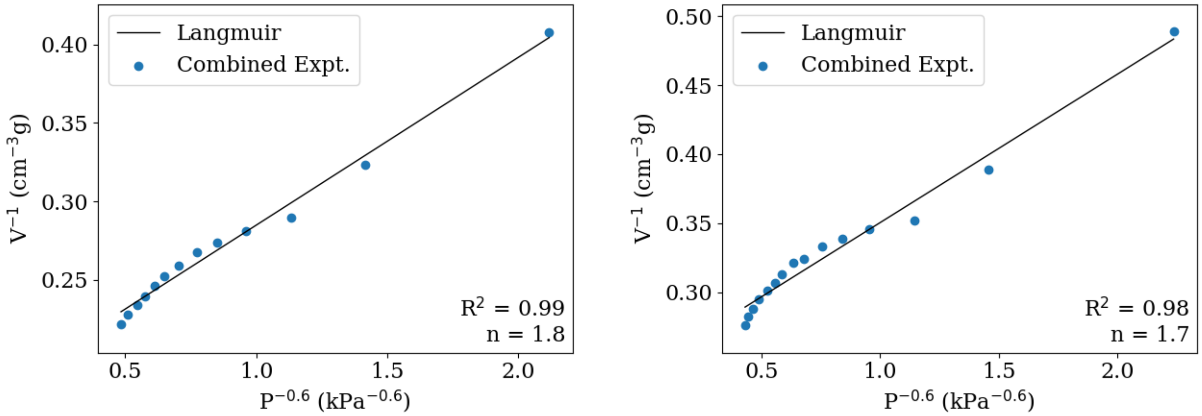

a) OVC 4x8 **b) NV 612**

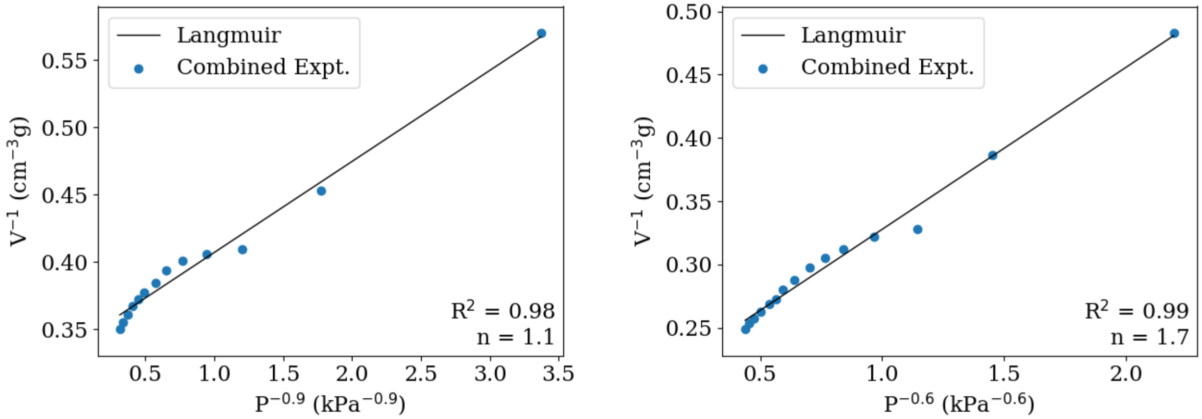

c) CTR 12x40 **d) OLC 12x40**

Figure 6.1: Langmuir method for granular activated carbons

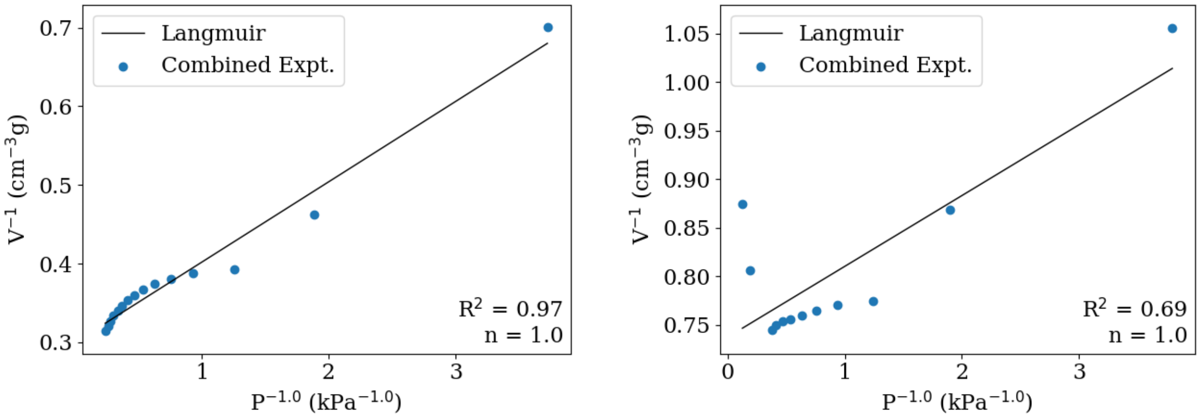

a) PAC 200 **b) MSC 30**

Figure 6.2: Langmuir method for powdered activated carbon

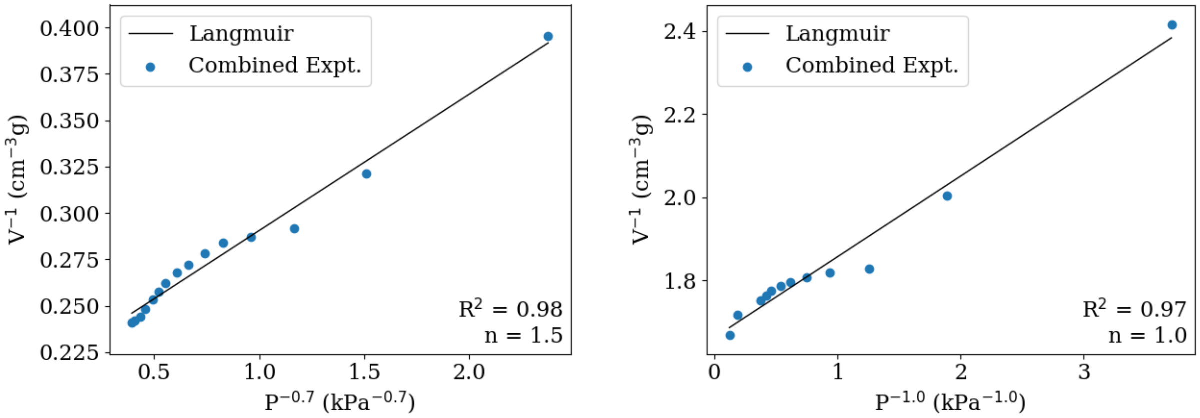

a) NRB 40M **b) Graphenit-OX**

Figure 6.3: Langmuir method for extruded activated carbon and graphene nanoplatelets

All the GACs showed a relatively good fit qualitatively and have R^2 values of 0.98 or 0.99 and n between 1.1 and 1.76. For the powdered activated carbons, the model showed larger deviations from the data for PAC 200 and did not fit well for MSC 30. The PAC errors were minimized with n = 1.0. The EAC shows a similar fit to the GACs again with an R^2 of 0.98 and an n value of 1.5, while the graphene had an R^2 of 0.7 and n = 1.0. While the Langmuir model significantly minimized the fitting residuals, there was a tendency of the data to cluster towards one extreme of the x-axis, due to the linearization method that is employed. The clustering was particularly noticeable for low values of n, resulting in an artificially low residual error. Thus, a biased mathematical minimization of n occurred when maximizing R^2, such that, in some cases, the model no longer represented its physical basis. For example, in graphene nanoplatelets, the optimized n value was found to be at 1.0, which implies pure molecular adsorption. However, there is sufficient literature data that informs us that dissociation of hydrogen on graphene should be a significant factor in the total adsorption [109][108]. Thus, care should be taken in drawing phenomenological conclusions from adsorption modeling alone, and the conclusions must be verified with other methods.

Temkin Method

The Temkin models for granular activated carbons are shown in Figure 6.4, for powdered activated in Figure 6.5 and for EAC and GNP in Figure 6.6.

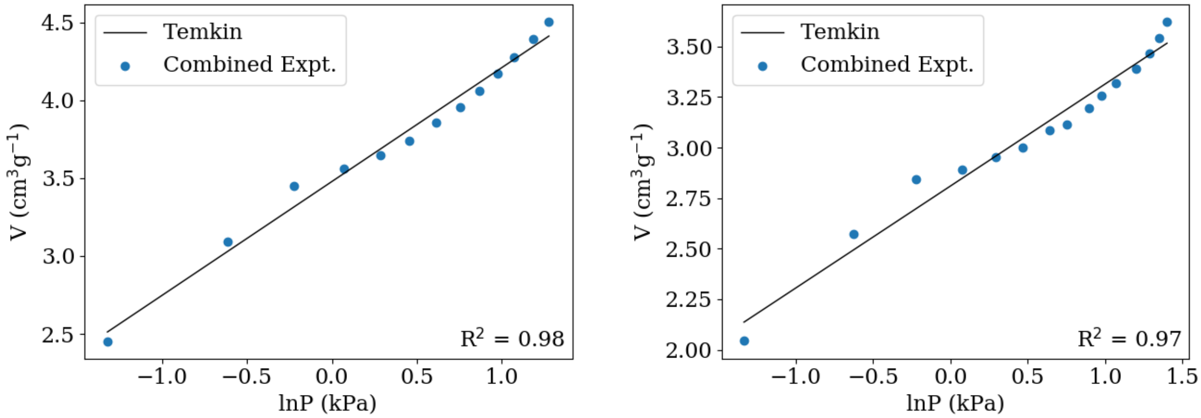

a) OVC 4x8 **b) NV 612**

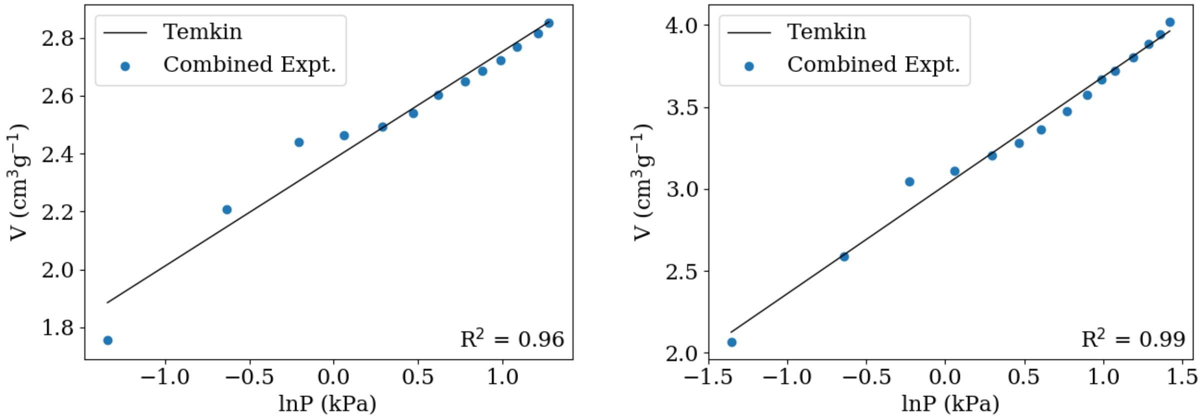

c) CTR 12x40 **d) OLC 12x40**

Figure 6.4: Temkin method for granular activated carbon

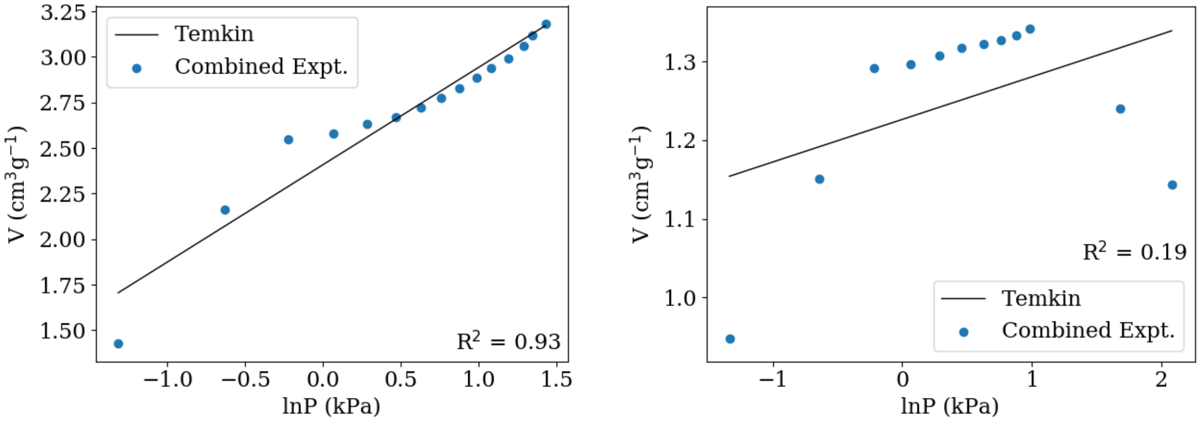

a) PAC 200 **b) MSC 30**

Figure 6.5: Temkin method for powdered activated carbon

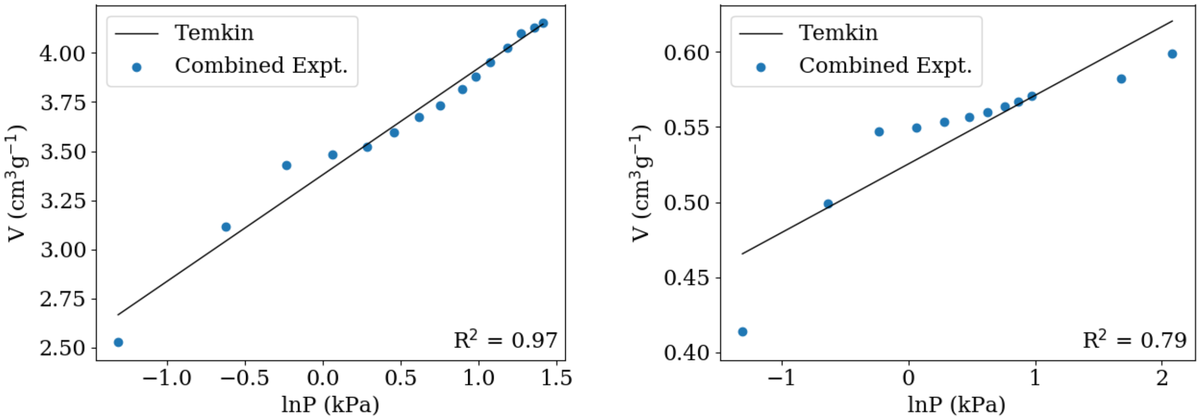

a) NRB 40M **b) Graphenit-OX**

Figure 6.6: Temkin method for extruded carbon and graphene nanoplatelets

The Temkin model was able to represent the experimental data for most materials with R^2 values between 0.97 and 0.99. For powdered activated carbons however, the fit was significantly worse than the Langmuir with R^2 values of 0.93 and 0.19 for PAC 200 and MSC 30 respectively. As for the EAC, the fit was similar to that of the GACs, while the Temkin model for GNP was shown to be significantly worse than the Langmuir model. In Figure 6.6b), the GNP data substantially deviated from the model for ln P between 0 and 1. Further, the R^2 value was only 0.79 for the Temkin model, compared to the R^2 of 0.97 for Langmuir's model.

Freundlich Method

The Freundlich model applied to the experimental data of granular activated carbon is shown in Figure 6.7. PAC isotherms are shown in Figure 6.8. EAC and GNP are shown in Figure 6.9. Similar to both the Langmuir and Temkin models, the granular activated carbons were modeled fairly well where the R^2 ranging between 0.96 and 0.99. Qualitatively, the data showed reasonable agreement with the model over the range of the experimental conditions.

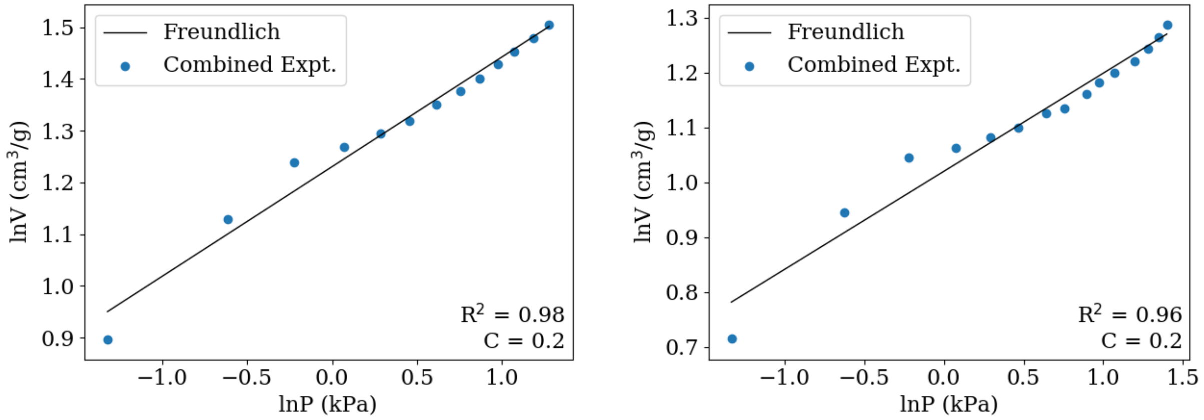

a) OVC 4x8 **b) NV 612**

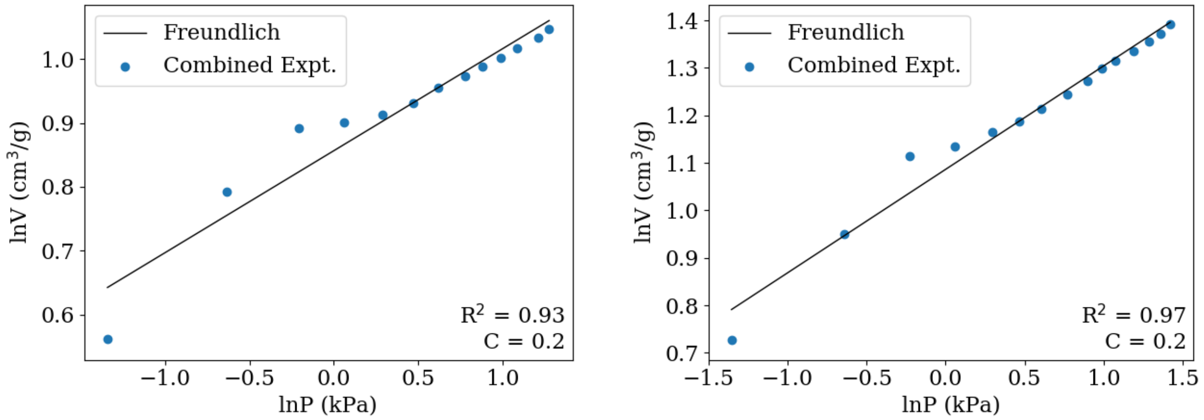

c) CTR 12x40 **d) OLC 12x40**

Figure 6.7: Freundlich method for granular activated carbon

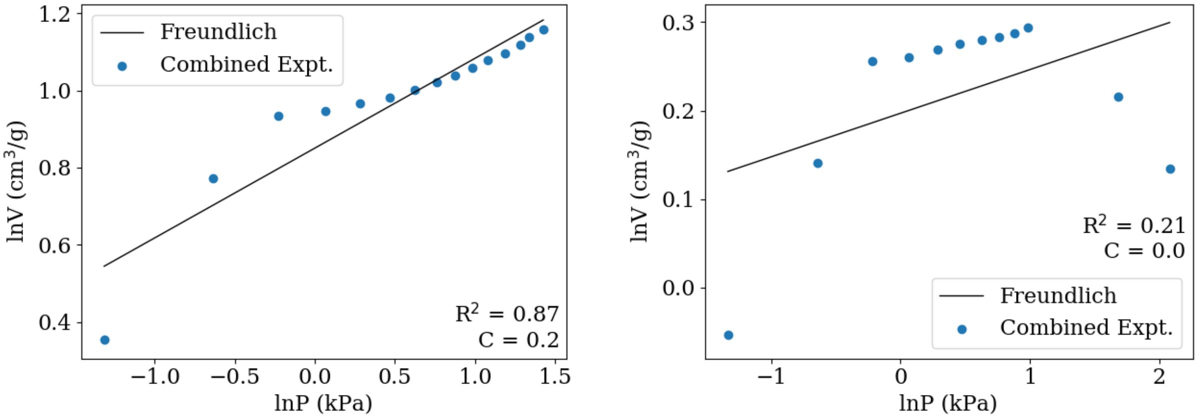

a) PAC 200 **b) MSC 30**

Figure 6.8: Freundlich method for powdered activated carbon

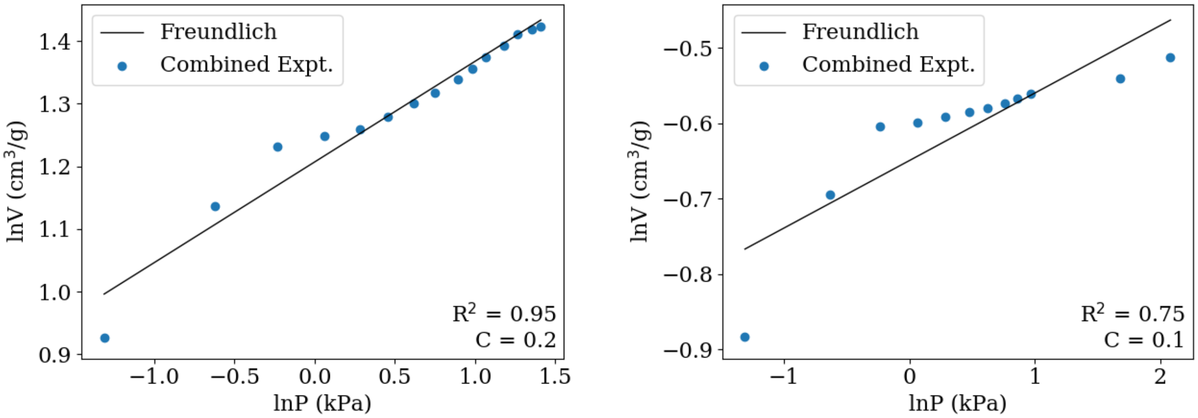

a) NRB 40M **b) Graphenit-OX**

Figure 6.9: Freundlich method for extruded carbon and graphene nanoplatelets

In comparison to the $1/P^{\frac{1}{n}}$ Langmuir plot, the Freundlich models showed a more gradual distribution of data points over the experimental range, which suggests that the error function R^2 value is a better measure of the model's applicability. In most cases, the C parameter representing adsorption intensity was 0.2, which is typical for chemisorption. With respect to powdered activated carbons, PAC 200 and MSC-30 showed the worst fit between the 3 models with an R^2 = 0.87 and 0.21 respectively. For extruded carbon NRB 40M, the fit was again similar to the granular activated carbons at R^2 = 0.95. Graphenit-OX again failed to be well-fitted to the Freundlich model with R^2 = 0.75. Significant divergence between the experimental data and the model was shown for Graphenit-OX in Figure 6.9b).

Method Summary for Combined Isotherms

For all three models, the granular activated carbons and extruded carbons were well-modeled with relatively low error. For powdered carbons, PAC 200 was best modeled with the Langmuir method, while all three models failed to provide a good fit for MSC 30 and Graphenit-OX. With the powdered activated carbon and graphene nanoplatelets, it is believed that isotherm data is affected by the reaction of hydrogen with the material itself. This was suggested last chapter due to the apparent decrease in the isotherm at higher pressures. Extending the pressure range in Figure 5.22, this decrease is shown more clearly in the Figure 6.10 below.

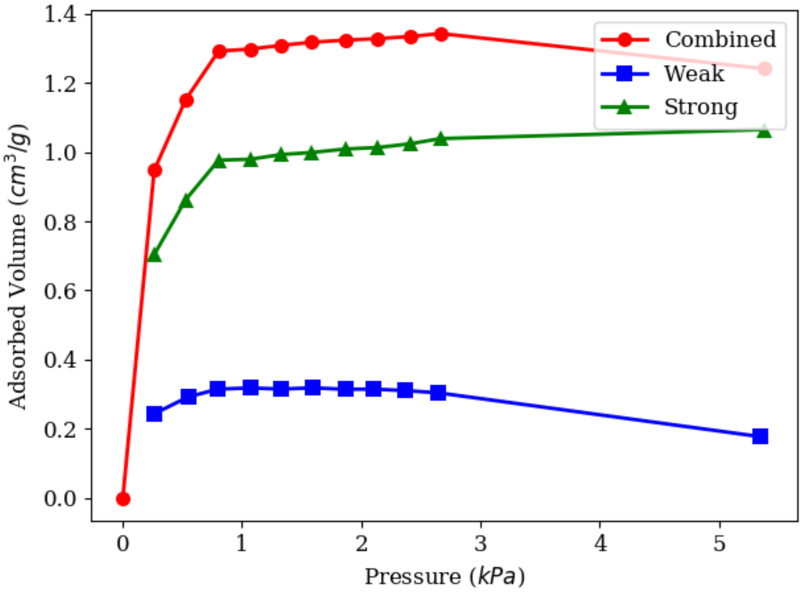

Figure 6.10: Combined, strong and weak chemisorption isotherm for MSC-30

The graphene material used is a chemically modified graphene, which contains ~5% oxygen. Thus, a reaction with oxygen functionals on the surface can cause production of gaseous products or cause the hydrogen to adsorb through multiple complex reaction pathways, which cause the isotherm behavior to deviate from the models [128].

In heterogeneous catalysis, it can often be useful to isolate the types of reactions that are occurring on a surface. For example, in metal catalysts on inert supports such as ceramic oxides, zeolites or graphite, the majority of dissociated hydrogen will exist and be strongly bonded to the metal, while hydrogen in the molecular form will diffuse into the inert material [53]. In order to isolate the catalyzed hydrogen, the strong isotherm can be analyzed independently. In the case of graphite and activated carbon, it is known that the adsorption of hydrogen can occur on a variety of dissimilar sites including molecular encapsulation in closed pores, trapping at gain edges, or trapping in between basal planes as discussed in Chapter 2.5.2. Thus, these interactions may be better modeled by the separated isotherms. The sections below show the models for the weak and strong isotherms, which yield the lowest R^2 values. These decoupled models were compared the modeling of the combined isotherm.

6.1.3. Strong Adsorption Isotherm Modeling

The strong adsorption isotherm was modeled with the generalized Langmuir, Temkin and Freundlich methods. In all cases, the model which minimized the error and maximized the correlation coefficient was Langmuir's model with the results summarized in Table 6.2.

Table 6.2: Best fit models for strong adsorption isotherm for various carbon materials

Generalized Langmuir Method*				
Material	K	V_m	n	R^2
NV 612	7.31	2.71	1.00	0.96
OVC 4x8	7.03	2.71	1.00	0.97
CTR 12x40	10.31	2.21	1.00	0.95
OLC 12x40	5.66	2.61	1.00	0.98
PAC 200	3.52	2.41	1.00	0.90
MSC 30	6.84	1.10	1.00	0.98
NRB 40M	8.79	3.10	1.00	0.96
Graphenit-OX	9.60	0.56	1.00	0.95

*Volume is in units of cm^3/g, pressure in units of kPa, and regression coefficients defined in 6.1.1

In all cases, the models were fairly well represented with R^2 between 0.90 and 0.98. In comparison with the combined method, the model was improved most for MSC-30, where the best fit for the combined isotherm still had a low $R^2 = 0.69$. Interestingly, the error distribution in all cases, was minimized for a reaction order of $n = 1.0$, which would be normally be indicative of molecular adsorption. However, it is known that dissociative adsorption typically creates a stronger bond with the carbon surface. Thus, the minimization of error at $n = 1.0$ is believed to be a model limitation or mathematical artifact. The model fitting is shown in Figure 6.11 to Figure 6.13. While the errors of the models were relatively low, each of these figures shows an inflection at close 1.3

kPa, which is not captured by the theoretical basis of the Langmuir model. A series of desorption experiments by Atsumi et. al previously suggested as many as 4 - 5 different adsorption modes, all of which had varying reaction orders and energies [30][129]. If these modes exist, the Langmuir assumption of monolayer and constant energy adsorption would not be valid. Atsumi identified that the strongest adsorption site was on intercalate cluster loops, which had zero order dependence on pressure. Thus, it is possible that the presence of these sites contributing to the strong curve suppressed the n value to 1. In such cases, more complex models have been used such as a dual site Langmuir model, which involves the regression of the linear combination of site models which can contribute to the overall adsorption [130].

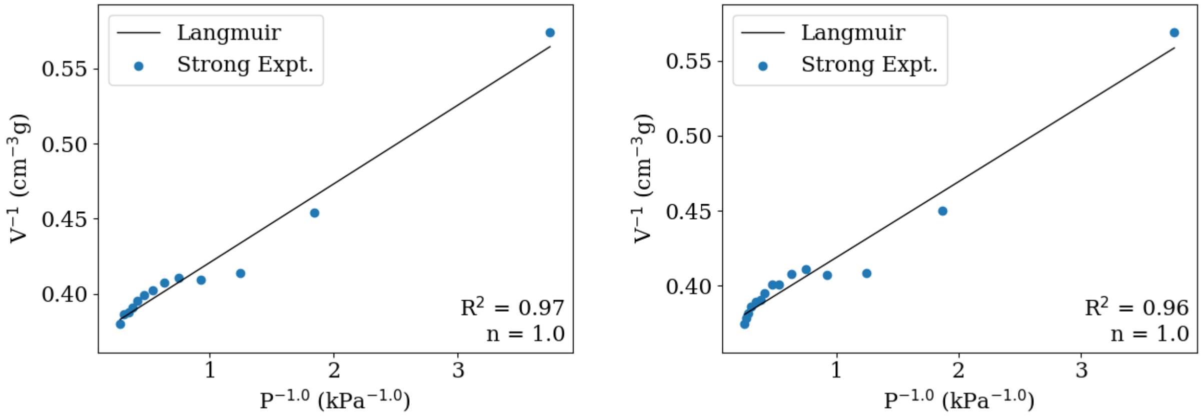

a) OVC 4x8 **b) NV 612**

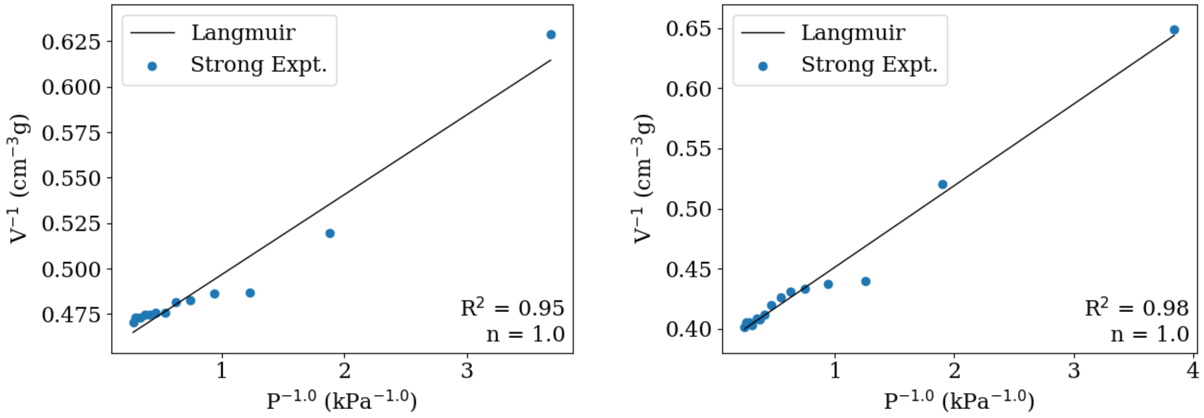

c) CTR 12x40 **d) OLC 12x40**

Figure 6.11: Method for strong adsorption with lowest error distribution for granular activated carbons

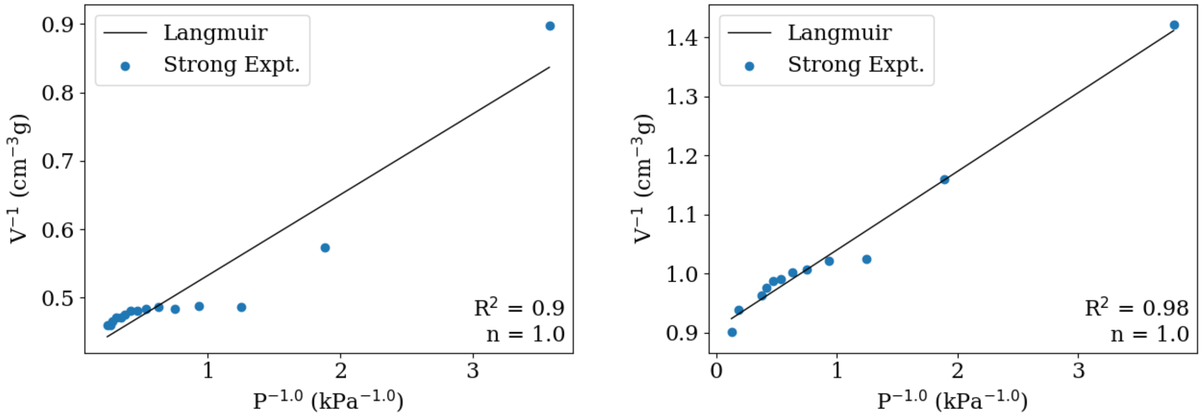

a) PAC 200 **b) MSC 30**

Figure 6.12: Method for strong adsorption with lowest error distribution for powdered activated carbons

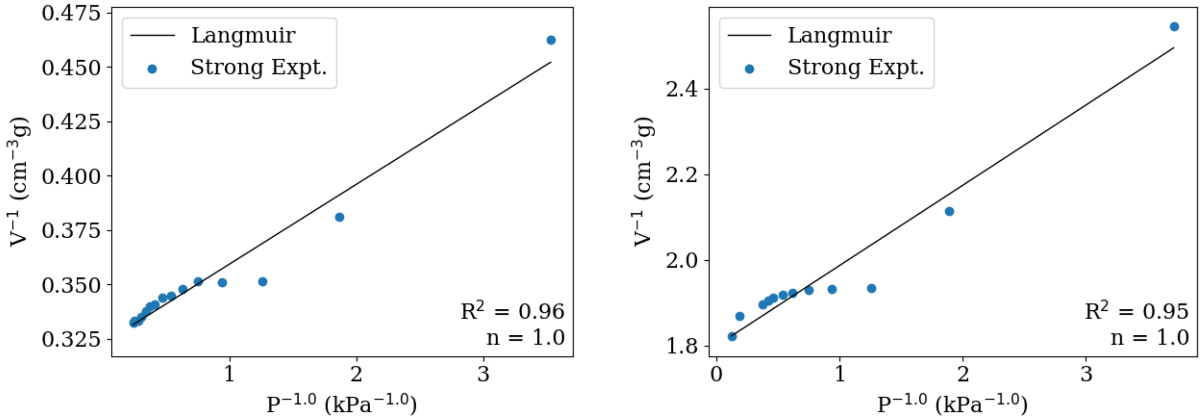

a) NRB 40M **b) Graphenit-OX**

Figure 6.13: Method for strong adsorption with lowest error distribution for extruded carbon and graphene nanoplatelets

Additionally, it can be seen in the figures that the minimization in the order n, resulted in the cluster of the high pressure data points towards the origin of the plot, which can artificially produce a lower error, using a model that does not physically represent the chemical processes involved in the adsorption of hydrogen. Since this effect is created by the linearization process, one possibility to eliminate this contribution would be to perform the regression on the non-linear forms of the isotherms as previously outlined [123].

6.1.4. Weak Adsorption Isotherm Modeling

For the weak isotherm, the generalized Langmuir, Temkin and Freundlich methods were employed again and the method chosen was based on the maximization of the coefficient of determination. These minimum-error models are shown in Table 6.3.

Table 6.3: Best fit models for weak adsorption isotherm for various carbon materials

Freundlich Method

Material	C	K_F	R^2
NV 612	0.43	0.46	0.97
OVC 4x8	0.37	1.12	0.99
OLC 12x40	0.37	0.84	0.99
PAC 200	0.39	0.53	0.99
MSC 30	-0.39	0.29	0.32
NRB 40M	0.40	0.63	0.99

Generalized Langmuir Method

Material	K	V_m	n	R^2
CTR 12 x40	0.64	0.98	1.18	0.99
Graphenit-OX	0.71	0.07	1.88	0.99

The majority of the weak isotherms were best modeled using the Freundlich method where the R^2 ranged from 0.97 to 0.99, excluding the powdered carbon MSC-30. In MSC-30, none of the models were applicable. Only the granular carbon CTR 12x40 and graphene nanoplatelets Graphenit-OX were modeled best with the generalized Langmuir equation. The plots of experimental data versus models are shown in Figure 6.14 to Figure 6.16.

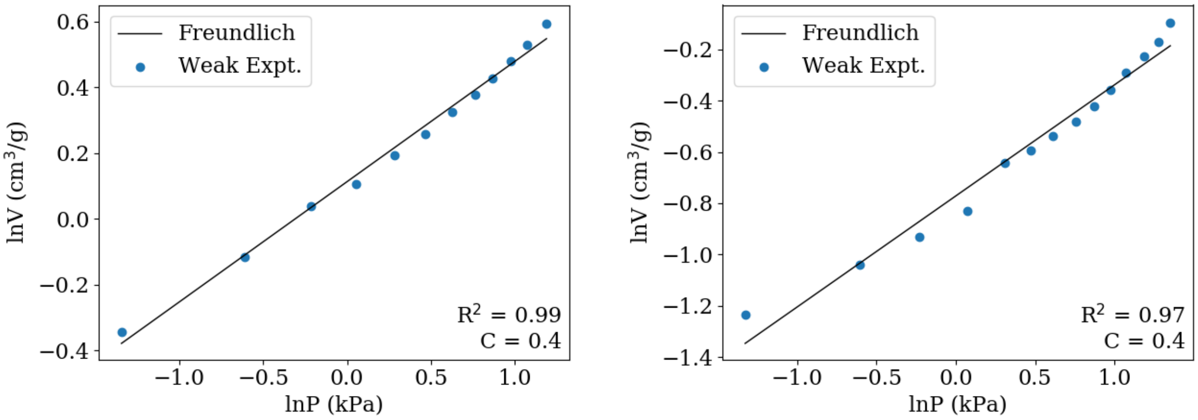

a) OVC 4x8 **b) NV 612**

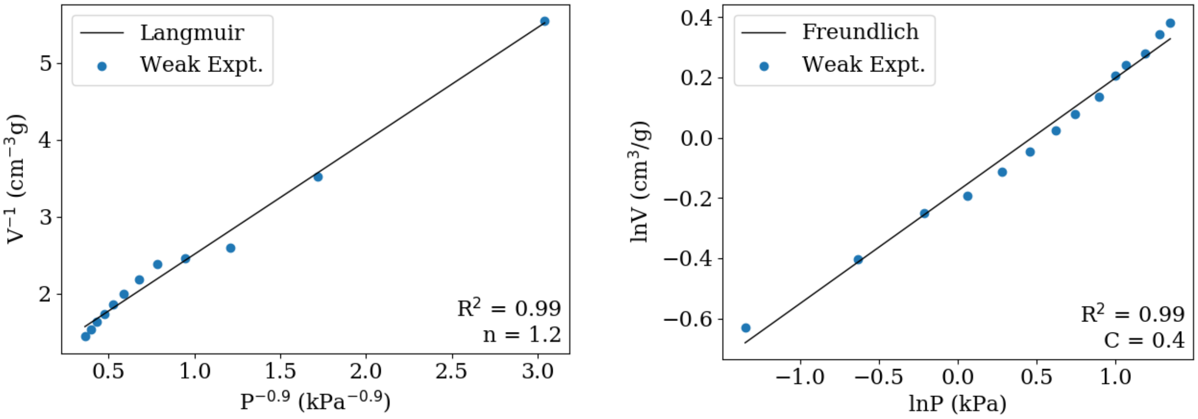

c) CTR 12x40 **d) OLC 12x40**

Figure 6.14: Method for weak adsorption with lowest error distribution for granular activated carbon

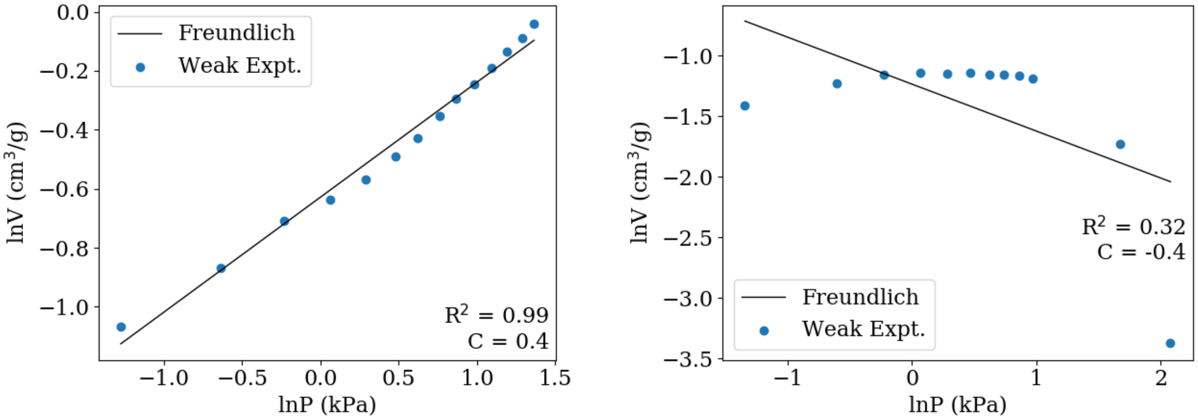

a) PAC 200 **b) MSC 30**

Figure 6.15: Method for weak adsorption with lowest error distribution for powdered activated carbon

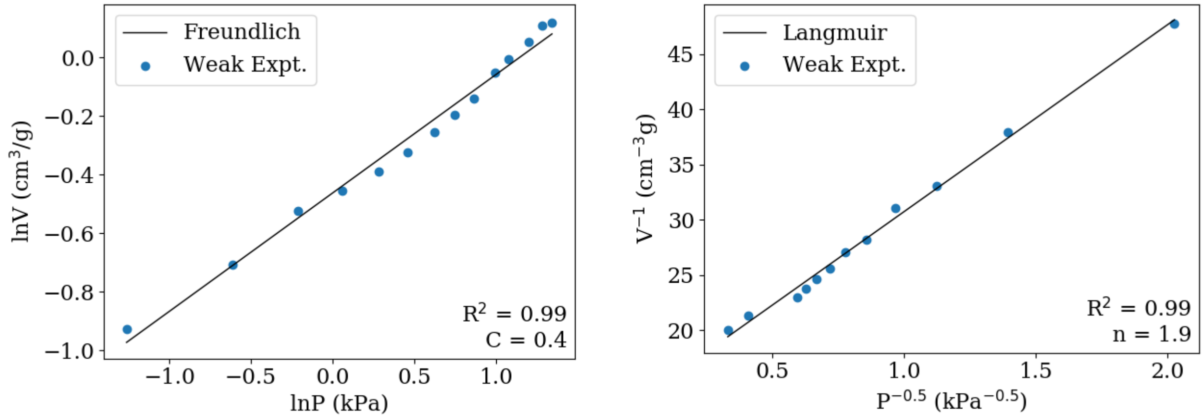

a) NRB 40M **b) Graphenit-OX**

Figure 6.16: Method for weak adsorption with lowest error distribution for extruded carbon and graphene nanoplatelets

The figures for weak isotherms show relatively good agreement with models for almost all materials with the exception of MSC-30. In all cases where Freundlich model was appropriate, the Freundlich coefficient C was 0.4, which is a typical value for chemisorption. Since the non-linear form the Freundlich equation is $V_{ads} = K_F P^C$, the low value of C indicates that adsorbate begins to approach saturation behavior relatively quickly. For Graphenit-OX and CTR 12x40 where the Langmuir model was used, the derived n was equal to 1.9 and 1.2 respectively. This suggests that for GNP, the weak adsorption was dominated by dissociative chemisorption (n close to 2), while in CAL TR 12x40, molecular adsorption played a more important role (n close to 1). For graphenit-OX, this would agree with most literature data, which has found that hydrogen can readily dissociate at active edge sites of graphene [107][109][131][132]. Further, Langmuir orders for these two materials suggest that adsorption on the weak curve encompasses to some degree both molecular and dissociative hydrogen adsorption.

6.1.5. Modeling the Total Solubility of Hydrogen in Carbon Materials

It was shown in the previous sections 6.1.2 to 6.1.4 that the solubility of hydrogen on carbon can be modeled as a combined, weak or strong isotherm. In previous tritium studies in graphite, only the combined total solubility was modeled using Langmuir's method for dissociative adsorption shown in Equation 2.22. While this method of modeling total solubility can produce relatively good agreement with experimental data, many fundamentally different adsorption processes are generalized and averaged within the model. By analyzing the strong and weak isotherms separately, complex effects, which give rise to the total solubility, could become de-convoluted and modeled independently, allowing better understanding of the processes. In this section, the modeling of combined isotherm is compared with separately modeling the weak and strong isotherms and joining them to yield the total solubility. For example, a strong curve modeled with Langmuir's method combined with Freundlich's weak isotherm is shown in Equation (6.7).

$$
\begin{gathered}
\mathrm{V_{ads}} = \mathrm{V_{weak}} + \mathrm{V_{strong}} \\
\mathrm{V_{ads}} = \mathrm{K_F P^C} + \mathrm{V_m} \frac{(\mathrm{K_L P})^{\frac{1}{n}}}{1 + (\mathrm{K_L P})^{\frac{1}{n}}}
\end{gathered}
\tag{6.7}
$$

This yields a non-linear relationship with pressure. In order to evaluate the predictive capability of an Equation (6.7) in comparison to the direct models of the combined isotherm, an objective function for error must be selected. Since $\mathrm{R^2}$ strictly applies only to linear functions, the standard error of regression was used, which is simply defined as follows:

$$
\mathrm{S_E} = \sqrt{\frac{\sum_{\mathrm{N}}\left(\mathrm{V_{meas}}(\mathrm{P_i}) - \mathrm{V_{model}}(\mathrm{P_i})\right)}{\mathrm{N}}}
\tag{6.8}
$$

Where N is the number of data points, $\mathrm{V_{meas}}(\mathrm{P_i})[\mathrm{cm^3 g^{-1}}]$ is the measured value of adsorption at the pressure$\mathrm{P_i}$ [kPa], and $\mathrm{V_{model}}(\mathrm{P_i})$ is the value predicted by the model. In the combined models of 6.1.2, all of the materials that exhibited the lowest error distribution and highest coefficient of determination were chosen. The standard error $\mathrm{S_E}$ of these models were then computed, and compared to standard errors of the model created by combining the weak and strong isotherms (chosen in 6.1.3 and 6.1.4). The results of this comparison are shown in Table 6.4.

Table 6.4: Comparison between modeling the combined adsorption and modeling the separated weak and strong interactions to predict total solubility

Material	Combined		Strong + Weak		Comparison[†]
	Model*	$\mathbf{S_E}$ $(\mathbf{cm^3 g^{-1}})$	**Model***	$\mathbf{S_E}$ $(\mathbf{cm^3 g^{-1}})$	$\%\boldsymbol{\Delta}\mathbf{S_E}$
NV 612	L	0.079	L + F	0.067	-15.22
OVC 4x8	L	0.079	L + F	0.062	-21.25
CTR 12x40	L	0.046	L + L	0.043	-5.08
OLC 12x40	L	0.068	L + F	0.058	-15.41
PAC 200	L	0.091	L + F	0.105	16.39
MSC 30	L	0.074	L + F	0.097	30.83

NRB 40M	L	0.072	L + F	0.056	-22.94
Graph-OX	L	0.009	L + L	0.010	13.18

† The relative change in standard error as a result of adopting the additive model for total solubility
* 'L' and 'F' designate the Langmuir and Freundlich Method respectively

As shown in the table, the modeling of the decoupled strong and weak interaction can actually lead to an overall reduction in error when estimating the total solubility. This is particularly true in carbons where the models showed good overall agreement with experimental data, including the GACs and EAC. For MSC-30, PAC 200 and Graphenit-OX however, the error increased by applying this method, in part due to the models being inapplicable to the adsorption process on these materials and in part due to experimental issues. MSC-30 had a best fit of $R^2 = 0.69$ at best when modeling the combined isotherm in 6.1.2, and the chemisorption isotherms of MSC-30 and Graphenit-OX previously suggested a gaseous reaction with hydrogen gas, interfering with the signal. Further, all the models applied to MSC 30, PAC 200 and Graphenit-OX, showed significantly worse fits compared to other carbon materials.

For the GACs and EAC, the average reduction in error was -15%, with the minimum as low as -23% in the case of NRB 40M. Overall, the data indicates that modeling of both the weak and strong isotherms can produce better predictability than with just the combined isotherm by the introduction of more fitting parameters even though these parameters were not adjusted simultaneously. Further, the separation of isotherms is a step in the deconvolution of the adsorption processes which occur in carbon materials. In addition to the calculations here, it should be noted that many other permutations of these methods are possible, such as the use of more complex models that explicitly account for the known adsorption processes or the simultaneous multi-parameter regression of the models chosen to represent the weak and strong interactions.

6.2. FHR Simulations with High-Performance Adsorbent

In Chapter 5, experimental data for hydrogen solubility at FHR conditions was taken for different carbon types. It was determined that at pressure under 5 kPa, the granular and extruded activated carbons had the highest solubility. In this section, the impact of using one of the high solubility materials on overall system tritium control performance was considered. Mainly, calculations similar to those in section 3.l were performed using TRIDENT with a new isotherm for a carbon with high-hydrogen solubility added to the code.

Various models were proposed for these carbons in Chapter 6.1. The carbon with the highest solubility overall was OVC 4x8, and two models were proposed for representing the combined isotherm. The first is the use of the generalized Langmuir isotherm, which is shown in (6.9).

$$V_{T_2,L}[\mathrm{cm}^3\mathrm{g}^{-1}] = 5.619\frac{(2.453P)^{1/1.7586}}{1+(2.453P)^{1/1.7586}} \pm 0.079 \tag{6.9}$$

The alternative model proposed was a Langmuir-Freundlich combined model in which the Langmuir method was used for the strong isotherm and the Freundlich model was used for the weak isotherm as shown in Equation (6.10):

$$V_{T_2,L-F}[\mathrm{cm}^3\mathrm{g}^{-1}] = 1.12\cdot P^{0.366} + 2.715\frac{7.032P}{1+7.032P} \pm 0.062 \tag{6.10}$$

The plots of these two models compared to the experimental data are shown in the Figure 6.17.

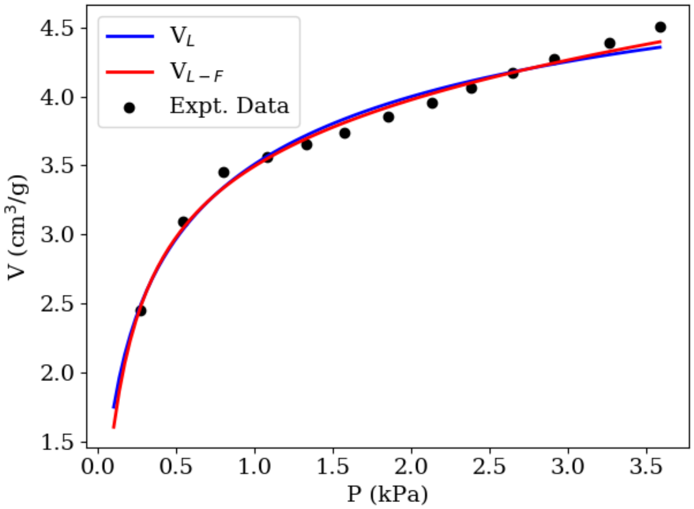

Figure 6.17: Langmuir and Langmuir-Freundlich combined models for the total solubility of H_2 in granular activated carbon OVC 4x8.

As shown in the previous section, both the models fit reasonably with relatively low standard errors. For the simulations in this section, the model of equation (6.9) was used to assess the effect of using a material with high solubility in the FHR. This simple model is selected since it provides nearly the same accuracy as the compound model and can be readily inverted for the computation of the boundary condition described in Chapter 3.1.2.

6.2.1. TRIDENT Simulation Input Parameters

For the main inputs of TRIDENT, the standard configuration for the FHR was used, which is shown in the Table 3.2. The simulation's optional inputs are shown in Table 6.5 where the total range of test conditions remained the same. The pellet density was changed from 1776 kg / m^3 to 450 kg / m^3 reflecting the change from ISO – 88 graphite to GAC CTR 12x40.

Table 6.5: TRIDENT required inputs for simulating optional adsorption column

Input Variables	**Value and Explanation**
`Tritiumproductionflag`	3 the tritium production rate varies with time according Eqn. (2.1)
`Tritiumcapturebedflag`	2 (on)
`Bed_frac_rep`	1/7, 1/13, 1/19, 1/25, 1/31
`Bed_vessel_radius`	1.5 (Inner radius of the packed bed [m])
`Bed_height`	4.5 (Height of the adsorbent zone in the bed [m])
`Particle_radius`	0.009, 0.013, 0.017, 0.021, 0.025 ([m])
`Particle_density`	0.45x10^6 (Density of graphite [g/m3])
`Bed_packingfraction`	0.60 (Packing fraction in the bed)

The geometry of pebbles was assumed to be spherical, as was the case for the previous simulations. In reality, the true geometry of granular activated carbon pellets may be inherently limited by the activation process, which dictates the material properties and sorption performance. If shape and size factor is found to be of critical importance, extruded activated carbons (i.e. NRB 40M) or carbon cloth should be considered since they are more geometrically controllable. As per the original simulations, the transfer of tritium to carbon was assumed to be limited by the interphase mass transfer film in the molten salt, which is in contact with the solid adsorbent surface. Since activated carbons have a much higher porosity and lower density, this approximation is theoretically more reasonable and should produce more conservative results than in ISO - 88.

6.2.2. Simulation Results from Sensitivity Analyses

Radius of Adsorbent Pebbles

With the same column dimensions used in Chapter 3.1.4 of R = 1.5 m and H = 4.5 m, the adsorbent particle was varied between 0.9 to 2.5 cm. The bed was regenerated continuously at an average rate such that the bed was completely replaced every 31 days. First, the release rates are shown in Figure 6.18.

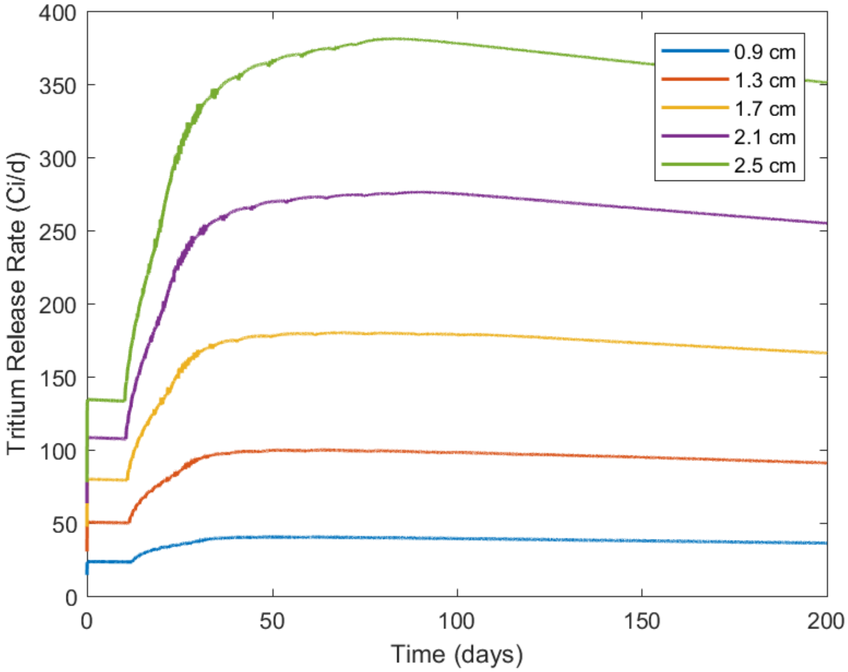

Figure 6.18: Tritium release rate (Ci/d) versus pebble radius in a 1.2 m R x 4.5 m H adsorption column with OVC 4x8 regenerated on average once every 31 days

At the maximum pebble size of 2.5 cm, the release rate peaked at near 400 Ci/day and was suppressed to 40 Ci/day when pebble size was reduced to 0.9 cm. During initial operation, tritium release rates were low until the core became saturated. The tritium release rose quickly due to the reaction with Li-6, after which stabilization occurred with Li-6 burnout at around 50 days. Figure 6.18 shows that as the pebble size decreased, the release rate decreased as expected due to increased hydrogen uptake accompanied by the increased surface area. In addition, as the radius was decreased, the difference between release rate curves also decreased, occurring despite the fact that the area of mass transfer scales with the inverse of radius (given the same tower dimensions and void fraction). At small pebble sizes, the incremental gain in further pebble size reduction decreased. This comes as a result of the surface area limitation of mass transfer becoming relaxed. Thus, even smaller adsorbent pebble sizes would have an increasingly small effect, with a sharply increasing pressure drop, increasing the capital and operating costs. The release rates ranged from 50 to 400 Ci/day over the 200 day simulation for OVC 4x8 for pebble sizes from 0.9 to 2.5 cm. In comparison, the same simulation conducted with ISO-88 in Figure 3.9 had release rates in the range of 180 – 600 Ci /day. Next, the tritium inventories in different parts of the system while varying the pebble size are shown in Figure 6.19 to Figure 6.22.

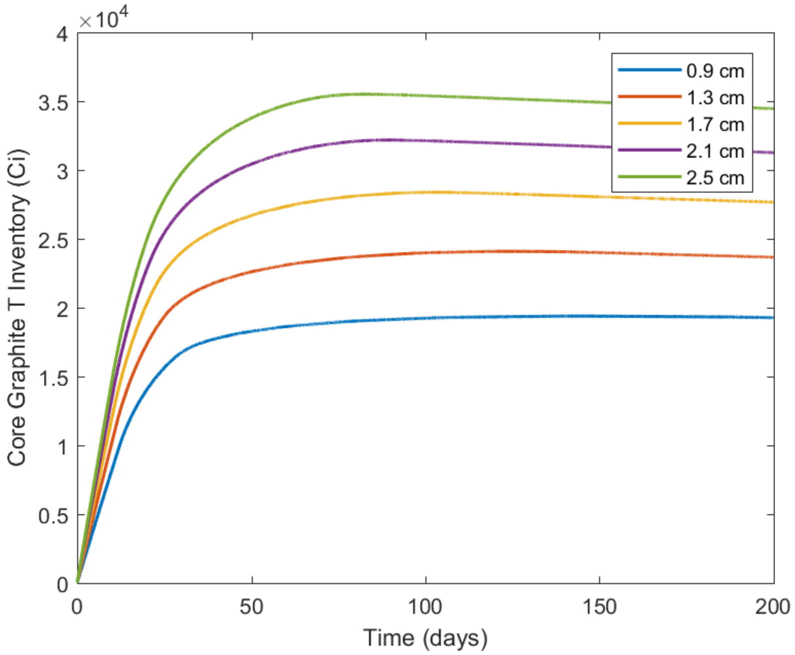

Figure 6.19: Tritium inventory in core graphite (Ci) versus pebble radius with 1.5 m R x 4.5 m H column, OVC 4x8 carbon, regenerated on average once every 31 days

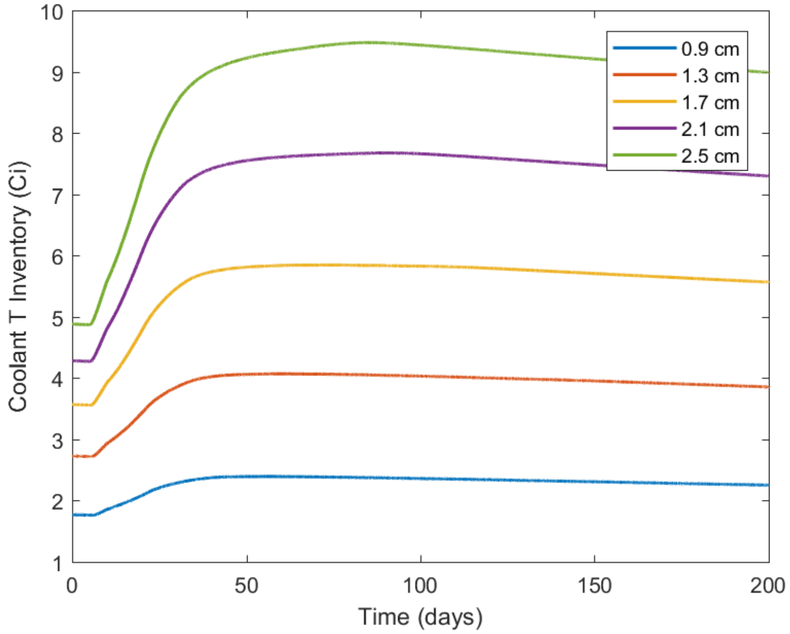

Figure 6.20: Tritium inventory in coolant versus pebble radius with 1.5 m R x 4.5 m H column, OVC 4x8 carbon, regenerated on average once every 31 days

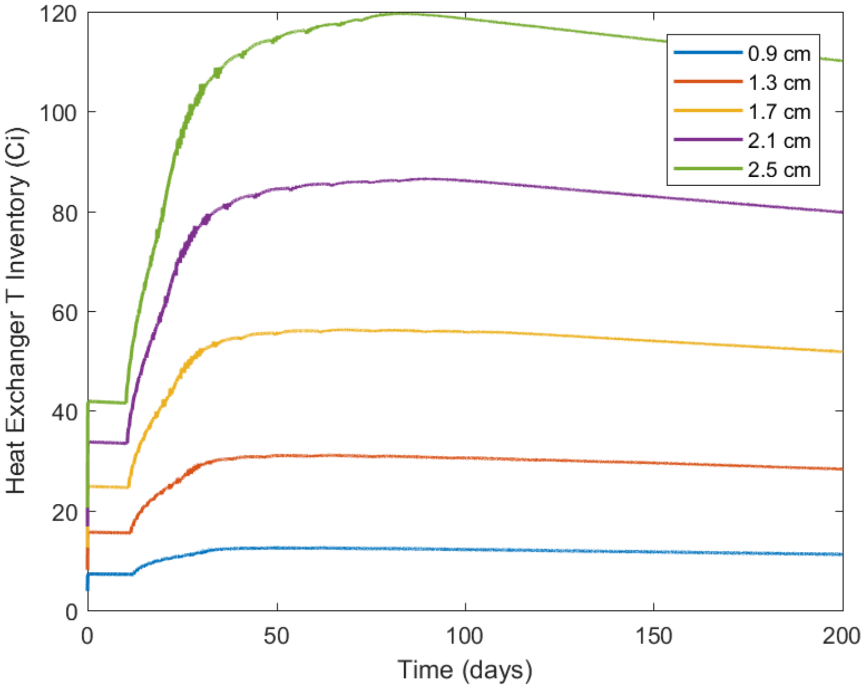

Figure 6.21: Tritium inventory (Ci) in heat exchanger tubing versus pebble radius with 1.5 m R x 4.5 m H column, OVC 4x8 carbon, regenerated on average once every 31 days

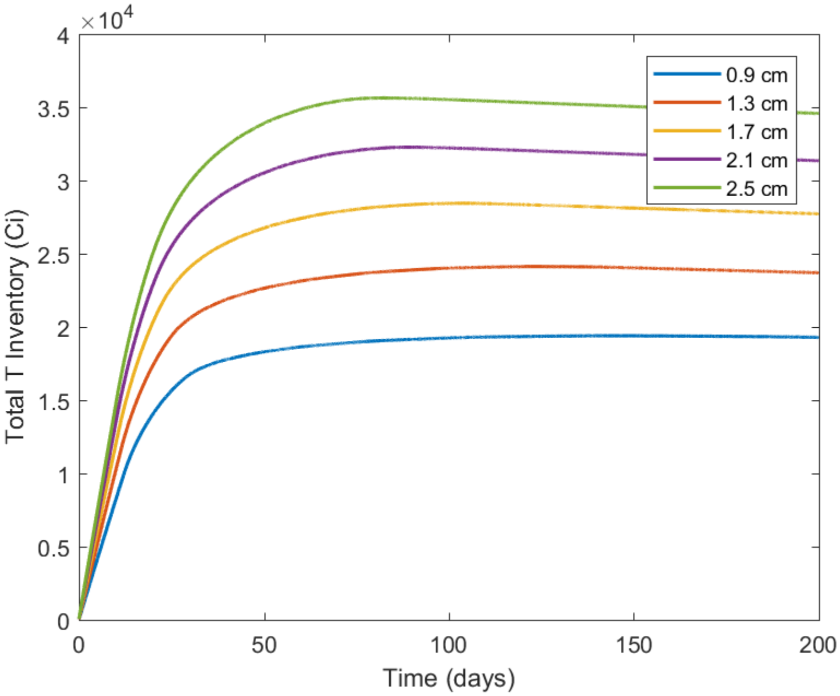

Figure 6.22: Total tritium inventory in primary loop (Ci) versus pebble radius regeneration rate with 1.5 m R x 4.5 m H column, OVC 4x8 carbon, regenerated on average once every 31 days

As expected, the tritium inventory in the core graphite, heat exchangers tubing and the flibe coolant decreased with decreasing pebble size. The graphite in the core has a much higher tritium solubility than both flibe coolant and the metal heat exchanger tubes and thus accounted for the majority of the total inventory. Decreasing the pebble radius from 2.5 cm to 0.9 cm, the core graphite inventory decreased from a maximum of 3.5 x 10^4 to 1.7 x 10^4 Ci, the coolant inventory decreased from 9.5 to 2.7 Ci and the heat exchanger tubing inventory decreased from 120 Ci to approximately 15. In all cases, the inventory in the system decreased significantly relative to the equivalent simulations run with IG-110U shown in Figure 3.15 to Figure 3.18. The minimum total coolant inventory calculated decreased by more than 30% when decreasing the pebble size from 2.5 cm to 0.9 cm, illustrating the potential impact of tuning this design parameter.

Regeneration Rates

It was found in Chapter 3 with adsorbent ISO-88 that decreasing the regeneration cycle (increasing the rate) had significant positive effects in decreasing the release rates, and tritium inventory in the coolant, core and heat exchangers. In contrast, it was found that with OVC 4x8, varying regeneration between 7 to 31 days, the release and inventories did not change significantly. For example, this is shown in Figure 6.23 for a pebble radius set to 2.5 cm, and the same bed size of 1.5 R x 4.5 H.

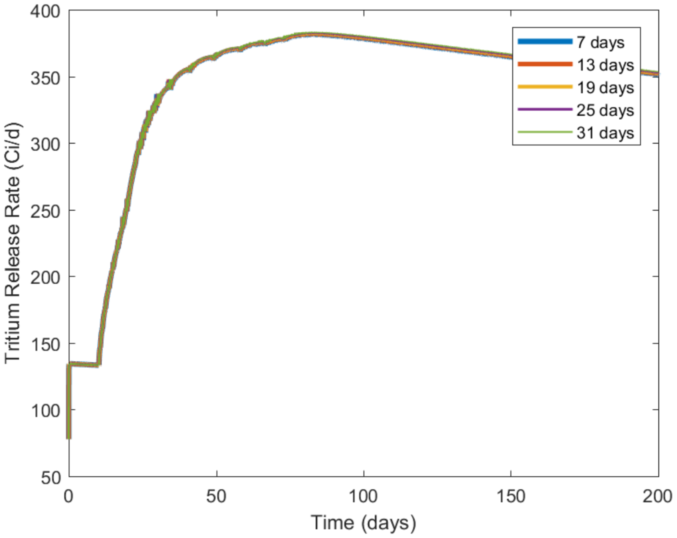

Figure 6.23: Tritium release for different regeneration cycles with 1.5 m R x 4.5 m H column, pebble radius of 2.5 cm and OVC 4x8 adsorbent

In all cases, the tritium release did not change and stayed at around 400 Ci/day given the column size and adsorbent diameter. This would imply that the mass transfer of tritium was not limited by the solubility of the material and increasing the regeneration rate to introduce fresh adsorbent provided a negligible benefit. The same was found for the system's tritium in inventories. In the subsection below, the sensitivity of pebble radius and regeneration rate is examined and directly compared between materials ISO-88 and OVC 4x8.

Sensitivity Analyses

In Figure 6.24 to Figure 6.27, the maximum release rate, core graphite tritium inventory, coolant tritium inventory and heat exchanger tritium inventory between ISO - 88 and OVC 4x8 are compared. The column size in both case was 1.5 m R x 4.5 m H. The regeneration cycle varied between 7 to 31 days and pebble radius varied between 0.9 and 2.5 cm. The minimum of release rates were found for the lowest pebble radius and shortest regeneration cycle, due to a maximization of the surface area and concentration gradient respectively. The minimum release rate achievable for IG-110U was close to 70 Ci/day at the pressure-limiting pebble size of 0.9 cm and practical regeneration cycle length of 7 days. In contrast, the same performance was achieved in OVC 4x8 at a pebble size of 1.2 cm (lowering pressure drop) and a much longer cycle past 30 days (reducing the operational demand, wear on adsorbent and operating cost). For OVC 4x8, the release rate reduced to lower than 40 Ci/day with the pebble size of 0.9 cm at any cycle length < 31 days.

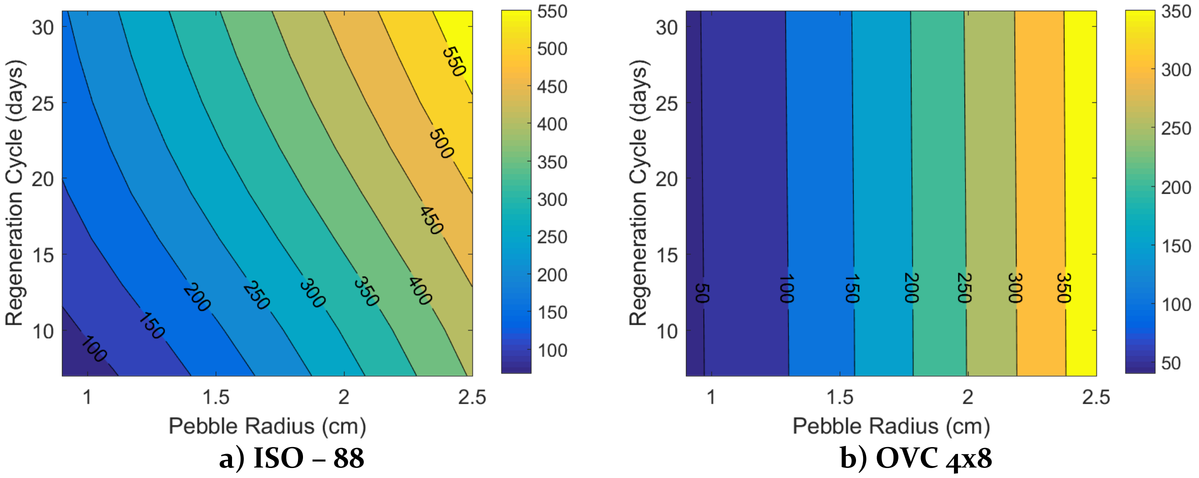

a) ISO – 88 **b) OVC 4x8**

Figure 6.24: Regeneration cycle and pebble radius versus release rates into power cycle for a) nuclear graphite ISO-88 [Same as Figure 3.19] and b) Granular Activated OVC 4x8.

As shown in Figure 6.25, core graphite was by far the largest sink of tritium in primary system (excluding the adsorption bed). The inventory trends were similar to those of the release rates, where the lowest inventory was achieved with the smallest pebble size and fastest regenerating rate. The inventory of graphite ranged from 2.2 to 4.0 x 10^4 Ci in ISO-88 and from 2.0 to 3.4 x 10^4 Ci in OVC 4x8. For a typical pebble radius of 1.5 cm and regeneration cycle of 14 days, the inventory was reduced from 30, 000 Ci to 26, 000, a 13% reduction by switching from ISO-88 to OVC 4x8 adsorbent. Although the inventories in graphite remained considerably high, a substantial amount of this inventory could potentially be retained on the core graphite in a transient depending on the maximum temperature and duration of the transient since tritium has a higher binding energy to graphite than other materials. Thus, Figure 6.26 and Figure 6.27 are shown for the coolant and heat exchanger tubing inventories.

The total inventory held in the coolant shown in Figure 6.26 was low since flibe has a relatively low tritium solubility that obeys Henry's law as discussed in Chapter 2.3. At the limiting conditions for ISO-88, the minimum inventory in coolant was just 4 Ci, but was less than 3 Ci for OVC 4x8. The inventory in HX tubing is shown in Figure 6.27. The stainless steel tubing of the HX adsorbs more tritium than the coolant with the minimum being close to 40 Ci when using adsorbent ISO-88 at best case scenario. By using OVC 4x8 and the pebble size of approximately 1 cm, this inventory reduced to less than 20 Ci while maintaining a flexible cycle length.

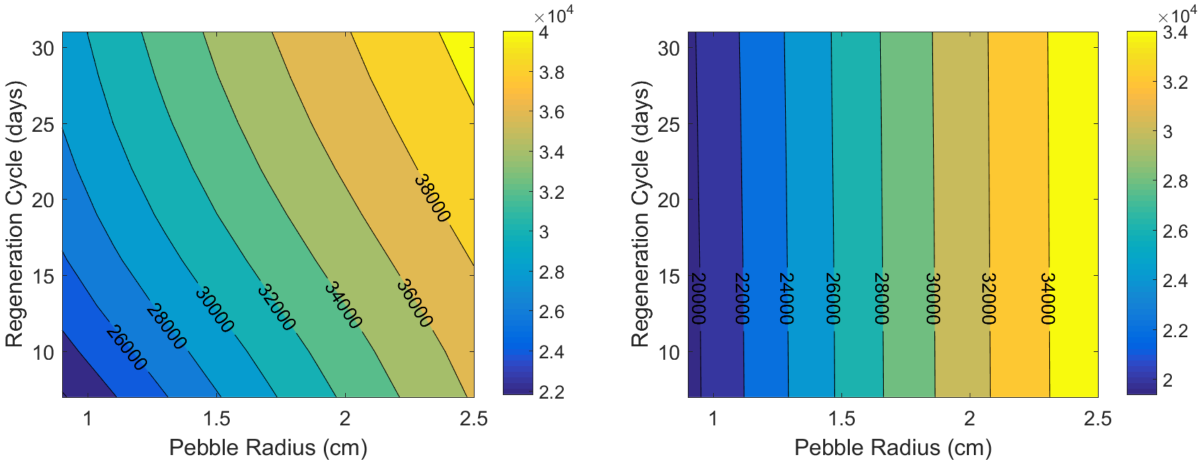

a) ISO – 88 **b) OVC 4x8**

Figure 6.25: Regeneration cycle and pebble radius versus core graphite tritium inventory for a) nuclear graphite ISO-88 and b) granular activated carbon OVC 4x8

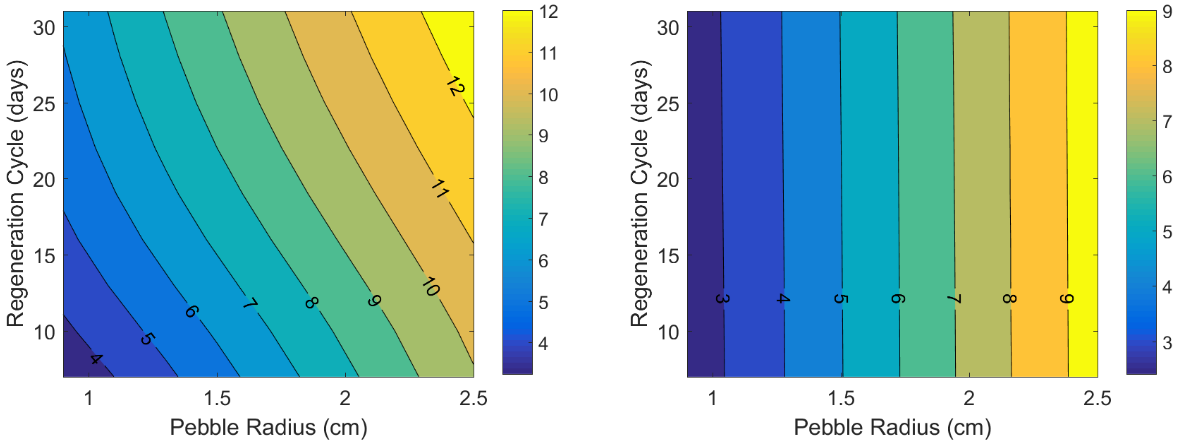

a) ISO – 88 **b) OVC 4x8**

Figure 6.26: Regeneration cycle and pebble radius versus primary coolant tritium inventory for a) nuclear graphite ISO-88 and b) granular activated carbon OVC 4x8

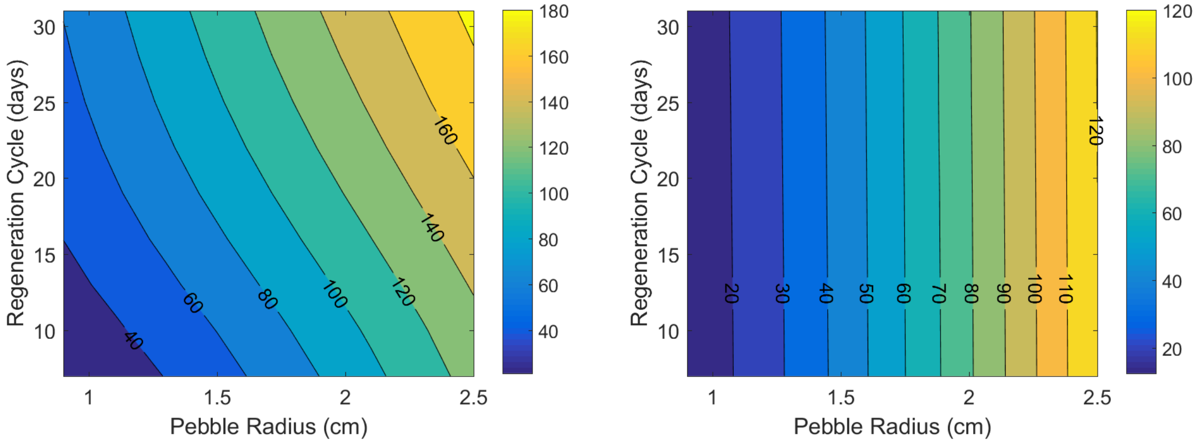

a) ISO – 88 **b) OVC 4x8**

Figure 6.27: Regeneration cycle and pebble radius versus primary HX tritium inventory for a) nuclear graphite ISO-88 and b) granular activated carbon OVC 4x8

In all of the contour plots discussed above, it was shown that within the chosen bounds of design, reducing the pebble radius and the cycle length reduced the total tritium release and inventory for ISO - 88, while it did result in an appreciable difference in OVC 4x8. The difference came primarily because of solubility limitations of ISO - 88. It was shown in Figure 3.6, that tritium, particularly in the form of TF began to saturate the graphite relatively quickly in operation, thus resulting in a decreased concentration gradient and mass flux to the pebble. For comparison, the adsorbed concentration relative to the solubility during the 200-day simulation on an OVC 4x8 adsorption column is shown in Figure 6.28 a) and b) for T_2 and TF respectively. The cycle length used for this simulation was 31 days and pebble size was 0.9 cm, to illustrate the conditions that would yield the maximum concentration in the adsorbent.

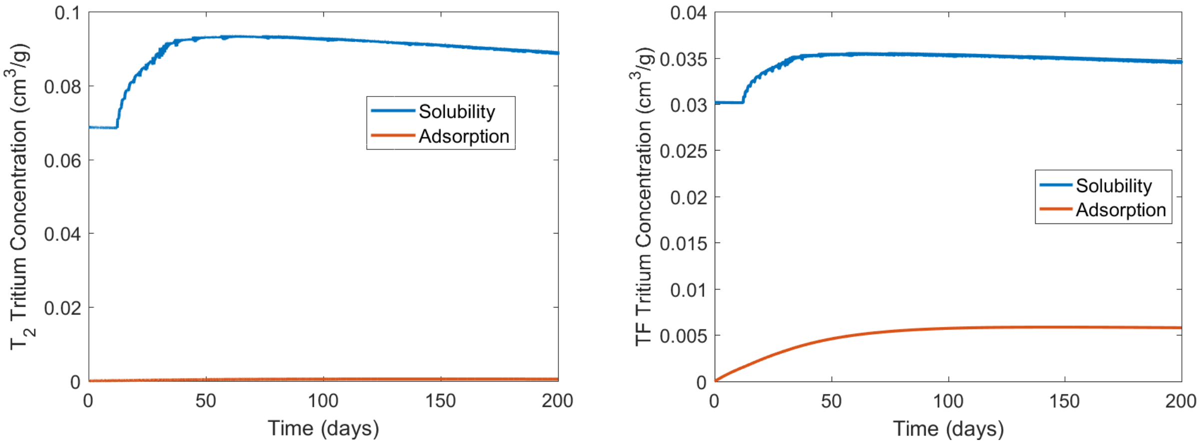

a) T_2 **b) TF**

Figure 6.28: Solubility versus adsorption of a) T_2 and b) T_2 on graphite bed during 200 days of operation for an OVC 4x8 column with 0.9 cm pebbles, regenerated at a cycle length of 31 days

The adsorbed tritium on the carbon pellets was very low relative to the total solubility since OVC 4x8 has a much higher capacity than ISO - 88. In terms of design, further reductions or increases in material capacity therefore would have only a small effect on the total capture of tritium since the concentration gradient and consequently the mass transfer rate only begins to decrease as the pellet becomes increasingly saturated. In such a case, it would therefore be more effective to increase the surface area to increase the rate of total transport or the turbulence in the system to increase the mass transfer coefficient [23]. Another method to potentially reduce capital and improve economics could be the optimization of the column size and dimensions. A comparison between an ISO - 88 column and OVC 4x8 columns at two different sizes is shown in Figure 6.29.

The OVC 4x8 column with dimensions of 1.5m R x 4.5m H had the lowest release rate at a maximum of 40 Ci/day compared to a column of the same material at 80% of its volume and the same size column of ISO-88. In these simulations, the minimum pebble size was used at 0.9 cm, with a regeneration cycle of 7 days. The smaller OVC 4x8 column still outperformed the full size ISO - 88 column with the max release at 50 Ci/day compared to 70 Ci /day for ISO - 88. While increasing the size of the column further could continue to reduce release rates, it may become practically and economically undesirable, which introduces another point of optimization.

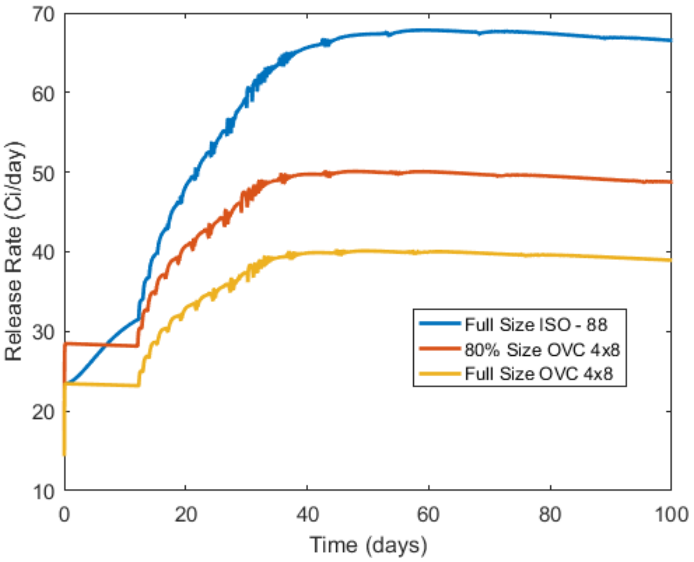

Figure 6.29: Column of ISO - 88 at 'full Size' of 1.5 R x 4.5 H versus the same size OVC 4x8 column and an OVC 4x8 column at 1.4 R and 4.2 H (80% size)

6.3. Material Feasibility in the FHR System

In Chapter 5, it was found that materials that had larger micropore volume fractions generally had a higher tritium solubility. In Chapter 6.2, carbons with hydrogen solubility at 700°C were used and significant reductions in tritium system inventory and tritium release rates were found. Thus, the use of pore size distribution will be useful criteria for the down-selection of materials. However, there remains many other considerations for the success of a tritium getting material in the FHR system.

6.3.1. Chemical Stability in the FHR

The molten salt in the FHR system is in simultaneous contact with both a proposed adsorbent material and the structural materials of the primary system, which means the relative stabilities of materials must be addressed. Various studies have found that that the use of highly reducing environments or a highly reducing mode of redox control such as Zr metal can cause carbide formation resulting in the degradation of graphite [39][15][41]. This indicates that the redox must be sufficiently well controlled to ensure carbon compatibility.

The stability of carbon in contact with clean molten salts is determined by calculating the Gibbs free energy of reactions, which transform beryllium and lithium carbide into their respective fluorides shown in Equation (6.11) and (6.12).

$$\mathrm{Be_2C + 2F_2 \leftrightarrow 2BeF_2 + C} \tag{6.11}$$

$$\mathrm{Li_2C_2 + 2F_2 \leftrightarrow 2LiF + 2C} \tag{6.12}$$

The Gibbs energies of reaction can indicate the general propensity of the forward reaction when compared with the bulk potential of the solution. If these potentials are lower than the system potential, the forward reaction is thermodynamically favoured. As a point of reference, the redox potential of the solution in the MSRE was used, which was previously derived by Stempien [9]. In addition to stability in clean salt, the stability of carbon must be know in the presence of corrosion products. Since CrF_2 is the primary corrosion product, energies of the chromium carbides reactions with fluorine were calculated. These reactions are shown in Equation (6.13) to (6.15).

$$\mathrm{Cr_3C_2 + 3F_{2(g)} \leftrightarrow 3CrF_2 + 2C} \tag{6.13}$$

$$\mathrm{Cr_7C_3 + 7F_{2(g)} + 3C} \tag{6.14}$$

$$\mathrm{Cr_{23}C_6 + 23F_{2(g)} \leftrightarrow 23CrF_2 + 6C} \tag{6.15}$$

The Gibbs free energies of reactions (6.11) to (6.15) were calculated with HSC Chemistry V6.0 and are shown against the baseline redox potential in Figure 6.30. In the range of operating temperatures of the FHR, the carbon will be stable in a clean salt solution since the BeF_2 and LiF producing reactions have a lower energy than the baseline MSRE potential. However, the plot also indicates that carbon materials in contact with the chromium fluoride corrosion product, can become destabilized. In addition to the carbon however, it must be noted that activated carbon materials contain various other elemental species (C, H, N, S, O) in non-trivial proportions (up to 10%) and complex functional groups (C-O, C=O, C(O)-O-C, etc.). With the MSRE, it was found that activated charcoals underwent an exothermic reaction with the fuel salt UF_4 [133]. With lithium and beryllium fluoride molten salts, the chemistry is unknown, and requires further investigation.

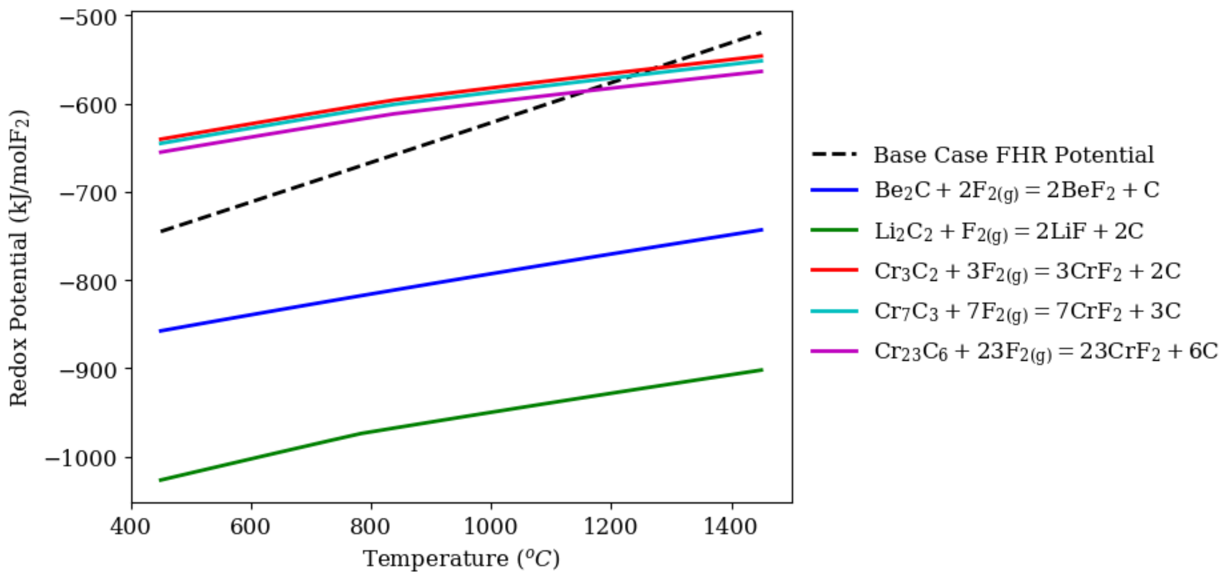

Figure 6.30: Gibbs free energy of reaction of salt carbides and chromium carbides compared to the base case redox potential

6.3.2. Regeneration of Spent Adsorbent

The use an adsorbent column for capture of tritium necessarily requires a discussion of regeneration processes and strategies since the eventual saturation of the adsorbent limits the total life of the adsorbent. It has been found previously that while hydrogen adsorption can have a large reversible component, some capacity is generally lost upon regeneration due to a component of irreversible retention on the adsorbent surface [134]. The initial and progressive loss of capacity can therefore be an important consideration in both the technological viability, and the long and short-term operating strategies of the tritium control mechanism.

In considering the adsorption column for tritium control in Chapter 2, it was suggested that the regeneration of spent adsorbent could be achieved through the application of a temperature gradient. The regeneration of hydrogen and other volatile compounds from carbon materials has been a rigorous field of research in the past decades due to interest in using carbon for hydrogen energy storage [135][134][136] or in the adsorption of gaseous environmental pollutants [137][138]. Various strategies have been proposed primarily involving the use of thermal desorption. The exact method of heating however, can vary substantially though. Conventionally, the spent carbon is removed from the process and transferred to a heated vessel or a vessel where heated fluid is introduced to desorb the hydrogen from the adsorbent. In order to reduce capital and operating cost and increase regeneration efficiency, improvement strategies have been researched. Some of these strategies for example, include the following:

- Induction heating of carbon cloth [139] and small grained activated carbon [138] to desorb VOCs
- Ultrasound assisted desorption for improving mass transfer by cavitation and acoustic streaming in pores [140]
- Microwave-assisted regeneration[137], which has been found to potentially reduce the thermal energy output required for regeneration

Most of the work done in this field has been conducted at low or room temperature but suggests that substantial desorption can be achieved with a temperature 300 - 400°C above the operating temperature.

At the high-temperature FHR conditions, the majority of adsorption & desorption research originates from fusion, where thermal desorption studies have provided insight into different hydrogen - graphite interactions [129][141][142] by applying temperature programmed desorption at temperatures of up to 1600K. In these experiments, the adsorbent materials were first saturated at a high temperature (700°). Following this, the sample temperature was increased at a constant rate while measuring the hydrogen from the off-gas stream of the sample. As the hydrogen desorbs, peaks are observed in a TDS spectrum. By varying the heating rate and measuring the temperature where the peak occurs $\mathrm{T_{peak}}$, the activation energy of desorption can be determined by Kissinger's equation [143]:

$$\ln\left(\frac{\beta}{\mathrm{T_{peak}^{2}}}\right)=\frac{\mathrm{E_a}}{\mathrm{RT_{peak}}}+\ln\left(\frac{\mathrm{AR}}{\mathrm{E_a}}\right)+\mathrm{C}$$

Where β is the heating rate, $\mathrm{E_a}$is the activation energy, R is the gas constant, and A and C are kinetic constants. Thus by determining β as a function of $\mathrm{T_{peak}}$, the activation energy of different sites can be determined, which then allows the desorption kinetics to be defined. While a lower activation energy will result in a sorbent that is more easily regenerated, the risk of accidental tritium release can increase during a reactor transient, thus creating a required trade-off.

In the chemisorption experiments presented in Chapter 5, which decoupled the weak and strong interactions, it was shown that the relative proportion of these interactions varied greatly between materials. The weak adsorption accounted for anywhere between 5 - 40 % of the total solubility, and correlated with the micropore volume content of the material. The weak adsorption, required only a vacuum (or sweep of non-adsorbent gas) to be removed from the surface while the strong adsorption showed remained adsorbed. Thus, the materials with significant weak adsorption (OVC 4x8, OLC 12x40, etc.) may prove desirable from an energy and cost reduction perspective. Ultimately, the exact desorption mechanics and optimal choice of technology will depend strongly on properties of the material (thermal resistivity, grain size, pore distributions) and the thermodynamic conditions of interest (ambient versus FHR operating conditions).

Chapter 7.

Conclusions and Future Work

Carbon materials show great potential in capturing and controlling tritium generated in solid-fuel fluoride high-temperature reactors (FHRs), dissolved fuel molten salt reactors (MSRs) and high-field fusion devices proposing to use a molten-salt breeding blanket; all technologies which can enable the path to a low-carbon energy future. Tritium transport simulations with a carbon-based adsorption column used in an FHR system indicate that radiological release rates can be limited to levels near those of conventional water reactors. This is a requirement which may ultimately be necessary in licensing of new reactor designs. Initial adsorption tests of a variety of materials indicate that microporous carbons exhibit high affinities to hydrogen even at reactor operating temperatures. This allows the relaxation of operating requirements, simplification of system design and provides an enabling technology in the development of molten-salt cooled nuclear power. The conclusions are elaborated in the following sections.

7.1. Results and Contributions

Adsorption has been a well-developed, long-standing technology used for the removal of gaseous waste products in environmental and chemical engineering processes for decades [144]. The work of this thesis combines simulation and experiment to demonstrate that existing adsorption technologies with minor modifications can be equally applicable in molten-salt environments and enable the advancement of the next generation of nuclear power.

7.1.1. Key Results

The important result of this thesis is the early demonstration of a technology that can resolve tritium control issues, which currently act as a technical roadblock in the long-term deployment of commercial molten salt reactors [4]. The research conducted for this thesis has provided a clearer path for continued development, supported by the following findings:

1. Significant reduction of tritium release to the environment by more than 90% with a single adsorption column in the primary system of the FHR can be achieved by

optimizing the regeneration rate and pebble size of a standard sized column. These results indicate the need for further optimization of parameters such as adsorption system size, geometry, material, etc. in order to improve attractiveness in both test reactor and commercial cases.

2. High hydrogen uptake occurs in porous carbon materials at the operating temperature of 700°C. These materials showed more than two orders of magnitude greater hydrogen solubility than graphite, which was known to be a large tritium sink in the MSRE. This provides a metric for rapid screening of materials that could be used as an adsorbent, while considering other conditions that must be met for this application, such as good regeneration characteristics and sufficient hardness and resistance to shear failure.

7.1.2. Major contributions

The primary contributions of this thesis are as follows:

1. Continued validation and development of the TRIDENT code to v1.1, which was originally written by Stempien [9] at MIT to simulate transient reactor behavior while capturing the coupled effects of tritium generation, mass transport and corrosion. Numerical correction of adsorption bed simulation, improvement of boundary layer model between molten-salt and graphite and addition of isotherms for high performance carbon materials.

2. Determination of adsorption technology design conditions that can lead to significant removal of tritium from the system, limiting the tritium inventory in the system that can be released in the event of an accident and the amount of tritium that is released during normal operation.

3. Experimental characterization of the surface area, pore volume, pore size distribution and surface morphology of various granular/powdered/extruded activated carbons, graphene nanoplatelets and nuclear graphite materials using gas adsorption techniques, microscopic thermodynamic modeling and scanning electron microscopy.

4. Measurement of hydrogen total solubility on various carbon materials, and decoupling interactions of two different binding strengths at FHR operating temperatures. Identification of increased hydrogen retention in carbons containing narrow micropores at these conditions.

5. Application of thermodynamic models of Langmuir, Temkin and Freundlich, showing that isotherms are best modeled by hydrogen adsorption occurring via a combination of molecular and dissociative binding on carbon materials.

7.2. Overall conclusions

- **Performance of a tritium adsorption column can be greatly improved by varying design and operating conditions.** For an adsorption column of 1.5 m R x 4.5 m H, the tritium release rate and system inventory was found to be almost 600 Ci/day and 40, 000 Ci respectively using ISO - 88 graphite pebbles of 2.5 cm R and a regeneration cycle of 31 days. For the same system, reducing the pebble size to 0.9 cm R greatly increased the mass transfer area and reducing the cycle length to 7 days increased the concentration gradient between the bulk and adsorbent surface, allowing for a reduction in release and inventory to less than 70 Ci/day and 22, 000 Ci respectively. Without any mitigation, the tritium release peaked at 2410 Ci/day and the equilibrium tritium inventory was 68, 365 Ci.

- **Carbon materials exhibit a high capacity for hydrogen capture even at the high temperatures relevant to FHR and other molten salt systems.** It was known that graphite adsorbed a large portion (> 15%) of tritium in the MSRE. Previous studies showed that 0.06 cm^3/g STP of hydrogen isotope adsorbed on graphite at a low pressure of 0.5 kPa and an extrapolated temperature of 700 ^oC. In this study, it was found that under the same conditions, activated porous carbons could adsorb more than 50 times this amount at up to 2.97 cm^3/g. This greatly improves performance of adsorption technologies in the FHR.

- **Materials with higher micropore volumes reversibly adsorbed greater amounts of hydrogen.** While previous studies suggested that graphite exhibiting high BET surface area generally exhibited higher adsorption [28], this was not found to be a good overall predictive indicator of H_2 solubility. Between total pore volume, average pore radius, BET surface area, and pore size distribution, good correlations were only found in detailed analyses of the pore size distribution. Carbons with higher volumes fractions in the micropore and narrow micropore regimes exhibited higher hydrogen solubility, especially with respect to increased weak, reversible adsorption. Weak adsorption made up as much as 40% of the total adsorption in some activated carbons.

- **Classical adsorption methods provide good models for hydrogen adsorption at high temperature and indicate a combination of dissociative and molecular adsorption.** Using the generalized Langmuir equation to model adsorption of combined, weak and strong isotherms, a reaction order between 1 and 2 was found for most carbon materials indicating the presence of both molecular and dissociative adsorption. Modeling the strong and weak adsorption separately and combining them to calculate the total solubility was found to reduce the modeling error by as much as 20% in AC materials.

- **Tritium release and system inventory can be reduced significantly by the use of a carbon adsorption column, a well-developed, readily deployable technology.** Using the GAC OVC 4x8, the tritium release rates were reduced to about 40 Ci/day, which is of a similar order of magnitude to release rates in existing reactors. The pebble size could be increased by more than 20% relative to ISO-88 while maintaining the same performance, which reduces pressure drop and pumping demand. The regeneration cycle could be increased to more than 31 days, reducing the operational demand and the risk of saturation and radiological release in the event of system failure and decreasing wear on adsorbent. This was achieved with basic established adsorption technologies without major extrapolation, lending itself to an increased probability of success in the FHR.

7.3. Summary of Simulation and Experimental Results

The results of this work have demonstrated that the use of adsorption technology for the control of tritium in molten salt systems shows great potential. A series of simulations and experiments were conducted, which in combination showed that tritium release rates can be reduced to tritium levels near LWRs by capture on an adsorbent. Furthermore, experiments have provided insight to the material properties that yield a high sorption performance, which can be used to guide further investigation and research in order to expedite technological development.

Since nuclear graphite is already in use in the reactor, system-level simulations were first conducted with the use of a graphite with known adsorption data at reactor conditions of 700°C in an adsorption column placed in the primary loop. At minimum, it was found that the radius of the bed should be greater than 1 m with pebbles larger than 1.0 cm in order to take the full flow of primary system without bearing excessive pressure drops of more than 45 kPa total and 10 kPa/m. A typical adsorption column of 1.5 m R x 4.5 m H was simulated, which is similar in dimension to the reactor core. The design parameters that were investigated were regeneration cycle (number of days per full bed regeneration) and pebble size. The cycle was varied from 7 to 31 days, while the pebble size was varied from 0.9 cm to 2.5 cm. In a baseline FHR without mitigation, the tritium release from the system was approximately 2410 Ci/day for a 236 MWt reactor, greatly exceeding tritium release rates of existing water-cooled technologies, which would not typically exceed 10 Ci/day given a reactor of similar size. With an adsorbent column of pebbles sized 2.5 cm, the maximum tritium release rate reduced from 600 to 400 Ci/day by reducing the regeneration cycle from 31 to 7 days. Further, it was found that changing the regeneration rate could reduce the inventory in the system by nearly 15%. Using a cycle of 31 days and varying the pebble size from 2.5 cm to 0.9 cm, the release rates decreased from 600 to 180 Ci/day due to the increased surface area and uptake on the graphite bed. By varying pebble size, the tritium inventories reduced by more than 30%, which would reduce the risk of radiological exposure during and accident or transient. In the best case scenario, a pebble size of 0.9 cm and a cycle length of 7 days was used, which resulted in a peak release of 80 Ci/day for ISO - 88 graphite.

Granular, powered and extruded activated carbons, graphene nanoplatelets and graphite materials were characterized using gas physisorption techniques. The BET surface area, total pore volume, average pore radius, and pore size distribution were determined. It was found that most activated carbons had surface areas between 900 - 1100 m^2/g with the exception of MSC-30, which had an area over 3100 m^2/g. The graphene platelets had a much lower area at 110 m^2/g and graphite IG-110U had the lowest at 0.6 m^2/g. The surface areas were more or less found to be independent on the shape and size factor indicating the majority of the accessible surface came from microscopic pores internal to the bulk of the material. By assuming a constant fluid density, the average pore size for activated carbons ranged between 8 to 11 Å, while graphene platelets and graphite had pore sizes between 32 and 33 Å. The specific pore volume was largest for MSC-30, which was 1.72 cm^3/g compared to activated carbons which were mostly near 0.5 cm^3/g, Graphenit-OX which was approximately 0.183 cm^3/g and graphite which was 1.0 x 10^{-3} cm^3/g. Next, non-local density functional theory was applied to CO_2 adsorption at 273K to determine the micropore distribution from 0.35 - 1 nm and quenched solid density functional theory was applied to N_2 adsorption at 77K for micropore to mesopores in the range of 2 - 40 nm. Three definitions were used to reference the pore size ranges: 1) narrow micropores < 0.7 nm, 2) micropores < 2.0 nm and 3) mesopores > 2.0 nm & < 40 nm. Activated carbons had the largest narrow micropore volume ranging from 0.1 cm^3/g for the extruded carbon NRB 40M to 0.17 cm^3/g for OVC 4x8. Graphite had the lowest narrow micropore volume at 0.0004 cm^3/g and Graphenit-OX had 0.014 cm^3/g. Similar trends were found for the micropores where MSC-30 had the largest micropore volume at 0.68 cm^3/g while other ACs had micropore volumes which ranged from 0.2 to 0.35 cm^3/g. IG-110U had and Graphenit-OX had much lower micropore volumes of 0.001 cm^3/g and 0.02 cm^3/g respectively. In the mesopore range, the activated carbons varied greatly where again MSC-30 had the largest mesopore volume of 0.86 cm^3/g, while OLC 12x40 had only 0.034 cm^3/g of mesopore volume. Graphenit-OX had a moderate mesopore volume of 0.2 cm^3/g, and IG-110U had the smallest with only 0.0021 cm^3/g. Overall, the activated carbons had a much higher narrow micropore and micropore volume than both graphite and graphene nanoplatelets, while the mesopore volume was independent on the carbon type. In the liquid DFT calculations, relatively good agreement with experimental data was found with the slit / cylindrical pore model for carbons, where the material was assumed to take a slit pore geometry for pores < 2 nm and a cylindrical geometry for pores > 2 nm. The NLDFT kernel fitting error was generally less than 1% with the exception of Graphenit-OX at 6% due to the non-porous nature of the material. The QSDFT errors were all generally less than 1% except for IG-110U, which had an error of 2.4 %.

Chemisorption experiments were conducted for the 9 materials at 700°C where all the activated carbons adsorbed between 2.5 to 4.5 cm^3 STP H_2/g at 4 kPa with the exception of MSC-30 which only adsorbed 1.2 cm^3 STP H_2/g, while Graphenit-OX adsorbed less than 0.5 cm^3 STP H_2/g and IG-110U did not adsorb a measurable amount of H_2. Based on the adsorption isotherm, MSC-30 appeared to have a reaction with hydrogen in the low-pressure range resulting in a downward inflection in the isotherm. Work investigating corrective techniques to measure ultra-low adsorption volumes for IG-110U and other graphite materials is currently underway. It was found that the total solubility of hydrogen could be divided into component 'weak' and 'strong' interactions which were measured by applying a low vacuum to the material after the total solubility isotherm was measured, then repeating the adsorption experiment. The component of weak and strong adsorption is significant as weak adsorption readily leaves the surface, and thus can be readily adsorbed and desorbed in a regeneration process while the strongly adsorbed hydrogen requires energy input to become liberated. The relative component of weak adsorption varied greatly among different materials and ranged between 20 to 40% at 3.5 kPa for activated carbons. Graphene nanoplatelets had a very low fractional weak adsorption of less than 10%, which would be the expectation if most of the hydrogen chemically dissociates on the graphene edge. The strongest correlations were found between the narrow micropore/micropore volume fractions and adsorbed hydrogen at pressures between 0.5 and 3.0 kPa. Particularly, it was found that materials with larger fractions of their total pore volume in the narrow micropore and micropore regimes exhibited higher capacities for weak adsorption with correlation R-values of 0.92 and 0.93 for narrow micropores and micropores respectively. Weaker correlations were found between strong adsorption and the narrow micropore and micropore volume fractions with R-values of 0.76 and 0.85 respectively. Further, the micropore volume fraction was correlated with the weak adsorption fraction with an R-value of 0.8, suggesting that the weak form of adsorption may occur in micropores, while strong adsorption does not. From scanning electron microscopy, it was found that materials with highly disorganized, rough 3-dimensional surfaces showed much higher hydrogen sorption compared to planar, smooth and macroscopically non-porous surfaces as was the case of IG-110U, Graphenit-OX and to a lesser extent MSC-30.

The experimental isotherms collected for hydrogen adsorption on these materials were then modeled with the classical methods of Langmuir, Freundlich, and Temkin. It was found that the experimental data could be well represented by the Langmuir model with coefficients of determination R^2 greater than 0.97 for all materials with the exception of MSC 30, which showed significant divergence from all three models that were used. In these models, the combined reaction orders were typically found to be a value between 1 and 2 suggesting that a combination of molecular and dissociative adsorption of hydrogen occurs, contrary to some previous studies of graphite, which assumed a purely dissociative process using Langmuir's equation with a reaction order of 2. Additionally, the weak and strong isotherms were modeled separately and it was found that the strong isotherm was best modeled with Langmuir's method, in which R^2 values were all above 0.95, except for PAC, which still had a high R^2 of 0.9. In comparison, the weak isotherms were all modeled best by Freundlich with the exception of CTR 12x40 and Graphenit-OX, which showed best agreement with Langmuir's generalized model. The R^2 values from the weak isotherm modeling were all above 0.97 with the exception of adsorption on MSC-30, which could not be modeled by the methods tested possibly due to surface reactions with hydrogen. Based on the mixed reaction orders of the weak isotherm, it was believed that the weak isotherm represents a combination of dissociative and molecular adsorption that cannot be precisely decoupled using this method. However, it was found that by combining methods applied to weak and strong isotherms, the error in modeling total solubility can in many cases be reduced by as much as 20%.

The hydrogen adsorption data for high capacity activated carbon OVC 4x8 was used for an adsorption tower in TRIDENT to simulate system-level tritium behavior in an FHR compared to the same tower using ISO - 88 nuclear graphite. It was found that for ISO - 88, the system was solubility limited and adsorbent pebbles were found to near the TF saturation relatively early (30 days) into operation. The consequence of approaching the solubility limit was a severe reduction in the mass transfer due to the drop in tritium concentration gradient between the molten salt fluid and the solid adsorbent interface. With restrictive parameters of 0.9 cm pebbles and continuous regeneration of the bed on average once every 7 days, the maximum release rate in the system was 70 Ci/day for ISO - 88. With GAC OVC 4x8, the increased solubility of the material relaxed the solubility limitation, and it was found that the system was then limited by the rate of transfer. During operation, the pellets consistently remained far below the solubility even when a very long regeneration cycle of 31 days was simulated. With OVC 4x8, a lower pressure drop could be maintained without loss in performance relative to ISO - 88 by increasing the pebble size. The minimum release rate using OVC 4x8 was 40 Ci/day, which is 30% less than the minimum release rate with ISO - 88, achievable even with a longer cycle length. Additionally, a smaller column was shown to be possible, where an OVC 4x8 column at 80% of the volume could still out-performed the ISO - 88 column with a max release of 50 Ci /day. Further, the total system tritium inventory could be reduced by more than 15% by switching from ISO - 88 to OVC 4x8, which significantly reduces the risk of radiological release.

7.4. Future work

The work done in this thesis shows that the use of adsorption for tritium capture and control has great potential to reduce the system's tritium release rates and inventory by being able to capture large amounts of tritium. Further experimentation and modeling must be completed in order to fully characterize adsorption and desorption of tritium in these materials, understand the effects on transient behavior the FHR system, and design a mitigation mechanism that optimizes performance and economics. Such studies include but are not restricted to the following:

- Full Analysis of Adsorption and Desorption - The studies in this thesis successfully measured initial equilibrium relationship between hydrogen and carbon materials at 700°C. The full range of operating temperatures (500 - 800°C) should be examined, which will allow measurement of the adsorption energy by application of the Clausius-Clapeyron equation or other adsorption models. The permeation of hydrogen into the bulk of the material should be investigated. One method that could provide insight may involve cleaving or breaking down the material to expose internal faces of the material and repeating the adsorption experiments to determine if a difference is observed. Equally, the desorption behavior should be measured with techniques such as temperature programmed desorption (TPD), where desorption mechanisms, rates, and energies can be determined [129]. Additionally, the reversibility and loss of capacity should be measured with successive cycles of adsorption and desorption. In these experiments, only H_2 adsorption was measured. In practice, a small amount of HF also exists, and would have different transport properties. Further, H and T solubility could vary slightly, due to differences in atomic radius when accessing narrow micropores.

- Kinetic Behavior Of Tritium - In addition to the solubility, it was found that the mass transfer rate can play an important role in dictating the efficiency of an adsorption column. Thus, the diffusion rates through carbon materials should be examined in depth. In order to determine the kinetic behavior, the transient pressure in an isolated cell of hydrogen-adsorbing sample can be measured, and the apparent diffusion into the material can be estimated [120]. These experiments, as well as the adsorption and desorption energies determined from the equilibrium experiments can be combined with modeling techniques such as molecular dynamics (MD) or Kinetic Monte Carlo (KMC) to study the bulk diffusion of hydrogen into porous carbons or graphite materials [145].

- Molten Salt Interaction Study - The experiments performed only investigated the reaction between the gas phase hydrogen with carbon materials, neglecting potential effects of a molten salt medium. This could undoubtedly affect the adsorption capacity, and alternative adsorption models with mathematical terms that explicitly account for solvent effects could be required. In order to the study molten-salt effects in existing experiments, precautions should be taken to prevent entrainment as molten salts have an appreciable vapor pressures [146], which may result in fouling of experimental tubing. Additionally, collaboration with other institutions such as UW Madison that are studying the graphite-salt interface could also yield useful data for hydrogen sorption [23].

- Study of Material Properties - This thesis provided at least one metric for screening materials and understanding the adsorption of hydrogen on carbon. It is clear that many other factors have the potential to influence this behavior, which means the material properties need to be fully characterized. Such characterization could include elemental analysis with SEM - Energy Dispersive Spectroscopy (EDS) and probing the electronic structure with X-ray Photoelectron Spectroscopy (XPS). Additionally for graphite, degree of graphitization is known to be a measure of the quantity of dangling bonds which can accept dissociated hydrogen atoms [147]. The crystallography can be determined using techniques such as X-Ray Diffraction (XRD). In addition to the properties of pristine materials, the properties of spent and regenerated adsorbent should also be investigated. Regeneration of sorbent at high temperature can result in morphological change due to annealing or thermal stress, which can change the sorption behavior over time. To prove a successful tritium adsorber, physical properties such as material toughness, shear strength, resistance to corrosion would also require examination.

- Reactor Experiments - The adsorption column proposed can be placed outside of the reactor core, reducing the demand for materials that are irradiation resistant. However, effect of small amounts of irradiation on these materials can still be tested with experiments in the MIT NRL [148]. In addition to irradiation, another benefit of in-core reactor experiments is the simultaneous experimentation of flibe-carbon interactions, as well as the use of tritium, instead of a surrogate hydrogen or deuterium. With these experiments, extensive study can be conducted on the isotopic effects and greatly inform hydrogen experiments.

- Detailed Engineering of Adsorption Column - The thesis provides a study with an adsorption column using various approximations to adapt to the existing TRIDENT code and provide system-level detail only. The effects of various operating parameters including regeneration time and pebble size were highlighted with reference to mass transfer limitations. However, a greater amount of design insight can be gained from a more detailed model of this technology. Various design configurations could be tested including the use of a counter-current or fluidized bed column, which increases the concentration gradient and mass transfer coefficient of tritium from the bulk coolant to the adsorbent. Further, the column could be combined with other processes such as the injection of hydrogen H-1 downstream of the bed to dilute tritium inventory in the system, and control redox potential simultaneously. In more detailed design, the spatial and temporal dependence of concentration can be assessed, transient response to operating scenarios can be simulated, and adsorbent breakthrough can be determined, all allowing for better optimization.

Bibliography

[1] C. W. Forsberg *et al.*, “Fluoride-Salt-Cooled High-Temperature Reactors (FHRs) for Base-load and Peak Electricity, Grid Stabilization, and Process Heat,” Massachusetts Institute of Technology: Center for Advanced Energy Systems, Cambridge, MIT-ANP-TR-147, 2013.

[2] C. W. Forsberg, “Commercialization Approaches and Challenges for Fluoride-Salt-Cooled High-Temperature Reactors (FHRs),” in *Transactions of the American Nuclear Society*, 2013, vol. 109, pp. 1088–1091.

[3] C. W. Forsberg, L. Hu, P. F. Peterson, and K. Sridharan, “Fluoride-Salt-Cooled High-Temperature Reactors for Power and Process Heat,” Massachusetts Institute of Technology: Center for Advanced Energy Systems, Cambridge, MIT-ANP-TR-157, 2014.

[4] D. E. Holcomb, G. F. Flanagan, G. T. Mays, W. D. Pointer, K. R. Robb, and G. L. Yoder, “Fluoride Salt-Cooled High-Temperature Reactor Technology Development and Demonstration Roadmap Prepared by,” Oak Ridge National Laboratory, Oak Ridge, Tennessee, ORNL/TM-2013/401, 2013.

[5] C. Andreades *et al.*, “Mark--1 PB--FHR Technical Description Technical Description of the ‘Mark 1’ Pebble-Bed Fluoride-Salt-Cooled High-Temperature Reactor (PB-FHR) Power Plant,” Berkeley, California, UCBTH-14-002, 2014.

[6] D. Curtis and C. Forsberg, “Market Performance of the Mark 1 Pebble-Bed Fluoride-Salt-Cooled High-Temperature Reactor,” in *Transactions of the American Nuclear Society*, 2014, vol. 110.

[7] R. C. Robertson, “Conceptual Design Study of a Single-Fluid Molten-Salt Breeder Reactor,” Oak Ridge National Laboratory, Oak Ridge, Tennessee, ORNL-4541, 1971.

[8] “TRISO-Coated Particle Fuel Phenomenon Identification and Ranking Tables (PIRTs) for Fission Product Transport Due to Manufacturing, Operations, and Accidents,” U.S. Nuclear Regulatory Commission, Washington, DC, NUREG/CR-6844, Vol.1.

[9] J. D. Stempien, “Tritium Transport and Corrosion Modeling in the Fluoride Salt-Cooled High-Temperature Reactor,” Ph.D. Thesis, Massachusetts Institute of Technology, 2015.

[10] D. A. Petti, P. A. Demkowicz, J. T. Maki, and R. R. Hobbins, “Triso-coated particle fuel performance,” in *Comprehensive Nuclear Materials*, Elsevier Inc., 2012, pp. 151–213.

[11] B. P. Collin, “AGR-3 / 4 Irradiation Test Final As-Run Report,” Idaho National Laboratory, Idaho Falls, Idaho, INL/EXT-10-18097, 2015.

[12] “Fluoride-Salt-Cooled High Temperature Reactor (FHR) Materials, Fuels and Components White Paper,” Berkeley, California, UCBTH-12-003, 2013.

[13] J. W. Koger, “Alloy Compatibility with LiF-BeF2 Salts Containing ThF4 and UF4,” Oak Ridge National Laboratory, Oak Ridge, Tennessee, ORNL-TM-4286, 1972.

[14] W. R. Grimes, “Chemical Research and Development for Molten-Salt Breeder Reactors,” Oak Ridge National Laboratory, Oak Ridge, Tennessee, ORNL-TM-1853, 1967.

[15] D. F. Williams, L. M. Toth, and K. T. Clarno, “Assessment of Candidate Molten Salt Coolants for the Advanced Highi-Temperature Reactor (AHTR).” Oak Ridge National Laboratory, Oak Ridge, Tennessee, 2006.

[16] W. D. Manly *et al.*, “Metallurgical Problems in Molten Fluoride Systems,” Oak Ridge National Laboratory, Oak Ridge, Tennessee, A/CONF.15/P/1990, 1958.

[17] M. S. Sohal, M. a Ebner, P. Sabharwall, and P. Sharpe, “Engineering database of liquid salt thermophysical and thermochemical properties,” Idaho National Laboratory, Idaho Falls, Idaho, INL/EXT-10-18297, 2010.

[18] R. E. Thoma, “Chemical Aspects of MSRE Operations -,” Oak Ridge National Laboratory, Oak Ridge, Tennessee, ORNL-4658, 1971.

[19] R. B. (ORNL) Briggs, “Tritium in Molten-Salt Reactors,” *React. Technol.*, vol. 14, pp. 335–352, 1971.

[20] D. E. Holcomb, G. F. Flanagan, G. T. Mays, W. D. Pointer, K. R. Robb, and G. L. Yoder, *Fluoride Salt-Cooled High-Temperature Reactor Technology Development and Demonstration Roadmap Prepared by*, no. September. 2013.

[21] A. Suzuki, T. Terai, and S. Tanaka, “Tritium release behavior from Li 2 BeF 4 molten salt by permeation through structural materials,” *Fusion Eng. Des.*, vol. 51, no. 52, pp. 863–868, 2000.

[22] IAEA, “Management of Waste Containing Tritium and Carbon-14,” *Manag. Waste Contain. Tritium Carbon-14*, no. 42, p. 109, 2001.

[23] C. W. Forsberg, S. Lam, D. M. Carpenter, and D. G. Whyte, “Tritium Control and Capture in Salt-Cooled Fission and Fusion Reactors: Status, Challenges, and Path Forward,” *Nucl. Technol.*, vol. 197, no. 2, 2017.

[24] J. Yin, J. Li, Y. Ma, H. Li, W. Liu, and D. Wang, “Study on the Air Core Formation of a Gas–Liquid Separator,” *J. Fluids Eng.*, vol. 137, no. 9, pp. 91301–91309, Sep. 2015.

[25] F. Rubio, E. D. Blandford, and L. J. Bond, “Survey of advanced nuclear technologies for potential applications of sonoprocessing,” *Ultrasonics*, vol. 71, pp. 211–222, 2016.

[26] X. Wu, D. Arcilesi, X. Sun, and R. Christensen, “Conceptual design of tritium removal facility for FHRs (2015),” in *International Topical Meeting on Nuclear Reactor Thermal Hydraulics (NURETH) 2015*, 2015, no. 6, pp. 4935–4948.

[27] C. Forsberg, J. Stempien, and R. Ballinger, “Tritium Removal from Salt-Cooled Reactors Using Carbon,” in *Transactions 2015 American Nuclear Society Winter Meeting*, 2015, p. 15199.

[28] R. A. Strehlow, "Chemisorption of tritium on graphites at elevated temperatures," *J. Vac. Sci. Technol. A Vacuum, Surfaces, Film.*, vol. 4, no. 1986, p. 1183, 1986.

[29] H. Atsumi, T. Tanabe, and T. Shikama, "Hydrogen behavior in carbon and graphite before and after neutron irradiation - Trapping, diffusion and the simulation of bulk retention," *J. Nucl. Mater.*, vol. 417, no. 1–3, pp. 633–636, 2011.

[30] H. Atsumi, T. Tanabe, and T. Shikama, "Trapping state of hydrogen isotopes in carbon and graphite investigated by thermal desorption spectrometry," *Fusion Sci. Technol.*, vol. 67, no. 2, pp. 245–249, 2015.

[31] G. C. Bond, *Metal-Catalysed Reactions of Hydrocarbons*. Rickmansworth, UK: Springer US, 2005.

[32] T. D. Burchell, "Graphite: Properties and characteristics," in *Comprehensive Nuclear Materials*, Oak Ridge, Tennessee: Elsevier Inc., 2012, pp. 285–305.

[33] B. N. Sorbom *et al.*, "ARC: A compact, high-field, fusion nuclear science facility and demonstration power plant with demountable magnets," *Fusion Eng. Des.*, vol. 100, pp. 378–405, 2015.

[34] J. Wagner, J. Gehin, D. Holcomb, and P. Peterson, "MSRs Today–Status and Challenges," in *Workshop on Molten Salt Reactor Technologies*, 2015.

[35] A. T. Cisneros, "Pebble Bed Reactors Design Optimization Methods and their Application to the Pebble Bed Fluoride Salt Cooled High Temperature Reactor (PB--FHR)," Ph.D. Thesis, University of California Berkeley, 2013.

[36] E. S. Kim and C. H. Oh, "Development and Verification of Tritium Analyses Code for a Very High Temperature Reactor," Idaho National Laboratory, Idaho Falls, Idaho, INL/EXT-09-16743, 2009.

[37] General Atomics, "Technical Basis for NGNP Fuel Performance and Quality Requirements," Battelle Energy Alliance, LLC, 911168/0, 2009.

[38] C. F. F. Baes, "The chemistry and thermodynamics of molten salt reactor fuels," *J. Nucl. Mater.*, vol. 51, no. 1, pp. 149–162, 1974.

[39] S. Cantor and W. R. Grimes, "Fused-Salt Corrosion and Its Control in Fusion Reactors," *Nucl. Technol.*, vol. 22, no. 1, pp. 120–126, Apr. 1974.

[40] D. Olander, "Redox condition in molten fluoride salts: Definition and control," *J. Nucl. Mater.*, vol. 300, no. 2–3, pp. 270–272, 2002.

[41] J. R. Engel, H. F. Bauman, J. F. Dearing, W. R. Grimes, E. H. McCoy, and W. A. Rhoades, "Conceptual Design Characteristics of a Denatured Molten-Salt Reactor with Once-Through Fueling," Oak Ridge National Laboratory, Oak Ridge, Tennessee, ORNL/TM-7207, 1980.

[42] A. P. Malinauskas and D. M. Richardson, “The Solubilities of Hydrogen, Deuterium, and Helium in Molten Li 2 BeF 4,” *Ind. Eng. Chem. Fundam.*, vol. 13, no. 3, pp. 242–245, 1974.

[43] P. E. Field and J. H. Shaffer, “The Solubilities of Hydrogen Fluoride and Deuterium Fluoride in Molten Fluorides,” *J. Phys. Chem.*, vol. 71, no. 10, pp. 3218–3222, 1967.

[44] P. Calderoni, P. Sharpe, M. Hara, and Y. Oya, “Measurement of tritium permeation in flibe (2LiF-BeF2),” *Fusion Eng. Des.*, vol. 83, no. 7–9, pp. 1331–1334, 2008.

[45] J. Oishi, H. Moriyama, S. Maeda, and Y. Asaoka, “Tritium recovery from molten LiF-BeF2 salt,” *Fusion Eng. Des.*, vol. 8, no. C, pp. 317–321, 1989.

[46] T. Tanabe, Y. Yamanishi, K. Sawada, and S. Imoto, “Hydrogen Transport in Stainless Steels,” *J. Nucl. Mater.*, vol. 123, pp. 1568–1572, 1984.

[47] R. E. Buxbaum and E. F. Johnson, “Use of Yttrium for the Recovery of Tritium from Lithium at Low Concentrations,” *Nucl. Technol.*, vol. 49, pp. 307–314, 1980.

[48] A. Zuttel, “Materials for hydrogen storage,” *Mater. Today*, vol. 6, no. 9, pp. 24–33, 2003.

[49] M. B. Ley *et al.*, “Complex hydrides for hydrogen storage - New perspectives,” *Mater. Today*, vol. 17, no. 3, pp. 122–128, 2014.

[50] T. D. Burchell, *Graphite: Properties and characteristics*, 1st ed., vol. 2. Elsevier Inc., 2012.

[51] H. Marsh and J. Griffiths, “Model of the carbonisation/graphitisation process,” in *International Symposium on Carbon, New Processes and New Applications*, 1982.

[52] E. L. Compere, S. S. Kirslis, E. G. Bohlmann, F. F. Blankenship, and W. R. Grimes, “Fission Product Behavior in the Molten Salt Reactor Experiment,” 1975.

[53] G. C. Bond, *Metal-Catalysed Reactions of Hydrocarbons*. Rickmansworth, UK, 2005.

[54] R. A. Causey, R. A. Karnesky, and C. San Marchi, “Tritium barriers and tritium diffusion in fusion reactors,” in *Comprehensive Nuclear Materials*, Livermore, CA: Elsevier Inc., 2012, pp. 511–549.

[55] General Atomics, “Tritium Distribution in the MHTGR,” United States Department of Energy, San Diego, CA, DOE-HTGR-88098, 1988.

[56] J. P. Redmond and P. L. Walker, “HYDROGEN SORPTION ON GRAPHITE AT ELEVATED TEMPERATURES1,2,” *J. Phys. Chem.*, vol. 64, no. 9, pp. 1093–1099, Sep. 1960.

[57] R. A. Causey, “The interaction of tritium with graphite and its impact on tokamak operations,” *J. Nucl. Mater.*, vol. 162–164, no. C, pp. 151–161, 1989.

[58] Y. Shirasu, S. Yamanaka, and M. Miyake, “Solubility of hydrogen isotopes in graphite,” *J. Nucl. Mater.*, vol. 179–181, pp. 223–226, 1991.

[59] H. Atsumi and M. Iseki, “Hydrogen absorption process into graphite and carbon materials,” *J. Nucl. Mater.*, vol. 283–287, pp. 1053–1056, 2000.

[60] H. Ã. Atsumi, “Mechanism of Hydrogen Trapping and Transport in Carbon Materials,” *Phys. Scr.*, vol. T103, no. 1, p. 77, 2003.

[61] H. Atsumi, M. Iseki, and T. Shikama, “Hydrogen solubility and diffusivity in neutron-irradiated graphite,” *J. Nucl. Mater.*, vol. 191–194, pp. 368–372, 1992.

[62] T. D. Burchell, “Radiation effects in graphite,” in *Comprehensive Nuclear Materials*, Oak Ridge, Tennessee: Elsevier Inc., 2012, pp. 299–324.

[63] H. Atsumi, A. Muhaimin, T. Tanabe, and T. Shikama, “Hydrogen trapping in neutron-irradiated graphite,” *J. Nucl. Mater.*, vol. 386–388, no. C, pp. 379–382, 2009.

[64] H. Atsumi, T. Tanabe, and T. Shikama, “Bulk hydrogen retention in neutron-irradiated graphite at elevated temperatures,” *J. Nucl. Mater.*, vol. 390–391, no. 1, pp. 581–584, 2009.

[65] H. Kwast, H. Werle, and C. H. Wu, “Tritium Retention in Neutron-Irradiated Carbon-based Materials and Beryllium,” *Phys. Scr.*, vol. T64, pp. 41–47, 1996.

[66] I. L. Tazhibaeva *et al.*, “Hydrogen release of reactor irradiated RGT-graphite,” *J. Nucl. Mater.*, vol. 237, no. 1996, pp. 1198–1201, 2000.

[67] C. H. Wu *et al.*, “EU results on neutron effects on PFC materials,” *Fusion Eng. Des.*, vol. 39–40, pp. 263–273, 1998.

[68] G. W. Hollenberg, E. P. Simonen, G. Kalinin, and A. Terlain, “Tritium/hydrogen barrier development,” *Fusion Eng. Des.*, vol. 28, pp. 190–208, 1995.

[69] A. Perujo and K. S. Forcey, “Tritium permeation barriers for fusion technology,” *Fusion Eng. Des.*, vol. 28, no. C, pp. 252–257, 1995.

[70] S. Whitaker, “Forced Convection Heat Transfer Correlations for Flow In Pipes, Past Flat Plates, Single,” *AIChE J.*, vol. 18, no. 2, pp. 361–371, 1972.

[71] J. M. Coulson and J. F. Richardson, “Chemical Engineering,” *Chem. Eng. Sci.*, vol. 2, 2002.

[72] H. Jin, Y. S. Lee, and I. Hong, “Hydrogen adsorption characteristics of activated carbon,” *Catal. Today*, vol. 120, no. 3–4 SPEC. ISS., pp. 399–406, 2007.

[73] L. Radosinski and B. Kuchta, “Hydrogen chemisorption on carbon structure with mixed sp2–sp3 hybridization: empirical potential studies,” *Adsorption*, vol. 20, no. 7, pp. 875–882, 2014.

[74] V. V Bhat, C. I. Contescu, and N. C. Gallego, “The role of destabilization of palladium hydride in the hydrogen uptake of Pd-containing activated carbons,” *Nanotechnology*, vol. 20, no. 20, p. 204011, 2009.

[75] V. V. Bhat, C. I. Contescu, and N. C. Gallego, "Kinetic effect of Pd additions on the hydrogen uptake of chemically-activated ultramicroporous carbon," *Carbon N. Y.*, vol. 48, no. 8, pp. 2361–2364, 2010.

[76] M. Thommes *et al.*, "Physisorption of gases, with special reference to the evaluation of surface area and pore size distribution (IUPAC Technical Report)," *Pure Appl. Chem.*, vol. 87, no. 9–10, pp. 1051–1069, 2015.

[77] S. Lowell, J. E. Shields, M. a. Thomas, and M. Thommes, *Characterisation of Porous Solids and Powders*. Kluwer Academic Publishers, 2004.

[78] Findenegg G.H. and Thommes M., *Physical Adsorption: Experiment, Theory and Applications*. Kluwer Academic Publishers, 1991.

[79] S. Dushman, "Scientific foundations of vacuum technique (Dushman, Saul)," *J. Chem. Educ.*, vol. 39, no. 8, p. A606, Aug. 1962.

[80] S. C. Liang, "On the Calculation of Thermal Transpiration," *J. Phys. Chem.*, vol. 57, no. 9, pp. 910–911, Sep. 1953.

[81] K. Poulter, M. J. Rodgers, P. Nash, T. Thompson, and M. Perkin, "Thermal transpiration correction in capacitance manometers," *Vacuum*, vol. 33, no. 6, pp. 311–316, 1983.

[82] M. Thommes, K. A. Cychosz, and A. V. Neimark, "Advanced Physical Adsorption Characterization of Nanoporous Carbons," in *Novel Carbon Adsorbents*, Elsevier Ltd, 2012, pp. 107–145.

[83] J. Silvestre-Albero, A. Silvestre-Albero, F. Rodríguez-Reinoso, and M. Thommes, "Physical characterization of activated carbons with narrow microporosity by nitrogen (77.4 K), carbon dioxide (273 K) and argon (87.3 K) adsorption in combination with immersion calorimetry," *Carbon N. Y.*, vol. 50, no. 9, pp. 3128–3133, 2012.

[84] J. Moellmer *et al.*, "Insights on Adsorption Characterization of Metal-Organic Frameworks: A Benchmark Study on the Novel soc-MOF," *Microporous Mesoporous Mater.*, vol. 129, no. 3, pp. 345–353, 2010.

[85] J. Garrido, A. Linares-Solano, J. M. Martin-Martinez, M. Molina-Sabio, F. Rodriguez-Reinoso, and R. Torregrosa, "Use of nitrogen vs. carbon dioxide in the characterization of activated carbons," *Langmuir*, vol. 3, no. 1, pp. 76–81, Jan. 1987.

[86] D. Cazorla-Amoros, J. Alcaniz-Monge, and A. Linares-Solano, "Characterization of activated carbon fibers by CO2 adsorption," *Langmuir*, vol. 12, no. 11, pp. 2820–2824, 1996.

[87] G. Y. Gor, M. Thommes, K. A. Cychosz, and A. V. Neimark, "Quenched solid density functional theory method for characterization of mesoporous carbons by nitrogen adsorption," *Carbon N. Y.*, vol. 50, no. 4, pp. 1583–1590, 2012.

[88] A. V. Neimark, Y. Lin, P. I. Ravikovitch, and M. Thommes, “Quenched solid density functional theory and pore size analysis of micro-mesoporous carbons,” *Carbon N. Y.*, vol. 47, no. 7, pp. 1617–1628, 2009.

[89] P. I. Ravikovitch and A. V. Neimark, “Density functional theory model of adsorption deformation,” *Langmuir*, vol. 22, no. 26, pp. 10864–10868, 2006.

[90] N. a. Seaton, J. P. R. B. Walton, and N. Quirke, “A new analysis method for the determination of the pore size distribution of porous carbons from nitrogen adsorption measurements,” *Carbon N. Y.*, vol. 27, no. 6, pp. 853–861, 1989.

[91] P. I. Ravikovitch, A. Vishnyakov, R. Russo, and A. V. Neimark, “Unified Approach to Pore Size Characterization of Microporous Carbonaceous Materials from N 2 , Ar, and CO 2 Adsorption Isotherms †,” *Langmuir*, vol. 16, no. 5, pp. 2311–2320, 2000.

[92] P. Tarazona, “Free-energy density functional for hard spheres,” *Phys. Rev. A*, vol. 31, no. 4, pp. 2672–2679, 1985.

[93] P. Tarazona, U. Marconi, and R. Evans, “Phase equilibria of fluid interfaces and confined fluids,” *Mol. Phys.*, vol. 60, no. 3, pp. 573–595, Feb. 1987.

[94] J. Landers, G. Y. Gor, and A. V. Neimark, “Density functional theory methods for characterization of porous materials,” *Colloids Surfaces A Physicochem. Eng. Asp.*, vol. 437, pp. 3–32, 2013.

[95] M. Thommes, B. Smarsly, M. Groenewolt, P. I. Ravikovitch, and A. V. Neimark, “Adsorption Hysteresis of Nitrogen and Argon in Pore Networks and Characterization of Novel Micro- and Mesoporous Silicas,” *Langmuir*, vol. 22, pp. 756–764, 2006.

[96] Y. Rosenfeld, D. Levesque, and J.-J. Weis, “Free-energy model for the inhomogeneous hard-sphere fluid mixture: Triplet and higher-order direct correlation functions in dense fluids,” *J. Chem. Phys.*, vol. 92, no. 1990, pp. 6818–6832, 1990.

[97] S. Brunauer, P. H. Emmett, and E. Teller, “Gases i n Multimolecular Layers,” *J. Am. Chem. Soc.*, vol. 60, no. 1, pp. 309–319, 1938.

[98] J. Rouquerol and P. Llewellyn, “Is the BET Equation Applicable to Microporous Adsorbents?,” *Stud. Surf. Sci. Catal.*, vol. 160, pp. 49–56, 2007.

[99] D. W. McKee, “The sorption of hydrocarbon vapors by silica gel,” *J. Phys. Chem.*, vol. 63, no. 9, pp. 1256–1259, 1959.

[100] L. G. Gurvich, “Gurvich 1915,” *J. Russ. Phys. Chim*, vol. 47, p. 805, 1915.

[101] QuantaChrome Inc., “Powder Tech Note 34: Some Aspects of Quantachrome’s NOVA (NO Void Analysis) Technology.” QuantaChrome Inc., Boynton Beach.

[102] “The status of graphite development of gas cooled reactors,” International Atomic Energy Agency, Tokai-mura, Japan, IAEA-TECDOC-690, 1991.

[103] T. Yamashina and T. Hino, “Plasma-surface interactions of graphite as nuclear fusion material,” *Appl. Surf. Sci.*, vol. 48–49, no. C, pp. 483–497, 1991.

[104] T. M. Alslaibi, I. Abustan, M. A. Ahmad, and A. A. Foul, “A review: Production of activated carbon from agricultural byproducts via conventional and microwave heating,” *J. Chem. Technol. Biotechnol.*, vol. 88, no. 7, pp. 1183–1190, 2013.

[105] H. P. Boehm, “Some aspects of the surface chemistry of carbon blacks and other carbons,” *Carbon N. Y.*, vol. 32, no. 5, pp. 759–769, 1994.

[106] W. Feng, S. Kwon, E. Borguet, and R. Vidic, “Adsorption of Hydrogen Sulfide onto Activated Carbon Fibers: Effect of Pore Structure and Surface Chemistry,” *Environ. Sci. Technol.*, vol. 39, no. 24, pp. 9744–9749, 2005.

[107] S. M. Lee and Y. H. Lee, “Hydrogen storage in carbon nanotubes,” *Carbon N. Y.*, vol. 39, no. 10, pp. 1447–1454, 2001.

[108] Y. Miura, H. Kasai, W. Diño, H. Nakanishi, and T. Sugimoto, “First principles studies for the dissociative adsorption of H2 on graphene,” *J. Appl. Phys.*, vol. 93, no. 6, pp. 3395–3400, 2003.

[109] W. A. Diño, Y. Miura, H. Nakanishi, H. Kasai, T. Sugimoto, and T. Kondo, “H2 dissociative adsorption at the armchair edges of graphite,” *Solid State Commun.*, vol. 132, no. 10, pp. 713–718, 2004.

[110] P. Chen, X. Wu, J. Lin, and K. L. Tan, “High H_2 uptake by alkali-doped carbon nanotubes under ambient pressure and moderate temperature,” *Science (80-.).*, vol. 285, no. July, p. 91, 1999.

[111] A. V. Neimark and P. I. Ravikovitch, “Capillary Condensation in MMS and Pore Structure Characterization,” *Microporous Mesoporous Mater.*, vol. 44–45, pp. 697–707, 2001.

[112] A. Saito and H. C. Foley, “Curvature and parametric sensitivity in models for adsorption in micropores,” *AIChE J.*, vol. 37, no. 3, pp. 429–436, 1991.

[113] J. N. Caguiat, “Nanoporous Carbons: Porous Characterization and Electrical Performance in Electrochemical Double Layer Capacitors,” M.A.Sc. Thesis, University of Toronto, 2013.

[114] R. Ryoo, S. H. Joo, M. Kruk, and M. Jaroniec, “Ordered mesoporous carbons,” *Adv. Mater.*, vol. 13, no. 9, pp. 677–681, 2001.

[115] J. C. Groen, L. A. A. Peffer, and J. P??rez-Ram??rez, “Pore size determination in modified micro- and mesoporous materials. Pitfalls and limitations in gas adsorption data analysis,” *Microporous Mesoporous Mater.*, vol. 60, no. 1–3, pp. 1–17, 2003.

[116] S. T. Lam *et al.*, “Tritium Management and Control Using Carbon in a Fluoride-Salt-Cooled High-Temperature Reactor,” *Fusion Sci. Technol.*, vol. 71, no. 4, pp. 644–648, 2017.

[117] E. G. (University of L. Derouane, “Zeolites as solid solvents.” 1997.

[118] V. Bolis, “Fundamentals in Adsorption at the Solid-Gas Interface. Concepts and Thermodynamic,” in *Calorimetry and Thermal Methods in Catalysis*, 2013.

[119] W. Zhao *et al.*, “Activated carbons with appropriate micropore size distribution for hydrogen adsorption,” *Int. J. Hydrogen Energy*, vol. 36, no. 9, pp. 5431–5434, 2011.

[120] H. Atsumi, “Hydrogen retention in graphite and carbon materials under a fusion reactor environment,” *J. Nucl. Mater.*, vol. 313–316, no. SUPPL., pp. 543–547, 2003.

[121] E. Widiatmoko, M. Abdullah, and Khairurrijal, “A method to measure pore size distribution of porous materials using scanning electron microscopy images,” *AIP Conf. Proc.*, vol. 1284, pp. 23–26, 2010.

[122] X. Py, A. Guillot, and B. Cagnon, “Activated carbon porosity tailoring by cyclic sorption/decomposition of molecular oxygen,” *Carbon N. Y.*, vol. 41, no. 8, pp. 1533–1543, 2003.

[123] B. H. Foo, K. Y. Hameed, “Insights into the modeling of adsorption isotherm systems,” *Chem. Eng. J.*, vol. 156, pp. 2–10, 2010.

[124] I. Langmuir, “the Adsorption of Gases on Plane Surfaces of Glass, Mica and Platinum.,” *J. Am. Chem. Soc.*, vol. 40, no. 9, pp. 1361–1403, 1918.

[125] H. M. F. . Freundlich, “Über Die Absorption in Lösungen,” *Z. Phys. Chem.*, vol. 57, no. 1906, pp. 385–470, 1909.

[126] M. Asgari, H. Anisi, H. Mohammadi, and S. Sadighi, “Designing a commercial scale pressure swing adsorber for hydrogen purification,” *Pet. Coal*, vol. 56, no. 5, pp. 552–561, 2014.

[127] K. V. Kumar, K. Porkodi, and F. Rocha, “Isotherms and thermodynamics by linear and non-linear regression analysis for the sorption of methylene blue onto activated carbon: Comparison of various error functions,” *J. Hazard. Mater.*, vol. 151, no. 2–3, pp. 794–804, 2008.

[128] A. Heya and N. Matsuo, “Graphene oxide film reduction using atomic hydrogen annealing,” *Thin Solid Films*, vol. 625, pp. 93–99, 2017.

[129] H. Atsumi, Y. Takemura, T. Miyabe, T. Konishi, T. Tanabe, and T. Shikama, “Desorption of hydrogen trapped in carbon and graphite,” *J. Nucl. Mater.*, vol. 442, no. 1–3 SUPPL.1, pp. S746–S750, 2013.

[130] R. Krishna, T. J. H. Vlugt, and B. Smit, “Influence of isotherm inflection on diffusion in silicalite,” *Chem. Eng. Sci.*, vol. 54, no. 12, pp. 1751–1757, 1999.

[131] P. Chen, “High H2 Uptake by Alkali-Doped Carbon Nanotubes Under Ambient Pressure and Moderate Temperatures,” *Science (80-.).*, vol. 285, no. 1999, pp. 91–93, 1999.

[132] R. Ströbel, J. Garche, P. T. Moseley, L. Jörissen, and G. Wolf, "Hydrogen storage by carbon materials," *J. Power Sources*, vol. 159, no. 2, pp. 781–801, 2006.

[133] G. D. Del Cul, L. D. Trowbridge, L. M. Toth, J. N. Fiedor, and D. F. Williams, "Some investigations of the reaction of activated charcoal with fuorine and uranium hexafuoride," Oak Ridge National Laboratory, Oak Ridge, Tennessee, ORNL/TM-13052, 1998.

[134] H. Takagi, H. Hatori, and Y. Yamada, "Reversible adsorption/desorption property of hydrogen on carbon surface," *Carbon N. Y.*, vol. 43, no. 14, pp. 3037–3039, 2005.

[135] Y. Kojima *et al.*, "Hydrogen adsorption and desorption by carbon materials," *J. Alloys Compd.*, vol. 421, no. 1–2, pp. 204–208, 2006.

[136] K. Shindo, T. Kondo, M. Arakawa, and Y. Sakurai, "H ydrogen adsorption / desorption properties of mechanically milled activated carbon," *J. Alloys Compd.*, vol. 359, pp. 267–271, 2003.

[137] K. Y. Foo and B. H. Hameed, "Microwave-assisted regeneration of activated carbon," *Bioresour. Technol.*, vol. 119, pp. 41–47, 2012.

[138] P. Mocho and P. Le Cloirec, "Regeneration by induction heating of granular activated carbon loaded with volatile organic compounds," in *Environmental Technologies and Trends*, R. K. Jain, Ed. Springer-Verlag Berlin Heidelberg, 1997, pp. 125–140.

[139] P. Le Cloirec, "VOC adsorption-desorption cycle with activated carbon cloth : regeneration by Joule effect," in *Adsorption Science and Technology*, 2000.

[140] B. S. Schueller and R. T. Yang, "Ultrasound enhanced adsorption and desorption of phenol on activated carbon and polymeric resin," *Ind. Eng. Chem. Res.*, vol. 40, no. 1–3, pp. 4912–4918, 2001.

[141] H. Atsumi, S. Tokura, and M. Miyake, "Absorption and desorption of deuterium on graphite at elevated temperatures," *J. Nucl. Mater.*, vol. 155–157, no. PART 1, pp. 241–245, 1988.

[142] H. Atsumi, Y. Takemura, T. Konishi, T. Tanabe, and T. Shikama, "Thermal desorption of hydrogen from carbon and graphite at elevated temperatures," *J. Nucl. Mater.*, vol. 438, no. SUPPL, pp. S963–S966, 2013.

[143] K. Christmann, "Introduction to Surface Physical Chemistry," *J. Chem. Inf. Model.*, vol. 1, no. 9, 1991.

[144] W. J. Thomas and B. Crittenden, "The development of adsorption technology BT - Adsorption Technology & Design," in *Adsorption Technology & Design*, Oxford: Butterworth-Heinemann, 1998.

[145] M. Warrier, R. Schneider, E. Salonen, and K. Nordlund, "Modeling of the diffusion of hydrogen in porous graphite," *Phys. Scr.*, vol. 2004, p. 85, 2004.

[146] D. R. Olander, G. T. Fukuda, and C. F. B. Jr, “Equilibrium Pressures over BeF2/LiF(Flibe) Molten Mixtures,” *Fusion Sci. Technol.*, vol. 41, 2001.

[147] H. Atsumi, M. Iseki, and T. Shikama, “Trapping and detrapping of hydrogen in carbon-based materials exposed to hydrogen gas,” *J. Nucl. Mater.*, vol. 212–215, no. PART B, pp. 1478–1482, 1994.

[148] D. Carpenter, “Planned FHR IRP-2 Tritium Experiments at the MIT NRL,” in *Workshop on Tritium Control and Capture in Salt-Cooled Fission and Fusion Reactors*, 2015.

[149] QuantaChrome Inc., “Autosorb iQ and ASiQwin Gas Sorption System Operating Manual,” *Characterizing Porous Materials and Powders*. QuantaChrome Inc., Boynton Beach, FL, 2017.

[150] QuantaChrome Inc., “Powder Tech Notes 5 - 58,” Boynton Beach, FL, 2017.

Appendix A.

Adsorption Reference Standards

The Autosorb IQ-C-XR was validated against the known reference materials provided by QuantaChrome Inc.:

- Physisorption: 5 Å Molecular Sieve, Surface Area Reference Material (SARM) Catalog 2012, Lot No. 3615.
- Chemisorption: 2 wt. % Platinum (Pt) on Alumina (Al_2O_3), 3.2 mm (1/8 inch) pellets, Chemisorption Reference Material (CHRM) catalog 7001, Lot. 2615.

The results of the validation tests are shown here below.

Physisorption

In order to validate the physisorption experiments, a BET surface area measurement was taken for a known reference sample shown in Figure A.1. This was done using the method described in Chapter 4.3.3. The numerical results are shown in Table A.1.

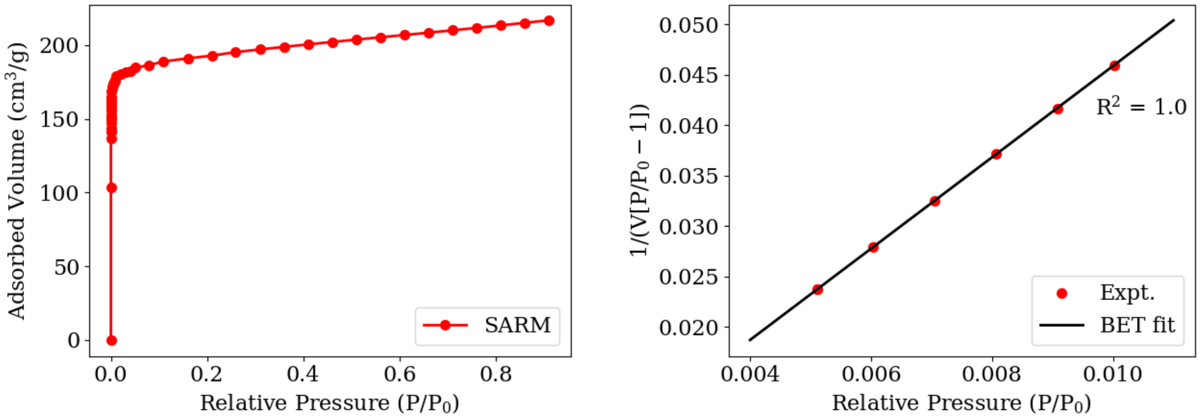

a) Adsorption Isotherm **b) BET Plot**

Figure A.1: Physisorption Reference Experiment with SARM 2012. a) Adsorption isotherm and b) BET plot to calculate surface area

Table A.1. BET physisorption validation – experimental results

Slope [1/g]	4.535
Intercept [1/g]	5.187
C constant	8743.76
Measured Surface Area (m²/g)	767.791
Known Surface Area (m²/g)	755.06 ± 68.70

Chemisorption

To validate the chemisorption experiments, the metal dispersion on a known reference sample is calculated. The dispersion is defined as the percentage of metal atoms that are available for chemisorption on the surface of material and is calculated by the equation [77]:

$$\delta = \frac{\mathrm{MN_a}}{\mathrm{L_{av}}} \cdot \frac{100}{\mathrm{W_s}\chi} \cdot 100\% \tag{A.1}$$

Where M is the molecular weight of the metal, $\mathrm{L_{av}}$ is avagadros number, $\mathrm{W_s}$ is the mass of the sample, χ is the mass of metal as a percentage of the total mass of the sample called the loading, and $\mathrm{N_a}$ is the number of exposed metal atoms. In the reference sample, the loading χ is known to be 2% platinum, which has a molecular weight of 95.08 g/mol. On platinum, it is known that each hydrogen atom dissociates and occupies two metal atoms and thus, the total number of exposed metal atoms is simply $\mathrm{N_a} = 2 \cdot \mathrm{N_m}$, where $\mathrm{N_m}$ is the number of gas molecules adsorbed on a monolayer of the metal. The $\mathrm{N_m}$ is related the volumetric monolayer volume for an ideal gas by the simple conversion:

$$\mathrm{N_m} = \frac{\mathrm{V_m L_{av}}}{22414} \tag{A.2}$$

For a platinum catalyst on the inert support alumina, the hydrogen undergoes dissociative adsorption on the platinum until it is saturated with a monolayer of hydrogen. Hydrogen adsorption continues due to spillover from the platinum to alumina and adsorbs weakly as a molecule on the support material creating a linear isotherm. Thus, running the chemisorption experiment at sufficiently high pressure and extrapolating the isotherm back to $\mathrm{P} = 0$, allows the determination of the saturated monolayer volume $\mathrm{V_m}$. The results of the chemisorption on the reference material is shown in Figure A.2. The results of the chemisorption experiment is shown in Table A.2.

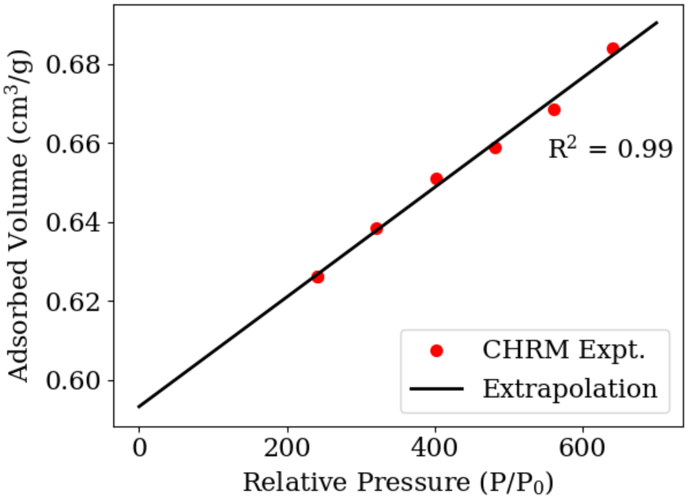

Figure A.2: Chemisorption reference material CHRM 7001 chemisorption isotherm

Table A.2: Metal dispersion chemisorption validation – experimental results

Slope	0.00014
Intercept	5.187
Monolayer Uptake N_m (μmol/g)	26.503
Measured Metal Dispersion (%)	51.708
Known Metal Dispersion (%)	58.15 ± 8.56

Appendix B.

Instrument Operation and Maintenance

Much of the sample pre-treatment, characterization and H_2 chemisorption experiments was done with the Autosorb IQ-C-XR. The data reduction was completed with ASIQ V4.01 software. The general theory and application was described in Chapter 4. The operation and methodological details were in accordance with recommendations that have been provided in the following manuals [149] and technical notes [150] that have been provided by QuantaChrome Inc.:

- Autosorb IQ and ASiQWin: Gas Sorption System Operating Manual
- Powder Tech Note 5: Representative sampling for surface area measurement
- Powder Tech Note 14: Sample conditioning
- Powder Tech Note 32: Practical solutions to prevent
- Powder Tech Note 31: Pore size analysis by gas adsorption
- Powder Tech Note 35: Micropore size analysis of porous carbons using CO_2 adsorption at 273.15K (0°C)
- Powder Tech Note 40: Application of quenched solid density functional theory - A novel density functional theory for accurate pore size analysis of disordered porous carbons
- Pore Tech Note 50: Physical adsorption characterization of mesoporous materials
- Powder Tech Note 52: Adsorptives for physisorption experiments: selection and their physical properties
- Powder Tech Note 53: Application of quenched solid density functional theory (QSDFT) for pore size analysis of cylindrical and spherical pore carbons
- Powder Tech Note 54: Automated software assistance for the proper calculation of BET area in microporous materials
- Powder Tech Note 58: Optimizing gas sorption parameters to minimize BET surface area analysis time

Appendix C.

Tritium Codes Functions, Inputs and Outputs

While some modifications have been made to the TRIDENT code, the fundamental structure the code remains the same and has been previously described in great detail [9]. The program consists of a set of MATLAB (R2013a) functions, which include an input file and several modules for calculating for corrosion, permeation, temperature profiles, tritium production, mitigation, and more. The files must be located in the same directory. The files in which changes were made for v1.1 are located in Table C.1.

Table C.1: TRIDENT main and supporting files. Refer to Table D.1. in Ref [9].

Function name and file extension	**Description**
run_TRIDENT.m	TRIDENT run file which calls the input file, main program, and prints results
TRIDENT_v1_1.m	TRIDENT main program
input_file.m	Input file for specifying a simulation in TRIDENT
polythermal_v1_1.m	Calculates tritium transport and mass transfer throughout the system. Handles coolant chemistry. Calls out to corrosion module and gas stripping modules. Calculates tritium uptake on graphite and diffusion through heat exchanger. Contains tritium mitigation system calculations (absorption on graphite and removal in permeation window)

C.1. TRIDENT Run File ‘run_TRIDENT.m’

Previously, in order to run the code, the user had to enter the main TRIDENT code file ‘TRIDENT.m’. In TRIDENT v1.1, the code run externally from a wrapper. This allows the code to be used more flexibly since TRIDENT can be called as required for a variety of analyses. Further, this simplifies the user interface and reduces the chance of the user inadvertently changing the main source code. During a standard simulation, TRIDENT.m should not require modification. The sections of the basic run file are shown and annotated below.

run_TRIDENT.m Header

```
%The run file performs the following actions
%1) Call input function
%2) Modify variables as required for looping
%3) Print Data or plot results
clear; clc;
```

Define and Modify TRIDENT Input Parameters

```
%Call the input file 'input_file'. The name of the input file can be
[Density_metal, MM, Wtfrac, Lattice_param, T_out, T_in, Rx_power, qo, T_avg, Days,
Elements, Corrosionflag, T_uptake, Redoxflag, Feedbackflag, Oxideflag, Kernel_d,
Buffer_t, IPyC_t, SiC_t, OPyC_t, TRISOperPebble, Pebble_radius, Core_height,
Core_mesh, CentralRef_radius, OuterRef_outradius, OuterRef_inradius,
Fuelzone_innerradius, Fuelzone_outerradius, pipe_d, pipe_l, Hot_mesh, pipe_d2,
pipe_l2, Cold_mesh, Hx_mesh, Hx_tube_od, Thick, A1, A2, C_Cr_initial_ppm, pipe_thick1,
pipe_thick2, pipe_zone1, pipe_zone2, slices1, slices2, slice_thick1, slice_thick2,
depth_inwall, flux, Tritiumproductionflag, GBflag, GasStrippingFlag, NStages_p,
NStages_s, G_s, G_p, Hour_Fraction, Birth_User, StrippingFlowFraction_p,
StrippingFlowFraction_s, PermeationFlag_primary, WindowArea_p, WindowThick_p, Vac_p,
PermeationFlag_secondary, WindowArea_s, WindowThick_s, Vac_s, PermElements,
Permp_tube_od, Perms_tube_od, Tritiumcapturebedflag, Bed_vessel_radius,
Bed_vessel_length, Particle_radius, Particle_density, Bed_packingfraction,
Bed_frac_rep, Restart, Restartfilename, Savefilename, Loops, PRFinput, PF, TubeNumber,
Hx1tubes, Hx2tubes, CoreGeometryAdjust, N_CoreFuelPebbles, N_CoreGrapPebbles,
CoreRefuelFrac, NumPermptubes_opt, NumberofPermeatorTubes,Ratio_TF_T2, Surf_area_gb,
Li7_enrichment, Tritiumcapturebedflag_s, Bed_frac_rep_s, Bed_vessel_radius_s,
Bed_surface_area_s, Particle_radius_s, Particle_density_s, Bed_packingfraction_s] =
input_file;

%Modify variables in the system as required (ie.For looping through simulations)
Bed_vessel_radius = 1.5; %[m]
Days = 1; %simulation time
```

TRIDENT Run Command

```
run TRIDENT_v1_1.m
```

Manipulate and Display Data

```
disp(['Maximum Release Rate: ', num2str(max(ReleaseRate_Ci))])
f1 = plot(x, ReleaseRate_Ci, 'LineWidth', 2.0);
xlabel('Time(days)'); ylabel('Tritium Release Rate (Ci/day)');
savefig(f1, savefig(f1, strcat(cd, '/output_files/', 'release_rate.fig'))
```

CODE OUTPUT

```
Maximum Release Rate: 65.0843
```

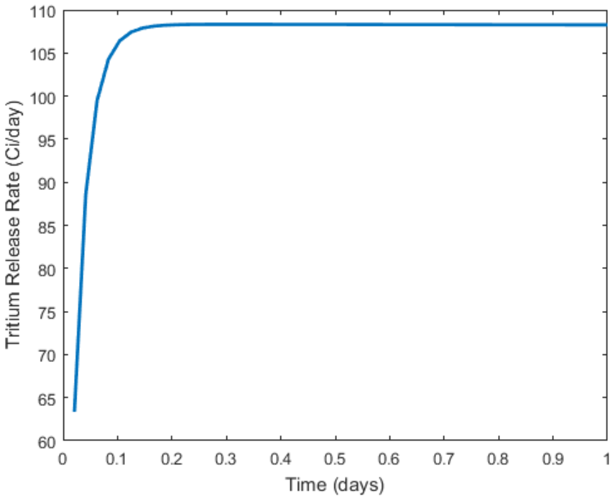

C.2. TRIDENT Main Program ‘TRIDENT_v1_1.m’

The main TRIDENT program can be identified by the header shown in the snapshot below. The main change to the code’s calculation are the fixes to the graphite bed calculation, which is located in the ‘polythermal_v_1.m’ file. In ‘TRIDENT_v1_1.m’, the initial reference to the input file and the plotting functions were removed since these actions are now called from an external run file. Additionally, output variables have been added which will be shown in C.4.

TRIDENT_v1_1.m Header

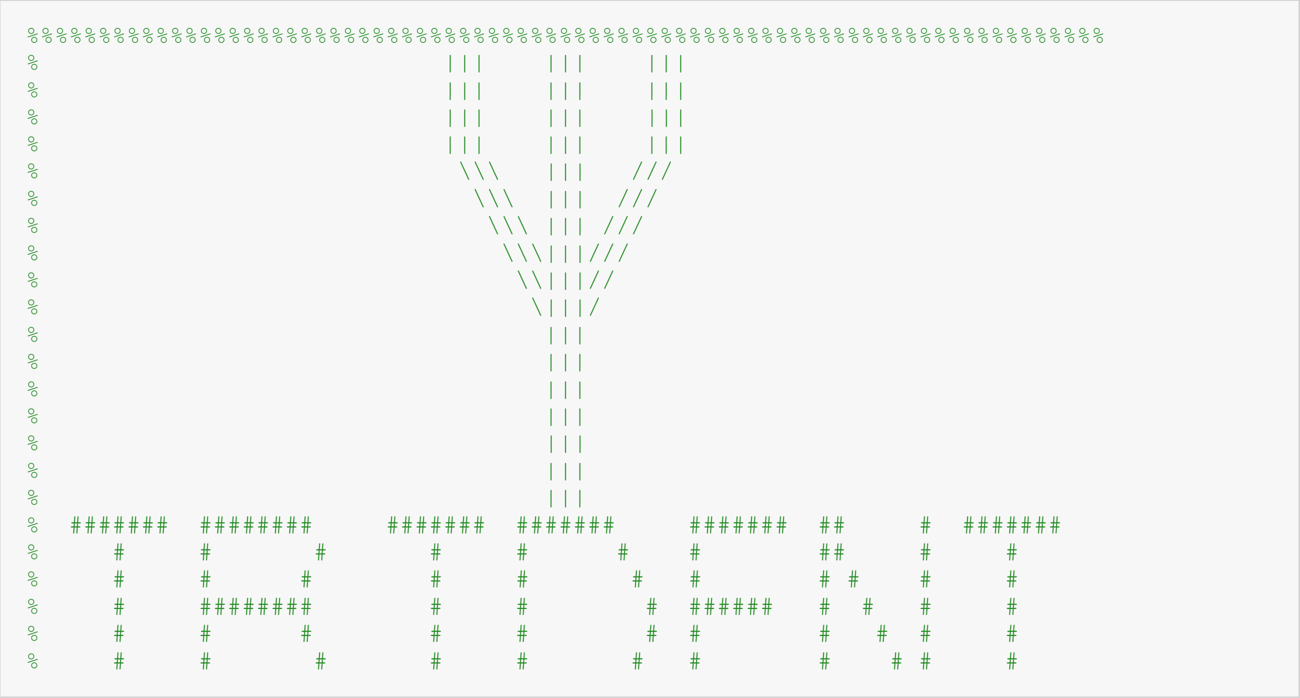

```
%%%%%%%%%%%%%%%%%%%%%%%%%%%%%%%%%%%%%%%%%%%%%%%%%%%%%%%%%%%%%%%%%%%%%%%%%%%
%                            |||    |||    |||
%                            |||    |||    |||
%                            |||    |||    |||
%                            |||    |||    |||
%                             \\\   |||   ///
%                              \\\  |||  ///
%                               \\\ ||| ///
%                                \\\|||///
%                                 \\|||//
%                                  \|||/
%                                   |||
%                                   |||
%                                   |||
%                                   |||
%                                   |||
%                                   |||
%                                   |||
%  #######  ########     #######  #######     #######  ##     #  #######
%     #     #       #       #     #      #    #        ##     #     #
%     #     #      #        #     #       #   #        # #    #     #
%     #     ########        #     #        #  ######   #  #   #     #
%     #     #      #        #     #        #  #        #   #  #     #
%     #     #       #       #     #       #   #        #    # #     #
```

```
%     #     #        #      #     #      #    #        #     ##     #
%     #     #        ##  #######  #######     #######  #     ##     #
%
%              TRItium Diffusion EvolutioN and Transport v1.1
%                                    by
%                              John D. Stempien
%             MIT, Department of Nuclear Science and Engineering
%                            Completed May 2015
%                            Last Updated 2017
%%%%%%%%%%%%%%%%%%%%%%%%%%%%%%%%%%%%%%%%%%%%%%%%%%%%%%%%%%%%%%%%%%%%%%%%%%%
%  Code Description:  Calculates tritium birth rates and concentrations in
%  the coolant loops of the FHR.  Simulates corrosion reactions of TF with
%  Cr and selective leaching of Cr from the structural metals in the
%  system.  Options exist to simulate tritium removal systems.
%
%  Now with fix to error in graphite capture bed.
%%%%%%%%%%%%%%%%%%%%%%%%%%%%%%%%%%%%%%%%%%%%%%%%%%%%%%%%%%%%%%%%%%%%%%%%%%%

%Use run_TRIDENT.m to initialize program
```

C.3. Input File ‘input_file.m’

The input file is described here starts with the function header, which creates the definitions, based on the user definitions in the preceding sections. The next sections include the base case simulation parameters and options outlined in Table 3.2 and Table 3.3, and the material properties of the metal surfaces in the system. The next sections contain the optional simulation configurations such as the adsorption bed options shown in Table 3.4, or the configurations for an optional gas stripping removal system, or permeation window. One change made to the adsorbent column input was the specification of the bed vessel length instead of the surface area. The last 2 sections of the input file contain the reactor core geometry, heat exchanger properties, primary system definitions, which haven taken or calculated from values in the Mk-1 technical report provided by UCB [5].

Input File Header

```
function [Density_metal, MM, Wtfrac, Lattice_param, T_out, T_in, Rx_power, qo, T_avg,
Days, Elements, Corrosionflag, T_uptake, Redoxflag, Feedbackflag, Oxideflag, Kernel_d,
Buffer_t, IPyC_t, SiC_t, OPyC_t, TRISOperPebble, Pebble_radius, Core_height,
Core_mesh, CentralRef_radius, OuterRef_outradius, OuterRef_inradius,
Fuelzone_innerradius, Fuelzone_outerradius, pipe_d, pipe_l, Hot_mesh, pipe_d2,pipe_l2,
Cold_mesh, Hx_mesh, Hx_tube_od, Thick, A1, A2, C_Cr_initial_ppm, pipe_thick1,
pipe_thick2, pipe_zone1, pipe_zone2, slices1, slices2, slice_thick1, slice_thick2,
depth_inwall, flux, Tritiumproductionflag, GBflag, GasStrippingFlag, NStages_p,
NStages_s, G_s, G_p, Hour_Fraction, Birth_User, StrippingFlowFraction_p,
StrippingFlowFraction_s, PermeationFlag_primary, WindowArea_p, WindowThick_p, Vac_p,
PermeationFlag_secondary, WindowArea_s, WindowThick_s, Vac_s, PermElements,
Permp_tube_od, Perms_tube_od, Tritiumcapturebedflag, Bed_vessel_radius,
Bed_vessel_length, Particle_radius, Particle_density, Bed_packingfraction,
```

```
Bed_frac_rep, Restart, Restartfilename, Savefilename, Loops, PRFinput, PF, TubeNumber,
Hx1tubes, Hx2tubes, CoreGeometryAdjust, N_CoreFuelPebbles, N_CoreGrapPebbles,
CoreRefuelFrac, NumPermptubes_opt, NumberofPermeatorTubes, Ratio_TF_T2, Surf_area_gb,
Li7_enrichment, Tritiumcapturebedflag_s, Bed_frac_rep_s, Bed_vessel_radius_s,
Bed_surface_area_s, Particle_radius_s, Particle_density_s, Bed_packingfraction_s] =
input_file
```

Base Case Simulation Parameters and Options

```
Restart = 1;  %If restarting a previous calculation, turn ON Restart = 2
              %If Restart = 1, restart is NOT used.  A fresh caclulation is performed
if Restart == 1
    Restartfilename = 'nothing';  %Only provide a file name to restart a calculation
if Restart = 2
elseif Restart == 2
    clear all
    Restart = 2;
    Restartfilename = strcat(cd, '\output_files\', 'restart_file.mat');  %Provide a
file name and directory to restart from if Restart = 2
end

Savefilename = strcat(cd, '\output_files\', 'output_file.mat');  %Provide a file name
and directory for saving the current run

%Reactor Temperature, time, time step, calculation model, and output options:
T_in = 873.15;   %Core inlet temperature [K]
T_out = 973.15;  %Core outlet temperature [K]
T_avg = 923.15;      %Core average temp in Kelvin. Used for the initial calculation of
flibe density
Rx_power = 236;      %Reactor power [MWt]
qo = 79.7221;        %Axial peak linear heat generation rate calculated from equation
in Ch. 14 of Todreas and Kazimi if core height and power are known [MWt]

Ratio_TF_T2 = 9.2E-5;  %Nominal = 9.2E-5 ratio of P_TF/Sqrt(P_T2) calculated at 650 C
for fluorine potential of -700.5 kJ/mol F2
Li7_enrichment = 99.995;  %wt % Li-7 enrichment in flibe.  Baseline is 99.995
Loops = 1;  %Number of coolant loops to simulate (options are 1 or 2).  Currently, any
secondary (intermediate loop uses the salt flinak)

Days = 1; %Total number of days of simulation

Hour_Fraction = 0.5;   %Record and store calculation results every fraction of an
hour.
                       %For example, if you want to record ouput every hour,
Hour_Fraction = 1. If you want to store output after every 30 minutes, Hour_fraction =
0.5
                       %This is useful for capturing behavior which occurs
                       %quickly.  Do not use less than 1 for long simulations.

%Calculation options
Elements = 6;     %Number of meshpoints for solving diffusion in HX.  When running
                    %finite difference, the number of Elements needs to be related
                    %to DT via the Fourier Number calculated lower down in
                    %the code

T_uptake = 2;      %Turn off/on tritium uptake on core graphite
                    %1 = off
                    %2 = on
CoreRefuelFrac = (1/30)/86400;  %Fraction of the core pebbles to "refuel" per second
                                %Set = 0 if not simulating core refueling
```

```
CoreGeometryAdjust = 2;   %Option to correct the pebble graphite surface areas in the
                          %core to account for non-uniform geometries.  TRIDENT
                          %only models concentric cylinders in the core, but there
                          %may be chutes and other geometries in a real core
                          %1 = off
                          %2 = on
                          %TRIDENT only uses the number of pebbles below if
CoreGeometryAdjust = 2
                          %Otherwise, TRIDENT calculates the number of pebbles in the
core based on the core geometry,
                          %the pebble size, and the pebble packing fraction in the
core
N_CoreFuelPebbles = 470000;  %Number of fuel pebbles in the core from Table 2-1 of Mk1
PB-FHR Report
N_CoreGrapPebbles = 218000;  %Number of graphite-only pebbles in the core from Table
2-1 of Mk1 PB-FHR Report

Redoxflag = 2;     %Turn off/on redox control
                    %1 = off - everything is T2, there is no TF and no corrosion
                    %2 = on, the user may specify a fixed redox condition as a ratio
via "Ratio_TF_T2" or

Feedbackflag = 2;  %Turn off/on redox feedback
                    %1 = off, calculates a fixed T2 and T+ generation rate based on an
initially specified redox potential, then
                    %  applies this generation rate for the entire calculation.  When
T2 diffusion occurs, this will change the overall redox
                    %  state in the coolant, but the T2 and T+ generation rate remains
constant.  Corrosion reactions do not alter the the T2 and T+ generation rate
                    %2 = on, Fixed redox: the generation rate of atoms T per second in
the reactor remains constant, but the portion of this
                    %  which is generated at T+ and the portion generated as T2 is
varied in order to maintain a fixed redox
                    %  potential in the coolant.  Any corrosion reactions are also
taken into account if Corrosionflag == 2 below
                    %3 = pseudo feedback, all T is produced as T+, corrosion reactions
produce T2, redox potential is allowed to
                    %  drift based on buildup of T+, consumption of T+ by corrosion,
generation of T2 by corrosion and diffusion
                    %  of T2.  Redox state is calculated, but not controlled

Oxideflag = 2;     %Turn off/on oxide layer permeation reduction on air side of HX
                    %1 = off
                    %2 = on
PRFinput = 10;     %Permeation reduction factor due to an oxide layer on the air-
facing side of the heat exchanger.  Only used if Oxideflag = 2


Corrosionflag = 1;  %Turn off/on corrosion of structural metals
                      %1 = off, no corrosion
                      %2 = on, corrosion is considered
GBflag = 2;         %Turn off/on corrosion surface area adjustment based on GB. Only
meaningful if Corrosionflag = 2
                      %1 = off, use whole surface area
                      %2 = on, adjust active surface area for corrosion to
                      %only the surface area of the grain boundaries
if GBflag ==2
    GB_diameter = 31.8E-6;   %Grain boundary diameter for 316 from azom.com (spacing
between grain boundaries) [m]
    % GB_diameter = 10E-6;  %304 L stainless fine grain size
%     GB_diameter = 23E-6;  %23E-6 304 L stainless from kestenbach, 1976 springer
```

```
    %     GB_diameter = 60E-6;    %Grain boundary diameter (spacing between grain
boundaries) for Hastelloy X  88 micron from Lippold 2013 [m]
    %     GB_diameter = 24E-6;    %Grain boundary diameter (spacing between grain
boundaries) for Hastelloy X. 24 micron from Abuzaid.  88 micron from Lippold 2013 [m]
    GB_width = 10E-9;      %Grain boundary width [m]  For 10 Ni atomic distances
2.48E-9 m

    %     GB_width = 0.01E-6;      %Grain boundary width [m]  For Hastelloy N, grain
width is about 0.5 nm?
    %     Surf_area_gb =
(4*(GB_diameter*GB_width)+GB_width^2)/(2*GB_diameter+GB_width)^2;  %Multiplier with
units of m2 GB surface per m2 of metal surface.  Typically around 3E-4
    %
    Circ_radius = (2*GB_diameter+sqrt(3)*GB_width/2)/2;
    Surf_area_gb =
((3*GB_diameter*GB_width)+(sqrt(3)/4)*GB_width^2)/(pi*(Circ_radius)^2); %Multiplier
with units of m2 GB surface per m2 of metal surface.

else
    Surf_area_gb = 1;  %Surface area not adjusted for grain boundaries
end
```

Define Material Properties

```
Density_metal = 8000;  %[kg/m^3] density of 316L SS from azom.com
%     Cr       Fe      Ni      C       Mn      P       S       Si      Mo     N
Molar Mass [g/mol]
MM = [51.9961; 55.845; 58.693; 12.011; 54.938; 30.974; 32.065; 28.086; 95.94; 14.007];
%  Note that the Fe wt fraction is set to 0.00 initially.  Iron is assumed to make up
the balance of SS, and is calculated separately after all the other elements are
specified
%         Cr    Fe    Ni    C       Mn    P        S       Si      Mo     N     Weight
fraction from aksteel.com for 316L SS
Wtfrac = [0.18; 0.00; 0.12; 0.0003; 0.02; 0.00045; 0.0003; 0.0075; 0.025; 0.001];
Wtfrac(2,1) = 1-sum(Wtfrac); %Iron is the balance of the 316 composition

Lattice_param = 0.359E-9;  %[m] lattice parameter for austenite in 316 L stainless
steel


C_Cr_initial_ppm = 25; %Initial Cr concentration [ppm] in the salt after processing
pipe_zone1 = 0.000254; %[m] Thickness over which corrosion calcs are done for TF
transport limited mode
pipe_zone2 = 0.000254; %[m] Thickness over which corrosion calcs are done for Cr
diffusion limited mode
slices1 = 10;  %number of slices at which to calc Cr concentration distribution
slices2 = 10;  %number of slices at which to calc Cr concentration for Cr diff limited
mode
slice_thick1 = pipe_zone1/slices1;  %[m] thickness of each slice of the pipe through-
wall thickness for TF-limited case
slice_thick2 = pipe_zone2/slices2;  %[m] thickness of each slice of the pipe through-
wall thickness for Cr diffusion-limited case
depth_inwall = (0:pipe_zone1/slices1:pipe_zone1);  %[m] depth of each slice in the
pipe wall

Tritiumproductionflag = 3;  %Turn off/on variable tritium production rate with time
                            %Tritium production rate in primary loop.  Moles of T
atoms per second
                            %1 = use BOL tritium generation rate, time variation is
OFF, BOL generation rate is used for entire calculation
```

```
                            %2 = use EOL tritium generation rate, time variation is
OFF, equilibrium production rate is used
                            %3 = variation is ON, tritium production varies
                            %as Li-6 is consumed and Be-9 is transmuted to Li-6 based
on a model from Cisneros, 2013
                            %4 = user specifies the tritium production rate in units
of [molt T/sec]
                            if Tritiumproductionflag == 4
                                Birth_User = (7.44486E-7);  %[Mole T/sec] for 900 MWt
PB-FHR based on AHTR estimates (7.44486E-7) used in ICAPP 2014 Paper
                            else
                                Birth_User = 0;  %Birth_User not used.  Use
Tritiumproduction flag 1, 2, or 3 to specify birth rate.
                            end

flux = 3.41E14;  %flux in coolant for tritium calculation (n/cm2-s).  From Cisneros,
2013
%%%%%%%%%%%%%%%%%%%%%%%%%%%%%%%%%%%%%%%%%%%%%%%%%%%%
```

Adsorption Column for Capture of Tritium

```
%%%%%%%%%%%%%%%%%%%%%%%%%%%%%%%%%%%%%%%%%%%%%%%%%%%%%%
%   Primary Graphite Bed for Capture of Tritium      %
%%%%%%%%%%%%%%%%%%%%%%%%%%%%%%%%%%%%%%%%%%%%%%%%%%%%%%

Tritiumcapturebedflag = 2;  %1 = tritium capture on separate graphite bed is turned
OFF
%2 = tritium capture on separate graphite bed is turned ON
%Model options for graphite bed
Bed_frac_rep = 1/31;      %Fraction of bed to be replaced aka replacement rate
[fraction of bed graphite/d]. If this is 0, then the bed is not replaced online
Bed_frac_rep = Bed_frac_rep*(1/86400);  %Fraction of bed being replaced per second
%Input variables for graphite absorption bed
Particle_radius = 0.015;  %[m] radius of particle/pebble assuming a spherical particle
Bed_packingfraction = 0.60;  %Packing fraction in the graphite bed. Fraction of bed
volume occupied by pebbles
Bed_vessel_radius = 1.5; %[m]
Particle_density = 0.45E6;  %From Calgon Carbon OVC 4x8 [g/m^3];
%Particle_density = 1.77E6 From Toyo Tanso density for IG-110U graphite [g/m^3];
Bed_vessel_length = 4.5;  %[m] Length of the bed vessel

%%%%%%%%%%%%%%%%%%%%%%%%%%%%%%%%%%%%%%%%%%%%%%%%%%%%%%
%   Secondary Graphite Bed for Capture of Tritium    %
%%%%%%%%%%%%%%%%%%%%%%%%%%%%%%%%%%%%%%%%%%%%%%%%%%%%%%
Tritiumcapturebedflag_s = 1;  %1 = tritium capture on separate graphite bed turned OFF
%2 = tritium capture on separate graphite bed is turned ON
%Model options for graphite bed
Bed_frac_rep_s = 1/31;      %Fraction of bed to be replaced aka replacement rate
[fraction of bed graphite/d]. If this is 0, then the bed is not replaced online
Bed_frac_rep_s = Bed_frac_rep_s*(1/86400);  %Fraction of bed being replaced per second
%Input variables for graphite absorption bed
Bed_vessel_radius_s = 1.2; %[m]
Bed_surface_area_s = 1945.3;  %[m2] total bed surface area
Particle_radius_s = 0.015;  %[m] radius of particle/pebble assuming a spherical part.
Particle_density_s = 1.77E6;  %From Toyo Tanso density for IG-110U graphite [g/m^3];
Bed_packingfraction_s = 0.60;  %Packing fraction in the graphite bed. Fraction of bed
volume occupied by pebbles
%%%%%%%%%%%%%%%%%%%%%%%%%%%%%%%%%%%%%%%%%%%%%%%%%%%%%%%
```

Gas Stripping for Tritium Removal

```
GasStrippingFlag = 1;  % Option for including counter current gas strippers at various
points in the system
                       % If stripping is used, strippers are located just before the
heat exchangers
                       % 1 = no gas strippers
                       % 2 = gas stripping in primary coolant system only
                       % 3 = gas stripping in secondary coolant system only
                       % 4 = gas stripping in both primary and secondary system
StrippingFlowFraction_p = 0.5;  %Put value from 0 to 1.  Specifies how much of the
primary flow rate is diverted into the gas stripper
                             %1 means that the full primary coolant flow is going
through the stripper
                             %Anything < 1 means that only a fraction of the coolant
flow is being diverted to the stripper
StrippingFlowFraction_s = 0.5; %Put value from 0 to 1.  Specifies how much of the
secondary coolant flow is diverted into the gas stripper
NStages_p = 10;  %Number of stages in primary gas stripper
NStages_s = 10;  %Number of stages in secondary gas stripper
Gas_hrflowrate_p = 20000;  %Stripping gas flow rate [L/hr] at STP in primary
G_p = (Gas_hrflowrate_p*0.987/(0.08206*273.15))*(1/3600); %Use IGL to conver stripping
gas flow rate in primary [mole/s]
Gas_hrflowrate_s = 20000;  %Stripping gas flow rate [L/hr] at STP in secondary
G_s = (Gas_hrflowrate_s*0.987/(0.08206*273.15))*(1/3600); %Use IGL to conver stripping
gas flow rate in secondary [mole/s];

%%%%%%%%%%%%%%%%%%%%%%%%%%%%%%%%%
```

Permeation Window for Removal of Tritium

```
%%%%%%%%%%%%%%%%%%%%%%%%%%%%%%%%%

%TRIDENT assumes that the flow area in the permeators is equal to the flow
%area of the pipe flowing into the permeator
NumPermptubes_opt = 2;  %Option to specify the number of tubes in the permeator or to
have TRIDENT calculate the number of tubes based on other input
                        %1 = off
                        %2 = on, user specifies number of tubes
NumberofPermeatorTubes = 2*13680; %Number of tubes to put in the permeator
PermElements = 6;  %Number of radial finite difference elements in the primary and/or
secondary permeator(s)
%Primary System
%%%%%%%%********NOTE: need to tell TRIDENT main program what the diffusion
%%%%%%%%coefficient is for the permeator so that it can calculate an
%%%%%%%%appropriate DT size (around line 680 in main program)
PermeationFlag_primary = 1;     %1 = off
                                %2 = on;  Permeation window is turned on in the
primary system.
WindowArea_p = 12000;   %Surface area of primary system permeation window (m^2)
WindowThick_p = 8.89E-4;  %(Hx thickness 8.89E-4 m)Thickness of primary system
permeation window tube walls (m)
Permp_tube_od = 0.00635;  %Primary permeator tube outer diameter [m]
Vac_p = 1E-6; %NOT USED -- Pressure on outside of permeation window (side opposite the
coolant flow) [Pa]
%Secondary System
PermeationFlag_secondary = 1;   %1 = off
                                %2 = on - permeation window is turned on in the
secondary system
WindowArea_s = 10082;   %Surface area of secondary system permeation window (m^2)
WindowThick_s = 8.89E-4;  %Thickness of secondary system permeation window (m)
```

```
Perms_tube_od = 0.00635; %Secondary permeator tube outer diameter [m]
Vac_s = 1E-6;  %NOT USED -- Pressure on outside of permeation window [Pa]

%Fuel pebble and TRISO particle properties  %From PB-FHR Mk1 Report
Kernel_d = 400E-6;      %Fuel kernel diameter [m]
Buffer_t = 100E-6;      %Buffer thickness [m]
IPyC_t = 35E-6;         %IPyC thickness [m]
SiC_t = 35E-6;          %SiC layer thickness [m]
OPyC_t = 35E-6;         %OPyC thickness [m]
TRISOperPebble = 4730;    %Number of TRISO particles per pebble
Pebble_radius = 1.5/100;  %Pebble radius [m]  3cm diameter pebble
PF = 0.60;           %Pebble packing fraction
```

Reactor Core Geometry

```
Core_height = 4.65;           %236 MWt core effective height based on Figure 2-17 in
p.61 of PB-FHR Mk1 Report [m]
Core_mesh = 10;               %Number of axial core divisions for polythermal loop
calculations
CentralRef_radius = 0.35;      %Central reflector radius [m]
OuterRef_outradius = 1.69;     %Outer reflector outer radius [m] Based on Table 1-5
OuterRef_inradius = 1.25;     %Outer refelctor inner radius [m]
Fuelzone_innerradius = 0.35;  %Fuel zone inner radius [m]
Fuelzone_outerradius = 1.05;  %Fuel zone outer radius [m]

%Reactor Hot Leg Pipe Parameters from p. 89 of Mk1 PB-FHR Report where the
%four manifold pipes are combined into a single pipe having equivalent
%inner cross sectional area
pipe_thick1 = 0.02;  %Pipe wall thickness [m]
pipe_d = 0.79196; %Pipe inner diameter [m]
pipe_l = 29.74;  %Pipe length [m]
Hot_mesh = 10;  %number of axial divisions for polythermal loop calculations

%Reactor Cold Leg pipe parameters
pipe_thick2 = 0.02;  %Pipe wall thickness [m]
pipe_d2 = 0.494975;  %Pipe inner diameter [m]
pipe_l2 = 35.443;   %Pipe length [m]
Cold_mesh = 10;  %number of axial divisions for polythermal loop calculations

%%%%%%%%%%%%%%%%%%%%%%%%%%%%%%%%%%%%%%%%%%%%%%%%%%%%%%%%%%%%%%%%%%%%%%%%%%
```

Heat Exchanger Properties, Coolant Volumes from Mk-1 Technical Description

```
%%%%%%%%%%%%%%%%%%%%%%%%%%%%%%%%%%%%%%%%%%%%%%%%%%%%%%%%%%%%%%%%%%%%%%%%%%
TubeNumber = 1;  %TubeNumber = 1: input number of tubes in the HX1 and HX2 if known
                 %TubeNumber = 0: number of HX tubes is calculated in
                 %TRIDENT assuming the total flow cross sectional area in
                 %the HX matches that in the hot leg pipe
Hx1tubes = 2*13680;  %Number of HX1 tubes (from Table 3-2 in Mk1 Report)
Hx2tubes = 2*13680;  %Number of Hx2 tubes

Hx_mesh = 10;  %number of axial mesh points for the primary HX for polythermal loop
calculations
Hx_tube_od = 0.00635; %[m] Heat exchanger tube outer diameter from MK1-PB-FHR paper
Thick = 8.89E-4; %Heat exchanger tube wall thickness from Mk1-PB-FHR [m]
%1.6E-3;  %Heat exchanger tube wall thickness [m] from ICAPP 2014 report
A1 = 2*5041;  %Primary heat exchanger surface area from MK1-PB-FHR paper [m^2]
A2 = 2*5041;  %Secondary heat exchanger surface area from MK1-PB-FHR paper[m^2]
```

```
end
```

C.4. Transport Calculation File ‘polythermal_v1_1.m’

The main changes in the ‘polythermal_v1_1.m’ are in the graphite bed section of the code, which includes the correction of previous numerical error, addition of the isotherm for OVC 4x8 and the implementation of the equilibrium boundary condition at the solid-fluid interface. The code for this section of the code is shown below.

Adsorption Column Calculation

```
C_TF = mt1_TF/Mole_flibe;  %Current concentration of TF in primary [mole TF/mol Flibe]
PP_TF = (C_TF/k_HenryTF)*101325;  %Partial pressure of TF above the melt [Pa]
Tgraphite_TF = 2*(5.618912575*((2.453167518*PP_TF/1000)^(1/1.75862069))/(1 +
(2.453167518*PP_TF/1000)^(1/1.75862069)))*(4.4643e-5); % ovc 4x8 capacity [moles TF
per gram graphite Pressure in Pa] Langmuir Equation
%Tgraphite_TF =
((((2*0.00019)*sqrt(PP_TF)*exp(19/(0.00831446*T)))*100)/(8314.46*273.15));  %Capacity,
[Moles TF per gram graphite] at T[K] and P[Pa]. From Atsumi, 1988
TF_bed_limit = Tgraphite_TF;       %solubility limit of the graphite pebble [mol TF
per gram graphite]

%%%%%%%%%%%%%%%%%%%%%%%%%%%%%%
% Capture TF on graphite bed %
%%%%%%%%%%%%%%%%%%%%%%%%%%%%%%

%Alter mtgbed_TF if graphite bed removal fraction is > 0.
%This means that some of the graphite in the bed is removed at some rate so that the
tritium can be removed and the graphite regenerated.  Thus, the total amount of TF on
the
%graphite has decreased but the bed mass remains constant
mtgbed_TF = mtgbed_TF*(1-Bed_frac_rep*DT);  %Bed_frac_rep is the fraction of the bed
graphite that is replaced per second.  If Bed_frac_rep = 0, then no replacement
occurs.
if mtgbed_TF < Tgraphite_TF*Bed_mass  %If moles of TF on grahpite in the absorption
bed has not been saturated, do transport
    mt1_TF_old = mt1_TF;  %Record old moles of TF in the primary coolant
    mtgbed_TF_old = mtgbed_TF;  %Record old moles of TF on the bed graphite

    %Solve for the concentration at the surface of the graphite by uisng solubilty
equaiton and henry's law
    %PP_TFeq =
((mtgbed_TF/Bed_mass)*(8314.46*273.15)/100/(exp(19/(0.00831446*T)))/(2*0.00019))^2;
%TF equilibrium pressure in Pa with the solid ISO-88
    PP_TFeq = (1/2.453167518)*(((2*5.618912575)/(mtgbed_TF/Bed_mass/(4.4643e-5)) -
1)^(-1.75862069))*1000;           %TF equilibrium pressure in Pa with the solid OVC4x8
LANGMUIR Model
    C_TF_surf = (PP_TFeq/101325)*k_HenryTF*(Mole_flibe/Vol_1);    %surface
concentration of TF using henry's law [mol TF/m^3 of flibe]
    %%%%%%%%%%%%%%%%%%%%%

    jgbed_TF = Bed_k_masspebble_TF_temp*((mt1_TF/Vol_1) - C_TF_surf);
```

```
    mtgbed_TF = mtgbed_TF + jgbed_TF*(Bed_surface_area)*DT;  %Calculate new total
moles of T+ adsorbed onto bed graphite [mol] assuming all T+ reaching graphite surface
is adsorbed
    CumulativeTF_old_gbed = CumulativeTF_gbed;  %Total, Cumulative moles of TF
absorbed on the graphite up to this point [moles TF]
    CumulativeTF_gbed = CumulativeTF_gbed + jgbed_TF*(Bed_surface_area)*DT; %New
cumulative amount of TF captured on graphite in the bed
    mt1_TF = mt1_TF - jgbed_TF*(Bed_surface_area)*DT;  %Calc new mt1_TF moles of TF in
the coolant after some has been adsorbed on graphite
    C_TF = mt1_TF/Mole_flibe;  %Update the current concentration of TF in primary
[mole TF/mol flibe]
    PP_TF = (C_TF/k_HenryTF)*101325;  %Calculate new partial pressure of TF above the
melt [Pa]
    %Tgraphite_TF =
((((2*0.00019)*sqrt(PP_TF)*exp(19/(0.00831446*T)))*100)/(8314.46*273.15));  %Calculate
new bed capacity for TF [mole TF/g graphite]
    %Tgraphite_TF = 2*(1.118943393*(PP_TF/1000)^(0.36582176) +
2.714730971*((7.032151715*PP_TF/1000)/(1 + 7.032151715*PP_TF/1000)))*(4.4643e-5);
    Tgraphite_TF = 2*(5.618912575*((2.453167518*PP_TF/1000)^(1/1.75862069))/(1 +
(2.453167518*PP_TF/1000)^(1/1.75862069)))*(4.4643e-5); % ovc 4x8 capacity [moles TF
per gram graphite Pressure in Pa] Langmuir Equation
    if mtgbed_TF > Tgraphite_TF*Bed_mass  %If this is true, the graphite has
saturated.  Return the values to the previous ones.
        mt1_TF = mt1_TF_old;
        mtgbed_TF = mtgbed_TF_old;
        CumulativeTF_gbed = CumulativeTF_old_gbed;
    else %Accept the values from the calculation and proceed
    end
else %Graphite is already saturated.  Do not transport to it any more
end

%%%%%%%%%%%%%%%%%%%%%%%%%%%%%%%%
% Capture T2 on graphite bed %
%%%%%%%%%%%%%%%%%%%%%%%%%%%%%%%%

C_T2 = mt1_T2/Mole_flibe;  %Current concentration of T2 in the primary [mole T2/mole
Flibe]
PP_T2 = (C_T2/k_HenryT2)*101325;  %Partial pressure of T2 above the melt [Pa]
%Tgraphite_T2 =
((((0.00019)*sqrt(PP_T2)*exp(19/(0.00831446*T)))*100)/(8314.46*273.15));  %Capacity,
[Moles T2 per gram graphite] at T[K] and P[Pa]. From Atsumi, 1988
%Tgraphite_T2 = (1.118943393*(PP_T2/1000)^(0.36582176) +
2.714730971*((7.032151715*PP_T2/1000)/(1 + 7.032151715*PP_T2/1000)))*(4.4643e-5);
Tgraphite_T2 = (5.618912575*((2.453167518*PP_T2/1000)^(1/1.75862069))/(1 +
(2.453167518*PP_T2/1000)^(1/1.75862069)))*(4.4643e-5); % ovc 4x8 capacity [moles T2
per gram graphite Pressure in Pa] Langmuir Equation
T2_bed_limit = Tgraphite_T2; %solubility limit of the graphite pebble [mol T2 per gram
graphite]

mtgbed_T2 = mtgbed_T2*(1-Bed_frac_rep*DT);  %Bed_frac_rep is the fraction of the bed
graphite that is replaced per second by fresh graphite. If Bed_frac_rep = 0, then no
replacement occurs.

if mtgbed_T2 < Tgraphite_T2*Bed_mass  %If moles of T2 on grahpite in the absorption
bed has not been saturated, do transport
    mt1_T2_old = mt1_T2;  %Record old moles of T2 in the primary coolant
    mtgbed_T2_old = mtgbed_T2;  %Record old moles of T2 on the bed graphite

    %Solve for the concentration at the surface of the graphite by uisng solubilty
equaiton and henry's law
```

```
    %PP_T2eq =
((mtgbed_T2/Bed_mass)*(8314.46*273.15)/100/(exp(19/(0.00831446*T)))/(0.00019))^2;
%ISO-88 TF equilibrium pressure in Pa with the solid
    PP_T2eq = (1/2.453167518)*(((5.618912575)/(mtgbed_T2/Bed_mass/(4.4643e-5)) - 1)^(-
1.75862069))*1000;           %OVC 48 Langmuir T2 equilibrium pressure in Pa with the
solid
    C_T2_surf = (PP_T2eq/101325)*k_HenryT2*(Mole_flibe/Vol_1);    %surface
concentration of T2 using henry's law [mol TF/m^3 of flibe]
    %%%%%%%%%%%%%%%%%%%%%


    jgbed_T2 = Bed_k_masspebble_T2_temp*((mt1_T2/Vol_1) - C_T2_surf);
    mtgbed_T2 = mtgbed_T2 + jgbed_T2*(Bed_surface_area)*DT;  %Calculate new total
moles of T2 adsorbed onto bed graphite [mol] assuming all T2 reaching graphite surface
is adsorbed
    CumulativeT2_old_gbed = CumulativeT2_gbed;  %Total, Cumulative moles of T2
absorbed on the graphite up to this point [moles T2]
    CumulativeT2_gbed = CumulativeT2_gbed + jgbed_T2*(Bed_surface_area)*DT; %New
cumulative amount of T2 captured on graphite in the bed
    mt1_T2 = mt1_T2 - jgbed_T2*(Bed_surface_area)*DT;  %Calc new mt1_T2 moles of T2 in
the coolant after some has been adsorbed on graphite
    C_T2 = mt1_T2/Mole_flibe;  %Update the current concentration of T2 in primary
[mole T2/mol flibe]
    PP_T2 = (C_T2/k_HenryT2)*101325;  %Calculate new partial pressure of T2 above the
melt
    %Tgraphite_T2 =
((((0.00019)*sqrt(PP_T2)*exp(19/(0.00831446*T))*100)/(8314.46*273.15));  %Calculate
new bed capacity for T2 [mole T2/g graphite]
    %Tgraphite_T2 = (1.118943393*(PP_T2/1000)^(0.36582176) +
2.714730971*((7.032151715*PP_T2/1000)/(1 + 7.032151715*PP_T2/1000)))*(4.4643e-5);
    Tgraphite_T2 = (5.618912575*((2.453167518*PP_T2/1000)^(1/1.75862069))/(1 +
(2.453167518*PP_T2/1000)^(1/1.75862069)))*(4.4643e-5); % ovc 4x8 capacity [moles T2
per gram graphite Pressure in Pa] Langmuir Equation

    if mtgbed_T2 > Tgraphite_T2*Bed_mass  %If this is true, the graphite has
saturated.  Return the values to the previous ones.
        mt1_T2 = mt1_T2_old;
        mtgbed_T2 = mtgbed_T2_old;
        CumulativeT2_gbed = CumulativeT2_old_gbed;
    else %Accept the values from the calculation and proceed
    end
else %Graphite is already saturated.  Do not transport to it any more
end

%Model corrosion/deposition here? If so, need mass transfer
%parameters

%Do redox balance for coolant exiting the bed if the redox is held constant in the
coolant
if Feedbackflag == 2;  %Feedback ON. Fraction P_TF/(P_T2)^0.5 is held constant in the
salt. Adjustment being made now after TF birth and T2 destruction from CrF2
precipitation
    C_total =  (mt1_TF + 2*mt1_T2)/(Mole_flibe); %[Mole of T atoms/Mole of flibe]
    C_T2 = (4*C_total*k_HenryT2+(k_HenryTF^2)*(Ratio_TF_T2^2)-
sqrt(8*C_total*k_HenryT2*(k_HenryTF^2)*(Ratio_TF_T2^2) ...
        +(k_HenryTF^4)*(Ratio_TF_T2^4)))/(8*k_HenryT2);  %[mole T2/mole flibe] This is
a generation rate for per unit dt. This is the solution from squaring and then using
quadratic formula
    C_TF = C_total -2*C_T2;        %[mole TF/mole flibe] mole fraction TF in flibe
    mt1_T2new = C_T2*(Mole_flibe) - mt1_T2;  %[Change in moles of T2 in primary] due
to redox control feedback.  mt1_Txnew is calculated in case the new value is less than
the old one, then mt1_new will be negative.
```

```
    mt1_TFnew = C_TF*(Mole_flibe) - mt1_TF;  %[Change in moles TF in primary] due to 
redox control feedback
    mt1_T2 = mt1_T2 + mt1_T2new;  %Current total T2 in total primary [mole T2] at 
entrance to hot leg
    mt1_TF = mt1_TF + mt1_TFnew;  %Current total TF in total primary [mole T+] at 
entrance to hot leg

else
end
```

C.5. TRIDENT Code Outputs

When a TRIDENT run is completed, all variables in the workspace are saved to a .mat file using the name and directory specified by `Savefilename` in the file input. The key results are saved in the `OutputData` matrix, which is composed of column vectors tracking the time-dependent simulation data. Some of the key results includes the time, tritium release, coolant activity, partial pressures, and redox condition vectors. Additionally, five new outputs have been added to provide better diagnostic of the adsorption bed behavior summarized in Table C.2.

Table C.2: Additions to time-dependent simulation data matrix `OutputData`. Refer to Table D.2. of Ref [9] for full list of available output

Column in `OutputData`	Vector Name	Description
24	`bed_TF_solubility`	Solubility limit of TF in adsorption bed (cm^3 STP/g)
25	`bed_TF_concentration`	Concentration of TF in adsorption bed (cm^3 STP/g)
26	`bed_T2_solubility`	Solubility limit of T_2 in adsorption bed (cm^3 STP/g)
27	`bed_T2_concentration`	Concentration of TF in adsorption bed (cm^3 STP/g)
28	`Tinventorycore_track *29263.83`	Instantaneous T activity in core graphite (Ci)